To the Graduate Council:

I am submitting herewith a dissertation written by Konstantin Dmitrievich Shmakov entitled "Study of Nonlinear QED Effects in Interactions of Terawatt Laser with High Energy Electron Beam." I have examined the final copy of this dissertation for form and content and recommend that it be accepted in partial fulfillment of the requirements for the degree of Doctor of Philosophy, with a major in Physics.

William Bugg, Major Professor

We have read this dissertation
and recommend its acceptance:

Accepted for the Council:

Associate Vice Chancellor and
Dean of The Graduate School

STUDY OF NONLINEAR QED EFFECTS IN INTERACTIONS OF TERAWATT LASER WITH HIGH ENERGY ELECTRON BEAM

A Dissertation
Presented for the
Doctor of Philosophy
Degree
The University of Tennessee, Knoxville

Konstantin Dmitrievich Shmakov
August 1997

ACKNOWLEDGMENTS

I would like to thank everybody in E144 Collaboration with whom I worked over the period of four years. Friendly and supportive atmosphere within the collaboration contributed to the success of the experiment, which sets an example of a high energy physics experiment conducted by a small multi-discipline group.

Every-week discussions within the group between Steve Boege, Chritian Bula, Clive Field, Glenn Horton-Smith, Thomas Koffas, and Theofilos Kotseroglou were the source of constant enthusiasm.

Computational support and programs developed by Christian Bula were state-of-the-art, and I learned a great deal about modern lasers and how to make them work from the discussions with Adrian Melissinos, David Meyerhofer and Theofilos Kotseroglou.

Working with Steve Berridge on detectors, and data acquisition, was a great experience and I am thankful to Dieter Waltz for his insights on setup optimization.

Discussions with Kirk McDonald of fundamental physics problems behind the experiment were very fruitful and appreciable.

Without the constant support of David Burke, and his efforts to make the best electron beam possible, the experiment could not be done.

Enthusiasm and encouragement of Adrian Melissinos were very important.

I am thankful to William Bugg for his support and encouragement. Without his insightful ideas, enthusiasm and his belief that work can never be overdone, this manuscript could not be written.

I am thankful to P. Chen and Y.S. Tsai for many useful conversations.

ABSTRACT

Nonlinear Compton scattering and electron-positron pair production have been observed in collisions of low-emittance 46.6 GeV electron beam with terawatt laser pulses from an Nd:glass laser at the experiment E144 at the Final Focus Test Beam at SLAC. In nonlinear Compton scattering up to four laser photons interact with an electron. The positrons are interpreted as arising from a two step process in which laser photons are backscattered to GeV energies by the electron beam followed by a collision between the high-energy photon and several laser photons to produce an electron-positron pair. These results are the first laboratory evidence for inelastic light-by-light scattering involving only real photons. Results are in agreement with theoretical calculations of strong-field QED.

This work was supported in part by DOE grant DE-FG05-91ER40627.

Contents

1 Introduction **1**

1.1 Overview of the experimental setup 1

1.2 Nonlinear QED 6

2 Theoretical motivation **12**

2.1 Strong QED field, definitions of η and Υ 12

2.2 Notation 15

2.3 An electron moving in the field of an electromagnetic plane wave . . . 17

2.4 Quasimomentum and "mass shift" 18

2.5 S-matrix, Born approximation, calculations of probabilities and cross-sections 19

2.6 Emission of a photon by an electron in the field of a strong electromagnetic wave 23

2.7 Kinematics of the multi-photon Compton scattering in a strong electromagnetic field 32

2.8 Energy of backscattered photons from multi-photon Compton process 36

2.9 Kinematics of e^+e^- pair production by a photon in a strong electromagnetic field 38

2.10 Expression of parameters α and β in terms of kinematic variables . . 41

2.11 Series expansion of cross-sections in terms of field intensity η 42

2.12 Cross-sections summary 46

3 Experimental Setup **54**

3.1 Electron beam 54

3.2 Spectrometer and calorimeters 56

3.3 Forward photon and n=1 electron detectors 58

3.4 Data acquisition system 59

4 Laser system **62**

4.1 Laser system 62

4.2 Confocal beam parameters 67

5 Space-time laser-electron beam overlap **73**

5.1 Calculation of four-dimensional overlap 73

5.2 General method 78

5.2.1 Infinite Rayleigh range ($z_R = \infty$) 79

5.2.2 Finite Rayleigh range ($z_R \neq \infty$) 80

5.2.3 Diagonalization of arbitrary quadratic form 81

5.3 One step process: $n = 1$ Compton scattering 83

5.3.1 Probability of electron scattering through the laser focus . . . 89

5.4 Multiphoton Compton scattering 90

6 General method of reconstruction of nonlinear Compton scattering via ECAL data **92**

6.1 Reconstruction of the signal in ECAL 92

6.2 Calibration data and Monte Carlo 93

6.3 The response kernel $K_i(y, y')$ 94

6.4 Backgrounds 99

6.5 Reconstruction algorithm 101

6.6 Calculation of matrices M and N 105

6.7 Reconstruction errors 107

6.8 Reconstruction summary 108

7 Nonlinear Compton scattering of 46.6 GeV electrons by circularly polarized laser light **110**

7.1 Sources of background 110

7.2 Measurements 111

7.3 Corrections 120

7.4 Data collection strategy 124
7.5 Data analysis 126
7.5.1 Electron calorimeter reconstruction 129
7.5.2 Cuts 130
7.5.3 Binning and error analysis 130
7.6 Simulation of the experiment 131
7.7 Results and comparison with theory 133

8 Nonlinear Compton scattering of 46.6 GeV electrons by linearly polarized laser light **142**
8.1 Event selection 145
8.2 Correction for the leakage in ECAL 147
8.3 Weighting of different events in data samples 149
8.4 Nonlinear Compton rate versus electron momentum p_{e^-} and laser intensity η 153
8.5 Discussion of results, comparison with simulation 157

9 Results on positron production **160**
9.1 Experimental setup and calibration 160
9.2 Data analysis 161
9.3 Results 164

10 Conclusion **167**

References **170**

Appendices

A Polarization of high energy photons produced in the interactions of intense linear polarized laser photons with an unpolarized electron beam **177**

B Polarization of high energy photons produced in the interactions of intense circular polarized laser photons with an unpolarized electron beam 190

C e^+e^- pair production in the interaction of intense linear polarized laser photons with linear polarized photons 200

D e^+e^- pair production in the interaction of intense circular polarized laser photons with circular polarized photons 210

E η^2 series expansions of the multi-photon cross-section for circular and linear polarized laser photons and unpolarized electron beam 218

F η^2 series expansions of the cross-sections for e^+ e^- pair production for circular and linear polarized laser photons and unpolarized electron beam 220

G Discussion of polarization effects in positron production below the kinematic threshold for one laser photon: E144 experiment 225

Vita 229

List of Tables

1 Position of the kinematic edges for N=1,2,3,4,5,6 electrons and photons. 4

2 Parameters b_1, b_2, w_1 for the kernel function $K(y, y')$ for different longitudinal segments of ECAL. 97

3 Parameters b_1, b_2, w_1 for the kernel function $K(y, y')$ for different combinations of longitudinal segments of ECAL. 98

4 Background in the center columns of ECAL for some XT-scans. . . . 116

5 Background ratio center/outer columns for some XT-scans. 117

6 Position of the kinematic edges for N=1,2,3,4,5,6 electrons calculated for two field intensities $\eta = 0.14$ and $\eta = 0.30$. 144

7 Deviation of the average from the central value for N=1,2,3,4,5,6 distributions. 153

8 Ratio of e^+e^- pair production rates for Linear/Circular laser polarizations versus the number of laser photons. 223

9 Ratio of e^+e^- pair production rates for Circular/Linear laser polarizations versus laser intensity. 224

List of Figures

1 Schematic of the 1-st stage of the experimental setup. 2

2 Example of photon spectra and electron spectra from nonlinear Compton scattering. 3

3 Schematic of the second stage of the experimental setup. 5

4 Schematic diagram for multi-photon Compton scattering. 34

5 Schematic diagram for multi-photon e^+e^- pair production. 40

6 n=1 Compton cross-section $\sigma^{(1)}_{Unp}$ and n=2 nonlinear Compton cross-section $\sigma^{(2)}_{Unp}/\eta^2$. 49

7 $n = 1, 2, 3, 4$ Compton cross-sections versus the fractional photon energy ω/E_{tot}. for *linear* polarized Green laser. 50

8 $n = 1, 2, 3, 4$ Compton cross-sections versus the fractional photon energy ω/E_{tot} for *circular* polarized Green laser. 50

9 Cross-sections of e^+e^- pair production with n=4,5,6 laser photons versus the fractional positron energy E_{e^+}/E_{tot} for *linear* polarized Green laser. 53

10 Cross-sections of e^+e^- pair production with n=4,5,6,7 laser photons versus the fractional positron energy E_{e^+}/E_{tot} for *circular* polarized Green laser. 53

11 Calculated trajectories of electrons and positrons of different momenta through the magnetic spectrometer. 56

12 W-Si electromagnetic calorimeter. 57

13 The response of the ECAL to 13-GeV incident electrons. 58

14 The forward photon monitor Cerenkov counter. 59

15 Hardware components of the data acquisition system. 60

16 Schematic of the laser system. 62

17 The optical elements in the interaction point enclosure. 63

18 Diagram of the timing system for the synchronization of the laser pulses with the electron beam. 66
19 A "timing curve" showing the number of electrons scattered into the top row of the electron calorimeter as a function of delay of the optical pulse. 67
20 IR laser parameters during March 1995 run operation. 72
21 Laser parameters with doubling crystal (green laser) during March 1995 run operation. 72
22 Schematic diagram for the geometry of the Gaussian electron beam. . 75
23 Schematic diagram for the geometry of the Gaussian laser focus. . . . 76
24 First plot: the effective overlap factor F_{ovlp} for the Compton scattering versus the angle α. 85
25 The effective overlap factor F_{ovlp} for the $n = 1$ Compton scattering versus the timing jitter. 87
26 Dependence of the effective overlap parameter F_{ovlp} for the $N = 1$ Compton scattering versus laser parameters. 88
27 Segmentation of the ECAL calorimeter. 93
28 Normalized response $G_i(\Delta y)/E$. 95
29 Parameterization of individual showers measured by central and outer columns of ECAL. 95
30 Background in rdifferent ows of ECAL. 100
31 The ratio of background in central and outer columns of ECAL. . . . 100
32 Example of XT-scan for IR circular polarized laser. 112
33 Example of different backgrounds for center and outer columns of ECAL. 114
34 Background in central and outer pads for IR laser operation. 118
35 Background in central and outer pads for GREEN-laser operation. . . 118
36 Ratio of the backgrounds Center/Outer pads versus ECAL position for IR laser runs. 119

37 Ratio of the backgrounds Center/Outer pads versus ECAL position for GREEN laser runs. 119
38 Flux of γ versus ECAL position for IR and Green laser. 122
39 Reconstructed signal and background for IR laser runs. 123
40 Reconstructed signal and background for GREEN laser runs. 123
41 Recoil electron rates and calculated trajectories of electrons of different momenta through the magnetic spectrometer. 124
42 Data collection strategy. 125
43 The crossing of the laser pulse and electron beam in the X-T plane. . 126
44 ECAL signal for IR laser of 400 mJ. 127
45 Laser parameters for all data taken with IR pulses. 128
46 Laser parameters for all data taken with green pulses. 128
47 The normalized differential yield of nonlinearly scattered recoil electrons for six different IR laser energies. 134
48 The normalized differential yield of nonlinearly scattered recoil electrons for six different green laser energies. 135
49 The scaled normalized differential yield of nonlinearly scattered recoil electrons for six different IR laser energies. 137
50 The scaled normalized differential yield of nonlinearly scattered recoil electrons for six different green laser energies. 138
51 The scaled recoil electron yield versus IR laser intensity for 4 representative momenta. 140
52 The scaled recoil electron yield versus green laser intensity for 2 representative momenta. 141
53 Ratio $\frac{N_\gamma^{(measured)}}{N_\gamma^{(simulated)}}$ for the ECAL scan 15271. 146
54 Reconstructed ECAL spectrum in central pads of ECAL and background in outer pads of ECAL versus momentum of electrons. 148
55 Error in η reconstruction. 149

56 Measured and simulated distributions for $\eta = 0.19 \pm 0.01$ and $p_{e^-} =$ $5.88 - 7.80$ GeV. 150
57 Effect of the fluctuation of the η^2_{actual} on nonlinear Compton rates. . . 152
58 Laser intensity η and the overlap parameter. 154
59 Momentum acceptance of the ECAL versus the incident momentum. . 155
60 ECAL spectrums $\frac{1}{N_\gamma}\frac{dN_e}{dp}$ versus electron momentum p_{e^-}. for $\eta = 0.14 -$ 0.22. 156
61 ECAL spectrums $\frac{1}{N_\gamma}\frac{dN_e}{dp}$ versus electron momentum p_{e^-} for $\eta = 0.22 -$ 0.30. 156
62 ECAL spectrums $\frac{1}{N_\gamma}\frac{dN_e}{dp}$ versus laser field intensity η for $p_{e^-} = 6.0 -$ 6.7 GeV. 158
63 ECAL spectrums $\frac{1}{N_\gamma}\frac{dN_e}{dp}$ versus laser field intensity η for $p_{e^-} = 7.0 -$ 8.3 GeV. 158
64 ECAL spectrums $\frac{1}{N_\gamma}\frac{dN_e}{dp}$ versus laser field intensity η for $p_{e^-} = 8.7 -$ 9.7 GeV. 159
65 Schematic layout of the experiment. 160
66 Calculated trajectories of positrons and electrons of different momenta through the magnetic spectrometer. 161
67 Cluster densities from positrons produced by a wire inserted at IP1. . 162
68 (a) Positron candidates. 163
69 Dependence of the positron rate per laser shot on the laser field-strength parameter η. 164
70 Dependence of the positron rate on the laser field-strength parameter η when the rate is normalized to the number of Compton scatters. . . 165
71 Linear polarization: schematic diagram for multi-photon Compton scattering. 178
72 $n = 1, 2, 3, 4$ polarization versus u and fractional photon energy for E144 Green linear polarized laser and 46.6 GeV electron beam. 184

73 $n = 1, 2, 3, 4$ average polarization $< P >$ versus the parameter x for linear polarized laser and field intensity $\eta \approx 0$. 186
74 Polarization of backscattered photons and differential cross-sections for $n = 1$ Compton scattering, linear polarized laser. 189
75 Polarization of backscattered photons and differential cross-sections for $n = 2$ Compton scattering, linear polarized laser. 189
76 Circular polarization: schematic diagram for multi-photon Compton scattering. 194
78 $n = 1, 2, 3, 4$ average polarization $< P >$ versus parameter x for circular polarized laser and field intensity $\eta \approx 0$. 196
79 Polarization of backscattered photons and differential cross-sections for $n = 1$ Compton scattering, circular polarized laser. 199
80 Polarization of backscattered photons and differential cross-sections for $n = 2$ Compton scattering, circular polarized laser. 199
81 $n = 4, 5, 6$ asymmetry versus u and fractional positron energy for E144 Green linear polarized laser and $E_{tot} = 29$ GeV photon. 205
82 $n = 4, 5, 6$ total asymmetry A_{tot} in pair production versus u_n for linear polarized laser.) 205
83 Total asymmetry for $n = 1$ positron production in the focus of linear polarized laser. 208
84 $n = 4, 5, 6, 7$ asymmetry versus u and fractional positron energy. . . . 213
85 $n = 4, 5, 6, 7$ total asymmetry A_{tot} in pair production. 213
86 Total asymmetry for $n = 1$ positron production in the focus of circular polarized laser. 216

1 Introduction

1.1 Overview of the experimental setup

Quantum electrodynamics (QED) has been tested extensively in the weak-field regime. It has also been tested at moderately strong fields in nonlinear optics, wherein focussed laser beams are used to produce fields of order $\mathcal{E}_{\rm lab} \approx 10^8$ V/cm and their interaction with atomic systems is investigated. Here we report on the measurement of quantum electrodynamic processes in a strong field $\mathcal{E}_{\rm lab} \approx 10^{11}$ V/cm, namely nonlinear Compton scattering of 46.6-GeV electrons from the photons at the focus of a terawatt laser

$$e^- + n\omega \rightarrow e^{-'} + \gamma, \tag{1}$$

and electron positron pair production by a collision between a high energy real photon and several laser photons

$$\gamma + n\omega \rightarrow e^+ + e^-, \tag{2}$$

where ω represents a photon from the strong electromagnetic wave, n indicates the number of such photons absorbed, and γ represents an emitted photon which is not coherent with the incident strong electromagnetic wave.

The scattering rates for processes which absorb more than one laser photon vary in a strongly nonlinear manner with the laser intensity.

The experiment E144 was carried out in the Final Focus Test Beam at the Stanford Linear Accelerator Center [1]. The incoming SLC electron beam is alternately polarized with the electron polarization changing randomly from pulse to pulse. The polarization of the electron beam was not measured in E144 and hence the electron beam can be considered as unpolarized. We will often refer to the incoming electron beam as an unpolarized electron beam keeping in mind this comment. The experiment was arranged in two stages. They use the same apparatus with only minor

modifications.

Stage 1

The electrons with energy 46.6 GeV collide with the tightly-focussed terawatt laser beam at an interaction point immediately upstream of magnets which served to bend the scattered electrons according to their momentum. The photons created in the collision proceed in the forward direction, whereas the scattered electrons are deflected out of the vacuum pipe (downward) and can reach the detector (called ECAL). ECAL is a W-Si segmented electromagnetic calorimeter. The scattered photons are detected in the Cerenkov counter (CCM1)

This arrangement, designed for the measurement of the nonlinear Compton spectrum of electrons, is shown schematically in Fig. 1.

Photons originating from ordinary (N=1) Compton scattering have energies less than the kinematic maximum ≈ 21 GeV for IR laser ($\lambda = 1053$ nm) and ≈ 29 GeV for green laser ($\lambda = 527$ nm). Photons with higher energy than the kinematic threshold can be scattered only through nonlinear Compton processes Eq. (1). Similarly electrons originating from ordinary Compton scattering have energy above the kinematic threshold ≈ 26 GeV for IR laser and ≈ 18 GeV for green laser. Electrons originating

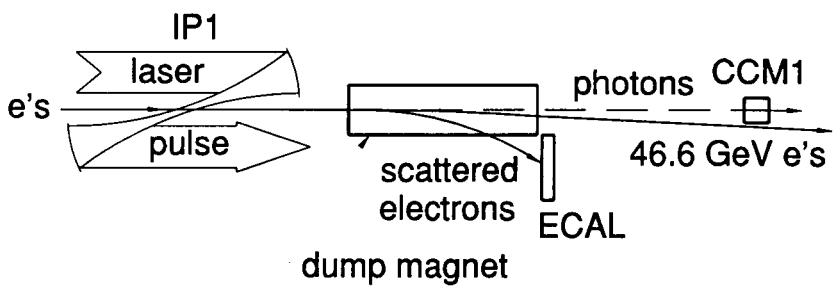

Figure 1: Schematic of the 1-st stage of the experimental setup: The laser pulses crossed through the electron beam at the interaction point. The scattered electrons were bent by the dump magnets into the electron calorimeter ECAL. The scattered photons were detected in the Cerenkov counter.

from nonlinear Compton scattering may have energies below the kinematic threshold. Example of the spectra of photons and electrons is shown in Figs. 2 for IR laser and laser field intensity $\eta = 0.32$ which is typical for this experiment.

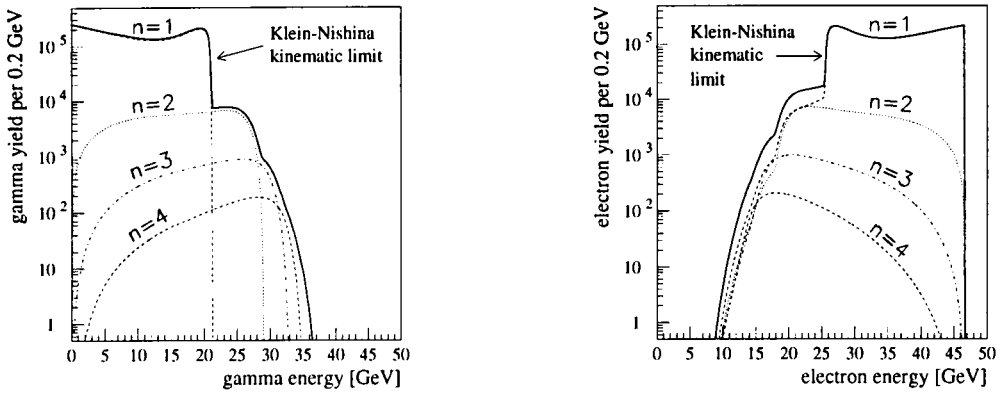

Figure 2: Example of photon spectra (left plot) and electron spectra (right plot) from nonlinear Compton scattering of 46.6 GeV electrons on IR laser with field intensity $\eta = 0.32$ (parameter η is explained in the following section). The solid line on both plots is the sum of all possible processes. The N=2, N=3 and N=4 processes are shown separately as well.

We adopt a right-handed coordinate system with Z in the undeflected electron beam direction and Y vertically upward. Kinematic limits for electrons and photons that correspond to the scattering of the 46.6 GeV electron beam from IR laser photons are located at positions given in Table 1.

In the first stage of our experiment we measure the spectra of electrons and photons in kinematic regions reachable by particles originating from nonlinear Compton processes. Based on the analysis of the spectra we conclude that interaction of an electron with up to 4 laser photons through the reaction Eq. (1) has been observed. In this paper we report the measurement of the nonlinear Compton scattering spectra for the electrons. The results are presented in Sections 7 and 8. Spectrum of backscattered photons also measured by the E144 experiment will be reported else-

Table 1: Position of the kinematic edges for N=1,2,3,4,5,6 electrons and photons. Edges are for 46.6 GeV electron beam, IR laser 1.17 eV, electron-laser crossing angle 17° and low field intensity.

	e^-	γ
N=1	25.6 GeV	21.0 GeV
N=2	17.6 GeV	29.0 GeV
N=3	13.5 GeV	33.1 GeV
N=4	10.9 GeV	35.7 GeV
N=5	9.1 GeV	37.5 GeV
N=6	7.9 GeV	38.7 GeV

where.

Stage 2

In the second stage of the experiment high energy photons produced in the reaction Eq. (1) interact at the laser focus with a few laser photons through the reaction Eq. (2) and produce electron positron pairs. Positrons are deflected out of the vacuum pipe upward and reach the detector (called PCAL). PCAL is W-Si segmented electromagnetic calorimeter which is similar to ECAL. The scattered photons are detected in the Cerenkov counter (CCM2) and Pb-Si electromagnetic calorimeter (GCAL). The CCD spectrometer and pair of W-Si calorimeters SCAL measure the electron-positron pairs from the conversion of the small fraction of the photons in gamma converter. Measurements of the electron-positron pair energy in this part of the setup (CCD spectrometer and two W-Si calorimeters SCAL) allow reconstruction of the spectrum of high energy photons. In this configuration the CCD spectrometer is thus tested for a future stage of the experiment in which positrons will be produced at the second laser-photon interaction point (not shown) which will replace the gamma converter, and the invariant mass of e^+e^- pairs will be measured.

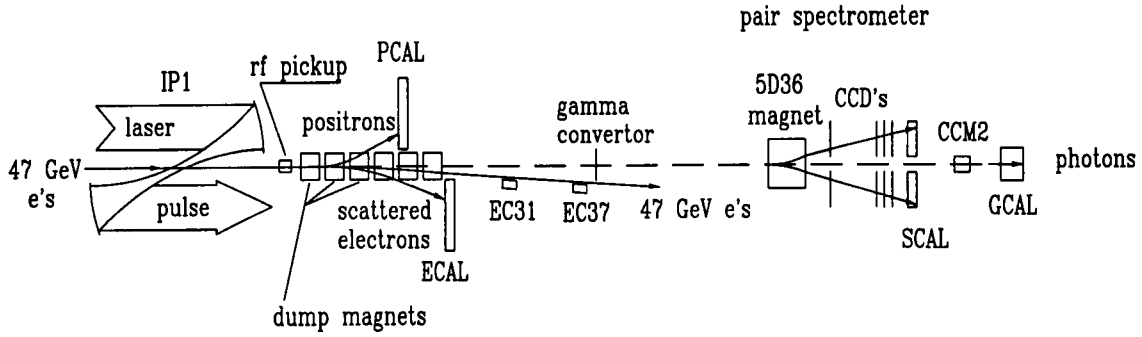

Figure 3: Schematic of the second stage of the experimental setup: Positrons produced at the interaction point were bent by the dump magnets upwards into the positron calorimeter (PCAL). Photon detectors (CCM2, GCAL), CCD spectrometer and two additional calorimeters (SCAL) are also shown.

Setup for the second stage of the experiment is shown in Fig. 3

Data were taken in a series of runs from April 1994 to August 1996. We report on data obtained during these runs in Sections 7 and 8, primarily on nonlinear Compton scattering, although Section 9 briefly describes results on photon-photon scattering.

1.2 Nonlinear QED

Soon after the positron was discovered by Anderson in 1932 [2], Bethe and Heitler [3] provided a theory of the production of electron-positron pairs as arising from the interaction of a real photon with a virtual photon of the electromagnetic field of a nucleus. Shortly thereafter, Breit and Wheeler [4] calculated the cross section for production of an electron-positron pair in the collision of two real photons,

$$\omega_1 + \omega_2 \rightarrow e^+ e^-, \tag{3}$$

to be of order r_0^2, where $r_0 = 2.82 \times 10^{-13}$ cm is the classical electron radius. Above the kinematic threshold for reaction (3) the cross section has the form

$$\sigma_{BW} \approx \pi\, r_0^2\, \frac{m^2}{\omega_1\, \omega_2} \sqrt{1 - \frac{m^2}{\omega_1\, \omega_2}}\,, \qquad \omega_1\, \omega_2 > m^2\,, (\qquad c = \hbar = 1)\,, \tag{4}$$

where ω_1 and ω_2 are energies of two photons colliding head on, m is the electron rest mass (0.511 MeV).

This cross section is of the same order of magnitude as that for Compton scattering that involves only one laser photon,

$$e^- + \omega \rightarrow e^{-\prime} + \gamma\,, \tag{5}$$

as the two processes are related by crossing symmetry (to use the language of Feynman diagrams). The cross-section for Compton scattering has the form

$$\sigma_{\text{Compton}} = \pi\, r_0^2 \frac{m^2}{E\, \omega}\, O(1)\,, \tag{6}$$

where ω and E are energies of photon and relativistic electron colliding head-on, $O(1)$ is a function of energy which is of the order of 1.

However, Breit and Wheeler commented that "it is hopeless to try to observe pair formation in laboratory experiments with two beams of x-rays or γ-rays meeting

each other on account of the small cross section and the insufficiently large available densities of quanta".

The cross section (4) for pair creation is always below πr_0^2 due to kinematic threshold $\omega_1 \omega_2 > m^2$. Hence the process requires enormous photon densities achievable only with modern lasers. But laser photons are in eV energy range and do not have enough energy for pair production. One of the colliding photons should be in the hundreds of GeV energy range.

On the other hand Compton scattering of an electron can be readily observed because the cross section (6) for Compton scattering is not limited by kinematic threshold and exceeds πr_0^2 by many orders of magnitude at low energies.

Pair creation by real photons has not been observed in the laboratory up to the present experiment, although creation of mesons by virtual photons is now commonplace at electron-positron colliding beam facilities via the reaction $e^+e^- \rightarrow e^+e^-\omega_1^\star\omega_2^\star$ $\rightarrow e^+e^-X$ where $\omega_1^\star$ and $\omega_2^\star$ are two virtual photons.

Breit and Wheeler also commented that "pair production due to collisions of cosmic rays with the temperature radiation of interstellar space is much too small to be of any interest". Recently De Jager *et al.* [5] have argued that the observed falloff of the spectrum of cosmic-ray photons above 10^{12} eV from relic supernova can be ascribed to electron-positron pair creation in collisions with intergalactic infrared photons.

After the invention of the laser in 1960 the prospect of intense laser beams led to reconsideration of the Breit-Wheeler process by Reiss [6] and Narozhny *et al.* [9, 7]. Of course, for production of an electron-positron pair the center-of-mass energy of the scattering photons must be at least $2mc^2 \approx 1$ MeV. This can be achieved by scattering a laser beam against a high-energy photon beam created, for example, by backscattering the laser beam off a high-energy electron beam.

With laser light of wavelength 527 nm (energy 2.35 eV), a photon of energy 111 GeV would be required for reaction (3) to proceed. However, with an electron beam

of energy 46.6 GeV as available at the Stanford Linear Accelerator Center (SLAC) the maximum Compton-backscattered photon energy from a 527-nm laser is only 29.2 GeV.

In strong laser fields the interaction need not be limited to initial states with two photons, but rather the number of interacting photons becomes large as the dimensionless, invariant parameter

$$\eta = \frac{e\mathcal{E}_{\rm rms}}{m\omega_0} = \frac{e\mathcal{E}_{\rm rms}\lambda\!\!\!^{-}_0}{m} \tag{7}$$

approaches and exceeds unity. In this, the laser beam has laboratory frequency ω_0, reduced wavelength $\lambda\!\!\!^{-}_0$, root-mean-square electric field $\mathcal{E}_{\rm rms}$; e and m are the charge and mass of the electron, respectively. The multiphoton Breit-Wheeler reaction (2) becomes accessible for $n \geq 4$ laser photons of wavelength 527 nm colliding with a 29.2 GeV photon.

For photons of wavelength 527 nm a value of $\eta = 1$ corresponds to laboratory field strength of $\mathcal{E}_{\rm lab} = 6 \times 10^{10}$ V/cm and intensity $I = 10^{19}$ W/cm^2. Such intensities are now practical in tabletop laser systems.

The number of interacting photons becomes also large at $\eta = 1$ for the reaction (1). In strong laser field with $\mathcal{E}_{\rm lab} = 6 \times 10^{10}$ V/cm multiphoton Compton scattering takes place for electrons with arbitrary energy due to the fact that η doesn't depend on the electron energy. Electron scattering in an intense laser field has recently been observed in the Thomson (nonrelativistic) regime [10]. As $\eta \to 1$ scattering by absorption becomes apparent through the transfer of longitudinal momentum to the scattered electron.

When a laser field of strength $\mathcal{E}_{\rm lab}$ is viewed in the rest frame of a relativistic, counter-propagating particle with laboratory energy E and Lorenz factor $\gamma = E/mc^2 \gg 1$ the laser field strength appears boosted to $\mathcal{E}^\star = 2\gamma\mathcal{E}_{\rm lab}$. For example, a 46.6-GeV electron has $\gamma = 9 \times 10^4$ so if it collides head on with a 527-nm laser pulse of strength $\eta = 1$ the field in the electron's rest frame is $\mathcal{E}^\star = 1.1 \times 10^{16}$

V/cm. This is close to the quantum electrodynamic (QED) critical field strength $\mathcal{E}_{\rm crit} = m^2c^3/e\hbar = 1.3 \times 10^{16}$ V/cm at which a static electric field would spontaneously break down into electron-positron pairs [13, 14, 15, 16], and at which the energy gain of an electron accelerating over a Compton wavelength is its rest energy.

Indeed, the predicted rates for the reaction (2) become large only when the dimensionless invariant

$$\Upsilon = \frac{\mathcal{E}^\star}{\mathcal{E}_{\rm crit}} = \frac{\sqrt{(F_{\mu\nu}p^\nu)^2}}{mc^2\mathcal{E}_{\rm crit}} \tag{8}$$

approaches unity. Here $F_{\mu\nu}$ is the laboratory electromagnetic field tensor of the laser beam and p^ν is the energy-momentum 4-vector of the high-energy electron. For given electron and photon energies E and ω_0 the parameters η and Υ are not independent. For example, for $E = 46.6$ GeV and $\hbar\omega_0 = 2.35$ eV they are related by $\Upsilon = 0.84\,\eta$.

Static fields with $\Upsilon > 1$ are unstable and do not exist in nature. The magnetic field at the surface of a neutron star is believed to approach $\Upsilon = 1$. The Coulomb field in heavy-ion collisions of nuclei of atomic numbers Z and Z' attains $\Upsilon_{\rm max} \approx (Z+Z')\alpha$ which can exceed unity, and electron-positron pair creation has been observed there [15]. The electric field at the surface of an electron bunch at a future linear collider approaches $\Upsilon = 1$ as viewed by the oncoming bunch, and numerous authors have discussed how the consequent pair creation would limit performance of the collider [16].

In reaction (2) where several laser photons interact at once it is useful to consider the interaction as taking place with the field rather than individual quanta. This leads to an interpretation of the pair creation as a barrier-penetration process. A virtual electron-positron pair in the vacuum can materialize if the charges separate by distance d sufficient to extract energy $2mc^2$ from the field, *i.e.* if $e\mathcal{E}d = 2mc^2$. The probability of penetration of this 'barrier' of thickness d is proportional to $\exp(-\pi\, m^2\, c^3/e\hbar\mathcal{E}) = \exp(-\pi/\Upsilon)$. Thus the pair creation rate is a strong function of

the parameter Υ.

In the present experiment we studied reactions (1) and (2) in the collision of a low emittance 46.6 GeV electron beam with terawatt pulses from a Nd:glass laser at 1053 nm and 527 nm wavelength in an experiment at the Final Focus Test Beam at SLAC. We studied interactions with both circular and linear polarized laser photons. Peak laser intensities of 10^{18} W/cm^2 have been achieved corresponding to value of 0.5 for the parameter η and to value of 0.3 for the parameter Υ.

In nonlinear Compton scattering (reaction 1) we observe the interaction of up to four laser photons with an electron. Differential spectra and rates are in agreement with theoretical calculations. It has been confirmed that rates depend nonlinearly on the laser intensity.

We observed a signal of 106$\pm$14 positrons above background from the reaction (2). Dependence of the positron rate on the field intensity and parameter Υ was found to be in excellent agreement with theoretical calculations.

Polarization of particles involved into processes (1) and (2) are important parameters for nonlinear QED processes. Theoretical calculations that include polarization of electrons and photons are revisited in this dissertation, and new and original results are obtained.

Plan of the dissertation by sections is as follows:

- In Section 2 we describe a theoretical apparatus used for the calculation of cross sections for nonlinear Compton scattering and pair production in a strong QED field. Polarization effects important for the understanding of the results of the experiment are discussed. A more detailed review of the polarization effects in Compton scattering and e^+e^- pair production will be left for the Appendices A-D where derivation of cross sections and polarization asymmetries will be reported. Most of the results for the polarization effects agree with other results or, in many cases, ar original results obtained by the author.

- Setup configuration, detectors, electron beam parameters will be discussed in Section 3.

- The laser system will be described in Section 4. Laser focus intensities achievable with present technology will be discussed.

- During the collision of pulsed beams of electrons and laser photons, densities of both bunches vary in space and time. Electrons passing through different portions of laser focus see different field intensities. Effects of the electron-laser overlap on the rates and spectra of electrons and photons are studied in Section 5.

- An algorithm for reconstruction of the detector signal in the presence of backgrounds is discussed in Section 6. This algorithm was developed by author and was successfully applied during E144 off-line data analysis.

- Results of the experiment on nonlinear Compton scattering (reaction Eq. 1) for circular and linear polarized lasers are presented in Sections 7 and 8 respectively. Measurements of the backgrounds, and their effect on reconstruction of the nonlinear Compton signal are discussed.

- Results of the experiment on electron-positron pair production (reaction Eq. 2) for linear polarized laser are presented in Section 9.

- In the conclusion Section 10 we summarize experimental results reported in this dissertation and discuss their applications.

- In Appendices A-G we present detailed results on cross-sections and asymmetries for nonlinear Compton scattering and e^+e^- pair production that were not included in Section 2 and discuss application of these results to the E144 experiment.

2 Theoretical motivation

2.1 Strong QED field, definitions of η and Υ

In quantum theory the interaction of electron with electromagnetic field in a weak field regime is treated as the interaction of electrons with individual photons of the field and collective effects of the photons are usually neglected. This approximation is not valid for very intense electromagnetic fields available with modern lasers. For a very strong electromagnetic field electron "feels" the presence of all photons of the field i.e. electron is dressed with the photons of the field. In strong QED field regime multi-photon effects and e^+e^- pair production in the interaction of an electron with more than one laser photon take place.

Multi-photon effects and e^+e^- pair production in a strong field are effects of *nonlinear* QED. Cross sections and production rates depend nonlinearly on the field intensity.

Nonlinear QED effects due to absorption of multiple photons become important in a wave field of frequency ω when the dimensionless parameter

$$\eta = \frac{e\,A_{rms}}{m\,c^2} = \frac{e\sqrt{-<A_\mu A^\mu>}}{m\,c^2} \tag{9}$$

approaches unity. Here e and m are the electron charge and rest mass and c is the speed of light; A_μ is the 4-vector potential of the incident field $A_\mu = (A_0, \vec{\mathbf{A}}) = (A_0, A_x, A_y, A_z)$, and A_{rms} is the RMS (root-mean-square) of the 4-vector potential $A_{rms} = \sqrt{-<A_\mu A^\mu>}$. The angle brackets indicate that an average over one cycle of the wave is taken.

The parameter η appears naturally when we consider an electron moving in a plane electromagnetic wave.

For a wave field with frequency ω and wave vector $\vec{k}$, the electromagnetic field $\vec{\mathcal{E}}$ and vector potential $\vec{A}$ are

$$\begin{aligned}\vec{\mathcal{E}} &= \vec{\mathcal{E}}_0 \exp\left(i\vec{k}\vec{x} - i\omega t\right) = \vec{\mathcal{E}}_0 \exp(i\phi)\,, \\ \vec{\mathbf{A}} &= \vec{\mathbf{A}_0} \exp\left(i\vec{k}\vec{x} - i\omega t\right) = \vec{\mathbf{A}_0} \exp(i\phi)\,.\end{aligned}$$

We use Lorenz gauge and set $A_0 = 0$, then

$$\vec{\mathcal{E}} = -\frac{1}{c}\frac{\partial \vec{\mathbf{A}}}{\partial t}\,.$$

Hence

$$-A^2 = \frac{c^2}{\omega^2}\mathcal{E}^2\,, \qquad - < A^2 >= \frac{c^2}{\omega^2}\mathcal{E}_{\rm rms}^2\,, \tag{10}$$

where $\mathcal{E}_{\rm rms}$ is the RMS (root-mean-square) of the field.

Parameter η can be written as

$$\eta = \frac{e\mathcal{E}_{\rm rms}}{\omega mc}\,. \tag{11}$$

Effects of vacuum polarization and creation of e^+e^- pairs are characterized by invariant parameter Υ

$$\Upsilon = \frac{e\hbar}{m^3c^5}\sqrt{(F_{\mu\nu}p^\nu)^2}\,, \tag{12}$$

where $F_{\mu\nu}$ is 4-tensor of an electromagnetic field which is probed by a particle with 4-momentum p_μ.

The parameter Υ appears naturally for an electron in a constant uniform electric field [17] and is closely related to Klein paradox [18]. It was shown in [17] that transitions between electron and positron states are possible due to a tunneling effect in electric field. Probability P for transition in a constant field is defined by formula

$$P \approx \exp\left(-\pi\frac{m^2c^3}{eE\hbar}\right) = \exp\left(-\pi\frac{1}{\Upsilon}\right)\,,$$

$$\Upsilon = \frac{e\mathcal{E}\hbar}{m^2c^3}. \tag{13}$$

In electromagnetic field with $\Upsilon = 1$ the electron gains energy equal to its rest mass when accelerated over an electron Compton wavelength $\lambda_c = \hbar/mc$. This field is called the "critical field"

$$\mathcal{E}_{\text{crit}} = \frac{m^2c^3}{e\hbar} = 1.3 \times 10^{16}\, V/cm\,. \tag{14}$$

In a critical field probability of transition between positron end electron states approaches unity and copious electron-positron pairs can be produced from the vacuum by a charged particle traveling through the field. This effect is called "sparking of the vacuum".

For an electron moving in a plain electromagnetic wave of frequency ω the parameter Υ is defined as

$$\Upsilon = \frac{e\mathcal{E}^*_{\text{rms}}\hbar}{m^2c^3}, \tag{15}$$

where $\mathcal{E}^*_{\text{rms}}$ is the RMS of the electric field in the electron's rest frame.

For a wave field of frequency ω parameters Υ and η are not independent. From Eqs. (11) and (15)

$$\Upsilon = \eta\frac{\hbar\omega^*}{mc^2}, \tag{16}$$

where $\omega^* = 2\gamma\omega$ is the laser photon frequency in the electron rest frame and γ is the relativistic boost factor to the electron's rest frame.

For a 46.6 GeV electron beam colliding head-on with a 527-nm laser, $\Upsilon = 0.84\eta$.

Note that Υ is defined for both constant fields and time-varying fields (lasers) while η is defined for periodic fields only. Υ has the meaning of the electron energy gain over the reduced Compton wavelength in units of the electron rest mass. The parameter η is related to the wavelength of the periodic field and is equal to the

electron energy gain over the reduced laser wavelength in units of the electron rest mass. The parameter η diverges for $\omega \longrightarrow 0$ i.e. for the constant field $\mathcal{E}_{\text{rms}}$.

Finally we note that the parameter Υ contains the Planck constant $\hbar$ and is responsible for the quantum effects while the parameter η is a classical parameter.

2.2 Notation

For 4-vectors we use the conventional metric $g_{\mu\mu} = (1, -1, -1, -1)$; the dot-product for two 4-vectors a and b is defined as

$$\begin{aligned}(a\,b) = a\,b = a_\mu b^\mu = a_0 b_0 - \vec{\mathbf{a}}\vec{\mathbf{b}} &= a_0 b_0 - a_1 b_1 - a_2 b_2 - a_3 b_3 \\ &= a_0 b_0 - a_x b_x - a_y b_y - a_z b_z\end{aligned}$$

where $\vec{\mathbf{a}}, \vec{\mathbf{b}}$ are usual 3-vectors. We will often use notation $a\,b$ instead of $(a\,b)$ for the product of two 4-vectors.

For a particle with 4-momentum $p_\mu = (E, \vec{\mathbf{p}}) = (E, p_1, p_2, p_3)$

$$p^2 = E^2 - (\vec{p})^2 = m^2\,,$$

where m is the rest mass of the particle ($c = 1$).

The square of the 4-vector potential $A_\mu A^\mu$ with $A_0 = 0$ is a negative number

$$< A^2 >= -a^2\,,\ \ a^2 > 0 \quad (a \text{ - some real positive number})\,.$$

Note that we use the standard metric in this paper but it is different from one used in original publications [7] and care should be taken when comparing with definitions and formulae from the original publications.

It is important to note that η is defined using the average value of the vector potential $< A^2 >$ as in Eq. (9), not the peak amplitude. We use this definition of η because circular and linear polarized laser beams of equal intensity have the same η with this definition. The amplitude of the field for the linear polarized wave

is $\sqrt{2}$ times higher than the amplitude of the field for the circular polarized wave. Either wave can be converted to the other with the use of quarter wave plate without (ideally) energy loss and hence it is natural to define the parameter η to be the same for both waves. This definition of η is different from one used in [7] where authors define η in terms of the amplitude value of the vector potential. As a consequence some formulae for the linear polarization derived in this dissertation differ from one in [7].

We will use units $c = \hbar = 1$. This simplifies the appearance of the formulae, and underlines their physical meaning (if necessary one can always reconstruct c and $\hbar$ from dimensional considerations). In the system $c = \hbar = 1$ and

$$\begin{aligned} 1\,MeV^{-1} &= 1.97 \times 10^{-11}\,cm\,, \\ 1\,MeV^{-1} &= 0.66 \times 10^{-21}\,s\,. \end{aligned}$$

The classical electron radius in these units

$$r_0 = \frac{e^2}{4\pi\, m} = \frac{\alpha}{m} = \frac{1}{137.0}\frac{1.97 \times 10^{11}\ cm}{0.511} = 2.82 \times 10^{-13}\ cm\,.$$

The electron Compton wavelength $\lambda\!\!\!^{-}_c$ and reduced laser wavelength $\lambda\!\!\!^{-}$

$$\begin{aligned} \lambda\!\!\!^{-}_c &= \frac{1}{m} = 3.86 \times 10^{-11}\ \mathrm{cm}\,, \\ \lambda\!\!\!^{-} &= \frac{1}{\omega}\,. \end{aligned}$$

Definitions of parameters η, Υ and critical field have clear physical meaning (compare to expressions from Section 2.1)

$$\begin{aligned} \Upsilon &= \frac{e\mathcal{E}_{\mathrm{rms}}\lambda\!\!\!^{-}_c}{m} = \frac{e\mathcal{E}_{\mathrm{rms}}}{m^2}\,, \\ m &= e\mathcal{E}_{\mathrm{crit}}\lambda\!\!\!^{-}_c\,, \end{aligned}$$

$$\eta = \frac{e\mathcal{E}_{\rm rms}\lambda\!\!\!^{-}}{m} = \frac{e\mathcal{E}_{\rm rms}}{\omega m},$$
$$\Upsilon = \eta\frac{\lambda\!\!\!^{-}_c}{\lambda\!\!\!^{-*}} \qquad (\lambda\!\!\!^{-*} \text{ is the laser wavelength in the electron rest frame}).$$

2.3 An electron moving in the field of an electromagnetic plane wave

An electromagnetic plane wave can be characterized by a 4-vector $k = (\omega, \vec{k})$ $(c = 1)$ and vector potential A_μ. In the above ω is the reduced wave frequency and $\vec{k}$ is the wave vector. $k^2 = \omega^2 - \vec{k}^2 = 0$. The 4-vector potential in any space-time point with coordinates $x = (t, \vec{x})$ is a function of one parameter $A_\mu = A_\mu(\phi)$ where phase $\phi = (kx) = \omega t - \vec{k}\vec{x}$.

An electron with 4-momentum $p = (p_0, p_1, p_2, p_3)$ is characterized by the wave function $\psi(p)$ and the propagation of the wave function $\psi(p)$ is defined by Dirac's equation. Exact solution of the Dirac's equation for an electron moving in the field of electromagnetic plane wave was first obtained by D.M.Volkov in 1937 [19]

$$\psi(p) = \left[1 + \frac{e}{2(kp)}(\gamma k)\,(\gamma A)\right] e^{iS(p)}\, u(p),$$
$$S(p) = (px) + \int_0^{(kx)} \left[\frac{e}{(kp)}(pA) - \frac{e^2}{2(kp)}A^2\right] d\phi. \qquad (17)$$

In the above formula $u(p)$ is a 4-component Dirac's spinor - solution of the Dirac equation without electromagnetic field. Dot-products (γk) and (γA) are products of Dirac's γ-matrices with the 4-vector. For example

$$(\gamma k) = \gamma_\mu k^\mu \equiv \gamma_0 k^0 - \gamma_1 k^1 - \gamma_2 k^2 - \gamma_3 k^3,$$

$$\gamma_0 = \begin{pmatrix} 1 & 0 & 0 & 0 \\ 0 & 1 & 0 & 0 \\ 0 & 0 & -1 & 0 \\ 0 & 0 & 0 & -1 \end{pmatrix}, \gamma_1 = \begin{pmatrix} 0 & 0 & 0 & 1 \\ 0 & 0 & 1 & 0 \\ 0 & -1 & 0 & 0 \\ -1 & 0 & 0 & 0 \end{pmatrix},$$

$$\gamma_2 = \begin{pmatrix} 0 & 0 & 0 & -i \\ 0 & 0 & i & 0 \\ 0 & i & 0 & 0 \\ -i & 0 & 0 & 0 \end{pmatrix}, \gamma_3 = \begin{pmatrix} 0 & 0 & 1 & 0 \\ 0 & 0 & 0 & -1 \\ -1 & 0 & 0 & 0 \\ 0 & 1 & 0 & 0 \end{pmatrix}.$$

Hence $(\gamma k)(\gamma A)$ in Eq. (17) is a 4x4 matrix which is the product of two 4x4 matrices, $e^{iS(p)}$ is a scalar.

2.4 Quasimomentum and "mass shift"

For the wave function of an electron moving in the field of electromagnetic plane wave Eq. (17) the average value of the modified momentum operator $\hat{p} - e\,A = i\partial - eA$ is

$$q^\mu = \langle \psi^* \,|\, \hat{p}^\mu - e\,A^\mu \,|\, \psi \rangle = p^\mu - \frac{e^2 < A^2 >}{2(kp)} k^\mu . \tag{18}$$

The four-vector q^μ is called quasi-momentum.

Using definition of η from Eq. (9) we get

$$\begin{aligned} q^\mu &= p^\mu + \frac{\eta^2 m^2}{2(kp)} k^\mu \\ q^2 &= m^2(1+\eta^2) = {m_*}^2 , \end{aligned} \tag{19}$$

where m_* is the effective mass of electron (positron) moving in the field of electromagnetic plane wave. The fact that the effective mass of an electron is different from its rest mass is known as the "mass shift" of an electron. The effect of the mass shift modifies kinematics of multi-photon Compton scattering and pair production. In a strong electromagnetic field an electron positron pair is produced with invariant mass $(2m_*) > (2m)$, where $m \approx 0.511$ MeV is the electron rest mass.

2.5 S-matrix, Born approximation, calculations of probabilities and cross-sections

We will follow notation defined in [22]. Transition of an electron from a state 1 with momentum p_1 to a state 2 with momentum p_2 is characterized by the element S_{21} of the electron scattering S matrix. Without interactions two states are identical $1 = 2$ and S-matrix is equal to the unit matrix I. Scattering takes place when non-diagonal elements of matrix S are different from 0

$$S = I + iT\,, \qquad T \neq 0\,.$$

The amplitude of the process M_{21} is defined as

$$S_{21} = (2\pi)^4 \delta^4(k_1 + p_1 - k_2 - p_2)\, M_{21}\,. \tag{20}$$

S-matrix elements for the emission of a photon by high-energy electrons moving in electromagnetic plane wave can be calculated in the Born approximation. The S-matrix element for the scattering of an electron with wave function $\psi(p_1)$ with 4-momentum p_1 to the state $\psi(p_2)$ with 4-momentum p_2 with emission of a photon with 4-momentum k_2 and polarization ϵ^* is

$$S_{21} = -ie \int \bar{\psi}(p_2)\,(\gamma\epsilon^*)\,\psi(p_1)\, e^{-ik_2x} d^4x\,. \tag{21}$$

Integration in the above equation is over 4-dimensional space.

Equation (21) describes the scattering of an electron in a field and not the interaction of an electron with individual photons. The electromagnetic field in this approach is treated semi-classically. It is characterized by the vector potential A_μ and the wave functions for incoming and outgoing electrons are modified by the presence of the field A_μ. There are 3 particles in equation (21): incoming electron, outgoing electron and photon. The square $|S_{21}|^2$ is the probability of transition of an electron from the state 1 to the state 2

$$w_{21} = |S_{21}|^2 = (2\pi)^4 \delta^4(k_1 + p_1 - k_2 - p_2)(2\pi)^4 \delta(0) \, |M_{21}|^2 \, .$$

Calculation of transition probabilities from continuous spectrum requires calculation of the phase space for the final states. Normalized transition probability per unit time can be written as in [22]

$$dw_{21} = \frac{|M_{21}|^2}{2E_1} d\Phi \, .$$

Here E_1 is the energy of the electron in the initial state.

The phase space $d\Phi$ of the final states is defined as

$$d\Phi = (2\pi)^4 \, \delta^4(k_1 + p_1 - k_2 - p_2) \, \frac{d^3\vec{p}_2 d^3\vec{k}_2}{(2\pi)^6 \, 2E_2 \, 2\omega_2} \, . \tag{22}$$

Here E_2 and ω_2 are the energies of the electron and photon in the final state, $\vec{p}_2$ and $\vec{k}_2$ are their momenta.

The normalized transition probability for the electron scattering is

$$dw_{21} = d\Gamma = \frac{|M_{21}|^2}{32\pi^2 E_1} \delta^4(k_1 + p_1 - k_2 - p_2) \frac{d^3\vec{p}_2 d^3\vec{k}_2}{E_2 \, \omega_2} \, . \tag{23}$$

$d\Gamma$ is the differential width, this underlines the fact that there is only one particle in the initial state and its transition probability is characterized by the width.

We will use invariant kinematic variables

$$u = \frac{(k_1 k_2)}{(k_1 p_2)} \, , \qquad y = \frac{(k_1 k_2)}{(k_1 p_1)} = \frac{u}{u+1} \, . \tag{24}$$

After integration in Eq. (23) over the final space $d^3\vec{p}_2 d^3\vec{k}_2$ restricted by $\delta^4(k_1 + p_1 - k_2 - p_2)$ we will have

$$\frac{d^3\vec{p}_2 d^3\vec{k}_2}{E_2 \, \omega_2} \longrightarrow \frac{du \, d\phi}{(1+u)^2} \, ,$$

$$dw_{21} = d\Gamma = \frac{|M_{21}|^2}{32\pi^2 E_1} \frac{du \, d\phi}{(1+u)^2} \, . \tag{25}$$

To calculate the differential cross-section $d\sigma$ of the interaction of an electron with individual photons of the field one must normalize the transition probability to the flux of the photons of the field. By definition

$$d\sigma = \frac{dw_{21}}{j}, \qquad j = c\, n_\gamma \equiv n_\gamma ,$$

where j is the photon flux density and n_γ is the photon density $(1/cm^3)$ in the rest frame of the electron $(c = 1)$.

From classical electrodynamics [21] we know that the energy flux of the electromagnetic wave with frequency ω_1 is characterized by the Poynting vector

$$| < \vec{P} > | = \frac{| < \vec{\mathcal{E}} \times \vec{\mathcal{H}}^* > |}{2} = \mathcal{E}^2_{\rm rms} =< A^2 > {\omega_1}^2 .$$

The angle brackets indicate an average over one cycle of the wave.

By definition of η Eq. (9) the photon flux j is therefore

$$j = \frac{| < \vec{P} > |}{\omega_1} =< A^2 > \omega_1 = \frac{\eta^2 m^2}{e^2}\omega_1 . \tag{26}$$

Hence the cross section that corresponds to the probability Eq. (25) is

$$d\sigma = \frac{|M_{21}|^2 e^2}{32\pi^2 E_1 \omega_1 m^2 \eta^2} \frac{du\, d\phi}{(1+u)^2} = \frac{{r_0}^2\, m^2}{2(k_1 p_1)} \frac{1}{\eta^2} \frac{|M_{21}|^2}{e^2 m^2} \frac{du\, d\phi}{(1+u)^2} , \tag{27}$$

where $r_0 = e^2/(4\pi\, m) = 2.82 \times 10^{-13}$ cm is the classical electron radius.

We also substitute $E_1\omega_1$ with invariant $(k_1 p_1)$. Indeed, in the rest frame of the electron (the frame where we calculate $dw_{21} = d\Gamma$)

$$E_1\omega_1 = (k_1 p_1) .$$

The matrix element M_{21} in equation (27) depends on polarization of the incoming electron and polarizations of particles in the final state.

In this dissertation we are interested mainly in the calculation of the cross-sections for unpolarized electrons. The incoming SLC electron beam is randomly polarized.

We are also not measuring the polarization of outgoing electrons. At the same time the polarization of backscattered photons is important because these photons will be involved in the second-step interaction with the laser photons resulting in e^+e^- pair production.

Calculation of $|M_{21}|^2$ for a randomly polarized electron beam involves averaging over the initial polarizations of the electrons and summing over the final states. Averaging introduces an additional multiplier $1/(2j_e+1)$ where j_e is the spin of the particle (for the electron $j_e = 1/2$). We will denote the matrix element after averaging over the initial electron states and summation over the final states as $\overline{|M_{21}|^2}$. We presented M_{21} in the form $M_{21} = \bar{u}(q_2)\,\mathcal{M}\,u(q_1)$ in order to have them handy for averaging over polarization of the incoming electron $u(q_1)$ and summation over polarization of outgoing electron $\bar{u}(q_2)$

$$\begin{aligned}
\overline{|M_{21}|^2} &= \frac{1}{2j_e+1}\sum_{spin_1}\sum_{spin_2}|M_{21}|^2 = \frac{e^2}{2}\sum_{spin_1}\sum_{spin_2}\left(\bar{u}(q_1)\,\bar{\mathcal{M}}\,u(q_2)\;\bar{u}(q_2)\,\mathcal{M}\,u(q_1)\right), \\
M_{21} &= \bar{u}(q_2)\,\mathcal{M}\,u(q_1)\,.
\end{aligned}$$

Matrices $\mathcal{M}$ will be calculated in the next section for the different laser polarizations.

Summation over final state electron polarization and averaging over initial state electron polarization significantly simplifies calculations. This can be done by calculating the trace of the matrix

$$\overline{|M_{21}|^2} = \frac{e^2}{2}\,\mathrm{Tr}\left[\bar{\mathcal{M}}\,(\gamma q_2 + m)\,\mathcal{M}\,(\gamma q_1 + m)\right]. \tag{28}$$

With an additional factor $1/2$ due to spin-statistics we rewrite Eq. (27) for unpolarized electrons in the following invariant form

$$d\sigma = 2r_0^2\,\frac{m^2}{(\mathrm{s}-m^2)}\,\frac{1}{\eta^2}\,\frac{\mathrm{Tr}\left[\bar{\mathcal{M}}(\gamma q_2 + m)\mathcal{M}(\gamma q_1 + m)\right]}{4\,m^2}\,\frac{du\,d\phi}{(1+u)^2}\,. \tag{29}$$

In this formula we use the invariant center of mass energy s that is related to $(k_1\, p_1)$ as

$$\mathrm{s} = (k_1 + p_1)^2 = 2(k_1\, p_1) + m^2\,.$$

It will be shown later that at the low field intensities the trace of the matrix Eq. (28) has leading term proportional to η^{2n} where $n \geq 1$ is the number of photons from the electromagnetic field involved in the reaction. This term cancels η^2 in the denominator of the equation (29) for low field intensities.

In terms of invariant variable y defined by Eq. (24) the cross-section Eq. (29) is

$$d\sigma = 2r_0^2\, \frac{m^2}{(\mathrm{s} - m^2)}\, \frac{1}{\eta^2}\, \frac{\mathrm{Tr}\left[\bar{\mathcal{M}}(\gamma q_2 + m)\mathcal{M}(\gamma q_1 + m)\right]}{4\, m^2}\, dy\, d\phi\,. \tag{30}$$

Calculations of cross-sections for polarized electrons and definition of degree of polarization for final electrons is also straightforward for nonlinear QED processes but will not be presented in this dissertation as they are not relevant to the experimental results presented here.

2.6 Emission of a photon by an electron in the field of a strong electromagnetic wave

Consider a plane electromagnetic wave propagating in z direction with vector potential A. Because $\vec{\mathcal{E}} = -\frac{1}{c}\frac{\partial \vec{\mathbf{A}}}{\partial t}$ (Lorenz gauge), only transverse component of the vector potential A is different from 0. We will consider two laser polarizations.

1. Circular polarized wave

$$\begin{aligned} A &= a_1 \cos\phi + a_2 \sin\phi\,, \\ a_1 &= (0, a, 0, 0)\,, \\ a_2 &= (0, 0, a, 0)\,. \end{aligned} \tag{31}$$

2. Linear polarized wave

$$\begin{aligned} A &= a_1 \cos\phi\,, \\ a_1 &= (0, a, 0, 0)\,. \end{aligned} \tag{32}$$

(We chose polarization of the linear polarized wave parallel to the x-axis.)

For linear polarization substituting Eq. (32) into Eq. (17) we have

$$\begin{aligned} S(p) &= (px) + \int_0^{(kx)} \left[\frac{e(pa)}{(kp)} \cos\phi - \frac{e^2a^2}{2(kp)} \cos^2\phi \right] d\phi \\ &= (px) + \frac{\eta^2 m^2}{2(kp)} kx + \frac{e(pa)}{(kp)} \sin(kx) + \frac{\eta^2 m^2}{4(kp)} \sin(2kx)\,. \end{aligned}$$

According to equation (9) $< A^2 >= -\frac{a^2}{2}$ for the linear polarization and $< A^2 >= -a^2$ for the circular polarization (the angle brackets indicate that the average over one cycle of the wave is taken).

Using definition of quasi-momentum Eq. (19) we can write the wave function of electron Eq. (17) for the linear wave in the following form

$$\psi(p) = \left[1 + \frac{e(\gamma k)(\gamma a)}{2(kp)} \cos\phi \right] e^{iqx + i\tilde{\alpha}\sin\phi - i\tilde{\beta} sin2\phi} u(p)\,, \tag{33}$$

where

$$\tilde{\alpha} = \frac{e(pa)}{(kp)}, \qquad \tilde{\beta} = -\frac{\eta^2 m^2}{4(kp)}\,.$$

We repeat the same calculations for a circular polarized wave. Substituting Eq. (31) into Eq. (17) for circular polarized wave we have

$$\begin{aligned} S(p) &= (px) + \int_0^{(kx)} \left[\frac{e(pa_1)}{(kp)} \cos\phi + \frac{e(pa_2)}{(kp)} \sin\phi - \frac{e^2a^2}{2(kp)} \right] d\phi \\ &= (px) + \frac{\eta^2 m^2}{2(kp)} (kx) + \frac{e(pa_1)}{(kp)} \sin(kx) - \frac{e(pa_2)}{(kp)} \cos(kx)\,. \end{aligned}$$

According to Eq. (9) $< A^2 >= -a^2$ for the circular wave. Using the definition of quasi-momentum Eq. (19) we write the wave function of electron Eq. (17) for the circular wave in the following form

$$\psi(p) = \left[1 + e\frac{(\gamma k)(\gamma a_1)}{2(kp)}\cos\phi + e\frac{(\gamma k)(\gamma a_2)}{2(kp)}\sin\phi\right] e^{iqx + i\tilde{\alpha}\sin(\phi-\phi_0)}\, u(p)\,, \quad (34)$$

where

$$\tilde{\alpha} = \sqrt{\alpha_1^2 + \alpha_2^2}\,, \quad \tan\phi_0 = \frac{\tilde{\alpha}_2}{\tilde{\alpha}_1}\,, \quad \tilde{\alpha}_1 = \frac{e(pa_1)}{(kp)}\,, \quad \tilde{\alpha}_2 = \frac{e(pa_2)}{(kp)}\,.$$

At this point we have all the information for writing the matrix element M_{21} for the scattering of an electron in a strong field of linear or circular polarized laser light. All we need is to substitute wave functions Eq. (33) for linear light polarization or Eq. (34) for circular light polarization into Eq. (21) and integrate over d^4x. The problem is that this integration is not a simple thing to do. Simplifications occur if we use the approach used by Nikishov and collaborators [7].

We will calculate now matrix elements S_{21} using this approach.

For a linear polarized laser we get

$$S_{21} = -ie\int e^{i\alpha\sin\phi - i\beta\sin 2\phi}\, e^{i(q_1x) - i(q_2x) - i(k_2x)}\bar{u}(p_2)\times$$
$$\left[(\gamma\epsilon^*) + \frac{e}{2}\left(\frac{(\gamma a)(\gamma k_1)(\gamma\epsilon^*)}{(k_1p_2)} + \frac{(\gamma\epsilon^*)(\gamma k_1)(\gamma a)}{(k_1p_1)}\right)\cos\phi + \frac{e^2a^2(\epsilon^*k_1)(\gamma k_1)}{2(k_1p_1)(k_1p_2)}\cos^2\phi\right]\times$$
$$u(p_1)\, d^4x\,, \quad (35)$$

where

$$\alpha = e\left(\frac{(ap_1)}{(k_1p_1)} - \frac{(ap_2)}{(k_1p_2)}\right), \qquad \beta = -\frac{\eta^2m^2}{4}\left(\frac{1}{(k_1p_1)} - \frac{1}{(k_1p_2)}\right). \quad (36)$$

For a circular polarized laser we get

$$
\begin{aligned}
S_{21} \;=\; & -ie \int e^{i\alpha \sin(\phi-\phi_0)}\, e^{i(q_1x) - i(q_2x) - i(k_2x)} \bar{u}(p_2) \times \\
& \left[(\gamma\epsilon^*) + \frac{e^2a^2(\epsilon^* k_1)(\gamma k_1)}{2(k_1p_1)(k_1p_2)} + \frac{e}{2}\left(\frac{(\gamma a_1)(\gamma k_1)(\gamma\epsilon^*)}{(k_1p_2)} + \frac{(\gamma\epsilon^*)(\gamma k_1)(\gamma a_1)}{(k_1p_1)} \right) \cos\phi + \right. \\
& \left. \frac{e}{2}\left(\frac{(\gamma a_2)(\gamma k_1)(\gamma\epsilon^*)}{(k_1p_2)} + \frac{(\gamma\epsilon^*)(\gamma k_1)(\gamma a_2)}{(k_1p_1)} \right) \sin\phi \right] u(p_1)\, d^4x
\end{aligned}
\tag{37}
$$

where

$$
\begin{aligned}
& \alpha = \sqrt{\alpha_1^2 + \alpha_2^2}\,, \qquad \tan\phi_0 = \frac{\alpha_2}{\alpha_1}\,, \\
& \alpha_1 = e\left(\frac{(a_1p_1)}{(k_1p_1)} - \frac{(a_1p_2)}{(k_1p_2)} \right), \qquad \alpha_2 = e\left(\frac{(a_2p_1)}{(k_1p_1)} - \frac{(a_2p_2)}{(k_1p_2)} \right).
\end{aligned}
\tag{38}
$$

The idea for the calculations is to express the ϕ-dependent part of the S_{21} as a Fourier series in $e^{(i\,n\,\phi)}$ (n goes from $-\infty$ to $+\infty$) with coefficients that are independent of phase ϕ (and hence of x). Any periodic function $f(\phi)$ can be presented as Fourier series

$$
f(\phi) = \sum_{n=-\infty}^{+\infty} C_n e^{i\,n\,\phi}\,. \tag{39}
$$

After we present integrals Eq. (37) and (35) as series in $e^{(i\,n\,\phi)}$ the dependence on coordinates x ($\phi = (k_1\,x)$) will be in the exponent and the integration can be simplified according to

$$
\int e^{i\,n\,(k_1x) + i(q_1x) - i(k_2x) - i(q_2x)} d^4x = (2\pi)^4 \delta^4(n\,k_1 + q_1 - k_2 - q_2) \tag{40}
$$

Using this "trick" we avoid integration over d^4x, instead we have to find coefficients C_n and calculate series.

For a linear polarized laser there are three functions $f(\phi)$

$$f(\phi) = (1\,,\,\cos\phi\,,\,\cos^2\phi) \times e^{i\alpha\sin\phi - i\beta\sin 2\phi}\,.$$

They have different orders $l = 0, 1, 2$ for $\cos^{(l)}\phi$. For each $l = 0, 1, 2$ we can write

$$\cos^{(l)}\phi\, e^{i\alpha\sin\phi - i\beta\sin 2\phi} = \sum_{n=-\infty}^{+\infty} A_l(\alpha,\beta,n)\, e^{i\,n\,\phi}\,, \tag{41}$$

where $A_l(\alpha,\beta,n)$ $(l = 0, 1, 2)$ are three different functions

$$A_l(\alpha,\beta,n) = \frac{1}{2\pi}\int_{-\pi}^{\pi} \cos^{(l)}\phi e^{i\alpha\sin\phi - i\beta\sin 2\phi - i\,n\,\phi}\, d\phi\,. \tag{42}$$

Functions in the integral Eq. (42) are odd functions of parameter ϕ, hence

- All coefficients A_l $(l = 0, 1, 2)$ are real,
- $\alpha A_1 - 4\beta A_2 + (2\beta - n)A_0 = 0$.

This last equation follows from

$$0 = \int_{-\pi}^{\pi} d\, e^{i\alpha\sin\phi - i\beta\sin 2\phi - i\,n\,\phi} = i\alpha A_1 - 2i\beta(2A_2 - A_0) - inA_0\,.$$

For a circular polarized laser there are three functions $f(\phi)$

$$f(\phi) = (1\,,\,\cos\phi\,,\,\sin\phi) \times e^{i\alpha\sin(\phi - \phi_0)}\,,$$

and we can write

$$\begin{aligned}
e^{i\alpha\sin(\phi-\phi_0)} &= \sum_{n=-\infty}^{+\infty} B_0(\alpha,n)\, e^{i\,n\,\phi}\,,\\
\cos\phi\, e^{i\alpha\sin(\phi-\phi_0)} &= \sum_{n=-\infty}^{+\infty} B_1(\alpha,n)\, e^{i\,n\,\phi}\,,\\
\sin\phi\, e^{i\alpha\sin(\phi-\phi_0)} &= \sum_{n=-\infty}^{+\infty} B_2(\alpha,n)\, e^{i\,n\,\phi}\,.
\end{aligned} \tag{43}$$

where $B_l(\alpha, n)$ $(l = 0, 1, 2)$ are three different functions

$$\begin{aligned} B_0(\alpha, n) &= \frac{1}{2\pi} \int_{-\pi}^{\pi} e^{i\alpha \sin(\phi - \phi_0) - i\, n\, \phi}\, d\phi\,, \\ B_1(\alpha, n) &= \frac{1}{2\pi} \int_{-\pi}^{\pi} \cos\phi\, e^{i\alpha \sin(\phi - \phi_0) - i\, n\, \phi}\, d\phi\,, \\ B_2(\alpha, n) &= \frac{1}{2\pi} \int_{-\pi}^{\pi} \sin\phi\, e^{i\alpha \sin(\phi - \phi_0) - i\, n\, \phi}\, d\phi\,. \end{aligned} \tag{44}$$

Because functions in integrals Eq. (44) are periodic functions with period 2π we can write

$$\int_{-\pi}^{\pi} d\left(e^{i\alpha \sin(\phi - \phi_0) - i\, n\, \phi}\right) = e^{-i\, n\, \phi_0} \int_{-\pi - \phi_0}^{\pi - \phi_0} d\left(e^{i\alpha \sin\phi - i\, n\, \phi}\right) = 0\,,$$

and therefore

$$0 = \int_{-\pi}^{\pi} d\left(e^{i\alpha_1 \sin\phi - i\alpha_2 \cos\phi - i\, n\, \phi}\right) = i\alpha_1 B_1 + i\alpha_2 B_2 - i\, n\, B_0\,,$$

or

$$\alpha_1 B_1 + \alpha_2 B_2 = n\, B_0\,. \tag{45}$$

The coefficients B_l $(l = 0, 1, 2)$ are not real in general case. Parameter ϕ_0 defined by Eq. (38) depends on orientation of the coordinate system (and hence polarization vectors $\vec{a}_1$ and $\vec{a}_2$) with respect to the electron scattering plane. But for the circular polarized wave there is an axial symmetry: the cross section does not depend on the orientation of the coordinate system with respect to the electron scattering plane. Therefore we can always choose the x-axis of the coordinate system to be in the electron scattering plane where $\phi_0 = 0$ according to definition of ϕ_0 Eq. (38). In this case coefficients B_0 and B_1 are real, B_2 is imaginary and $\alpha_2 = 0$.

Eq. (45) becomes

$$\alpha_1 B_1 = n\, B_0\,.$$

Coefficients B_l $(l = 0, 1, 2)$ have simple interpretation in terms of Bessel functions of the 1-st kind. By definition of the Bessel-Fourier series

$$e^{i\alpha \sin\phi} = \sum_{n=-\infty}^{+\infty} J_n(\alpha)\, e^{i\alpha\phi}\,. \tag{46}$$

Functions $J_n(\alpha)$ are Bessel functions of the 1-st kind of real argument α. Functions $J_n(\alpha)$ are real.

Therefore we can rewrite Eqs. (44) the definition of coefficients B_n (for $\phi_0 \neq 0$)

$$\begin{aligned} B_0 &= J_n\, e^{i\,n\,\phi_0}\,, \\ B_1 &= \frac{1}{2}\left(J_{n-1}\, e^{-i\phi_0} + J_{n+1}\, e^{+i\phi_0}\right) e^{i\,n\,\phi_0}\,, \\ B_2 &= -\frac{i}{2}\left(J_{n-1}\, e^{-i\phi_0} - J_{n+1}\, e^{+i\phi_0}\right) e^{i\,n\,\phi_0}\,. \end{aligned} \tag{47}$$

or in coordinate system where $\phi_0 = 0$

$$\begin{aligned} B_0 &= J_n\,, \\ B_1 &= \frac{1}{2}\left(J_{n-1} + J_{n+1}\right)\,, \\ B_2 &= -\frac{i}{2}\left(J_{n-1} - J_{n+1}\right)\,. \end{aligned} \tag{48}$$

For Bessel functions an equality similar to Eq. (45) holds

$$\alpha\,\left(J_{n-1} + J_{n+1}\right) = 2\,n\,J_n\,. \tag{49}$$

The S-matrix element Eq. (35) presented as Fourier series for linear polarized wave is

$$\begin{aligned} S_{21} &= -ie(2\pi)^4 \sum_{n=-\infty}^{+\infty} \bar{u}(q_2)\,\mathcal{M}^{(n)}\,u(q_1)\;\delta^4(n\,k_1 + q_1 - k_2 - q_2)\,, \\ \mathcal{M}^{(n)} &= A_0\,(\gamma\epsilon^*) + A_1\,\frac{e}{2}\left(\frac{(\gamma a)(\gamma k_1)(\gamma\epsilon^*)}{(k_1 p_2)} + \frac{(\gamma\epsilon^*)(\gamma k_1)(\gamma a)}{(k_1 p_1)}\right) + \end{aligned}$$

$$A_2 \frac{e^2 a^2 (\epsilon^* k_1)(\gamma k_1)}{2(k_1 p_1)(k_1 p_2)} . \tag{50}$$

The S-matrix element Eq. (37) presented as Fourier series for circular polarized wave is

$$\begin{aligned} S_{21} &= -ie(2\pi)^4 \sum_{n=-\infty}^{+\infty} \bar{u}(q_2)\, \mathcal{M}^{(n)}\, u(q_1)\, \delta^4(n\,k_1 + q_1 - k_2 - q_2)\,, \\ \mathcal{M}^{(n)} &= J_n \left((\gamma\epsilon^*) + \frac{e^2 a^2 (\epsilon^* k_1)(\gamma k_1)}{2(k_1 p_1)(k_1 p_2)} \right) \\ &\quad + J_{n-1}\, \frac{e}{4} \left(\frac{((\gamma a_1) - i(\gamma a_2))(\gamma k_1)(\gamma \epsilon^*)}{(k_1 p_2)} + \frac{(\gamma\epsilon^*)(\gamma k_1)((\gamma a_1) - i(\gamma a_2))}{(k_1 p_1)} \right) \\ &\quad + J_{n+1}\, \frac{e}{4} \left(\frac{((\gamma a_1) + i(\gamma a_2))(\gamma k_1)(\gamma \epsilon^*)}{(k_1 p_2)} + \frac{(\gamma\epsilon^*)(\gamma k_1)((\gamma a_1) + i(\gamma a_2))}{(k_1 p_1)} \right) . \end{aligned} \tag{51}$$

Using the definition for scattering amplitudes Eq. (20)

$$S_{21} = (2\pi)^4 \sum_{n=-\infty}^{+\infty} \delta^4(n\,k_1 + q_1 - k_2 - q_2) M_{21}^{(n)}\,,$$

we can write M_{21} as

$$M_{21}^{(n)} = -i\,e\,\bar{u}(q_2)\,\mathcal{M}^{(n)}\,u(q_1)\,, \tag{52}$$

where $\mathcal{M}^{(n)}$ are defined according to Eqs. (50) and (51) for linear and circular wave polarizations.

Formulae Eq. (50) and (51) are valid for arbitrary polarization of the incident electron characterized by spinor $u(q_1)$, recoil electron characterized by spinor $u(q_2)$ and backscattered photon characterized by polarization 4-vector ϵ^*.

Individual amplitudes $M_{21}^{(n)}$ with different n do not interfere because of the presence of the delta-function $\delta^4(n\,k_1 + q_1 - k_2 - q_2)$. Calculation of $|M_{21}|^2$ can be done directly from Eqs. (50) and (51). We have

$$\begin{aligned} |M_{21}|^2 &= \sum_s |M_{21}^{(n)}|^2 \\ &= e^2 \sum_n \left(\bar{u}(q_1)\, \bar{\mathcal{M}}^{(n)}\, u(q_2)\, \bar{u}(q_2)\, \mathcal{M}^{(n)}\, u(q_1) \right) . \end{aligned} \tag{53}$$

In the case of arbitrary electron polarization calculation of $|M_{21}|^2$ requires lengthy calculations after substitution of specific polarization states $u(q_1)$, $u(q_2)$ and ϵ^*. These calculations represent the only technical difficulty, primarily because of the presence of 5 γ-matrices in $|M_{21}|^2$.

The author used the commercially available program MAPLE and the free shareware copy of FORM v1.2 to carry out the calculations. FORM is good for simplification of 4-vector products involving γ-matrices, multiplications of matrices and calculation of traces. Unfortunately FORM v1.2 (and FORM in general) is not suitable for simplification of lengthy expressions and has output that is very difficult to read. FORM was used by the author to carry out initial calculations involving γ-matrices.

Output from FORM was fed into MAPLE which handles complicated expressions and performs simplifications. MAPLE has powerful series expansion tools that allow approximation of the cross-sections as a series in the field intensity η^2. With the use of MAPLE it was demonstrated (see Appendices A, B, C, D) that well known Klein-Nishina and Breit-Wheeler formulae for ordinary Compton scattering and pair production can be obtained as low-intensity approximations for nonlinear QED processes. Numerical calculations were performed with the assistance of MAPLE. Some of these results will be presented in Appendices A, B, C, D.

At the end of this section we present results for unpolarized cross-sections which are derived in Appendices A and B for multiphoton Compton scattering. Unpolarized cross sections correspond to the case when all particles (except laser photons) are unpolarized including high energy backscattered photons.

We use equations (29) and (30) from section 2.5 and results from sections A and B.

For the linear polarized laser

$$\frac{d\sigma^{(n)}_{Lin,Unp}}{du\,d\phi} = 2r_0^2 \frac{m^2}{(s-m^2)} \frac{1}{(1+u)^2} \frac{1}{\eta^2} \left[-2A_0^2 + 2\eta^2 \left(2 + \frac{u^2}{(1+u)} \right) (A_1^2 - A_0 A_2) \right],$$

or

$$\frac{d\sigma^{(n)}_{Lin,Unp}}{dy\,d\phi} = 2r_0^2 \frac{m^2}{(s-m^2)} \frac{1}{\eta^2} \left[-2A_0^2 + 2\eta^2 \left(2 + \frac{y^2}{(1-u)} \right) (A_1^2 - A_0 A_2) \right] .$$

For the circularly polarized laser

$$\frac{d\sigma^{(n)}_{Circ,Unp}}{du} = 4\pi r_0^2 \frac{m^2}{(s-m^2)} \frac{1}{(1+u)^2} \frac{1}{\eta^2} \left[-2\,{J_n}^2 + \eta^2 \left(1 + \frac{u^2}{2\,(u+1)} \right) ({J_{n-1}}^2 + {J_{n+1}}^2 - 2\,{J_n}^2) \right] ,$$

or

$$\frac{d\sigma^{(n)}_{Circ,Unp}}{dy} = 4\pi r_0^2 \frac{m^2}{(s-m^2)} \frac{1}{\eta^2} \left[-2\,{J_n}^2 + \eta^2 \left(1 + \frac{y^2}{2\,(1-y)} \right) ({J_{n-1}}^2 + {J_{n+1}}^2 - 2\,{J_n}^2) \right] .$$

The cross section for circular polarization does not depend on the polar angle ϕ of the electron Compton scattering and we integrated over $d\phi$ which gave additional factor 2π.

2.7 Kinematics of the multi-photon Compton scattering in a strong electromagnetic field

Consider the multi-photon Compton scattering of an electron

$$n\,\omega + e^- \to \gamma + e^- ,$$

where $n\,\omega$ stands for "n" laser photons, γ for backscattered high energy photon and e^- for the electron.

Incoming laser photons and electron have 4-momenta $n\,k_1$ and p_1; backscattered high energy photon and electron have 4-momenta k_2 and p_2.

4-momenta of electrons are modified when they pass through the region of a strong electromagnetic field. Kinematics are defined by quasi-momenta q_1 and q_2

$$\begin{aligned} q_1 &= p_1 + \frac{\eta^2 m^2}{2(k_1 p_1)} k_1 , \qquad q_1^2 = m_*^2 = m^2(1+\eta^2) \\ q_2 &= p_2 + \frac{\eta^2 m^2}{2(k_1 p_2)} k_1 , \qquad q_2^2 = m_*^2 = m^2(1+\eta^2) . \end{aligned} \tag{54}$$

Invariant dimensionless parameters u, u_n, x and the center of mass energy square s are defined as

$$\begin{aligned} u &= \frac{(k_1 k_2)}{(k_1 p_2)} , \qquad u_n = \frac{n\,x}{1+\eta^2} , \qquad x = \frac{2(k_1 p_1)}{m^2} , \\ \mathrm{s} &= (k_1 + p_1)^2 = (1+x)\,m^2 . \end{aligned}$$

The center Of Mass (COM) frame is defined by the condition $n\vec{k_1} + \vec{q_1} = 0$ where n is the number of laser photons. Note that the COM frame is different for different orders n and different field intensities η.

Energy-momentum conservation requires that

$$n\,k_1 + q_1 = k_2 + q_2 .$$

In the COM frame the electron can be scattered by any angle Θ given by $\cos\Theta = [-1, 1]$. Let the energy of the electron in the COM frame be Q_0, momentum Q. A schematic view of the reaction in the COM frame is shown in Fig. 4. From the energy-momentum conservation we write down 4-momentum components of all particles in the COM frame

$$\begin{aligned} k_1 &= \frac{1}{n}(Q,\, 0,\, 0,\, Q) , \\ q_1 &= (Q_0,\, 0,\, 0,\, -Q) , \\ k_2 &= (Q,\, Q\sin\Theta,\, 0,\, Q\cos\Theta) , \\ q_2 &= (Q_0,\, -Q\sin\Theta,\, 0,\, -Q\cos\Theta) . \end{aligned} \tag{55}$$

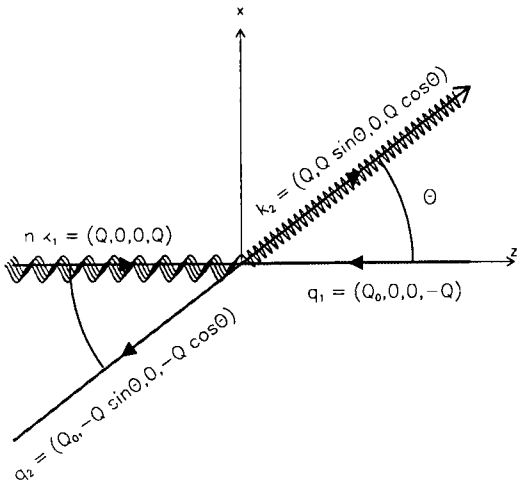

Figure 4: Schematic diagram for multi-photon Compton scattering. In the COM frame electrons moving in $-z$ direction interact with n laser photons moving in $+z$ direction. Recoil electron scatters by an angle Θ (See text).

Using these components of 4-vectors in the COM frame we can write two equations

$$m_*^2 u_n = 2\,n\,(k_1\,q_1) = 2QQ_0 + 2Q^2\,,$$
$$Q_0^2 - Q^2 = m_*^2\,.$$

Their solution for Q and Q_0 defines parameters of the COM frame

$$Q = \frac{m_*}{2}\frac{u_n}{\sqrt{1+u_n}}\,,$$
$$Q_0 = \frac{m_*}{2}\frac{u_n+2}{\sqrt{1+u_n}}\,. \tag{56}$$

Relativistic boost factor $\gamma_{\rm COM} = 1/\sqrt{1-\beta^2}$ ($\beta = v/c$) from the LAB frame to the COM frame is defined by relation $E_1 = \gamma_{\rm COM}Q_0 + \beta\gamma_{\rm COM}Q \approx \gamma_{\rm COM}(Q+Q_0)$ (E_1 is the incoming electron beam energy in the LAB frame). Hence

$$\gamma_{COM} \approx \frac{E_1}{m_*\sqrt{1+u_n}}\,. \tag{57}$$

This factor is of course different from the boost factor γ_e from the LAB frame to the electron rest frame:

$$\gamma_e = \frac{E_1}{m_*} . \tag{58}$$

Using definitions of invariants $u = (k_1k_2)/(k_1p_2)$ and $y = (k_1k_2)/(k_1p_1)$ and noting that $(k_1p_2) = (k_1q_2)$ and $(k_1p_1) = (k_1q_1)$ we find directly from Eqs. (55) and (56) that

$$u = \frac{u_n(1-\cos\Theta)}{2+u_n(1+\cos\Theta)} = [0...u_n] , \tag{59}$$

$$y = \frac{1-\cos\Theta}{2}\frac{u_n}{1+u_n} = \left[0...\frac{u_n}{1+u_n}\right] . \tag{60}$$

The scattering angle of an electron in the COM frame $\cos\Theta = [-1,1]$ corresponds to the range of parameters $u = [0,u_n]$ and the range of parameters $y = \left[0,\frac{u_n}{1+u_n}\right]$ ($\cos\Theta = -1$ corresponds to the lower limit 0 for both variables).

The maximum energy of backscattered photons and the minimum energy of recoil electrons corresponds to $\cos\Theta = -1$ ($\Theta = 180°$). Using definition of y we can therefore write

$$y_{max} = \frac{u_n}{1+u_n} = \frac{2\omega_1\omega_{2,max}}{\omega_1(E_1+p_1)} \approx \frac{\omega_{2,max}}{E_1} .$$

Approximate sign is due to $p_1 \approx E_1$; at relativistic energies $E_1 = 46.6$ GeV the difference between E_1 and p_1 is so negligible that correction is of the order of 10^{-5}.

Hence the maximum energy of backscattered photons and the minimum energy of recoil electrons are

$$\begin{aligned} \omega_{2,max} &= E_1\, y_{max} = E_1\frac{u_n}{1+u_n} = E_1\frac{n\,x}{n\,x+1+\eta^2} , \\ E_{2,min} &= E_1(1-y_{max}) = E_1\frac{1}{1+u_n} = E_1\frac{1+\eta^2}{n\,x+1+\eta^2} . \end{aligned} \tag{61}$$

For completeness we write down the conventional Mandelstam variables s, t and $\tilde{u}$ for multi-photon Compton scattering in a strong electromagnetic field (we use notation $\tilde{u}$ because the symbol u is used for kinematic invariant $u = (k_1k_2)/(k_1p_2)$)

$$
\begin{aligned}
\mathrm{s} &= (n\,k_1 + q_1)^2 = m_*^2 + 2\,n\,(k_1\,q_1) = m_*^2(1+u_n)\,, \\
\mathrm{t} &= (n\,k_1 - k_2)^2 = -2\,n\,(k_1\,k_2) = -2Q^2(1-\cos\Theta) = -2\,n\,\omega_1\omega_2(1-\cos\Theta_{lab})\,, \\
\tilde{u} &= (n\,k_1 - q_2)^2 = m_*^2 - 2\,n\,(k_1\,q_2)\,,
\end{aligned}
$$

where Q is absolute value of 3-momentum of particles in the COM frame (Fig. 4); Θ - angle of the scattered photon in the COM frame; ω_1, ω_2 and Θ_{lab} - laser photon energy, backscattered photon energy and angle in the laboratory frame.

t is the momentum transfer that corresponds to the multi-photon Compton scattering.

From the energy-momentum conservation and equality $\mathrm{s} + \mathrm{t} + \tilde{u} = 2m_*^2$ it follows that

$$
y = \frac{-\mathrm{t}}{m_*^2\,u_n}\,, \qquad u = \frac{-\mathrm{t}}{m_*^2 - \tilde{u}} = \frac{-\mathrm{t}}{m_*^2\,u_n + \mathrm{t}}\,. \tag{62}
$$

The invariant t depends on the scattering angle Θ in the COM frame:

$$
\mathrm{t} = -m_*^2 \frac{u_n}{1+u_n} \frac{1-\cos\Theta}{2}
$$

The scattering angle of an electron in the COM frame $\cos\Theta = [-1, 1]$ corresponds to the range of momentum transfer $\mathrm{t} = \left[-m_*^2 \dfrac{u_n}{1+u_n},\, 0\right]$.

2.8 Energy of backscattered photons from multi-photon Compton process

There is a unique correspondence between the energy of the backscattered photon and its angle for any order n of the multi-photon Compton scattering (n is the number of laser photons involved) and field intensity η. We will write down Lorenz transformation for the energy and momentum from the COM frame to the LAB frame

$$\omega_2 = \gamma Q - \gamma\beta Q\cos\Theta\,,$$
$$\omega_2\cos\Theta_{lab} = \gamma Q\cos\Theta - \gamma\beta Q\,,$$
$$\omega_2\sin\Theta_{lab} = Q\sin\Theta_{lab}\,.$$

Dividing the second and third equations by the first one we get

$$\begin{aligned}\sin\Theta_{lab} &= \frac{1}{\gamma}\frac{\sin\Theta}{1-\beta\cos\Theta}\,,\\ \cos\Theta_{lab} &= -\frac{\beta-\cos\Theta}{1-\beta\cos\Theta}\,.\end{aligned} \tag{63}$$

The exact solution for the energy versus the scattered angle can be written in parametric form for parameter $r = \cos\Theta$ in the interval $[-1,1]$

$$\begin{aligned}\omega_2 &= \gamma Q(1-\beta r)\,,\\ \sin\Theta_{lab} &= \frac{1}{\gamma}\frac{\pm\sqrt{1-r^2}}{1-\beta r}\,.\end{aligned} \tag{64}$$

Due to the relativistic boost factor $1/\gamma \approx 10^{-5}$ photons with the energy $\omega_2 > 1$ MeV are backscattered in the very forward region $\Theta_{lab} < 10^{-3}$. In this very forward region we can write

$$\sin\Theta_{lab} \simeq \frac{1}{\gamma}\sqrt{\frac{1+\cos\Theta}{1-\cos\Theta}}\,,$$
$$\cos\Theta \simeq \frac{(\gamma\sin\Theta_{lab})^2 - 1}{(\gamma\sin\Theta_{lab})^2 + 1}\,,$$
$$\omega_2 \simeq \gamma Q(1-\cos\Theta) \simeq \frac{2\gamma Q}{(\gamma\Theta_{lab})^2+1}\,.$$

One can rewrite the above expression for ω_2 using Eqs. (56)

$$\omega_2 \simeq E_1\,\frac{u_n}{1+u_n}\,\frac{1}{(\gamma\Theta_{lab})^2+1}\,. \tag{65}$$

From which the maximum photon energy that corresponds to $\Theta_{lab} = 0$ coincides with that obtained before for the maximum value of y Eq. (61).

What is the energy of the photons beyond this forward region?

From the second equation (63) we can see that $\cos\Theta_{lab}$ is almost always negative except for a very small region of $\beta \leq \Theta \leq 1$ where $\cos\Theta_{lab}$ is positive. (Negative values of $\cos\Theta_{lab}$ correspond to the backscattering of photons in the LAB frame). Let us calculate the energy of the photon for this small region of Θ when $\beta \leq \Theta \leq 1$

$$\omega_2 = \gamma Q(1 - \beta\cos\Theta) < \gamma Q(1 - \beta^2) = \frac{Q}{\gamma}.$$

Or using Eqs. (56) and (57) for Q and γ

$$\omega_2 < \frac{m_*^2 u_n}{2E_1} = n\,\omega_1(1 + \cos\alpha)\,,$$

where α is the crossing angle of the colliding beams ($\alpha = 17°$ for E144). We see that photons scattered in the forward direction in the LAB frame have energy comparable to the energy of the laser photons and hence out of the scope of interest for this experiment.

2.9 Kinematics of e^+e^- pair production by a photon in a strong electromagnetic field

Consider the reaction of pair production by photon in a strong electromagnetic field

$$n\,\omega + \gamma \to e^+ + e^-\,,$$

where again $n\,\omega$ stands for "n" laser photons interacting with a high energy photon γ, e^+ and e^- are outgoing positron and electron.

The incoming laser photon and high energy photon have 4-momenta k_1 and k_2; electron and positron have 4-momenta p_1 and p_2; their momenta are modified in the laser field according to Eq. (54).

Invariant dimensionless parameters u, u_n, x and center of mass energy square s are defined as

$$\begin{aligned} u &= \frac{(k_1 k_2)^2}{4(k_1 p_1)(k_1 p_2)}, \qquad u_n = \frac{n\,x}{1+\eta^2}, \qquad x = \frac{(k_1 k_2)}{2\,m^2}, \\ \mathrm{s} &= (k_1 + k_2)^2 = 4x\,m^2 . \end{aligned}$$

The COM frame is defined by the condition $n\,\vec{k_1} + \vec{k_2} = 0$ where n is the number of laser photons. Note that the COM frame is different for different orders n.

The energy-momentum conservation requires that

$$n\,k_1 + k_2 = q_1 + q_2 .$$

In the COM frame the electron (as well as positron) can be produced at any angle Θ with respect to the incoming photon given by $\cos\Theta = [-1, 1]$. Let the energy of the electron in the COM frame be Q_0, momentum Q. The schematic view of the reaction is shown in Fig. 5. From energy-momentum conservation we write down 4-momentum components of all particles in the COM frame

$$\begin{aligned} k_1 &= \frac{1}{n}\,(Q_0,\, 0,\, 0,\, Q_0)\,, \\ k_2 &= (Q_0,\, 0,\, 0,\, -Q_0)\,, \\ q_1 &= (Q_0,\, Q\sin\Theta,\, 0,\, Q\cos\Theta)\,, \\ q_2 &= (Q_0,\, -Q\sin\Theta,\, 0,\, -Q\cos\Theta)\,. \end{aligned} \tag{66}$$

Using these components of 4-vectors in the COM frame we can write two equations

$$\begin{aligned} 2m_*^2 u_n &= n\;(k_1\,k_2) = 2Q_0^2\,, \\ Q_0^2 - Q^2 &= m_*^2\,. \end{aligned}$$

Their solution for Q and Q_0 defines parameters for the COM frame

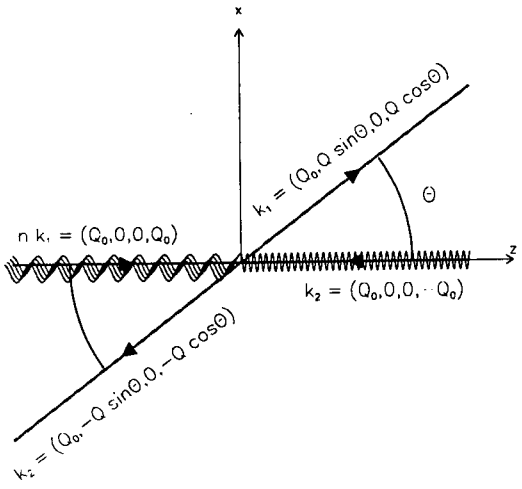

Figure 5: Schematic diagram for multi-photon e^+e^- pair production. In the COM frame photon moving in $-z$ direction interacts with n laser photons moving in $+z$ direction. Electron and positron are created at an angle Θ (See text).

$$\begin{aligned} Q &= m_*\sqrt{u_n - 1}\,, \\ Q_0 &= m_*\sqrt{u_n}\,. \end{aligned} \tag{67}$$

Relativistic boost factor $\gamma_{\rm COM} = 1/\sqrt{1-\beta^2}$ ($\beta = v/c$) from the LAB frame to the COM frame is defined by relation $\omega_1 = \gamma_{\rm COM}Q_0 + \beta\gamma_{\rm COM}Q_0 \approx 2\,\gamma_{\rm COM}Q_0$ (ω_1 is the energy of high energy photon in the LAB frame). Hence

$$\gamma_{COM} \approx \frac{\omega_1}{2m_*\sqrt{u_n}}\,. \tag{68}$$

Using the definition of invariant $u = (k_1k_2)^2/[4(k_1p_1)(k_1p_2)]$ and noting that $(k_1p_2) = (k_1q_2)$ and $(k_1p_1) = (k_1q_1)$ we find directly from Eqs. (66) and (67)

$$u = \frac{u_n}{u_n - (u_n - 1)\cos^2\Theta} = [1...u_n]\,. \tag{69}$$

The angle of an electron in the COM frame $\Theta = 90^\circ \Rightarrow \cos\Theta = 0$ (see Fig. 5)

corresponds to $u = 1$; the angle $\Theta = 0°$ or $\Theta = 180° \Rightarrow \cos\Theta = \pm 1$ corresponds to $u = u_n$.

2.10 Expression of parameters α and β in terms of kinematic variables

Cross-sections for multi-photon Compton scattering and pair production in the field of a plain electromagnetic wave have a complicated dependence on the field intensity η and number of photon n involved in the process. This is manifested by the introduction of functions $A_i(\alpha, \beta, n)$ for the linear polarized laser and Bessel functions $J_n(\alpha)$ for the circular polarized laser in the expressions for cross-sections.

Arguments α, β of the functions A_0, A_1, A_2 and argument α of the Bessel's functions J_n can be expressed in terms of the invariant kinematic variable u and the field intensity η.

Recall the definition of u for electron scattering

$$u = \frac{(k_1 k_2)}{(k_1 p_2)},$$

where k_1, p_1 stands for 4-momenta of the incoming photon and electron and k_2, p_2 for 4-momenta of the outgoing photon and electron.

Definition of u for the pair production is

$$u = \frac{(k_1 k_2)^2}{4(k_1 p_1)(k_1 p_2)},$$

where k_1, k_2 stands for 4-momenta of the two photons and p_1, p_2 for 4-momenta of the outgoing electron and positron.

Using these definitions and results of sections 2.7 and 2.9 for 4-momenta in the COM frame we get for a linear polarized laser

$$\alpha_{Lin} = -2\sqrt{2}\, n \frac{\sqrt{u(u_n - u)}}{u_n} \frac{\eta}{\sqrt{1+\eta^2}} \cos\phi,$$

$$\beta_{Lin} = \frac{n\,u}{2u_n}\frac{\eta^2}{1+\eta^2}, \tag{70}$$

and for a circular polarized laser

$$\alpha_{Circ} = -2\,n\frac{\sqrt{u(u_n-u)}}{u_n}\frac{\eta}{\sqrt{1+\eta^2}}. \tag{71}$$

Note that

$$\alpha_{Lin} = \sqrt{2}\;\alpha_{Circ}\cos\phi\,,$$

where factor $\sqrt{2}$ is due to different definitions of η as a function of peak field intensity a for two polarizations.

Dependence of α and β on η and u are the same for the multi-photon Compton scattering of an electron and pair production in light by light scattering though the definition of the kinematic invariant u is different for these two processes.

2.11 Series expansion of cross-sections in terms of field intensity η

The goal of this section is to demonstrate how to present cross-sections as series in terms of the laser intensity η.

We start with rewriting results of the previous section (expressions 70 and 71) in different way.

Parameter α for circular polarized laser has the form

$$\alpha_{Circ} = -\frac{2\eta}{x}\sqrt{u(n\,x-u-u\eta^2)}\,,$$

which is the same for Compton scattering and pair production.

Parameters α and β for linear polarized laser also have the same form for electron scattering and pair production

$$\alpha_{Lin} = -\frac{2\sqrt{2}\eta}{x}\sqrt{u(n\,x-u-u\eta^2)}\cos\phi\,,$$
$$\beta_{Lin} = \frac{u}{2x}\eta^2\,.$$

For two processes (electron scattering and pair production) the meaning of the invariant u and hence its range is different.

For electron scattering

$$u = \frac{u_n(1-\cos\Theta)}{2+u_n(1+\cos\Theta)} = [0...u_n]\,,$$
$$u_n = n\,u_1 = \frac{n\,x}{1+\eta^2}\,,$$
$$x = \frac{2(k_1p_1)}{m^2} = \frac{2\omega_1E_1(1+\cos\alpha)}{m^2}\,.$$

For pair production

$$u = \frac{u_n}{u_n-(u_n-1)\cos^2\Theta} = [1...u_n]\,,$$
$$u_n = n\,u_1 = \frac{n\,x}{1+\eta^2}\,,$$
$$x = \frac{(k_1k_2)}{2m^2} = \frac{\omega_1\omega_2}{m^2}\,.$$

Note that in the above expressions parameter x does not depend on the field intensity η; x is defined by kinematics of the incoming particles only.

Parameter u_n varies with the field strength. Hence the range of u which is $[0..u_n]$ for Compton scattering and $[1..u_n]$ for the pair production varies with the field strength as well.

Now we present arguments that alternative and more natural kinematic and field variables for both processes in a strong field (electron scattering and pair production) are $u^\star$ and $\eta^\star$ defined as follows

$$\begin{aligned} \eta^\star &= \frac{\eta}{\sqrt{1+\eta^2}} = [0...1]\,, \\ u^\star &= u(1+\eta^2)\,. \end{aligned}$$

Transition from u,η to $u^\star$,$\eta^\star$ in all equations can be done using substitutions

$$\begin{aligned} \eta &= \frac{\eta^\star}{\sqrt{1-\eta^{\star 2}}}\,, \\ u &= u^\star(1-\eta^{\star 2})\,, \\ u &= u^\star/(1+\eta^2)\,. \end{aligned}$$

Substituting $u = u^\star/(1+\eta^2)$ in the expressions for α and β we get

$$\begin{aligned} \alpha_{Circ} &= -\frac{2}{x}\sqrt{u^\star(n\,x-u^\star)}\frac{\eta}{\sqrt{1+\eta^2}}\,, \\ \alpha_{Lin} &= -\frac{2\sqrt{2}}{x}\sqrt{u^\star(n\,x-u^\star)}\frac{\eta}{\sqrt{1+\eta^2}}\cos\phi\,, \\ \beta_{Lin} &= \frac{u^\star}{2x}\frac{\eta^2}{(1+\eta^2)}\,. \end{aligned}$$

Or substituting $\eta/\sqrt{1+\eta^2} = \eta^\star$

$$\begin{aligned} \alpha_{Circ} &= -\frac{2}{x}\sqrt{u^\star(n\,x-u^\star)}\eta^\star\,, \\ \alpha_{Lin} &= -\frac{2\sqrt{2}}{x}\sqrt{u^\star(n\,x-u^\star)}\eta^\star\cos\phi\,, \\ \beta_{Lin} &= \frac{u^\star}{2x}\eta^{\star 2}\,. \end{aligned}$$

The range of variable $u^\star$ is different from that of u. Because $u_n = n\,x/(1+\eta^2)$, the range of $u^\star$ for Compton scattering is

$$u^\star = [0...n\,x]\,.$$

This range is independent of the field intensity.

The range of $u^\star$ for pair production is

$$u^\star = [\frac{1}{1-\eta^{\star 2}} ... n\, x]\,,$$

which has the field dependence in the lower limit.

The real advantage of using $u^\star$, $\eta^\star$ instead of u, η becomes obvious if we write definition of A_0, A_1, A_2 and Bessel functions J_n in terms of $u^\star$, $\eta^\star$

$$\begin{aligned} J_n(u^\star, \eta^\star) &= \frac{1}{2\pi} \int_{-\pi}^{\pi} e^{i c_0 \sin\phi\, \eta^\star - i\, n\, \phi}\, d\phi\,, \\ A_l(u^\star, \eta^\star, n) &= \frac{1}{2\pi} \int_{-\pi}^{\pi} \cos^{(l)} \phi e^{i c_1 \sin\phi\, \eta^\star - i c_2 \sin 2\phi\, \eta^{\star 2} - i\, n\, \phi}\, d\phi\,, \end{aligned}$$

with c_0, c_1, c_2

$$\begin{aligned} c_0(u^\star) &= -\frac{2}{x}\sqrt{u^\star(n\, x - u^\star)}\,, \\ c_1(u^\star) &= \sqrt{2} c_0(u^\star) \cos\phi\,, \\ c_2(u^\star) &= \frac{u^\star}{2x}\,. \end{aligned}$$

This form of functions A_0, A_1, A_2 and J_s has parameters $u^\star$ and $\eta^\star$ separated which allows the expansion of the above functions in series of the field intensities $\eta^\star$ for small intensities. We will write such series expansions in the next sections. The field strength parameter $\eta^\star$ varies in the range [0...1] while η varies in the range $[0... + \infty]$.

Calculation of the total cross-section for the electron scattering is significantly simplified by the use of the parameter $u^\star$ instead of u. It involves the integration over the range of $u^\star = [0...n\, x]$ which is a fixed range of integration. Use of conventional u would require the integration in the range $[0...u_n] = [0..n\, x/(1+\eta^2)]$ which depends on the field intensity η.

We write down for reference the total cross-section integrals for the Compton scattering in terms of $\eta^\star$ and $u^\star$

$$\sigma_{Lin}^{(n)} = \frac{2{r_0}^2}{x}\frac{(1-\eta^{\star 2})^2}{\eta^{\star 2}}\int_0^{2\pi} d\phi \int_0^{n\,x} \frac{du^\star}{(1+u^\star(1-\eta^{\star 2}))^2} \times$$
$$\left[-2\,{A_0}^2 + 2\frac{\eta^{\star 2}}{1-\eta^{\star 2}}\left(2+\frac{u^{\star 2}(1-\eta^{\star 2})^2}{u^\star(1-\eta^{\star 2})+1}\right)({A_1}^2 - A_2\,A_0)\right],$$
$$\sigma_{Circ}^{(n)} = \frac{4\pi{r_0}^2}{x}\frac{(1-\eta^{\star 2})^2}{\eta^{\star 2}}\int_0^{n\,x} \frac{du^\star}{(1+u^\star(1-\eta^{\star 2}))^2} \times$$
$$\left[-2\,{J_n}^2 + \frac{\eta^{\star 2}}{1-\eta^{\star 2}}\left(1+\frac{u^{\star 2}(1-\eta^{\star 2})^2}{2\,(u^\star(1-\eta^{\star 2})+1)}\right)({J_{n-1}}^2 + {J_{n+1}}^2 - 2\,{J_n}^2)\right].$$

For positron production the total cross-section involves the integration over the range of $u^\star = [1/(1-\eta^{\star 2})...n\,x]$ instead of $u = [1...u_n] = [1...n\,x/(1+\eta^2)]$ - both have η or $\eta^\star$ dependence in the range of integration.

We will write down also the total cross section integrals for pair production in terms of $\eta^\star$ and $u^\star$

$$\sigma_{Lin}^{(n)} = \frac{2{r_0}^2}{x}\frac{1}{\eta^{\star 2}}\int_0^{2\pi} d\phi \int_{1/(1-\eta^{\star 2})}^{n\,x} \frac{du^\star}{u^\star\sqrt{u^\star(u^\star - \frac{1}{1-\eta^{\star 2}})}} \times$$
$$\left[+2\,{A_0}^2 + 4\,\frac{\eta^{\star 2}}{1-\eta^{\star 2}}\left(2\,u^\star(1-\eta^{\star 2})-1\right)({A_1}^2 - A_2\,A_0)\right],$$
$$\sigma_{Circ}^{(n)} = \frac{4\pi{r_0}^2}{x}\frac{1}{\eta^{\star 2}} \int_{1/(1-\eta^{\star 2})}^{n\,x} \frac{du^\star}{u^\star\sqrt{u^\star(u^\star - \frac{1}{1-\eta^{\star 2}})}} \times$$
$$\left[+2\,{J_n}^2 + \frac{\eta^{\star 2}}{1-\eta^{\star 2}}\left(2\,u^\star(1-\eta^{\star 2})-1\right)({J_{n-1}}^2 + {J_{n+1}}^2 - 2\,{J_n}^2)\right].$$

2.12 Cross-sections summary

In this section we present results of theoretical calculations and examples of cross-sections for nonlinear Compton scattering of an electron and e^+e^- pair production by

high energy photons in a field of a plain electromagnetic wave (laser). We will leave derivation of this results for Appendices A, B, C, D.

Polarization of a real photon plays an important role in e^+e^- pair production at the laser focus. We will also leave this discussion for Appendix sections.

Results on polarization effects are independent, or in some cases original results obtained by author. They predict for example a strong suppression of e^+e^- pairs production by circular polarized laser compared to linear polarized laser in E144 at small laser intensities, $\eta \approx 0.2 - 0.3$. Effects of polarization of high energy photon contribute to a $20 - 30$ % suppression of positron production with linear polarized laser.

Note that positrons were observed in E144 with linear laser polarization.

At higher laser intensities, $\eta \approx 0.3 - 0.8$, positron production with linear polarized laser has a few times higher rate compared to circular polarized laser in E144.

At very high laser intensities $\eta > 1$ e^+e^- pairs will be produced with the same probability by both laser polarizations.

Cross-sections for nonlinear Compton scattering have opposite dependence. With an exception of $n = 1$ Compton scattering when cross-sections for both laser polarizations are equal, nonlinear Compton rate for $n \geq 2$ scattering is higher for circular laser polarization than that for linear laser polarization. The difference between two polarizations is a factor of $\approx 1.5 - 1.6$ for $n = 3, 4$ and for E144 parameters and increases with order n.

NONLINEAR COMPTON SCATTERING

The differential spectrum of electrons from nonlinear Compton scattering of an electron by linear and circular polarized laser can be calculated according to

$$d\sigma_{Comp}^{\text{linear}} = 2r_0^2 \frac{m^2}{(s - m^2)} \frac{1}{\eta^2} \frac{du\, d\phi}{(1+u)^2} \sum_{n=1}^{\infty} \left[-2A_0^2 + 2\eta^2 \left(2 + \frac{u^2}{(1+u)} \right) (A_1^2 - A_0 A_2) \right] ,$$

$$d\sigma_{Comp}^{\text{circular}} = 4\pi r_0^2 \frac{m^2}{(s-m^2)} \frac{1}{\eta^2} \frac{du}{(1+u)^2}$$
$$\sum_{n=1}^{\infty} \left[-2\,{J_n}^2 + \eta^2 \left(1 + \frac{u^2}{2\,(u+1)} \right) ({J_{n-1}}^2 + {J_{n+1}}^2 - 2\,{J_n}^2) \right] ,$$

where n is the number of laser photons. An arbitrary number of photons can be involved in nonlinear Compton scattering and summation over all n from 1 to ∞ should be made. In practice for low field intensities only small n contribute to the total cross-section because each order n contribute to the total cross-section proportionally to $\eta^{(2n-2)}$ for small η.

Examples of $n = 1$ and $n = 2$ total cross-sections are presented in Fig. 6 for linear and circular laser polarizations.

In these plots we compare cross section $\sigma_{Unp}^{(1)}$ with $\sigma_{Unp}^{(2)}/\eta^2$ (divided by η^2) because $\sigma_{Unp}^{(1)}$ does not depend on the field intensity and $\sigma_{Unp}^{(2)} \sim \eta^2$ for low field intensities. Note that the $n = 2$ cross-section is higher for circular laser polarization than that for linear laser polarization. The $n = 1$ cross section is the same for two polarizations.

Below we present theoretical results for nonlinear Compton spectra of photons produced by linear and circular polarized lasers. Electron spectra are symmetric: the total energy of electron plus photon equals the incident electron energy, 46.6 GeV.

Examples of unpolarized and polarized differential cross-sections as a function of the fractional photon energy for $n = 1, 2, 3, 4$ and $\eta = 0.1$ are shown in Fig. 7 for linear laser polarization and in Fig. 8 for circular laser polarization.

The polarized differential cross-section is a cross-section for high energy photon backscattered with certain polarization. For linear polarized light these are two states of linear polarization of the backscattered photon parallel or perpendicular to polarization of the laser. For circular polarized light these are two states of circular polarization of the backscattered photon with helicity equal or opposite to that of the original laser. Polarization effects in Compton scattering will be discussed in details in Appendices A, B.

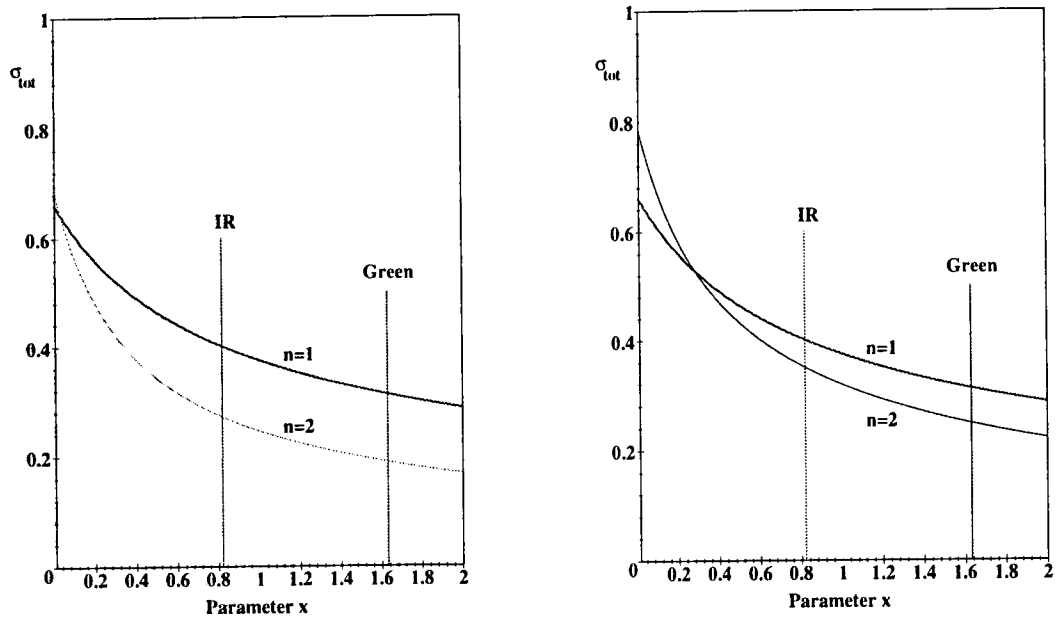

Figure 6: n=1 Compton cross-section $\sigma^{(1)}_{Unp}$ (thick curve) and n=2 nonlinear Compton cross-section $\sigma^{(2)}_{Unp}/\eta^2$ (thin curve) as functions of the parameter x for linear (left plot) and circular (right plot) laser polarizations. Low field intensity $\eta < 0.3$. Two vertical lines $x = 0.82, 1.64$ correspond to IR, Green laser and 46.6 GeV electrons in collision with laser beam at 17°. Cross-sections are in barns.

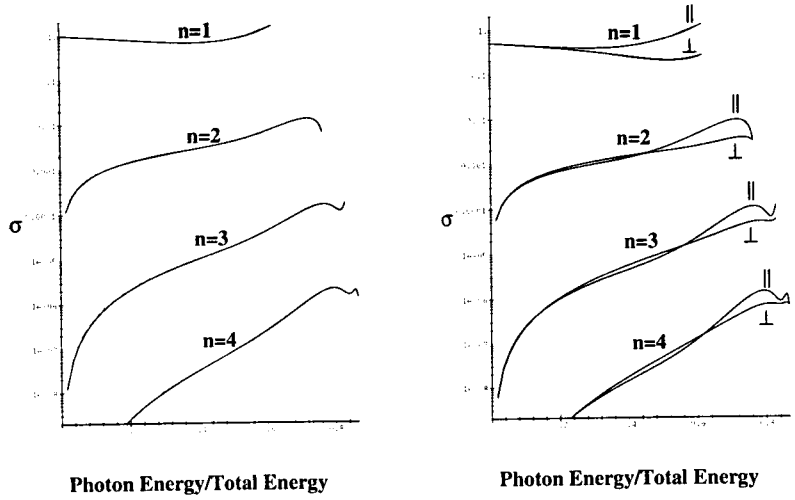

Figure 7: $n = 1, 2, 3, 4$ Compton cross-sections versus the fractional photon energy ω/E_{tot} for *linear* polarized Green laser, 46.6 GeV electron beam and $\eta = 0.1$. Left plot - unpolarized cross-sections, right plot - polarized cross-sections. Higher orders n have higher ω_{max} and lower cross-sections. Vertical scale is $2r_0^2m^2/(\mathrm{s} - m^2)$ units.

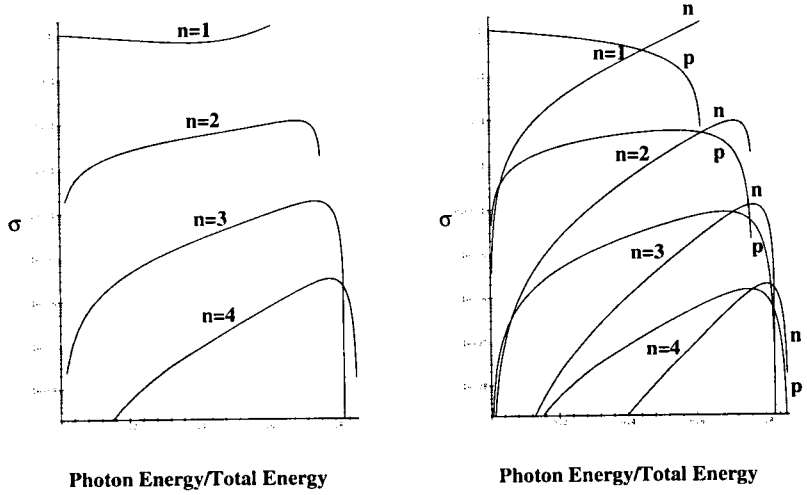

Figure 8: $n = 1, 2, 3, 4$ Compton cross-sections versus the fractional photon energy ω/E_{tot} for *circular* polarized Green laser, 46.6 GeV electron beam and $\eta = 0.1$. Left plot - unpolarized cross-sections, right plot - polarized cross-sections. Higher orders n have higher ω_{max} and lower cross-sections. Vertical scale is $2r_0^2m^2/(\mathrm{s} - m^2)$ units.

PAIR PRODUCTION

The differential spectrum of e^+e^- pairs produced by high energy photon interacting with linear and circular polarized laser can be calculated according to

$$d\sigma_{e^+e^-}^{\text{linear}} = 2\,r_0^2\frac{m^2}{\mathrm{s}}\frac{1}{\eta^2}\frac{du\,d\phi}{u\sqrt{u(u-1)}}\sum_{n=n_0}^{\infty}\left[A_0^2+2\eta^2(2u-1)(A_1^2-A_0A_2)\right],$$

$$d\sigma_{e^+e^-}^{\text{circular}} = 4\pi r_0^2\frac{m^2}{\mathrm{s}}\frac{1}{\eta^2}\frac{du}{u\sqrt{u(u-1)}}\sum_{n=n_0}^{\infty}\left[{J_n}^2+\frac{\eta^2}{2}(2u-1)({J_{n-1}}^2+{J_{n+1}}^2-2\,{J_n}^2)\right].$$

n in the above expression is the number of laser photons involved in e^+e^- pair production. The reaction of e^+e^- pair production has a kinematic threshold: both high energy and laser photons should have enough energy to produce e^+e^- pair. This threshold is high in the intense laser field because both electron and positron should be produced with masses higher than the electron rest mass m without field ($m \approx 0.511$ MeV). As it is discussed in Section 2.4 the mass m_* of an electron or positron in a strong electromagnetic field of intensity η is

$$m_* = m\sqrt{1+\eta^2}\,.$$

The minimum number of laser photons n_0 required to produced e^+e^- pair is

$$n_0 = \frac{(2\,m)^2}{\mathrm{s}}\,(1+\eta^2)\,,$$

where s is the center of mass energy square of the high energy photon and one laser photon. For example for a 29 GeV photon

$$\mathrm{s} = (0.522\ \text{MeV})^2\,, \qquad n_0 = 3.83\,(1+\eta^2) \text{ for green laser},$$

$$\mathrm{s} = (0.369\ \text{MeV})^2\,, \qquad n_0 = 7.66\,(1+\eta^2) \text{ for IR laser}.$$

Because the number of photons should be an integer it is required at least $n_0 = 4$ laser photons to produce a e^+e^- pair with green laser and $n_0 = 8$ laser photons with IR laser.

An arbitrary number of photons $n > n_0$ can be involved in e^+e^- pair production and summation over all n from n_0 to ∞ should be made. In practice, for low field intensities, only small $n \sim n_0$ contribute to the total cross-section. By analogy with Compton scattering, order n contributes to the total cross-section proportionally as $\eta^{(2n-2)}$ for small η. Because e^+e^- pairs are produced near the threshold for $n \sim n_0$ the limited final phase-space of the reaction additionally reduces the cross-section. In addition the polarization of the high energy photons also contribute to the cross-section.

As a result the maximum contribution to the e^+e^- cross-section has $n > n_0$ for circular laser polarization. For linear laser polarization $n \approx n_0$ has maximum contribution to the cross-section.

Examples of unpolarized and polarized differential cross-sections as a function of the fractional positron energy for $n = 4, 5, 6$, and $\eta = 0.1$ are shown in Fig. 9 for linear laser polarization and in Fig. 10 for circular laser polarization.

The polarized differential cross-section is a cross-section for e^+e^- pair production by high energy photons with specific polarization. For linear polarized light these are two states of linear polarization of high energy photon parallel or perpendicular to the polarization of the laser light. For circular polarized laser these are two states of circular polarization of high energy photon with helicity equal or opposite to that of the original laser light. Polarization effects in e^+e^- pair production will be discussed in details in Appendices C, D.

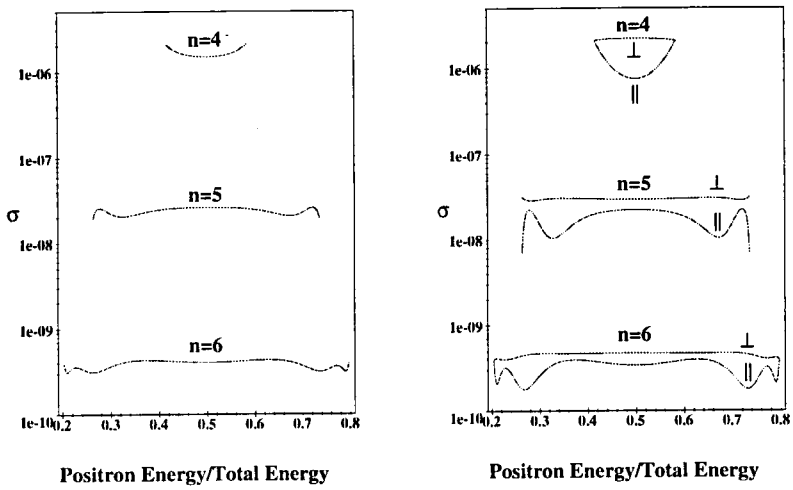

Figure 9: Cross-sections of e^+e^- pair production with n=4,5,6 laser photons versus the fractional positron energy E_{e+}/E_{tot} for *linear* polarized Green laser, 29 GeV high energy photon and $\eta = 0.1$. Left plot - unpolarized cross-sections, right plot - polarized cross-sections. Higher orders n have higher $E_{e+,max}$. Vertical scale is $2r_0^2m^2/s$ units.

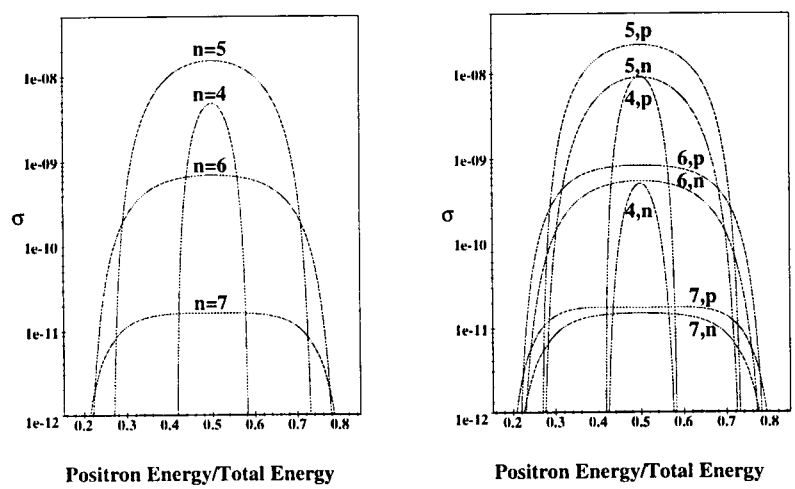

Figure 10: Cross-sections of e^+e^- pair production with n=4,5,6,7 laser photons versus the fractional positron energy E_{e+}/E_{tot} for *circular* polarized Green laser, 29 GeV high energy photon and $\eta = 0.1$. Left plot - unpolarized cross-sections, right plot - polarized cross-sections. Higher orders n have higher $E_{e+,max}$. Vertical scale is $2r_0^2m^2/s$ units.

3 Experimental Setup

3.1 Electron beam

The experiment was carried out in the Final Focus Test Beam (FFTB) which is a specially designed, low-emittance electron beam [1]. The laser-electron interaction point (IP1) was located at a secondary focus 12 m downstream from the FFTB's primary focus. At IP1, it was possible to tune the beam to a transverse size of $\sigma_x = \sigma_y = 60\mu$m. Longitudinally the electron pulse could be adjusted to σ_z between 0.5 and 1 mm. The horizontal and vertical dimensions were measured by scanning the electron beam over 20 μm thick Al wires placed perpendicularly to each other. Scanning of the electron beam was done using dipole steering magnets in the FFTB line upstream of IP1. A photon counter (described in section 3.3) was used as the primary detector of the scattered gammas. The whole procedure was integrated in the SLC Control Program [50]. The longitudinal dimension of the bunch could be tuned by varying the bunch compressor voltage settings. Calibration of the system, which gave the σ_z of the bunch for a specific voltage setting, was performed prior to the run [51]. The effect of timing jitter on the synchronization of the 1.5 ps laser pulses with the electron bunches was less for longer electron bunches. For this reason, the electron bunches were kept longer than is usual for FFTB running, around 3.6 ps (rms).

The FFTB gets its beam directly from the SLAC two-mile linac. Unlike a recirculating collider, the constant production and extraction of bunches in a single-pass system means that the beam halo is repopulated on each bunch, which requires a vigorous collimation system to eliminate particles at large excursions in position, angle and energy. The FFTB's primary collimation system is the SLAC linac collimators, which comprise a set of movable jaws in the last three sectors of the linac. The first set of these collimators does the primary collimation, while the second set is used to remove particles that were scattered of the first set. The linac collimators do not

eliminate large energy oscillations, nor they are adequate for regions with enormous betatron functions as the FFTB. For this reason FFTB itself has a set of movable collimators, located in the first section of the FFTB line. The collimation was set up in such a way that neither too much beam was allowed to pass through (causing backgrounds by scraping on tight magnet apertures or the beam pipe itself), nor too much beam was cut away (causing off-energy repopulation and worse backgrounds).

The electron beam parameters recorded in a typical run were the total bunch charge distribution, the energy spread of the beam relative to the central energy of 46.6 GeV and the position and angle of the beam in the transverse axes as measured by the beam position monitors (BPMs) located close to the IP. Nominal values for the electron beam charge and its pusle-to-pulse variation were 5×10^9 electrons per bunch and $\pm 0.3\%$, respectively. Although the repetition rate of the electron beam could be set as high as 30 Hz, the experiment was limited by the laser repetition rate, which was 0.5 Hz in normal operating conditions; however, it was desirable to collect electron beam background data when the laser was not firing. For this reason, the electron beam was operated at 10 Hz. The FFTB energy and launch feedbacks, although optimized for 30 Hz repetition rates, performed reliably in this lower frequency regime. During parasitic detector calibration runs [52] the beam rate was as high as 120 Hz. Some data were taken with a new mode of linac operation in which pulses of as few as 10^7 electrons were transmitted at 1 Hz for 9 seconds, alternating with 30 Hz pulses of 5×10^9 electrons for 1 second.

After passing through IP1, the electron beam and essentially all scattered particles continued in the forward direction to six permanent dipole magnets. In addition to bending the primary electron beam down into the beam dump, these magnets served as the experiment's electron and positron spectrometer.

3.2 Spectrometer and calorimeters

The spectrometer consisted of six permanent magnets with a mean field of 0.5 T across a 2 inch by 36 inch poleface, providing a transverse kick of 816 MeV/c in the vertical plane to the primary electron beam. Because of the short height of the poleface, the magnets were aligned as shown in Fig. 11; trajectories of electrons and positrons for typical momenta are indicated as well. On each side of the IP were located soft bends of 0.05 and 0.5 milliradians (at 46.6 GeV) to reduce synchrotron radiation in the direction of the forward photons. Recoil electrons and positrons exit the vacuum chamber through 1/4-inch stainless steel windows and were detected by sampling calorimeters positioned as shown in Fig. 11. The electron calorimeter could be moved in the vertical direction so that it would detect only electrons below a given momentum.

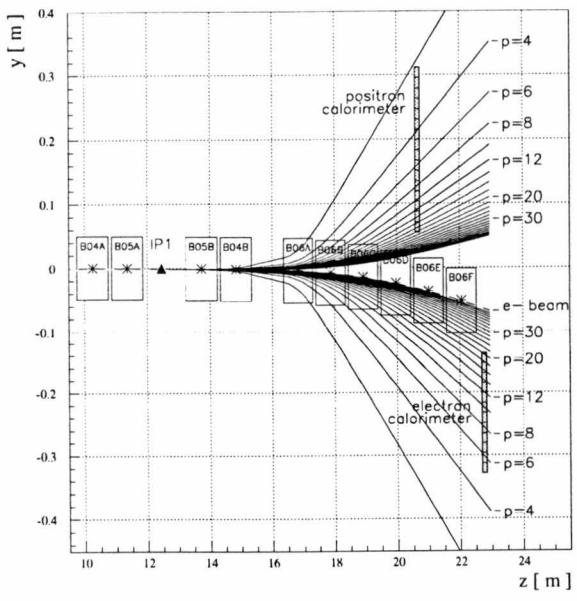

Figure 11: Calculated trajectories of electrons and positrons of different momenta through the magnetic spectrometer. W-Si electromagnetic calorimeters ECAL and PCAL are shown.

The calorimeters, referred to as ECAL and PCAL are of similar constructions and made of alternating layers of silicon and tungsten; each layer of tungsten was one radiation length thick, and each silicon layer was 300 microns thick, resulting in a sampling fraction of 1.1%. Each of the layers in ECAL was divided into 12 rows and 4 columns with 1.6 × 1.6 cm^2 active area pads. The longitudinal layers for each tower are ganged into 4 segments, as shown in Fig. 12 [53]. PCAL has the similar segmentation except that for PCAL only 8 rows were read out. Electrons and positrons produced at the IP could only reach the two central (inner) columns of the calorimeters, so that the outer pads could be used for background subtraction.

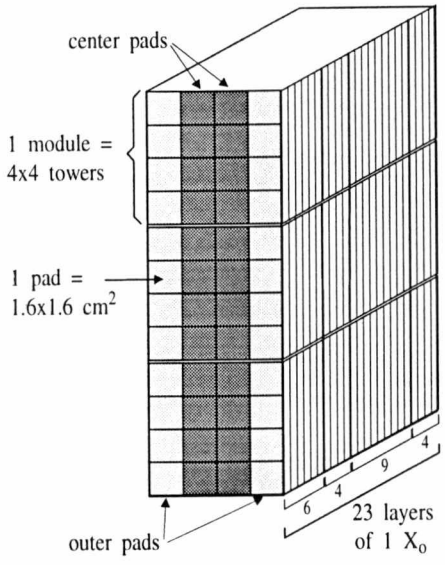

Figure 12: W-Si electromagnetic calorimeter ECAL (PCAL has a similar construction).

The calorimeters were read out with modules built for a liquid argon calorimeter used in a Fermilab experiment [54]. The calorimeters were calibrated in the FFTB line using low flux at variable momentum. The results of a calibration run for 13-GeV electrons are shown in Fig. 13. The resolution was found to be

$$\sigma_{\mathcal{E}}^2 = (0.19)^2\mathcal{E} + (0.4)^2 + (0.05)^2\mathcal{E}^2 \tag{72}$$

where $\mathcal{E}$ is the electron energy in GeV. The transverse profile of the shower resulted

in less than 6% leakage from the inner to the outer pads. Finally, the gain in ECAL was set so that a single 10-GeV electron could be detected, whereas at a total energy of 10 TeV in a single tower the readout was saturated. The gain in PCAL was set 30 times higher than that in ECAL because only individual positrons were detected by PCAL.

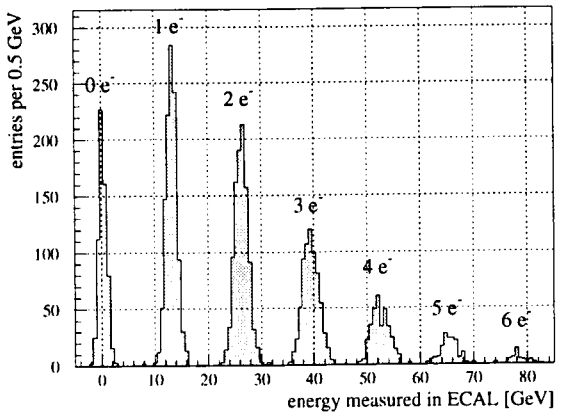

Figure 13: The response of the ECAL to 13-GeV incident electrons. The peaks due to the simultaneous arrival of up to six electrons are clearly distinguished.

3.3 Forward photon and n=1 electron detectors

The forward-going photons served as the primary monitor of the interaction rate and were detected by an air-Cerenkov counter [55] placed in the 0° line. We used a detector based on Cerenkov radiation, which was less sensitive to major sources of background radiation such as bremsstrahlung or beam scraping.

Two Cerenkov counters were used in the first and second stages of the experiment refered to as CCM1 and CCM2 (see Figures 1 and 3 from the Introduction). Figure 14 is a schematic of the CCM1 counter, which used 0.2 radiation lengths of aluminum as a converter and 2.5 cm of air as a radiator. The counter was calibrated by inserting a thin foil in the electron beam at the IP. By adjusting the photomultiplier gain and use of optical filters for the Cerenkov light, the dynamic range of the counter could be varied over six orders of magnitude. A silicon-tungsten calorimeter at the end of

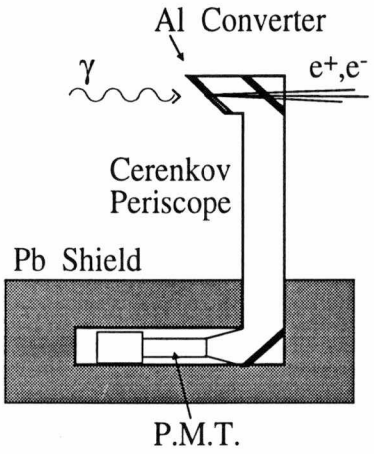

Figure 14: The forward photon monitor Cerenkov counter.

the forward line was used as a redundant photon monitor.

CCM2 counter has similar construction.

3.4 Data acquisition system

The data acquisition system (DAQ) collected data from the detectors as well as information on the laser system and the electron beam. Although the accelerator provided electrons at 10 or 30 Hz, the DAQ recorded data less frequently. Physics events were recorded at the 0.5 Hz repetition rate of the laser. Every beam crossing when the laser fired constituted an event to be recorded in this experiment. In addition, events were collected on the electron beam pulses 400 msec and 200 msec prior to each laser shot, in order to measure electron-beam-related backgrounds in the detectors. A third set of events, obtained by dumping the electron beam far upstream in the linac, was used to measure the pedestal mean value and noise in the detectors and readout electronics during data-taking. These events occurred at a rate of 0.05 Hz, and one third of them coincided with laser shots.

The moderate event rate and data volume of the experiment allowed a low-cost solution for the data acquisition system, which is shown schematically in Fig. 15. The system was based on IBM compatible personal computers connected by a local

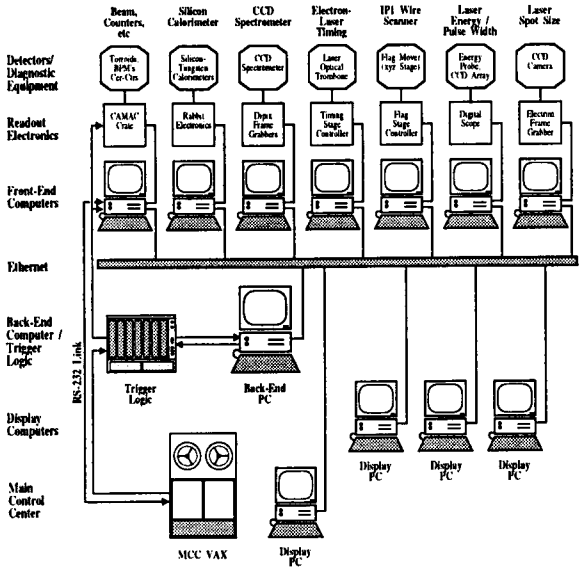

Figure 15: Hardware components of the data acquisition system.

Ethernet. The communication between the computers was established using the standard TCP/IP and UDP protocols. The main part of the DAQ system consisted of one back-end computer and several front-end computers. The back-end computer controled and synchronized the DAQ system and provided the interface to the user, while the front-end computers collected data from the detectors and diagnostic equipment and responded to command messages received from the back-end computer . A standard interface between the programs running on the back-end computer and the front-end computers allowed for a modular and very flexible DAQ. The third type of personal computer shown in Fig. 15, the display computers, provided detailed online monitoring of the collected data.

The readout cycles were controlled by the trigger logic, which received triggers from the SLAC control system and distributed them to the readout electronics and/or front-end computers. Once a trigger signal passed through the logic, further triggers were blocked until the logic was reset by a 'READY' signal from the back-end computer . Upon receiving a trigger signal, each front-end computer collected its assigned set of data and sent it over the Ethernet link to the back-end computer , where the

data were assembled, analyzed and stored to disk. As soon as the back-end computer finished processing the event, it reset the trigger logic and broadcast the full event information to the display computers. The display computers, running unsynchronized to the readout cycle, allowed online monitoring of the experiment or individual front-end equipment, as well as CPU-intensive data processing. One display computer was set up in the accelerator control room, guiding operators in tuning the electron beam for low background in the detectors.

An RS-232 link between one of the front-end computers and the master computer of the SLAC control system made it possible to bring additional experimental parameters into the data stream as well as to control the position of the IP box and the ECAL. The ability to move these devices by the DAQ program was essential in performing scans where the scattering rate was measured as a function of these positions.

4 Laser system

4.1 Laser system

The laser was a 0.5 Hz repetition rate, table top terawatt (T^3) laser, that operated at 1,053 nm wavelength (IR), or at 527 nm (green) after efficient ($\sim$ 45%) frequency doubling. While it has delivered 2.4 J in the IR at the interaction point, during this part of the experiment the maximum energy was 800 mJ of IR and 320 mJ of green. The laser has been focused to better than 2 times the diffraction limited area. The shortest pulse-length achieved during the running period was 1.5 ps FWHM. Intensities above 10^{18} W/cm^2 at the laser focus have been produced. The laser was based on the chirped pulse amplification technique [12] and consisted of a mode-locked Nd:YLF oscillator, Nd:glass regenerative amplifier, a two pass Nd:glass rod amplifier and a flashlamp-pumped Nd:glass slab amplifier. The laser system is described in more detail in [40] and is shown schematically in Fig. 16.

Slab amplifiers [41] have highly efficient cooling compared to large diameter rod amplifiers and therefore can be operated at a repetition rate of 1-2 Hz. Small signal gain of 600 was achieved with three passes at 6 kJ of flashlamp energy. The elliptical beam size in the slab was 1 cm $\times$ 4 cm and after recirculation, spatial filtering and further expansion, the beam was directed to the compression stage, which consisted

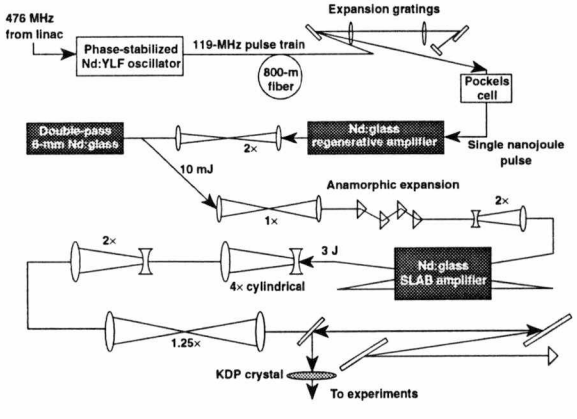

Figure 16: Schematic of the laser system.

of two 1760 line/mm, gold-coated 160 mm × 220 mm holographic gratings used in the near Littrow, double pass configuration with a separation distance of 164 cm [42]. The grating distance depends on the oscillator bandwidth which must be kept fixed during the running period. After compression the frequency of the laser pulse could be doubled by using 4-mm- or 8-mm-thick Type II KDP crystals [43], the thicker crystal being used at lower intensities, < 30 GW/cm^2. Efficiencies of 45% were obtained compared to a theoretically predicted value of 50%. After frequency doubling the laser pulse can be circularly polarized using a liquid crystal polarizer in order to make measurements with circular polarization. Further details on the laser can be found in [26].

The laser beam was transported to the interaction point and focussed onto the electron bunch by an off-axis paraboloid (OAP) [44] and then recollimated by a second OAP for return to the laser room. These optics were located in the IP box which is shown in Fig. 17. The IP box was placed on a mover which could position the IP in the horizontal (x) and vertical (y) directions and could also introduce a roll in the $X - Y$ plane. The three motors used for the IP mover were interfaced into the SLAC Control Program [45] and were used to scan the laser focus with respect to the electron beam, since the laser path was fixed with respect to the IP box.

The laser pulse was returned to the laser room in order to measure its energy, pulse-width and focal area, and to allow accurate alignment of the transport and focusing optics. Good wavefront quality of the beam returning to the laser room

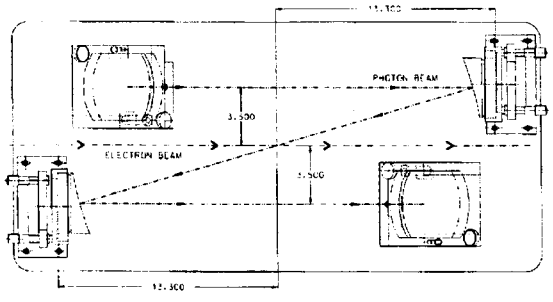

Figure 17: The optical elements in the interaction point enclosure. Dimensions are in inches.

was an indication that the alignment of the OAP pair was correct and that the pointing of the beam incident on the first OAP coincided with the OAP axis. We used a co-propagating, continuous-wave, frequency-stabilized He-Ne beam with a large diameter ($\simeq$ 7.5 cm) co-injected into the transport. After its return from the IP it interfered with the original beam, in a Mach-Zehnder interferometer configuration. The laser transport line was $\sim$12 m long and was under vacuum, but separate from the electron beam vacuum. Entrance and exit windows were 1-inch thick BK7 glass, which contributed some wavefront distortion [46]. Further details on the transport can be found in [47].

The laser energy was measured both by a leakage monitor behind one of the mirrors before the transport line and behind a flat in the diagnostic line after the transport. The IR pulse-width was measured with a single shot autocorrelator in the diagnostic line while the green pulses were measured with a streak camera. The power as a function of time was fitted to a Gaussian shape,

$$P(t) = \frac{U}{\sqrt{2\pi}\sigma_t} e^{-\frac{1}{2}t^2/\sigma_t^2} \tag{73}$$

where U is the total energy. Since the peak power is given by $U/\sqrt{2\pi}\sigma_t$, we define

$$\tau = \sqrt{2\pi}\sigma_t \tag{74}$$

which differs from the FWHM of the pulse by 6%.

Dimension of the focal spot at the interaction point was measured indirectly using the equivalent target plane technique after the return of the laser beam into the laser room. For this purpose the beam was refocused after the transport with a 4 m focal length lens, reflected off four flats which attenuated the beam energy by 10^6, and further attenuated using neutral density filters. The focus was imaged with a 5$\times$ microscope objective onto a CCD camera. For 500 mJ IR laser pulses, the focal spot had a 4 μm radius at the 1/e point in intensity and so had a 50 μm^2 area. For the frequency doubled pulses the area decreased to about 30 μm^2. The diffraction limit

for the radius of the focal spot is given by

$$w_{\text{diff}} = \sqrt{2}\frac{\lambda f_N}{\pi}, \tag{75}$$

where λ is the laser wavelength and f_N is so called "f-number" of the laser system approximately equal to the ratio of the focal length to the diameter of the parabolic mirror. Parameters of the laser focus will be discussed in more details in the following section.

We define the diffraction limited area as

$$A_{\text{diff}} = \pi w_{\text{diff}}^2 . \tag{76}$$

We use $f_N \simeq 6$, so that $A_{\text{diff}} = 25.5\ \mu\text{m}^2$ for IR and $6.4\ \mu\text{m}^2$ for the frequency doubled pulses, but the actual spot sizes attained were larger as noted above.

Measurements of the laser energy, focal spot area, and pulse width are used to determine the peak laser intensity and hence the peak value of the parameter η. For the infrared laser data all three quantities were measured for every pulse. The uncertainty in the pulse width was $\pm 20\%$ because of diffraction of the laser beam. Fluctuations in the energy probe calibration led to a $\pm 13\%$ uncertainty in the energy measurement. Because of laser light scattering, filtering, and a non-Gaussian shape of the focal spot, the uncertainty in the area was $\pm 20\%$. The overall uncertainty in peak IR intensity was therefore $\pm 30\%$. For the green laser data, the energy and focal area were measured for each pulse, but the pulse width is known only on average for each data set from streak-camera measurements, and varied between $\tau = 1.5$ to 2.5 psec. Thus we assign an uncertainty of $+50/-30\%$ in intensity for the green laser data.

The synchronization of the laser pulse with the electron beam was achieved by using a subharmonic of the accelerator master oscillator frequency to drive the mode locker in the laser oscillator. This is shown schematically in Fig. 18. The accelerator master oscillator, located in the injector area 3 km from the laser room, provided

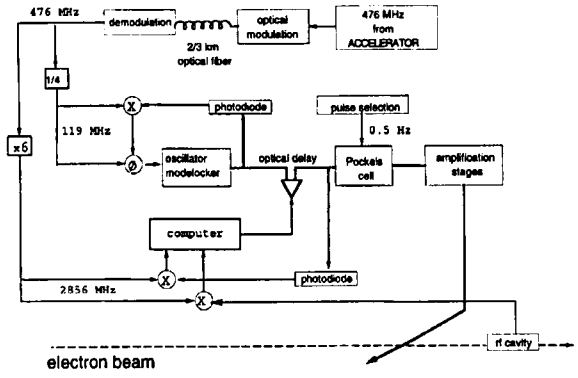

Figure 18: Diagram of the timing system for the synchronization of the laser pulses with the electron beam.

20 Watts of radio-frequency (RF) power at 476 MHz. This signal was transmitted via the Main Drive Line, a rigid coax cable that runs the length of SLAC's klystron gallery, and was then transported by optical fiber [48] to the laser room. Here it was demodulated by a "fiducial output" module which delivered the 4th subharmonic at 119 MHz; this signal was sent to the timing stabilizer [49] which controlled the mode-locker. The laser pulse train was viewed by a 2 GHz bandwidth photodiode whose output was compared in the timing stabilizer with the phase of the reference RF and kept the two signals locked. A detailed description of the synchronization system and performance is given in [27].

One pulse was selected from the laser oscillator pulse train for further amplification and delivery to the interaction region. This was accomplished by using Pockels cells triggered by the software-defined SLC triggers which were synchronized with the master accelerator clock. The fine timing of this pulse was set by adjusting an optical delay line with subpicosecond resolution. A ringing cavity in the electron beam line provided a reference signal which was used to compare the phase of the laser signal to that of the electron bunch. Final timing was established by observing the scattering rate as a function of optical delay. Such a timing curve is given in Fig. 19 and has a (standard deviation) $\sigma = 4.3$ ps; the spread can be attributed to the electron beam

length which was $\sigma_{ez} \simeq 3$ ps and timing jitter of about the same magnitude. A detailed analysis of the fluctuations in the collision rate [27] shows that the timing jitter between the laser pulses and the arrival of the electron bunch was typically of order $\sigma_j \simeq 2$ ps to 3 ps.

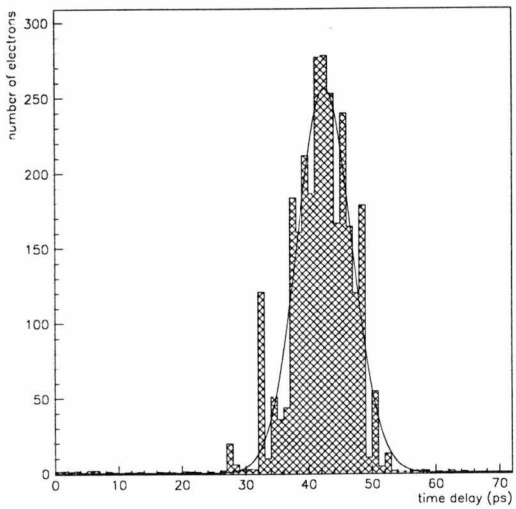

Figure 19: A "timing curve" showing the number of electrons scattered into the top row of the electron calorimeter as a function of delay of the optical pulse. The standard deviation of the curve is $\sigma = 4.3$ ps.

4.2 Confocal beam parameters

Gaussian beams in optics are defined using the following parameterization for the amplitude of the electromagnetic field $u(x, y, z)$ [46]

$$
\begin{aligned}
|\mathrm{u}(x,y,z)| &= \sqrt{\frac{2}{\pi}}\frac{1}{\omega(z)} e^{\left(-\frac{x^2+y^2}{\omega(z)^2}\right)}, \\
\omega(z) &= \omega_{diff}\sqrt{1+\frac{z^2}{{z_R}^2}}, \qquad (77) \\
z_R &= \frac{\pi\,{\omega_{diff}}^2}{\lambda}, \qquad (78)
\end{aligned}
$$

where $\omega(z)$ is called the waist and it contains $\frac{1}{e}$ of the field or $\frac{1}{e^2}$ of the field intensity. The beam is Gaussian and propagates in the z direction. At the limit $z >> z_R$ we have

$$\begin{aligned} \omega(z) &= \frac{\omega_{diff}\, z}{z_R}, \\ \Rightarrow \omega(f) &= \frac{\omega_{diff}\, f}{z_R}, \end{aligned} \tag{79}$$

where $\omega(f)$ is the size of the beam at the (parabolic) mirror which is at a distance f from the focus. Substituting the value for z_R into the above expression we have

$$\omega(f) = \frac{\lambda f}{\pi\, \omega_{diff}}. \tag{80}$$

By definition $w(f) = \frac{d}{2}$ and $f_N = \frac{f}{d}$. Parameter f_N is called the f-number. Diameter d is the limiting aperture of the parallel Gaussian beam and it corresponds to $\frac{1}{e^2}$ of the beam intensity. The diameter d is usually equal to the diameter of the mirror. We can rewrite the above expression and find ω_{diff}

$$\omega_{diff} = 2\,\frac{f_N\,\lambda}{\pi}. \tag{81}$$

We can also rewrite z_R in terms of f_N

$$z_R = 4\,\frac{\lambda\, {f_N}^2}{\pi}. \tag{82}$$

For the calculation of cross-sections in in electron-laser interactions it is convenient to parameterize the laser density distribution (number of laser photons per unit volume) as a standard Gaussian distribution. For instance density of the laser beam in the plane perpendicular to the beam direction is

$$\rho_l \sim e^{\left(-\frac{x^2+y^2}{2\,\sigma(z)^2}\right)}.$$

Laser beam density is proportional to u^2 and according to Eq. (78) in terms of confocal beam parameters is proportional to

$$\rho_l \sim e^{\left(-2\,\frac{x^2+y^2}{\omega(z)^2}\right)}.$$

From which we can conclude that

$$\sigma(z) = \frac{\omega(z)}{2}. \tag{83}$$

Now we can find size of the laser beam intensity at the diffraction limit σ_{diff} and at any distance z

$$\begin{aligned} \sigma_{diff} &= \frac{f_N\,\lambda}{\pi}, \\ \sigma(z) &= \sigma_{diff}\sqrt{1+\frac{z^2}{{z_R}^2}}. \end{aligned} \tag{84}$$

Experimentally the laser spot size is measured by measuring the intensity distribution and by fitting it with Gaussian distribution. By *definition* the area A of the laser spot is

$$A = 2\,\pi\,\sigma_x\,\sigma_y\,,$$

or for the round beam

$$A = 2\,\pi\,\sigma^2\,. \tag{85}$$

If the laser beam is not perfectly focused to the diffraction limit the laser spot size is

$$\sigma(z) = \sigma_{diff}\sqrt{\frac{A_{meas}}{A_{diff}} + \frac{z^{\,2}}{z_R}}\,, \tag{86}$$

where A_{diff} is defined as the (theoretical) diffraction limited area for the beam, A_{meas} is defined from the measurements

$$
\begin{aligned}
A_{diff} &= 2\,\pi\,{\sigma_{diff}}^2 = 2\,\frac{{f_N}^2\,\lambda^2}{\pi}\,, \\
A_{meas} &= 2\,\pi\,\sigma_x\,\sigma_y\,.
\end{aligned}
$$

As an example we present parameters for diffraction limited green and IR lasers with $f_N = 6$ (typical for E144 with $f = 30$ cm, $d = 5$ cm)

$$
\begin{aligned}
A_{diff}^{green} &= 6.37\,\mu m^2\,, \quad \sigma_{diff}^{green} = 1.01\,\mu m\,, \quad z_R^{green} = 24.2\,\mu m\,, \\
A_{diff}^{IR} &= 25.5\,\mu m^2\,, \quad \sigma_{diff}^{IR} = 2.02\,\mu m\,, \quad z_R^{IR} = 48.4\,\mu m\,.
\end{aligned}
$$

In E144 the typical measured focal area was $20 - 30\,\mu m^2$ for green laser and $40 - 60\,\mu m^2$ for IR laser. That corresponds to $r_{diff} = \dfrac{A_{meas}}{A_{diff}} = 3.1$ to 4.7 for green laser and $r_{diff} = \dfrac{A_{meas}}{A_{diff}} = 1.6$ to 2.4 for IR laser.

Photon density ρ_l is related to laser intensity η^2 by the formula

$$
\rho_l = \frac{\omega\,m^2}{e^2}\eta^2\,, \tag{87}
$$

where ω is the photon energy, m and e are electron mass and charge. Using

$$
\begin{aligned}
\alpha &= \frac{e^2}{4\pi} = \frac{1}{137}\,, \\
r_0 &= \frac{e^2}{4\pi\,m} = 2.82 \times 10^{-9}\,\mu m\,,
\end{aligned}
$$

the above relation can be rewritten in the form

$$
\rho_l = \frac{\alpha^2}{4\pi}\frac{\omega}{m}\frac{1}{r_0^3}\eta^2\,.
$$

For green laser $\omega = 2.34$ eV, for IR $\omega = 1.17$ eV. Hence

$$
\rho_l = 0.866\,10^{15}\,\eta^2\left[\frac{1}{\mu m^3}\right], \quad \eta^2 = 1.15\,10^{-15}\,\rho_l \text{ for green laser}\,,
$$

$$\rho_l = 0.433\,10^{15}\,\eta^2\left[\frac{1}{\mu m^3}\right], \quad \eta^2 = 2.30\,10^{-15}\,\rho_l \text{ for IR laser}.$$

The maximum density of laser photons is

$$\begin{aligned}
\rho_l^{(max)} &= \frac{N_\gamma}{(2\pi)^{3/2}\,\sigma(0)^2\,\sigma_z}, \\
\sigma(0)^2 &= \sigma_{diff}^2\, r_{diff} = \frac{4\,f_N^2}{\omega^2}\, r_{diff}, \\
N_\gamma &= \frac{P}{\omega},
\end{aligned}$$

where P is the laser energy in eV. Hence

$$\eta_{max}^2 = \frac{1}{2\,(2\pi)^{1/2}}\frac{r_0}{\sigma_z}\frac{P}{m}\frac{1}{r_{diff}\,f_N^2}. \tag{88}$$

Substituting $P = \dfrac{10^{19}}{1.6}\dfrac{eV}{J}\,P_J$ where P_J is the laser pulse energy in Joules and pulse width $\tau = \tau_{FWHM} = 2.355\,\dfrac{\sigma_z}{300\mu m}$ (ps) measured at full width half maximum we have

$$\eta_{max}^2 = 54.0\frac{P_J}{\tau\, f_N^2\, r_{diff}}. \tag{89}$$

Substituting E144 parameters $f_N = 6$ and $\tau = 1.5$ps we get

$$\eta_{max}^2 = 1.00\,\frac{P_J}{r_{diff}} \text{ (for } \tau = 1.5 \text{ ps)}.$$

The above relation is independent of laser frequency and valid for $\tau = 1.5$ ps pulse duration - the shortest pulse length for E144. One could reach $\eta = 1$ in E144 with diffraction limited spot area and 1 J of laser energy. Actual values are lower mainly because the laser area was 2-5 times bigger than the diffraction limited one. Examples of laser parameters for IR and Green laser during operation in March 1995 (when nonlinear Compton data were collected at moderate laser intensity) are shown in Figs. 20 and 21.

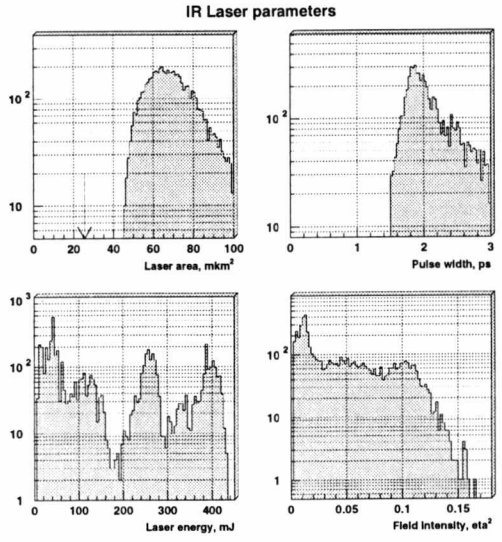

Figure 20: IR laser parameters during March 1995 run operation. Laser area, pulse duration, total laser energy and parameter η^2 are shown. Arrow on laser area plot shows the diffraction limited spot-size.

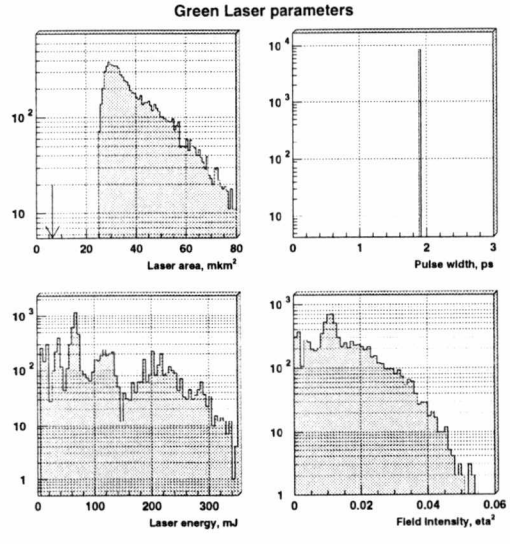

Figure 21: Laser parameters with doubling crystal (green laser) during March 1995 run operation. Laser area, pulse duration, total laser energy and parameter η^2 are shown. Arrow on laser area plot shows the diffraction limited spot-size. Individual pulse duration diagnostics were not available and measurements were made periodically with different diagnostics which average value is plotted.

5 Space-time laser-electron beam overlap

5.1 Calculation of four-dimensional overlap

Nonlinear Compton processes and pair production occur during the passage of the electron beam through the laser focus. Total number of interactions depends on the cross-section of the process and the effective space-time overlap of the electron and laser beams.

Electron density ρ_e $(1/\mu\text{m}^3)$ and laser photon density ρ_l $(1/\mu\text{m}^3)$ are functions of 3 spatial coordinates x, y, z and time t. We will use notations $\rho_e(x,y,z,t) = \rho_e(x)$, $\rho_l(x,y,z,t) = \rho_l(x)$ to avoid lengthy arguments.

In the following we assume that *there is no depletion of electron or laser beams* during interaction i.e. density of electron and laser beams along their path is constant. For laser photons this condition is always true because the photon density is $\approx 10^{15}$ photons per μm^3 compared to the total $\approx 10^{10}$ electrons in the electron beam. For the electrons this condition may be violated for intense laser pulses. We consider this option in a later section.

For a one-step process with cross-section σ_n the total number of particles produced N_n and the differential energy spectrum of particles dN_n/dE can be calculated from the formulae

$$\begin{aligned} N_n &= |\vec{v_e} - \vec{v_l}| \int \rho_e(x)\rho_l(x)\sigma_n(\rho_l)d^4x\,, \\ \frac{dN_n}{dE} &= |\vec{v_e} - \vec{v_l}| \int \rho_e(x)\rho_l(x)\frac{d\sigma_n(\rho_l)}{dE}d^4x\,, \end{aligned} \tag{90}$$

where $\vec{v_e}$ is the velocity of the electron beam and $\vec{v_l}$ is the velocity of the photon beam. For crossing angle α between two beams

$$|\vec{v_e} - \vec{v_l}| = 2\cos\frac{\alpha}{2} \qquad (c=1)\,,$$

because $|\vec{v_l}| = 1$ and $|\vec{v_e}| \approx 1$.

For a two-step process with cross-sections σ_1 for the 1-st process and σ_2 for the second process we first must find the density of particles created in the first process

$$\frac{d\rho_1}{dE_1} = |\vec{v_e} - \vec{v_l}| \int\limits_{\tau=-\infty}^{0} \rho_l(x, y, z-\tau, t-\tau)\rho_e(x, y, z-\tau, t-\tau)\frac{d\sigma_1(\rho_l)}{dE_1}d\tau\,. \qquad (91)$$

The above formula is valid for secondary particles with energy in the range $(E_1, E_1 + dE_1)$ moving in the same direction as the electron beam with the speed of light. This assumption is valid for most secondary particles created in the laser focus.

We have to substitute expression for $d\rho_1/dE_1$ into formula (90) to obtain the total number of interactions N_{12} for the two-step process

$$\begin{aligned} N_{12} &= |\vec{v_1} - \vec{v_l}|^2 \int\limits_{E_1=E_{min}}^{E_{max}} dE_1 \int\limits_{\tau=-\infty}^{0} d\tau \int d^4x\ \frac{d\sigma_1(E_1, x, \tau)}{dE_1}\sigma_2(E_1, x)\ \times \\ &\quad \rho_l(x)\,\rho_l(x, y, z-\tau, t-\tau)\,\rho_e(x, y, z-\tau, t-\tau)\,. \end{aligned} \qquad (92)$$

We will consider the relativistic electron beam propagating in the direction $-\tilde{z}$ in the coordinate system $(\tilde{x}, \tilde{y}, \tilde{z})$ with the velocity $v \approx 1$ $(c = 1)$. Electron beam density for a Gaussian beam can be written in the form

$$\begin{aligned} \rho_e(x) &= N_e\,\rho_{0e}(x) = \frac{N_e}{(2\pi)^{3/2}\,\sigma_{ex}\,\sigma_{ey}\,\sigma_{ez}} e^{-\frac{\tilde{x}^2}{2\,\sigma_{ex}^2} - \frac{\tilde{y}^2}{2\,\sigma_{ey}^2} - \frac{(\tilde{z}+\tilde{t})^2}{2\,\sigma_{ez}^2}}\,, \qquad (93) \\ &\int \rho_e(x)\,dx\,dy\,dz = N_e\,, \quad \int \rho_{0e}(x)\,dx\,dy\,dz = 1\,. \end{aligned}$$

Here N_e is the total number of electrons in the beam, σ_{ex}, σ_{ey} are the x and y transverse size of the beam and σ_{ez} is longitudinal size of the beam. ρ_{0e} is the density normalized to the total number of electrons, i.e. $\rho_{0e}(x)\,dx\,dy\,dz$ is the fraction of the number of electrons in volume $dx\,dy\,dz$. A schematic view of the electron beam geometry is shown in Fig. 22.

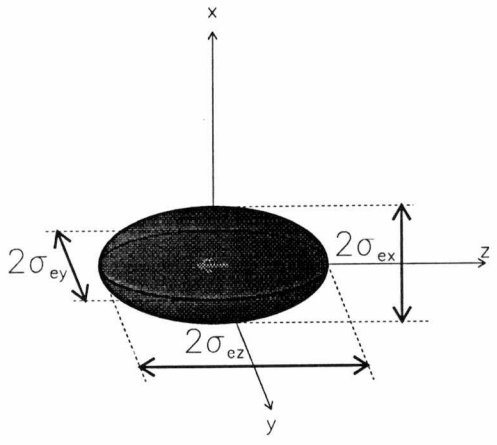

Figure 22: Schematic diagram for the geometry of the Gaussian electron beam propagating in the $-\tilde{z}$ direction. Electron beam parameters are σ_{ex}, σ_{ey} and σ_{ez}.

The laser beam is propagating along the $+z$ direction in the coordinate system (x, y, z) with the speed of light $c = 1$. For the laser beam focused to a spot with an area A which is $n_{diff} = A/A_{diff}$ times diffraction limited, the standard Gaussian approximation for the density of laser photons is

$$\rho_l(x) = N_l\, \rho_{0l}(x) = \frac{N_l}{(2\pi)^{3/2}\, \sigma_{lr}^2\, \sigma_\tau} e^{-\frac{(x^2+y^2)}{2\,\sigma_{lr}^2} - \frac{(z-t)^2}{2\,\sigma_\tau^2}}\,, \tag{94}$$

$$\sigma_{lr} = \sigma_{lr0}\sqrt{n_{diff} + \left(\frac{z}{z_R}\right)^2}\,, \quad \int \rho_l(x)\, dx\, dy\, dz = N_l\,, \quad \int \rho_{0l}(x)\, dx\, dy\, dz = 1\,.$$

Here N_l is the total number of photons in the laser beam, σ_{lr} is the transverse size of the beam, σ_{lr0} is the size of the diffraction limited spot, σ_τ is the longitudinal size of the beam, and z_R is the Rayleigh range. ρ_{0l} is the density normalized to the total number of laser photons.

A schematic view of the laser beam geometry is shown in Fig. 23.

Note that parameterization (94) for the laser focus has only one parameter σ_{lr} to characterize the transverse size of the focus (not two as for the electron beam). This

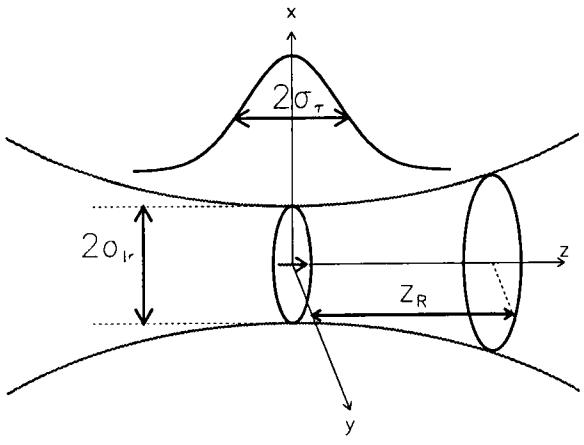

Figure 23: Schematic diagram for the geometry of the Gaussian laser focus. Laser beam propagates in the $+z$ direction. Laser beam parameters are σ_{lr}, σ_τ and z_R (Rayleigh range, see text).

is true for a round Gaussian beam even if it is focused with the off-axis paraboloid at $\alpha = 17°$ (E144).

Angle α between the electron and laser beams defines the transformation between the two coordinate systems. If we assume that both beams are in $x - z$ plane and the laser beam is focused to the center of the electron beam, then

$$\begin{aligned} \tilde{z} &= z\cos\alpha + x\sin\alpha\,, \\ \tilde{x} &= -z\sin\alpha + x\cos\alpha\,, \\ \tilde{y} &= y\,. \end{aligned} \tag{95}$$

For ideal timing between electron and laser beams $\tilde{t} = t$. If the timing jitter ζ is present, $\tilde{t} = t + \zeta$.

Equations (90), (91), (92), (93), (94) and transformation (95) define completely the number of particles and their spectrum produced during electron-laser interaction. To find functional dependence of production rate on parameters of the laser focus we

must simplify those expressions.

For instance, it will be shown in the next section that the expression Eq. (90) for the total number of interactions can be rewritten in general form

$$N_n = 2\cos\frac{\alpha}{2} N_e N_l \int \rho_{0e}(x)\rho_{0l}(x)\sigma_n(\rho_l)d^4x = S\, N_e\, N_l\, \sigma_n^{max}\,, \qquad (96)$$

where S is a parameter that characterizes the electron-laser overlap and σ_n^{max} is the cross-section at the laser focus that corresponds to the maximum field intensity. Parameter S has dimension μm^{-2}.

For ordinary Compton scattering ($n = 1$) and head-on collision of the electron and laser beams the parameter S is approximately equal to the inverse transverse area of the electron bunch $S \approx \dfrac{1}{A_e}$ for the laser beam focused to an area smaller than the electron beam. Equation (96) for the rate of high energy backscattered γ's in this case is

$$N_\gamma \approx \frac{N_e}{A_e} N_l\, \sigma_C\,,$$

where σ_C is the Compton cross-section that is independent of the field intensity (except for fields approaching critical field $\eta \approx 1$). The above expression becomes an equality for a laser beam with infinite Rayleigh range.

Parameter S characterizes the effectiveness of the electron-laser overlap. It depends on the angle between electron and laser beams, parameters of the laser focus, relative timing of two beams, and the dependence of the cross-section on the laser field intensity. The cross-section for nonlinear processes depends on the laser field intensity and hence should be taken into account during calculations of the parameter S.

The goal of the following sections is to estimate and calculate the parameter S as it is defined by equation (96). We use ordinary (s=1) Compton scattering and nonlinear Compton scattering as examples of one-step processes.

5.2 General method

We consider equation (90) with electron and laser densities parameterized according to Eqs. (93) and (94).

We assume that the cross-section σ_n can be presented as a series in the photon density ρ_l or equivalently in the laser field intensity η^2

$$\begin{aligned}
\sigma_n &= \sigma_0 \left(\frac{\rho_l}{\rho_l^{max}}\right)^{(n-1)} + \sigma_1 \left(\frac{\rho_l}{\rho_l^{max}}\right)^{n} + \ldots = \sum_{i=0}^{\infty} \sigma_i \left(\frac{\rho_l}{\rho_l^{max}}\right)^{(n-1+i)}, \qquad (97)\\
\sigma_n &= \sigma_0 \left(\frac{\eta}{\eta^{max}}\right)^{2(n-1)} + \sigma_1 \left(\frac{\eta}{\eta^{max}}\right)^{2n} + \ldots = \sum_{i=0}^{\infty} \sigma_i \left(\frac{\eta}{\eta^{max}}\right)^{2(n-1+i)},
\end{aligned}$$

where σ_0, σ_1, ... are constants (cross-sections). We assume that these series converge which is true for moderate field intensities $\eta < 1$.

In the following we describe the general analytical method for the calculation of the effective overlap parameter S.

Substituting Eq. (97) in the Eq. (90) we have

$$N_n = N_e\, N_l\, \sigma_n^{max}\, |\vec{v_e} - \vec{v_l}| \sum_{i=0}^{+\infty} \frac{\sigma_i}{\sigma_n^{max}} \rho_{0l}^{max} \int \left(\frac{\rho_{0l}(x)}{\rho_{0l}^{max}}\right)^{s+i} \rho_{0e}(x)\; d^4x\,, \qquad (98)$$

or

$$\begin{aligned}
N_n &= S\, N_e\, N_l\, \sigma_n^{max}\,,\\
S &= |\vec{v_e} - \vec{v_l}| \frac{\sum_i \sigma_i\, S_i}{\sum_i \sigma_i}\,,\\
S_i &= \rho_{0l}^{max} \int \left(\frac{\rho_{0l}(x)}{\rho_{0l}^{max}}\right)^{n+i} \rho_{0e}(x)\; d^4x\,. \qquad (99)
\end{aligned}$$

This equation has the form of equation (96) from the previous section.

Substituting expressions Eqs. (93) and (94) for ρ_{0e} and ρ_{0l} we have

$$S_i = \frac{1}{(2\pi)^3\, \sigma_{lr}^2(0)\, \sigma_\tau\, \sigma_{ex}\, \sigma_{ey}\, \sigma_{ez}} \int \exp(-R_{n+i})\; d^4x\,,$$

$$R_{n+i} = \frac{(x^2+y^2)}{2\sigma_{lr}/(n+i)} + \frac{(z-t)^2}{2\sigma_{\tau}/(n+i)} + \frac{\tilde{x}^2}{2\sigma_{ex}^2} + \frac{\tilde{y}^2}{2\sigma_{ey}^2} + \frac{(\tilde{z}+\tilde{t})^2}{2\sigma_{ez}^2}. \quad (100)$$

The coordinate transformation Eq. (95) express $(\tilde{x}, \tilde{y}, \tilde{z}, \tilde{t})$ through (x, y, z, t).

Calculation of the overlap parameter S and the total rate are reduced to calculations of integrals $\int \exp(-R_{n+i})\, d^4x$.

5.2.1 Infinite Rayleigh range ($z_R = \infty$)

Integration can be done immediately for the laser beam with infinite Rayleigh range for arbitrary crossing angle α. In this case functions R_{s+i} are quadratic forms over variables (x, y, z, t) because σ_{lr} is constant

$$R = R_0 + \sum_{i,j=1}^{4} m_{ij}\, x_i\, x_j\,, \quad (101)$$

where $m_{ij}(4,4)$ is the matrix of coefficients for quadratic form and R_0 is a constant.

By proper coordinate transformation (rotation in 4-dimensional space), quadratic form R can be reduced to diagonal quadratic form that depends only on x^2, y^2, z^2 and t^2

$$R' = R_0 + \sum_{i=1}^{4} m'_{ii}\, x'^2_i\,, \quad (102)$$

where m'_{ij} is a new matrix which is diagonal.

For such a diagonal form each integration will give $\sqrt{\pi}/\sqrt{m'_{ii}}$; the rotation does not change the norm of the quadratic form $\det(m') = \det(m)$ and hence

$$\int \exp(-R_{n+i})\; d^4x = \frac{\pi^2 e^{-R_0}}{\sqrt{\det(m)}}. \quad (103)$$

Integration is reduced to calculation of the determinant. It is not necessary to find the exact transformation that diagonalizes the quadratic form; only determinant of the coefficient matrix $\det(m)$ is important.

5.2.2 Finite Rayleigh range ($z_R \neq \infty$)

In this case function R is quadratic plus linear form over 3 variables (x, y, t) (with coefficients as functions of z)

$$R = R_0 + \sum_{i,j=(x,y,t)} m_{ij}\, x_i\, x_j + \sum_{i=(x,y,t)} n_i\, x_i\,, \tag{104}$$

where $m_{ij}(3,3)$ is the matrix of coefficients for quadratic form; n_i is vector of coefficients for linear form; R_0 is constant.

By proper coordinate transformation (rotation in 3-dimensional space) this form can be reduced to diagonal form that depends only on x^2, y^2, t^2, x, y, t

$$R' = R_0 + \sum_{i=(x,y,t)} \left(m'_{ii}\, x'^2_i + n'_i\, x'_i \right)\,, \tag{105}$$

and then by translation

$$x'_i + \frac{n'_i}{2\, m'_{ii}} = x''_i\,,$$

to the form

$$\begin{aligned} R' &= R'_0 + \sum_{i=(x,y,t)} m'_{ii}\, x''^2_i\,, \\ R'_0 &= R_0 + \sum_i \frac{n'^2_i}{4\, m'_{ii}}\,. \end{aligned} \tag{106}$$

Hence

$$\int \exp(-R_{n+i})\; d^4x = \int dz\, \frac{\pi^{3/2} e^{-R'_0}}{\sqrt{\det(m)}}\,. \tag{107}$$

We use again the fact that $\det(m') = \det(m)$ i.e. rotation and translation do not change the norm of the quadratic form.

Integration is reduced to calculation of the determinant and integration over variable z. It is necessary to find transformation matrix F $(x = Fx')$ to find elements of

the vector n' and eigenvalues $\lambda_i = m'_{ii}$ (defined by equation $\det(F - \lambda) = 0$) in order to calculate constant R'_0. Finding eigenvalues and eigenvectors is a classical problem of linear algebra and we will present this method in the following section.

5.2.3 Diagonalization of arbitrary quadratic form

Consider an arbitrary quadratic form for "n" real variables x_1, x_2, ... x_n with real coefficients

$$\sum_{i,j=1}^{n} m_{ij}\, x_i\, x_j = x^T M x\,. \tag{108}$$

Here $M(n,n)$ is a symmetric matrix with coefficients of the quadratic form; x is the column of variables x_i; x^T is the row of variables x_i (T stands for the transpose operation).

Coordinate transformation

$$x_i = \sum_{i=1}^{n} f_{ij}\, x'_j = F\, x'\,, \tag{109}$$

where $F(n,n)$ is the transformation matrix with real coefficients $\det(F) \neq 0$; x - column of variables x_i; x' - column of new variables x'_i will transform quadratic form Eq. (108) into quadratic form that depends on new variables x'_i

$$x^T\, M\, x = x'^T\, F^T\, M\, F\, x' = x'^T\, M'\, x'\,, \tag{110}$$

where M' is a new matrix of the quadratic form

$$M' = F^T\, M\, F\,. \tag{111}$$

The matrix M' is symmetric also.

For any real symmetric quadratic form Eq. (108) there is linear coordinate transformation Eq. (109) that transforms matrix M into diagonal matrix M'

$$x'^T M' x' = \sum_{i=1}^{n} m'_{ii} x'^2_i \tag{112}$$

An important property of the transformation matrix F that transform M to diagonal form is that it is an *orthogonal* matrix

$$F^{-1} = F^T . \tag{113}$$

Matrix F can be composed of eigenvectors $\vec{\xi}(i)$ of the matrix M which correspond to eigenvalues λ_i

$$F = \left(\frac{\vec{\xi}^{(1)}}{\lambda_1}, \frac{\vec{\xi}^{(2)}}{\lambda_2}, \ldots \frac{\vec{\xi}^{(n)}}{\lambda_n} \right) . \tag{114}$$

Eigenvalues λ_i are defined by the equation $\det(M - \lambda) = 0$.

Because F is an orthogonal matrix it does not change the norm of the quadratic form

$$\det(M') = \det(F^T M F) = \det(F^{-1} M F) = \det(M) . \tag{115}$$

If matrix F which transforms quadratic form to the sum of squares is known then coefficients of the linear form can be calculated as well. For combination of quadratic and linear forms considered in the previous subsection

$$\sum_{i,j=1}^{n} m_{ij} x_i x_j + \sum_{i=1}^{n} n_i x_i = x^T M x + n x , \tag{116}$$

where n is the row of coefficients of the linear form. Coordinate transformation Eq. (109) with coordinate matrix Eq. (114) will transform n into new string of coefficients

$$n x = n F x' = n' x' , \tag{117}$$

where

$$
\begin{aligned}
n' &= n\,F\,, \\
n'_i &= n\,\vec{\xi}^{(i)} = \sum_{j=1}^{n} n_j\,\xi_j^{(i)}\,.
\end{aligned}
\tag{118}
$$

Additional term $R'_0 = R_0 + \sum_i \frac{n'^2_i}{4\,m'_{ii}}$ from the equation (106) can be rewritten as

$$
R'_0 - R_0 = \sum_i \frac{n'^2_i}{4\,m'_{ii}} = \sum_i \frac{n'^2_i}{4\,\lambda_i} = \sum_i \frac{\left(\vec{n}\,\vec{\xi}^{(i)}\right)^2}{4\,\lambda_i}\,. \tag{119}
$$

Hence R'_0 is defined by eigenvectors $\vec{\xi}^{(i)}$ and eigenvalues λ_i of the matrix M as well as by the vector of coefficients of the original linear form $\vec{n}$ and constant R_0.

5.3 One step process: $n = 1$ Compton scattering

For the ordinary Compton scattering ($n = 1$) the cross-section σ_C is independent of the field intensity (except for very strong fields) and hence we can rewrite equations (99) as

$$
\begin{aligned}
N_\gamma &= S\,N_e\,N_l\,\sigma_C\,, \\
S &= |\vec{v_e} - \vec{v_l}| \int \rho_{0l}(x)\,\rho_{0e}(x)\;d^4x\,.
\end{aligned}
\tag{120}
$$

In previous section we described the general method for calculation of the integral in the above expression. Exact analytical formula for S for focused laser beam is too lengthy to present. For the special case of "cylindrical" laser beam with infinite Rayleigh range $z_R = \infty$ we get

$$
S^{-1} = 2\,\pi\,\left(\sigma_{ey}^2 + \sigma_L^2\right)^{1/2} \sqrt{(\sigma_{ex}^2 + \sigma_L^2)\cos^2\frac{\alpha}{2} + (\sigma_{ez}^2 + \sigma_\tau^2)\sin^2\frac{\alpha}{2}}\,, \tag{121}
$$

where $2\,\pi\,\sigma_L^2 = 2\,\pi\,\sigma_{lr0}^2\,n_{diff}$ is the effective area of non-diffraction limited spot.

For the cylindrical laser beam crossing the electron beam at $\alpha = 0°$ the effective overlap area has especially simple form

$$S_0^{-1} = 2\,\pi\,\sqrt{(\sigma_{ex}^2 + \sigma_L^2)(\sigma_{ey}^2 + \sigma_L^2)}\,. \tag{122}$$

We will use special notation S_0 for this value of the parameter S.

For the laser focus much smaller than the electron beam

$$S_0^{-1} \approx A_e = 2\,\pi\,\sigma_{ex}\sigma_{ey}\,,$$

where A_e is the area of the electron beam.

Below we show the dependence of the effective overlap parameter S of the Compton scattering plotted versus crossing angle with different parameters of the laser focus and time jitter for typical E144 parameters.

It is convenient to normalize the effective overlap parameter S to S_0 and define the dimensionless overlap parameter F_{ovlp} as $F_{ovlp} = S/S_0$ where $S_0 = S(\alpha = 0, z_R = \infty)$ as defined above. Formula (120) for the total Compton rate can then be presented as

$$\begin{aligned} N_\gamma &= S_0\,N_e\,N_l\,\sigma_C\,F_{ovlp}\,, \\ F_{ovlp} &= S/S_0\,, \qquad S_0^{-1} = 2\,\pi\,\sqrt{(\sigma_{ex}^2 + \sigma_L^2)(\sigma_{ey}^2 + \sigma_L^2)}\,. \end{aligned} \tag{123}$$

Through this and the following sections we will use one typical example of E144 parameters for the electron beam and IR laser beam which we will call "set of IR E144 parameters"

$$\begin{aligned} &\sigma_{ex} = 60\,\mu\text{m}\,, \quad \sigma_{ey} = 67\,\mu\text{m}\,, \quad \sigma_{ez} = 650\,\mu\text{m}\,, \sigma_\tau = 255\,\mu\text{m}\ (2.0\ \text{ps})\,, \\ &\sigma_{lr0} = 2.02\,\mu\text{m}\ (A_{diff} = 25.5\,\mu\text{m}^2)\,, \quad n_{diff} = 2.7\,. \end{aligned} \tag{124}$$

Dependence of the overlap factor $F_{ovlp} = S/S_0$ on the crossing angle α is plotted in Fig. 24 for two Rayleigh ranges $z_R = \infty$ (solid curve) and $z_R = 48.4\,\mu$m (boxes) for the set of IR E144 parameters.

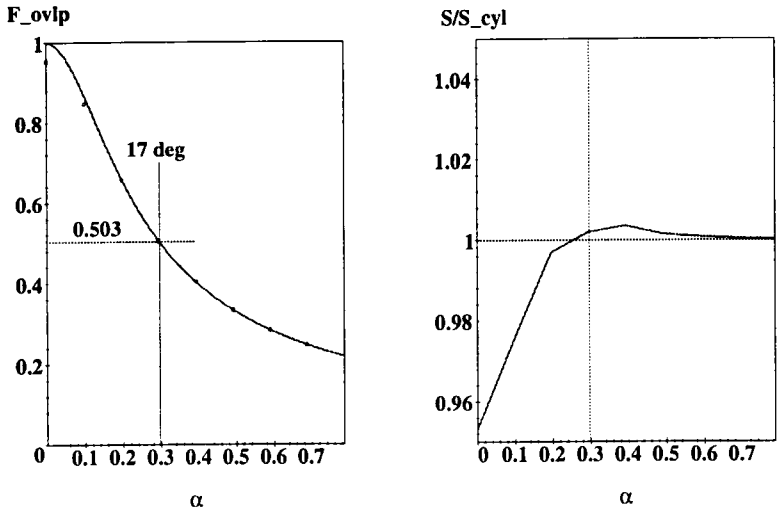

Figure 24: First plot: the effective overlap factor F_{ovlp} for the Compton scattering versus the angle α for cylindrical laser beam $z_R = \infty$ (solid line) and focused laser beam $z_R = 48.4\,\mu$m (points) for the set of IR E144 parameters. Second plot: F_{ovlp} with $z_R = 48.4\,\mu$m over F_{ovlp} with $z_R = \infty$ versus the angle α.

The total rate of backscattered photons or electrons is almost the same for the infinite Rayleigh range and $z_R = 48.4\,\mu$m (assuming the area of the laser focus is the same) for any crossing angle α. Overlap factor F_{ovlp} versus angle α follows the dependence defined by the equation (121)

$$F_{ovlp} \approx \frac{1}{\sqrt{\cos^2\frac{\alpha}{2} + \frac{\sigma_{ez}^2 + \sigma_\tau^2}{\sigma_{ex}^2 + \sigma_L^2}\,\sin^2\frac{\alpha}{2}}}\,. \tag{125}$$

For the E144 crossing angle, $\alpha = 17°$, (shown by lines), the effective overlap factor $F_{ovlp} = 0.502$ for cylindrical laser beam geometry, and 0.503 for focused laser beam geometry. Ordinary Compton scattering rate is only two times less for $\alpha = 17°$ than that for $\alpha = 0°$ crossing angle.

$S_0^{-1} = 2.53 \times 10^4\,\mu\text{m}^2$ for the set of IR E144 parameters, $\sigma_C = 0.401\,\text{Barn} = 0.401\,10^{-16}\,\mu\text{m}^2$. Hence

$$N_\gamma = 4.27\,10^7\,\frac{1}{1\,\text{J}}\,\frac{1}{10^{10}\,e^-} \quad \text{(for IR laser)}\,.$$

Dependence of the effective overlap factor on the timing jitter $\zeta = t - t'$ between electron and laser beams for cylindrical laser beam $z_R = \infty$ (solid curve) and focused laser beam $z_R = 48.4\,\mu$m (points) for $\alpha = 17°$ and for the set of IR E144 parameters are plotted in Fig. 25.

Notice that jitter effect is much less important for a focused laser beam (small f_N) than that for a cylindrical laser beam ($f_N \to \infty$). This has a natural explanation. The width of the laser beam is larger at distances greater than the Rayleigh range. If the electron beam misses the focus of the laser beam it still can interact at distances greater than Rayleigh range.

Dependence of the overlap factor F_{ovlp} on the focal area follows the prediction of equation (125) for cylindrical beam; σ_L is much smaller than other parameters. F-number dependence is almost constant except for very small f-numbers. For $f_N < 2$ predictions for cylindrical beam and focused beam geometries begin to disagree (f-number affects only the area for cylindrical beam and both area and z_R for focused beam). Laser pulse width dependence follows prediction of equation (125) and n_{diff} dependence is equivalent to the laser area dependence.

Dependence of the effective overlap factor on the laser focal area, laser f-number f_N, laser pulse length τ and n_{diff} is plotted in Fig.26.

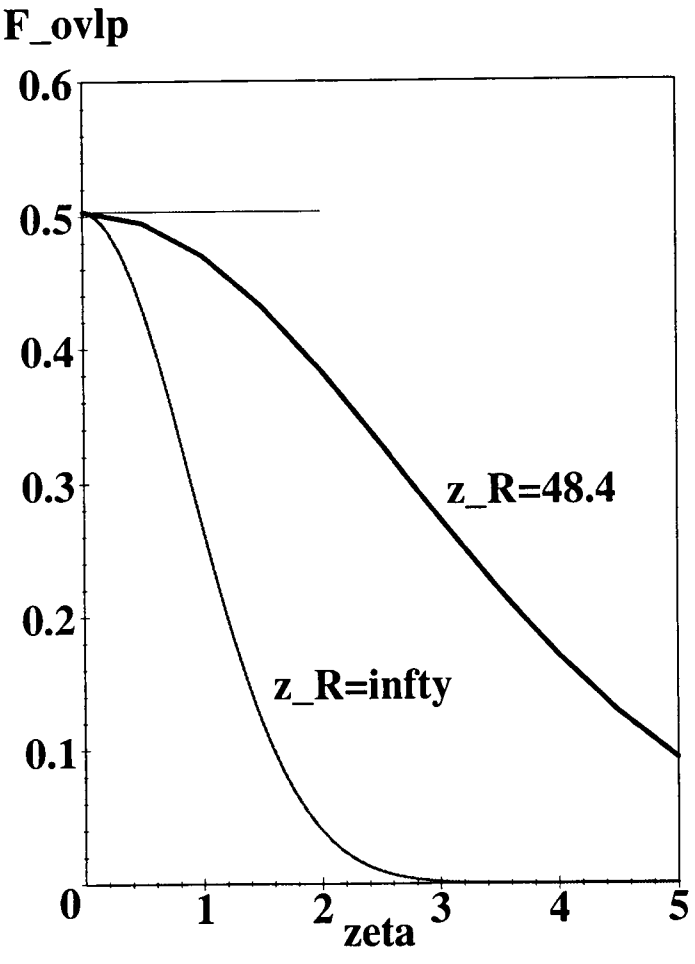

Figure 25: The effective overlap factor F_{ovlp} for the $n = 1$ Compton scattering versus the timing jitter $\zeta = t - t'$ for cylindrical laser beam $z_R = \infty$ and focused laser beam $z_R = 48.4\,\mu$m for the set of IR E144 parameters (and $\alpha = 17°$).

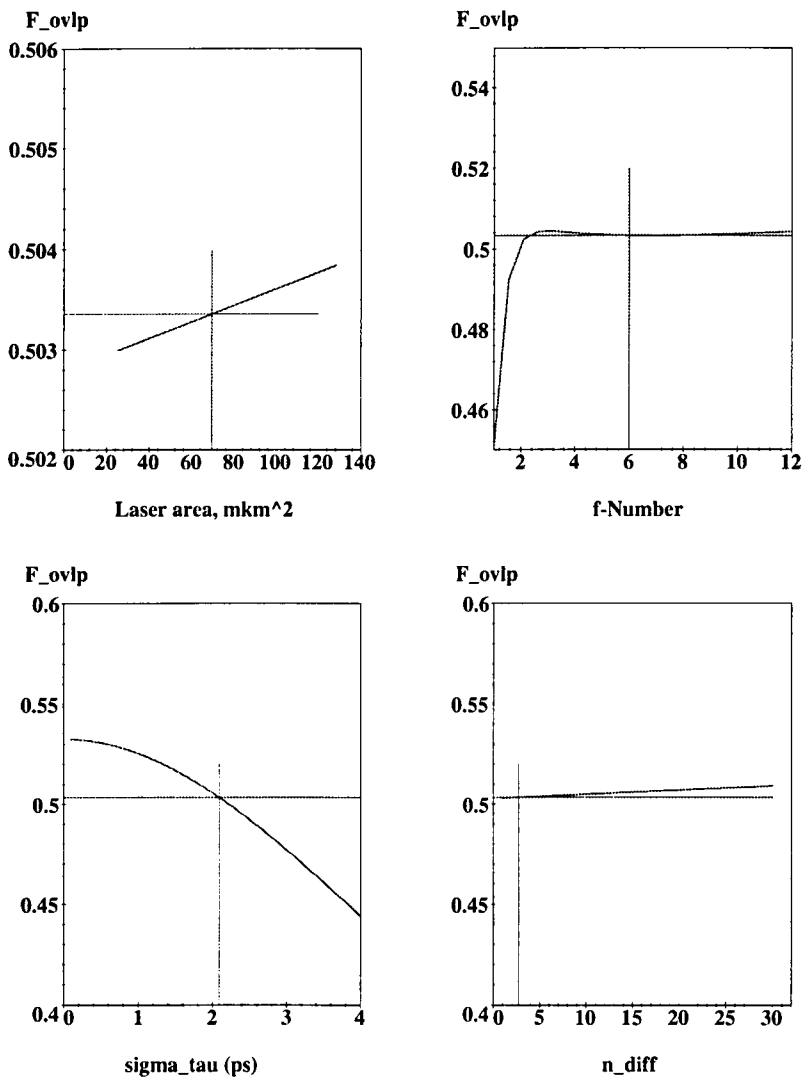

Figure 26: Dependence of the effective overlap parameter F_{ovlp} for the $N = 1$ Compton scattering versus laser parameters. 1-st plot: F_{ovlp} versus the laser focal area. 2-nd plot: F_{ovlp} versus the laser f-number. 3-rd plot: F_{ovlp} versus the laser pulse length. 4-th plot: F_{ovlp} versus n_{diff}. Horizontal and vertical crossing lines correspond to the typical set of E144 parameters (see text).

5.3.1 Probability of electron scattering through the laser focus

The previous formulae were derived on the assumption that there is no depletion of the electron beam. That is, the probability of electron scattering through the laser focus is much less than 1. The average probability of electrons scattered in an electron bunch is defined by the ratio N_γ/N_e (equation 120). The maximum probability for electron scattering occures when the electron passes through the laser focus and is given by

$$\begin{aligned} p &= S\, N_l\, \sigma_C\,, \\ S^{-1} &\approx 2\,\pi\,\sigma_L \sqrt{\sigma_L^2 \cos^2\frac{\alpha}{2} + \sigma_\tau^2 \sin^2\frac{\alpha}{2}}\,. \end{aligned} \tag{126}$$

The effective overlap parameter S in the above expression is defined by formula (121) for a cylindrical laser beam where we set $\sigma_{ex} = \sigma_{ey} = \sigma_{ez} = 0$ for individual electrons. The approximation is due to the small difference between cylindrical and focused laser beams.

According to the above formula the effective overlap parameter $S = 1/820\,\mu\mathrm{m}^{-2}$ for the set of IR E144 parameters. Hence for the set of IR E144 parameters

$$p = 0.26 \quad \text{per 1 Joule of laser energy}\,.$$

For 500 mJ IR laser the probability of electron scattering for average laser pulse is only 13 %. Because the average laser pulse for IR laser has area $69\,\mu\mathrm{m}^2$ which is 2.7 times more than diffraction limited spot for diffraction limited spot the probability would be 35 % for 500 mJ laser.

It is therefore safe to use the approximation of constant electron flux density through the electron path even for extreme variations of the laser parameters in E144 experiment.

Probability p can be interpreted as the thickness of the laser focus in radiation lengths

$$
\begin{aligned}
p &= h_{X_0}\,, \\
h_{X_0} &\approx \frac{N_l\,\sigma_C}{2\,\pi\,\sigma_L\,\sqrt{\sigma_L^2\cos^2\frac{\alpha}{2}+\sigma_\tau^2\sin^2\frac{\alpha}{2}}}\,.
\end{aligned}
$$

If the thickness of the laser focus h_{X_0} exceeds one radiation length we can expect to observe multiplication processes similar to those that occur during the passage of an electron through bulk material of thickness h_{X_0}.

5.4 Multiphoton Compton scattering

For moderate QED fields ($\eta < 1$) the cross-section for any order "n" can be presented as series in the photon density or equivalently in the laser field intensity η^2 Eq. (97). For $\eta \ll 1$ only the lowest term dominates and we can write

$$
\begin{aligned}
\sigma_n &\approx \sigma_0\left(\frac{\rho_l}{\rho_l^{max}}\right)^{(n-1)}\,, \\
\sigma_n &\approx \sigma_0\left(\frac{\eta}{\eta^{max}}\right)^{2(n-1)}\,.
\end{aligned}
\tag{127}
$$

The number of interactions according to Eq. (98) is defined by

$$
\begin{aligned}
N_n &= S\,N_e\,N_l\,\sigma_n^{max}\,, \\
S &= |\vec{v_e}-\vec{v_l}|\,\rho_{0l}^{max}\int\left(\frac{\rho_{0l}(x)}{\rho_{0l}^{max}}\right)^n\rho_{0e}(x)\;d^4x\,.
\end{aligned}
\tag{128}
$$

Following the general method described previously we can calculate the integral in the above expression. For the special case of cylindrical laser beam with infinite Rayleigh range $z_R = \infty$ we get

$$
S^{-1} = 2\,\pi\,n^{3/2}\left(\sigma_{ey}^2+\frac{\sigma_L^2}{n}\right)^{1/2}\sqrt{\left(\sigma_{ex}^2+\frac{\sigma_L^2}{n}\right)\cos^2\frac{\alpha}{2}+\left(\sigma_{ez}^2+\frac{\sigma_\tau^2}{n}\right)\sin^2\frac{\alpha}{2}}\,, \tag{129}
$$

where $2\,\pi\,\sigma_L^2 = 2\,\pi\,\sigma_{lr0}^2\,n_{diff}$ is the effective area of non-diffraction limited spot.

For the cylindrical laser beam crossing the electron beam at $\alpha = 0°$ the effective overlap parameter

$$S_{0n}^{-1} = 2\,\pi\,n^{3/2}\sqrt{\left(\sigma_{ex}^2 + \frac{\sigma_L^2}{n}\right)\left(\sigma_{ey}^2 + \frac{\sigma_L^2}{n}\right)}\,. \tag{130}$$

We use special notation S_{0n} for this value of the parameter S.

For laser focus much smaller than the electron beam

$$S_{0n}^{-1} \approx 2\,\pi\,n^{3/2}\,\sigma_{ex}\sigma_{ey} = n^{3/2}A_e\,,$$

where A_e is the area of the electron beam.

We see that the effective overlap parameter for multiphoton processes in the case of a cylindrical laser beam $z_R = \infty$ is $\approx n^{3/2}$ times less than that for $n = 1$ Compton scattering.

For the focused laser beam the total rate for nonlinear processes can be estimated from one for Compton scattering by using the scaling factor $\dfrac{\sigma_n^{max}}{n^{3/2}\,\sigma_C}$.

6 General method of reconstruction of nonlinear Compton scattering via ECAL data

6.1 Reconstruction of the signal in ECAL

Spectrometer magnets disperse the Compton electrons vertically in the y direction. There is therefore a correlation between an electron momentum and the y-coordinate at which electrons enters the ECAL. The spectrometer magnets which are a set of Final Focus Test Beam (FFTB) dump magnets bend electrons downward and positrons upward. Electrons with higher momentum enter ECAL with higher y-coordinate and with low momentum are bent more and enter ECAL with lower y-coordinates.

ECAL (Fig. 27) is segmented in Y into 12 horizontal rows $i = 1, 2, ...12$ with index $i = 1$ corresponding to the top row of ECAL. Usable signals are found in only the top four rows since typically the signals in row 4 are of the order 1% of those in row 1 so we use only the top 4 rows in the analysis. The rest of the ECAL is used for monitoring backgrounds.

ECAL is segmented transversely (x direction) into 4 vertical columns and longitudinally (z direction) into 4 segments. In the analysis longitudinal segment 4 of ECAL is ignored (shown in Fig. 27 as the rear 4 layers of the calorimeter) and the signals in segments $1 - 3$ added. We group the horizontal columns in a given row into a logical inner column ("I") consisting of the two inner physical columns, and a logical outer column ("O") consisting of the two outer physical columns. The incident Compton electrons reach the calorimeter at the middle of the inner columns ($x = 0$).

Due to the spreading of the electromagnetic shower in the calorimeter the signal measured by a row of ECAL differs from the energy flux of particles incident on the row. A few factors contribute to such effects:

1. leakage from adjacent rows into the row increases the measured signal,

2. leakage from the row itself reduces the measured signal,

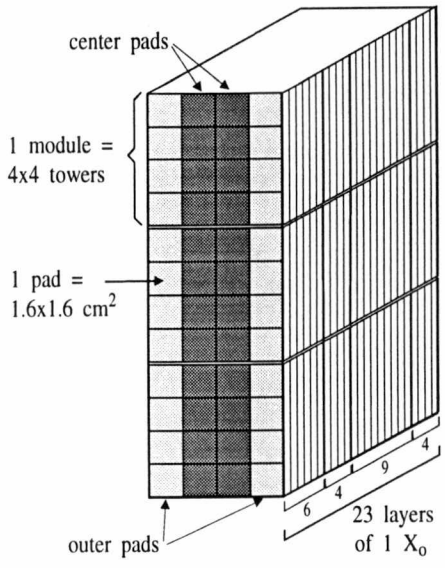

Figure 27: Segmentation of the ECAL calorimeter.

3. background due to scattered electrons adds to the measurement.

The large difference in electron fluxes between adjacent rows and spreading of electromagnetic showers in the calorimeter result in leakage which contribute to the measurements of the signal in each row. The signal must be corrected in order to reconstruct the original flux in front of ECAL.

6.2 Calibration data and Monte Carlo

Studies of ECAL performance have been made in parasitic runs of the Final Focus Test Beam at SLAC (FFTB). Pulses of 1-100 electrons were obtained at a selected momentum in the range 5-25 GeV. The beam-spot size was about 1mm. The vertical position of ECAL was varied in small steps and the energy response of each ECAL segment to an electron entering the front of ECAL at height y with energy E was determined.

We use notation G_i for the energy detected by central column of ECAL for row i and O_i for the energy detected by outer column of ECAL for row i. In addition we

choose the ADC gain conversion constants so that the the energy deposited by an electron in all inner columns is equal to the incident electron energy

$$\sum_i G_i = E\,. \tag{131}$$

Note that an electron incident on ECAL will deposit energy in outer columns by leakage as well. Thus the signal measured by all vertical columns of ECAL will be greater than the incident electron energy because of this normalization Eq. (131). This choice is made for convenience of E144 analysis.

For an electron entering ECAL at vertical position Δy with respect to the center of each row the normalized response $G_i(\Delta y)/E$ was measured to be reasonably independent of energy in the range 5-30 GeV.

Normalized response $G_i(\Delta y)/E$ for a 13 GeV electron beam is plotted in Fig. 28. These data are taken during one of the calibration runs. Longitudinal profile of the shower in the 4 longitudinal segments of ECAL is also shown.

Monte Carlo study of the ECAL reproduces the calibration data rather well (see for example Fig. 28). Calibration data and Monte Carlo allows parameterization of response of different segments of the ECAL to a point-like electron beam in form of the energy independent response functions $G_i(\Delta y)/E$ and $O_i(\Delta y)/E$. An example of the response functions and their parameterization for central and outer columns is shown in Fig. 29 for Monte Carlo simulated electrons of 10 GeV. Parameterization functions will be discussed in the next section. These functions are used to calculate the response of the calorimeter to nonlinear Compton spectrum incident on ECAL.

6.3 The response kernel $K_i(y, y')$

An electron develops a shower in the volume of the calorimeter which can be characterized by a function $K(y, y', E)$ where the electron enters ECAL at height y and deposits fractional energy at height y' in a vertical slice dy'. We normalize the response function to the incident energy and integrate over horizontal direction x.

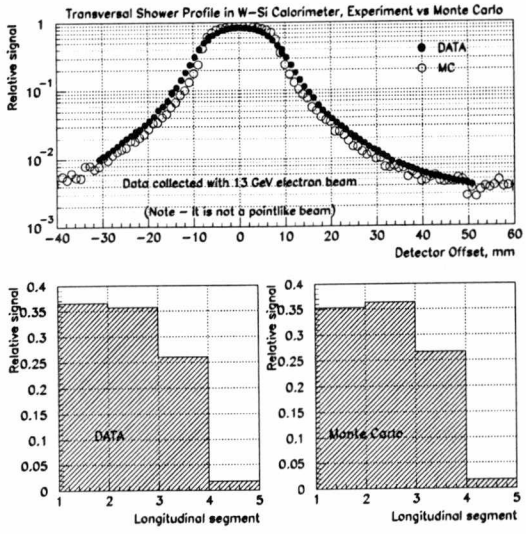

Figure 28: Top plot: normalized response $G_i(\Delta y)/E$ for 13 GeV electron beam is plotted as a function of the electron vertical position with respect to the center of the row Δy. The electron beam has $\approx 1mm$ transverse spread. Data (solid circles) and Monte Carlo (open circles) are shown. Bottom two plots: longitudinal profiles in ECAL from 13 GeV electrons are shown for the data (left plot) and Monte Carlo (right plot).

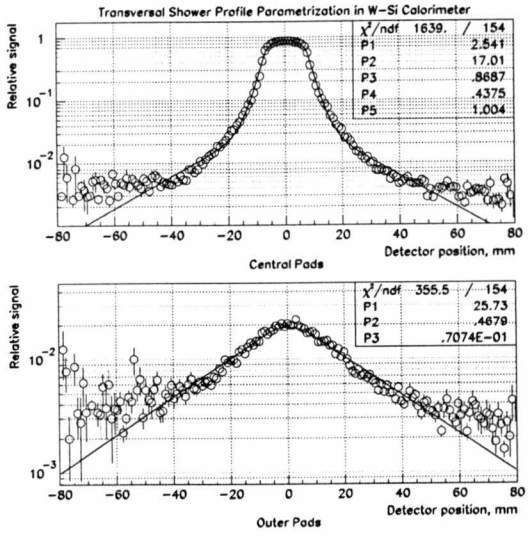

Figure 29: Parameterization of individual showers measured by central and outer columns of ECAL.

The energy response S_i of an ECAL segment i to the electron with the energy E is

$$S_i(y,E) = \int_{y_i}^{y_i+1} K(y,y',E)\,dy'\,. \tag{132}$$

In the range of electron energies 5-30 GeV the energy dependence of the kernel function $K_i(y,y',E)$ and response function $S_i(y,E)$ is negligible. Hence we can write

$$S_i(y) = \int_{y_i}^{y_{i+1}} K(y,y')\,dy'\,. \tag{133}$$

Experimental data $S_i(y)$ are parameterized using the response kernel $K(y,y')$ in the form of a sum of two exponentials

$$K(y,y') = \frac{w_1}{2b_1} e^{\left(-\frac{|y-y'|}{2b_1}\right)} + \frac{(1-w_1)}{2b_2} e^{\left(-\frac{|y-y'|}{2b_2}\right)}, \tag{134}$$

$$\int_{-\infty}^{\infty} K(y,y')\,dy' = 1\,.$$

That is an electromagnetic shower from 5-30 GeV electrons in W-Si ECAL calorimeter can be parameterized by the sum of two exponentials with two decay lengths b_1 and b_2 and relative weights w_1 and $(1-w_1)$. The parameters are determined from beam test calibration data.

Coefficients b_1, b_2 and w_1 are summarized in two tables: Table 2 for different longitudinal segments of the ECAL and Table 3 for different groups of longitudinal segments of the calorimeter. For the data analysis we use parameters for the group of 3 longitudinal segments of central columns of ECAL from the Table 3.

Parameterization for the outer columns has $w_1 = 0$, i.e. the kernel function for the outer columns can be approximated by a single exponential

$$L(y,y') = C\,\frac{1}{2b_2} e^{\left(-\frac{|y-y'|}{2b_2}\right)}\,. \tag{135}$$

Table 2: Parameters b_1, b_2, w_1 for the kernel function $K(y, y')$ for different longitudinal segments of ECAL and different vertical columns.

Longitudinal Segment	Vertical Columns	b_1 (mm)	b_2 (mm)	w_1	normalization factor
1	all	1.09	9.9	0.795	1
	central	1.05	8.2	0.807	0.966
	outer	-	17.7	0	0.034
2	all	1.85	10.0	0.684	1
	central	1.78	8.6	0.702	0.951
	outer	-	15.7	0	0.049
3	all	3.24	12.6	0.529	1
	central	3.19	11.4	0.591	0.888
	outer	-	17.1	0	0.112
4	all	5.18	16.4	0.279	1
	central	4.64	14.2	0.329	0.767
	outer	-	20.1	0	0.233

Table 3: Parameters b_1, b_2, w_1 for the kernel function $K(y, y')$ for different combinations of longitudinal segments of ECAL and different vertical columns.

Longitudinal Segment	Vertical Columns	b_1 (mm)	b_2 (mm)	w_1	normalization factor
1	all	1.09	9.9	0.795	1
	central	1.05	8.2	0.807	0.966
	outer	-	17.7	0	0.034
1+2	all	1.55	10.0	0.741	1
	central	1.49	8.6	0.758	0.956
	outer	-	16.5	0	0.044
1+2+3	all	2.00	10.9	0.669	1
	central	1.94	9.6	0.703	0.935
	outer	-	16.9	0	0.065
1+2+3+4	all	2.02	11.1	0.660	1
	central	1.97	9.7	0.696	0.932
	outer	-	17.2	0	0.068

The constant C (overall normalization factor) is 7.13% (for sum(1+2+3)) which corresponds to the total leakage of the shower to outer columns of the calorimeter. Notice that constant C for parameterization in the central columns was set to to 1. This corresponds to the fact that during absolute calibration of the calorimeter calibration constants were chosen so that the total energy measured by central columns equals the incident energy. As an example suppose a 10 GeV electron hits row 2 of ECAL, then the sum of signals (after smearing by leakage) measured by all central columns of ECAL is 10 GeV and by all outer columns $\approx$ 0.7 GeV.

6.4 Backgrounds

From measurements at very low ECAL positions and $x - t$ scans (which will be described in Section 7) we determine background in central and outer columns of the calorimeter. The measurements are presented in Section 7. The background originates from scattered electrons. The flux of N=1 electrons is typically several orders of magnitude higher than the flux of electrons from nonlinear Compton processes. The following features of the background are important for reconstruction algorithm:

- Background decreases exponentially with distance of the ECAL from the beam pipe. The decay length for the exponent is 30-70mm. See for example Fig. 30 for background measured with IR laser with setup configuration from March 95 Run. Background falls off relatively slowly compared to 16 mm detector cell size with a slope depending on the row number.

- Background is different for central and outer columns. There is more background in central columns. The ratio of background in central columns of ECAL to that in outer columns is shown in Fig. 31 for March 95 Setup configuration with IR laser. Background in central and outer columns of ECAL is almost equal for low ECAL positions, i.e. the ratio of central to outer columns approaches 1 for low ECAL positions.

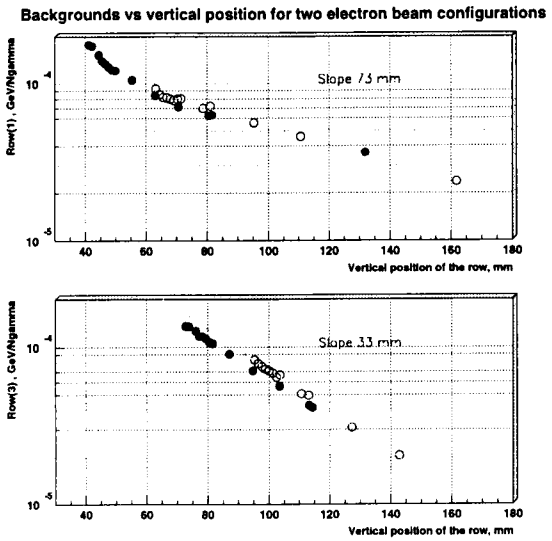

Figure 30: Background in Row 1 (top plot) and Row 3 (bottom plot) of ECAL normalized to the N=1 γ-flux (GeV/1γ) plotted as a function of vertical distance of the row (mm) from the beam pipe.

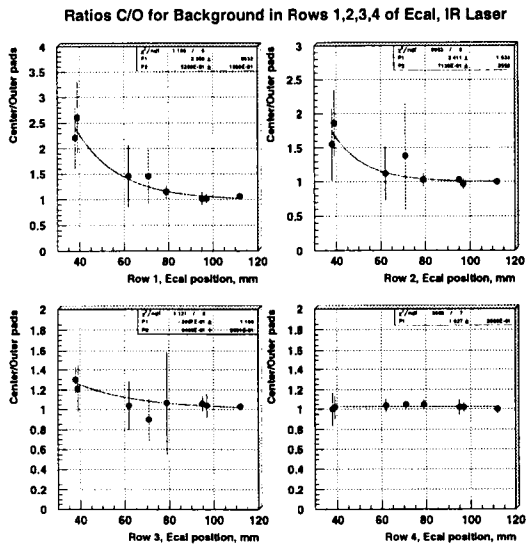

Figure 31: The ratio of background in central columns to that in outer columns is plotted as a function of vertical distance of the row (mm) from the beam pipe.

Monte Carlo simulation of the detector shows that a significant fraction of the background is generated by N=1 electrons that scatter in the beam pipe on top of ECAL and produce more background in the central columns of ECAL. The same Monte Carlo shows that background decreases rapidly with ECAL position as it is observed in the experiment.

6.5 Reconstruction algorithm

In E144 experiment electrons from nonlinear Compton scattering have a a continuous spectrum. We denote the incident energy flux as $f(y)$. $f(y)dy$ is the total energy flux in the vertical range $[y, y+dy]$. The response function of the calorimeter to the spectrum $f(y)$ is a function $g(y)$. $g(y)dy$ is the total energy deposited in ECAL in the vertical range $[y, y+dy]$. By definition of the kernel function

$$g(y) = \int_a^b K(y,y')\, f(y')\, dy', \tag{136}$$

where a and b is the vertical range of the ECAL.

Our goal is to reconstruct the function $f(y)$ from measurements $g(y)$ while the function $K(y,y')$ is known from calibration data.

In the theory of linear integral equations [56] the integral equation (136) is known as Fredholm linear equation of the first kind. There are two difficulties with solution of equation (136).

1) From the theory of integral equations it is known that Fredholm linear equation of the first kind is an example of an ill-posed problem. That is the solution $f(y)$ does not depend continuously on the data function $g(y)$. A very small perturbation on $g(y)$ can give rise to an arbitrarily large perturbation in $f(y)$. As an example let us observe that (Riemann-Lebesgue theorem [56])

$$\lim_{n\to\infty} \int_a^b K(y,y')\, \cos(ny')\, dy' = 0\,. \tag{137}$$

The above example shows that for solution $f(y)$ there is also solution $f(y) + A\cos(ny)$, where n is large enough and A is arbitrarily big. In general high-frequency components become attenuated by the detector. Some such loss of information is inevitable. The fact that the problem is "ill posed" doesn't mean that it has been incorrectly formulated. A great many physical problems do give rise to integral equations of first kind.

One way to solve the problem is to make some assumptions about the function $f(y)$ i.e. select a class of functions or combination of trial functions among which function $f(y)$ should be found and look for solutions within this class of functions only. Another way is to use "filtering algorithm" or so called regularization method which effectively suppresses higher-frequency harmonics in $f(y)$. Detailed discussion of these methods can be found in [56].

For our experiment a straightforward assumption about the function $f(y)$ is that it is monotonically decreasing function. We cannot assume additional information such as the position of $N = 2/N = 3$ edges which is equivalent to introducing higher-harmonics in $f(y)$ in our reconstruction because $N = 2/N = 3$ edge is the observation we want to reconstruct from our measurements.

We choose a polyline approximation of the function $f(y)$ as trial functions for reconstruction. This approximation function is continuous and has constant slope within each row. This simple form of approximation is dictated by limited information available - only 4 measured points are available; one cannot have more than 4 free parameters in the approximation function.

2) The detector measures $g(y)$ only at a few points (4 in this analysis), each measurement represents the integral of $g(y)$ over the row. We do not need to reconstruct $f(y)$, the goal of reconstruction is to find integrals of the incident flux F_i over the row of ECAL from the measured signal G_i

$$G_i = \int_{y_i}^{y_{i+1}} g(y)\,dy\,,$$
$$F_i = \int_{y_i}^{y_{i+1}} f(y)\,dy\,.$$

We will use the matrix $M_{(i,j)}(f)$ defined as

$$G_i = \sum_{j=1}^{n} M_{i,j}(f)\,F_j\,. \tag{138}$$

Elements of the matrix $M_{(i,j)}(f)$ depend on the spectrum $f(y)$. If matrix $M_{(i,j)}(f)$ is known than the incident flux F_i can by calculated as

$$F_i = \sum_{j=1}^{n} \left(M_{i,j}(f)\right)^{-1} G_j\,. \tag{139}$$

Both matrices M and $(M)^{-1}$ depend on $f(y)$. We use the following approximation technique to determine these matrices:

- Use a trial function $f_p(y)$ which is a polyline approximation of the incident spectrum $f(y)$. The polyline approximation function has the form:

$$f_p(y) = \sum_{i=1}^{4} a_i(1 + k_i(y - i))\,, \tag{140}$$

a_i - signal at the center of the row i ,

k_i - linear slope for the row i: $k_i = [0, +2]$,

$(y - i)$ - position within the row i: $(y - i) = [-0.5, +0.5]$,

$a_i\left(1 + \frac{k_i}{2}\right) = a_{i+1}\left(1 - \frac{k_{i+1}}{2}\right)$ continuity condition.

- Find matrix $M_{(i,j)}(f_p)$ using the parameterization of the Kernel function from Table 3.

- Use equation (139) to find a new trial function $f_p(y)$ in the form of polyline approximation to the incident flux.

- Iterate this procedure until two successive trial functions $f_y(p)$ corresponding to iteration steps n and $n+1$ differ by less than the required accuracy.

If no backgrounds were present the above interaction procedure reconstructs the incident flux F_i using only the measurements G_i in the central columns of ECAL.

In the presence of background we should include outer columns in the analysis as well. The total signal in the outer columns of the ECAL consist of backgrounds and leakage from the central columns of ECAL.

Leakage from the central columns to the outer columns of the ECAL O_i are

$$\begin{aligned} o(y) &= \int_a^b L(y,y')\, f(y')\, dy' , \\ O_i &= \int_{y_i}^{y_{i+1}} o(y)\, dy , \end{aligned}$$

where $L(y,y')$ is the Kernel function for the outer columns, a and b is the vertical range of the ECAL.

By analogy with the matrix M for the central columns of ECAL we define matrix N for the outer columns

$$O_i = \sum_{j=1}^{n} N_{i,j}\, F_j \,. \tag{141}$$

The nonlinear Compton spectrum incident in front of ECAL varies by 2-3 orders of magnitude over the four top rows of ECAL for the experiment. Background varies relatively slowly over the face of the calorimeter and we can assume that there is no effective leakage of the background flux between central and outer columns of ECAL, i.e. background leakage from central to outer columns are equal to leakage from outer to central columns.

We will use symbol B_i for the background in the outer column of ECAL incident on row i. Background in the central column i of ECAL is r_i times of that in the outer column B_i. We will use a diagonal matrix R with elements $R_{i,i} = r_i$.

Measured signal G in central columns of ECAL is the sum of the nonlinear Compton signal $M\,F$ and background in the central columns $R\,B$

$$G = M\,F + R\,B\,. \tag{142}$$

Signal O in outer columns of ECAL will be the sum of the leakage from nonlinear Compton signal $N\,F$ and background in the outer columns B

$$O = N\,F + B\,. \tag{143}$$

Subtracting R times Eq. (143) from Eq. (142) we get

$$G - RO = (M - R\,N)\,F\,.$$

Hence

$$F = [M - R\,N]^{-1}\,(G - RO)\,. \tag{144}$$

Equation (144) is the solution for a nonlinear Compton signal as a function of the measured signals in the central and outer columns of ECAL assuming that matrices M, N and R are known.

We apply iterative procedures described above to find the incident electron flux F.

6.6 Calculation of matrices M and N

Matrices M and N do not depend directly on the incident electron flux F_i, but only on the slopes k_i of polyline functions used for parameterization of F_i.

As an example we consider a simple Monte Carlo model of the calorimeter without leakage from the top. The matrices M and N have an especially simple form in this case. Then we show matrices M and N for the actual reconstruction.

Matrix M for calorimeter without leakage from the top is:

$$\mathbf{M} = \begin{bmatrix} .77 & .10 - .024k_2 & .011 - .002k_3 & .0021 - .0003k_4 \\ .10 + .024k_1 & .77 & .10 - .024k_3 & .011 - .002k_4 \\ .011 + .002k_1 & .10 + .024k_2 & .77 & .10 - .024k_4 \\ .0021 + .0003k_1 & .011 + .002k_2 & .10 + .024k_3 & .77 \end{bmatrix}$$

Where k_1, k_2, k_3, k_4 are parameters of polyline approximation Eq. (140) for spectrum $f(y)$.

For example from the third line of the matrix M above one can conclude that for uniform input energy flux in front of ECAL ($k_1 = k_2 = k_3 = k_4 = 0$) measurement in row 3 is the sum of four incident energy fluxes: $\approx 1.1\%$ of the flux incident on row 1 plus $\approx 10\%$ of that for row 2 plus 77.1% of that for row 3 plus $\approx 10\%$ of that for row 4 .

Matrix N for calorimeter without leakage from the top is:

$$\mathbf{N} = \begin{bmatrix} .025 & .014 - .001k_2 & .0055 - .0004k_3 & .0021 - .0002k_4 \\ .014 + .001k_1 & .025 & .014 - .001k_3 & .0055 - .0004k_4 \\ .0055 + .0004k_1 & .014 + .001k_2 & .025 & .014 - .001k_4 \\ .0021 + .0002k_1 & .0055 + .0004k_2 & .014 + .001k_3 & .025 \end{bmatrix}$$

One can see that due to the slow exponential component of the shower leakage to the outer columns, contributions from different rows are comparable. For example outer columns of row 3 have $\approx 0.5\%$ of the signal in row 1, $\approx 1.4\%$ of the signal in row 2 and $\approx 2.5\%$ of the signal in row 3. Note that row 1 has large signal compared to row 2, 3 and 4. Hence the main contribution to outer columns leakage is from row 1.

In the E144 setup, ECAL motion is limited in the upward vertical direction by the beam pipe and there is additional shielding on top of ECAL. In practice there is an adjustment to matrices M and N, presented above, to account for the energy leaking down into ECAL from showers due to Compton electrons that hit tungsten plate above it. Additional adjustment are made to bring the results into better agreement with the calibration data. The revised matrices are:

$$\mathbf{M} = \begin{bmatrix} .87 - .081k_1 & .089 - .016k_2 & .0083 - .0007k_3 & .0035 - .0007k_4 \\ .097 + .008k_1 & .789 & .089 - .016k_3 & .0083 - .0007k_4 \\ .0104 - .002k_1 & .089 + .016k_2 & .789 & .089 - .016k_4 \\ .0056 - .001k_1 & .0083 + .0007k_2 & .089 + .016k_3 & .789 \end{bmatrix}$$

and

$$\mathbf{N} = \begin{bmatrix} .026 - .0083k_1 & .010 - .0010k_2 & .0055 - .0004k_3 & .0021 - .0002k_4 \\ .014 + .001k_1 & .025 & .014 - .001k_3 & .0055 - .0004k_4 \\ .0055 + .0004k_1 & .014 + .001k_2 & .025 & .014 - .001k_4 \\ .0021 + .0002k_1 & .0055 + .0004k_2 & .014 + .001k_3 & .025 \end{bmatrix}$$

6.7 Reconstruction errors

The reconstruction algorithm uses an iterative procedure to unfold the Compton spectrum. It is checked by generating trial data from a known spectrum, simulating the response of ECAL to this spectrum and applying the reconstruction algorithm to the simulated data to unfold the original spectrum. The unfolded spectrum is compared with the original spectrum and the error in reconstruction is estimated. The error σ_1/F_1 in results from row 1 was to be $\approx 5\%$. The error in row 1 is due to approximation of the continuous spectrum by the polyline function. Because the leakage from rows 2,3 and 4 into row 1 are negligible this error is dominated by the error in the approximation of the continuous spectrum in row 1 only.

For rows 2,3 and 4 the situation is different. Errors in approximation of the

continuous spectrum in the top rows "propagate" to the lower rows due to leakage between rows.

For the reconstructed signal in row i we have equation (144)

$$F_i = \sum_j \left[(M - RN)^{-1} G\right]_{i,j} + \sum_j \left[(M - RN)^{-1} RO\right]_{i,j} . \qquad (145)$$

The relative error in each of this terms is $\approx \sigma_1/F_1$ because it represents the contribution to the reconstruction error in each row from the approximation of the continuous spectrum in the same row. We assume that all these errors are of the same order. Hence

$$\frac{\sigma_i}{F_i} = \frac{\sigma_1}{F_1}\sqrt{\left[\sum_j (M - RN)^{-1} G\right]^2 + \left[\sum_j (M - RN)^{-1} RO\right]^2} . \qquad (146)$$

6.8 Reconstruction summary

- Reconstruction method is based on experimental data collected during calibration runs and Monte Carlo simulations checked against the experimental data.
- Showering of the electron in ECAL is taking into account by the use of smearing matrices M for central columns and N for outer columns of ECAL. Smearing matrices depend only on parameters of polyline approximation for the incident electron spectrum.
- Iterative procedures for the electron flux reconstruction are employed which permit the reconstruction of the spectrum within 2-3 iterations.
- Comparison with Monte Carlo simulations shows that reconstruction accuracy for the top-most row of ECAL (row 1) is $\approx 5\%$.
- Reconstruction errors "propagate" from the top rows to the bottom. Row 1 has small relative error because it has the maximum signal and relatively small background. Error in row 2 combines the absolute error of reconstruction in

row 1 with weight ($\approx 10\%$) and the error in row 2. It has larger relative error due to a smaller signal compared to background. Error in row 3 combines the absolute reconstructed error in row 1 with weight $\approx 1.2\%$, error in row 2 with weight $\approx 10\%$ and the error in row 3.

7 Nonlinear Compton scattering of 46.6 GeV electrons by circularly polarized laser light

7.1 Sources of background

Electrons originating from nonlinear Compton processes are bent by the spectrometer magnet and detected by the electromagnetic calorimeter (ECAL). At the same time electrons from ordinary N=1 Compton scattering are also bent by the spectrometer magnet through a smaller angle (due to higher energy) and pass above the ECAL. Recall that the nonlinear Compton signal from N=2,3,4 interactions measured by ECAL is in the range $10^2 - 10^4$ GeV. At the same time the flux of ordinary N=1 Compton electrons is of the order of $10^6 - 10^8$ GeV. These electrons leave the vacuum chamber and pass through several materials. Small fraction of this flux is scattered into ECAL. This complicates the measurement of the nonlinear Compton signal. Three main sources of background were identified:

1. Fe window of the vacuum chamber. Though the thickness of the window is small (9mm), the location of the window in front of ECAL allows N=1 electrons scattered through a relatively small angle of $10 - 30°$ to reach ECAL. This background dominates in the front longitudinal section of ECAL.

2. Beam pipe above ECAL. A fraction of the N=1 electron flux strikes the walls of the stainless steel beam pipe (1/16" thick) at a very small angle $\approx 1°$. Electrons scattering in the beam pipe strike ECAL from above at angles $\approx 90°$. Because this background originates above ECAL it has the greatest effect on the top row. Also, shielding on top contributed during the March 1995 run.

3. N=1 electrons exit the beam pipe and hit flanges of the beam pipe and other materials behind ECAL. Splash-back from these electrons (albedo) reaches ECAL causing background mainly in the rear longitudinal section.

Changes in the design of the beam pipe and vacuum chamber window made prior to August 96 run reduced backgrounds from sources (1) and (2) to a level more than an order of magnitude smaller than the signal. Background from the 3-rd source (splash-back) is reduced by Pb-brick shielding behind ECAL. Finally the last segment of the ECAL ($\approx 4X_0$) was not used in the analysis and hence serves as additional shielding.

Backgrounds which are uniformly distributed in the transverse direction (perpendicular to the beam pipe) can be effectively subtracted from the signal by the design of the calorimeter. ECAL has 4 readout segments in the transverse direction - 2 central and 2 outer columns. Electrons from the nonlinear Compton processes are deflected vertically along the center line of ECAL and develop electromagnetic showers in 2 central columns with $\approx 10\%$ of those showers leaking to the outer columns. Hence subtraction of the signal in the outer columns from that in the central columns (taking into account the shower leakage) can eliminate uniform background even it exceeds the signal.

A difficulty for reconstruction of the nonlinear Compton signal is in the nonuniform component of the background in the transverse direction. Monte Carlo studies identified sources of this nonuniform background and helped to define a strategy to reduce it. The nonuniform component in the background is primarily due to the scattering in front of ECAL (source 1) and on top of ECAL (source 2). Albedo from the back (source 3) is almost uniform, and subtraction of outer columns almost completely eliminates this background. This result is confirmed by direct measurements.

7.2 Measurements

Backgrounds are measured when only N=1 Compton scattering occurs at the electron-laser interaction, without higher order processes. This condition could be achieved by defocusing the laser beam to increase the area of the laser focus with low maximum laser intensity. However in E144 it was not possible to change the area of the laser focus so an alternative method of effectively "defocusing" the laser beam was used.

Due to the 17° crossing angle between electron and laser beams it was possible to move the laser focus outside the electron beam in the horizontal X-direction (perpendicular to the electron beam) and still have collisions by adjusting the relative timing of the electron and laser beams. A typical two dimensional X-T scan is shown in Fig. 32. The signal during X-T scan is measured by two detectors - one detector (CCM1 or EC31) is used to measure the rate of N=1 Compton processes and one detector (ECAL) to measure the rate of nonlinear (N=2) processes. When the laser focus is inside the electron beam one sees the clear signal in N=2 detector as well as in N=1 detector. With the laser focus outside the electron beam there are no nonlinear processes while the N=1 rate is still high.

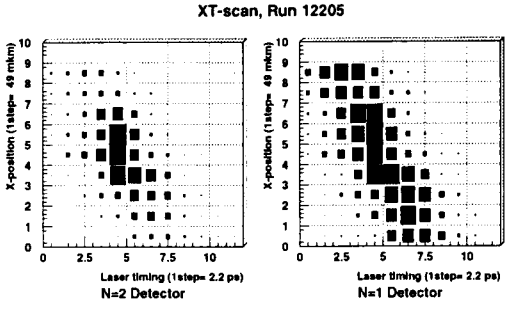

Figure 32: Example of XT-scan (run 12205) for IR circular polarized laser. Horizontal axis - timing of the laser (ps), vertical - X-position of the laser IP box (μm). Area of the boxes is proportional to the signal. Two detectors are shown - ECAL in the position where it measures N=2 signal and N=1 gamma counter (CCM1). The slope of N=1 signal is due to 17° crossing angle between electron and laser beams.

The slope of N=1 rate on X-T plot corresponds to 17° crossing angle between the electron and laser beams. From geometrical consideration the relation between Δx and Δt is

$$\Delta x \left(\frac{1}{\sin \alpha} + \frac{1}{\tan \alpha} \right) = c \Delta t \,,$$

where $\alpha = 17°$ is the crossing angle. Because $c = 299.8\, \mu m/ps$ we find that the expected slope is

$$\Delta x \, [\mu m] \; = \; 44.80 \, \Delta t \, [ps] \,.$$

X-T scans were made frequently during the data acquisition to monitor and adjust the position and the timing of the laser. They were taken with a variety of ECAL positions and laser intensities.

To measure backgrounds in ECAL caused by re-scattering of N=1 electrons one can look at the asymptotic behavior of the ECAL signal for center and outer columns while the laser focus is outside the electron beam. Higher order processes should not contribute to the measurements when the laser focus is completely outside the electron beam and the only source of the signal is then the background from N=1 processes. Normalizing the ECAL signal to the N=1 γ-flux (measured by CCM1) one expects this signal to go asymptotically to some constant level presumably different for center and outer pads of ECAL.

Fitting these distributions by Gaussian plus a constant term

$$F = \frac{1}{\sqrt{2\pi}\sigma} e^{\frac{(x-x_0)^2}{2\sigma^2}} + C\,, \tag{147}$$

one can determine backgrounds in center and outer pads normalized to the N=1 flux, and study their behavior versus ECAL position. The ratio of the two is the measure of nonuniformity of the background.

Figure 33 shows an example of normalized ECAL signals for the four top rows of the ECAL plotted against X-position of the laser focus. Each plot shows central columns (solid circles) and outer columns (open circles). The ratio of the center to the outer columns (ratio of constants C from equation 147) is indicated.

The horizontal axis is the X-position of the laser focus in μm and the vertical axis is the ECAL signal in GeV normalized to the γ-flux (per 10^4 γ's).

A total of about 25 XT-scans were taken during March 95 run at two laser wavelengths and with both linear and circular polarization. Most IR laser runs had a 12mm W-plate on top of ECAL that served as shielding from backgrounds. During green laser operation this plate was removed.

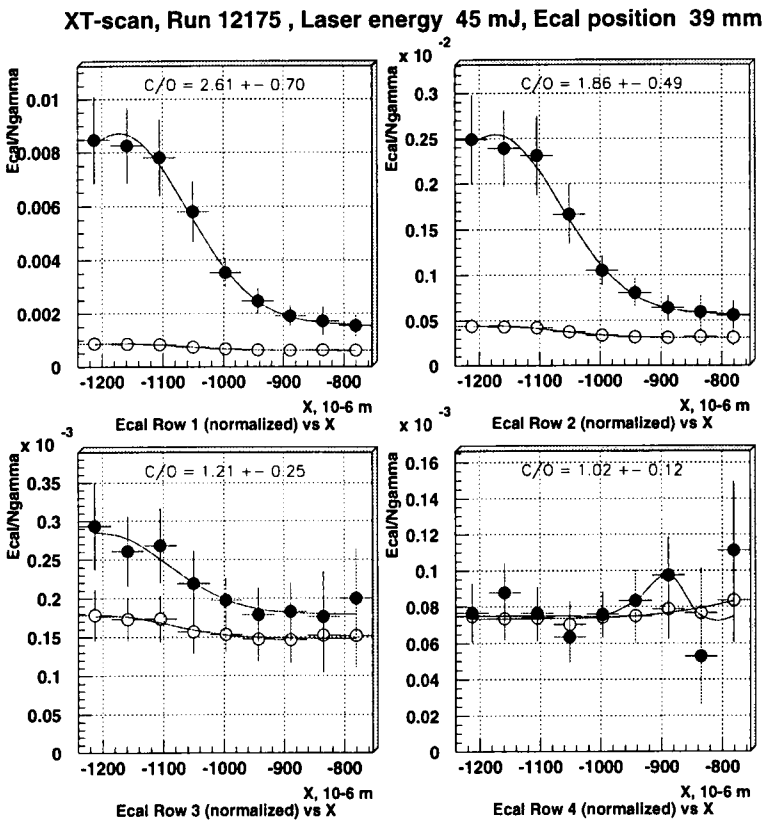

Figure 33: Example of different backgrounds for center and outer columns for XT-scan 12175. ECAL central columns (solid circles) and outer columns (open circles) signals are normalized to N=1 signal and plotted versus X-position of the laser IP box and therefore of the laser focal point. Four plots correspond to four top rows of ECAL; ratios of central to outer columns signals out of focus are also shown with corresponding errors.

Tables 4 and 5 present results from XT-scans for most of these 25 runs (for the rest, results were not reliable either because run had only 4-5 points or because they were not completed). Table 4 contain backgrounds in four top rows of ECAL for center columns in GeV per 10^4 γ. Backgrounds and errors correspond to the parameter C from the fit of distributions by the function (147).

Table 5 shows the ratio of the backgrounds in center and outer pads for the same runs.

The same data plotted in graphical form are presented in Figs 34, 35,36 and 37.

Notice that the background in the center pads and outer pads become almost equal for low ECAL positions. This naturally suggests that the ratio of two backgrounds should go asymptotically to one. Background became uniform for low ECAL positions. Figures 36 have a fit by function

$$R(y) = 1 + e^{p_1 - y\,p_2}, \tag{148}$$

which asymptotically approaches 1.

Table 4: Background in the center columns of ECAL for some XT-scans. Background (GeV) is per 10^4 γ measured by N=1 monitor. Symbol $^{\odot}$ corresponds to circularly polarized laser, $^{||}$ linearly polarized laser, * shielding on top of ECAL (see text).

Run	ECAL mm	Laser energy	Row 1 GeV	Row 2 GeV	Row 3 GeV	Row 4 GeV	Laser
12116	28	18 mJ	15.20±1.48	1.46±.22	.38±.04	.09±.05	IR$^{\odot}$
12164	38	18 mJ	15.49±4.01	5.37±1.72	2.11±.16	.76±.10	IR$^{\odot\star}$
12175	39	45 mJ	15.87±3.50	5.70±1.18	1.80±.28	.75±.06	IR$^{\odot\star}$
12205	62	126 mJ	2.83±1.02	1.02±.28	.54±.09	.36±.02	IR$^{\odot\star}$
12250	71	243 mJ	1.99±.23	.81±.10	.42±.10	.31±.01	IR$^{\odot\star}$
12257	79	311 mJ	1.70±.15	.69±.05	.38±.04	.25±.01	IR$^{\odot\star}$
12297	95	443 mJ	1.24±.15	.56±.01	.30±.02	.18±.01	IR$^{||\star}$
12338	97	930 mJ	1.22±.10	.51±.04	.28±.03	.17±.01	IR$^{\odot\star}$
12351	112	722 mJ	1.08±.03	.44±.01	.23±.01	.14±.01	IR$^{\odot\star}$
12388	82	12 mJ	4.51±.72	2.18±.51	.65±.35	-.26±.07	green$^{\odot}$
12411	81	123 mJ	7.83±.92	4.85±.57	1.42±.17	.15±.02	green$^{\odot}$
12419	114	200 mJ	.78±.17	.13±.01	.05±.01	.03±.01	green$^{\odot}$
12430	113	255 mJ	1.54±.21	.20±.02	.09±.01	.03±.01	green$^{\odot}$
12445	81	30 mJ	3.79±.64	2.13±.37	.70±.11	.15±.01	green$^{||}$
12474	82	13 mJ	5.63±.60	2.51±.34	1.16±.16	.27±.02	green$^{||}$

Table 5: Background ratio center/outer columns for some XT-scans. Symbol $^{\odot}$ corresponds to circularly polarized laser, $^{\|}$ linearly polarized laser, * shielding on top of ECAL (see text).

Run	ECAL mm	Row 1 C/O	Row 2 C/O	Row 3 C/O	Row 4 C/O	Laser
12116	28	1.87±.21	1.54±.27	1.14±.17	.71±.37	IR$^{\odot}$
12164	38	2.21±.62	1.55±.54	1.30±.13	1.00±.17	IR$^{\odot\star}$
12175	39	2.61±.70	1.86±.49	1.21±.24	1.02±.12	IR$^{\odot\star}$
12205	62	1.46±.61	1.12±.39	1.04±.24	1.04±.07	IR$^{\odot\star}$
12250	71	1.45±.54	1.38±.78	.90±.21	1.05±.05	IR$^{\odot\star}$
12257	79	1.15±.13	1.03±.10	1.07±.52	1.05±.05	IR$^{\odot\star}$
12297	95	1.02±.13	1.03±.05	1.06±.08	1.02±.08	IR$^{\|\star}$
12338	97	1.02±.09	.97±.08	1.04±.12	1.02±.05	IR$^{\odot\star}$
12351	112	1.06±.05	1.00±.04	1.03±.04	1.00±.04	IR$^{\odot\star}$
12388	82	2.35±.39	2.53±.62	1.52±.83	-	green$^{\odot}$
12411	81	6.14±.90	7.32±1.09	4.78±.70	1.37±.19	green$^{\odot}$
12419	114	3.40±.83	1.30±.22	.91±.09	1.10±.08	green$^{\odot}$
12430	113	5.39±.98	1.49±.23	1.33±.17	.98±.10	green$^{\odot}$
12445	81	3.92±.77	3.52±.64	2.60±.44	1.01±.22	green$^{\|}$
12474	82	2.42±.28	2.38±.37	1.70 ±.26	2.36±1.05	green$^{\|}$

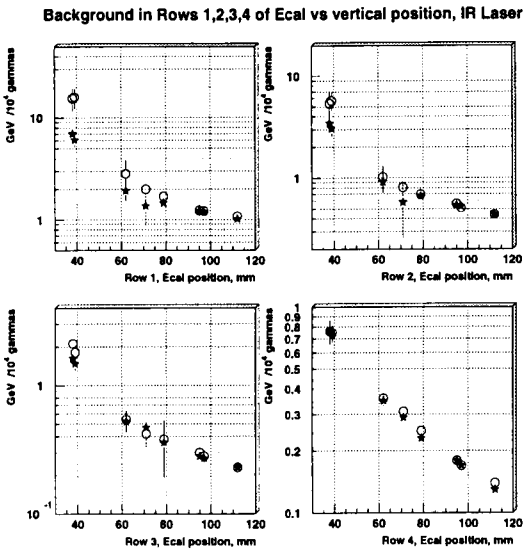

Figure 34: Background for central pads (open circles) and outer pads (stars) for 4 rows of ECAL versus ECAL position for IR-laser runs. Background (GeV) is normalized to γ-flux of 10^4 γ.

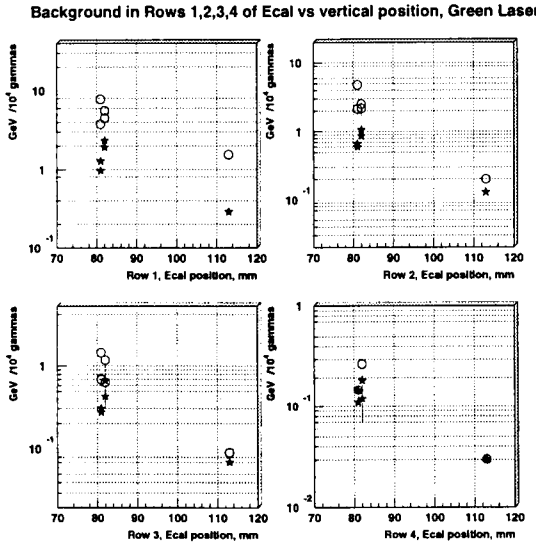

Figure 35: Background for central pads (open circles) and outer pads (stars) for 4 rows of ECAL versus ECAL position for GREEN-laser runs. Background (GeV) is normalized to the γ-flux of 10^4 γ.

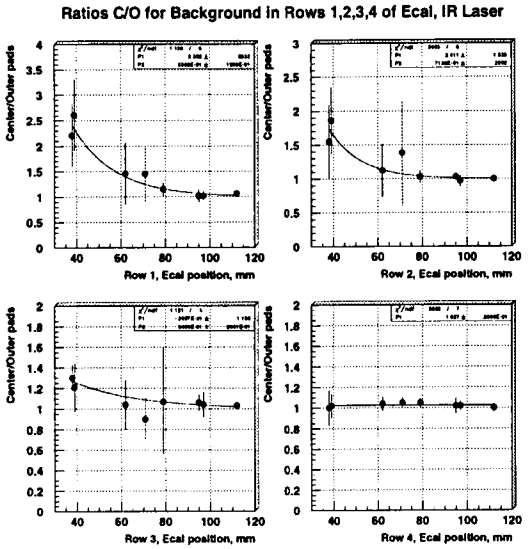

Figure 36: Ratio of the backgrounds Center/Outer pads versus ECAL position for IR laser runs. Solid curves are result of the fit by function R(y) (see text).

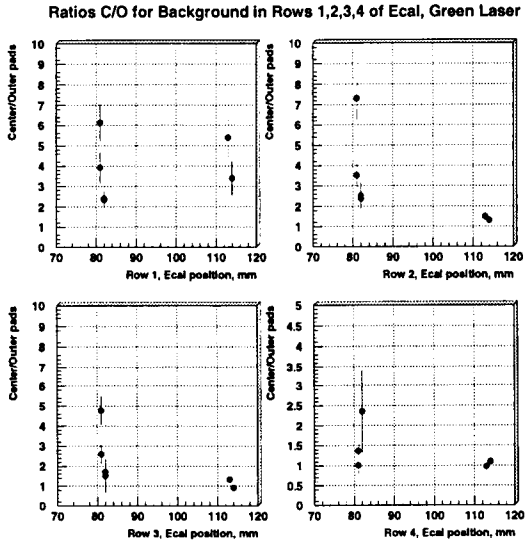

Figure 37: Ratio of the backgrounds Center/Outer pads versus ECAL position for GREEN laser runs.

7.3 Corrections

First, let us note that the N=1 background analyzed above does not include contribution from the plural N=1 scattering of an electron in the laser field. By plural scattering we mean the process when a single electron scatters two or more times by N=1 Compton scattering. This can be noticed by comparing XT-scans with the same ECAL position and different laser energies. Normalized background in central pads (Table 4) does not depend on laser intensity (for instance IR runs 12164 and 12175, 12297 and 12338 with the same ECAL position). Recall that the two step N=1 process is proportional to the square of laser intensity; after normalization to the N=1 rate it should be proportional to laser intensity.

Laser polarization does not affect backgrounds (IR runs 12297 and 12338, Green runs 12388 and 12445).

Shielding on top of ECAL does not improve the situation with backgrounds. Though we have only IR run 12116 without shielding (in this analysis) it shows significantly lower backgrounds especially in rows 3 and 4 of ECAL.

Though Green laser data has higher normalized backgrounds in the top row for the same ECAL positions (compare runs IR-12257 and Green-12411) they have backgrounds decreasing rapidly for rows 2, 3 and 4. This can be explained by the different spectrum of N=1 electrons for Green laser but more likely decreasing backgrounds can be attributed to the absence of shielding on top of ECAL.

Nonuniformity of the background (ratio of the center to outer columns) decreases i.e goes to 1 for low ECAL positions because the ECAL is further away from the path of scattered electrons.

For IR runs one can see from Plot 36 that statistically significant nonuniformity of the background can be seen only in rows 1 and 2 of ECAL for high ECAL positions. For row 3 though there is an indication of a slightly nonuniform background at the high ECAL position. The constant fit ($R = 1$) to the data for this row has χ^2 not significantly different from χ^2 from the exponential fit. For row 4 there is no indication

of nonuniform backgrounds.

Green laser runs (Fig. 37) have significantly higher background in the center columns than in the outer columns for ECAL position 81-82 mm. In this position ECAL is located close to the N=1 edge of electron spectrum. There are only 2 positions for XT-scans for Green laser and it is difficult to draw conclusions. Still one suggestion is apparent: there is a danger of overestimating the N=2 signal for the high ECAL position which corresponds to low laser intensity because there is much more background in the center columns compared to the outer columns.

To find background in GeV one must multiply the normalized background in ECAL by the γ-flux. This flux is different for different ECAL positions. Because of the limited dynamic range of ECAL the calorimeter was positioned lower for high laser intensities than for lower laser intensities. There is thus a correlation between typical γ flux (and hence the background) and ECAL position in the data runs. This dependence for all data runs is presented in Fig. 38 separately for IR and Green laser polarizations.

We compare the reconstructed signal in ECAL compared to the reconstructed background. Reconstruction of the signal and background takes into account shower leakage between different rows and between center and outer pads of ECAL and is described in the previous section. Two plots, Fig. 39 and Fig. 40, show backgrounds in ECAL compared to the nonlinear Compton signal for IR and Green laser polarizations.

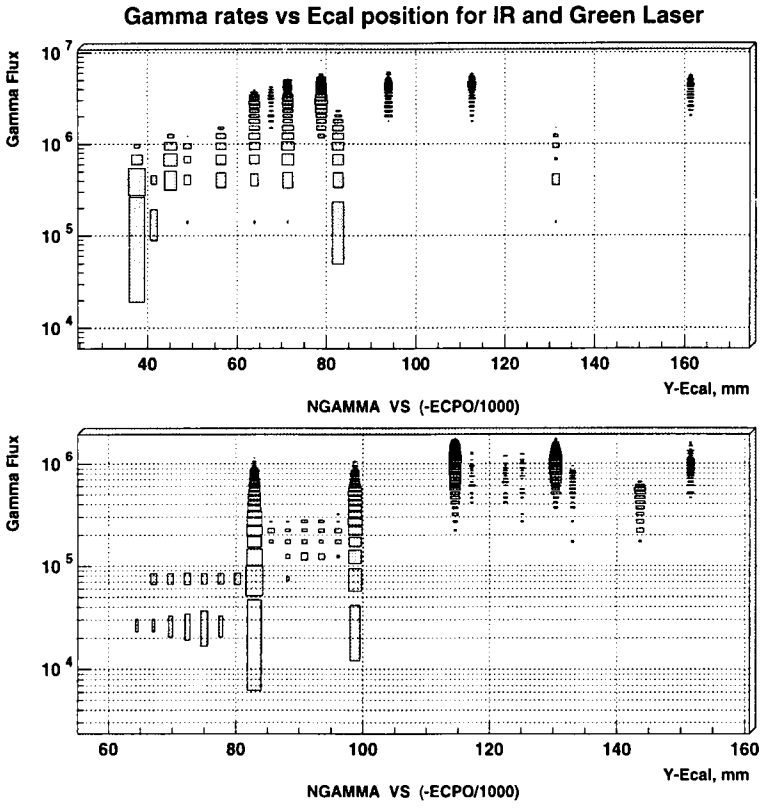

Figure 38: Flux of γ versus ECAL position for IR and Green laser. All Data runs used in the analysis of the nonlinear Compton signal in ECAL are represented.

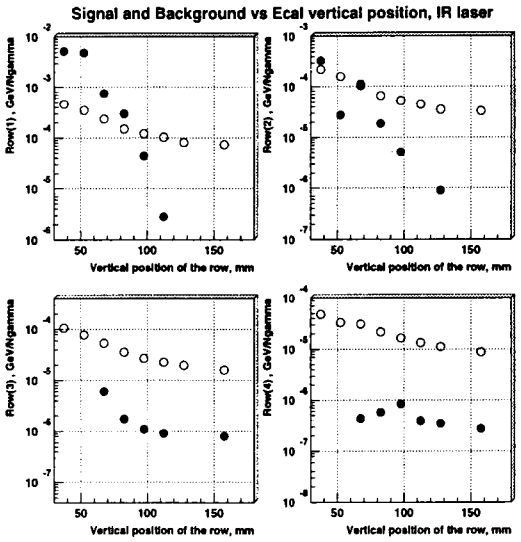

Figure 39: Reconstructed signal (solid circles) and background (open circles) for all IR laser data runs. Signal and background are normalized to the number of photons - GeV/Nγ. 4 plots correspond to 4 rows of ECAL. Some points for the signal (in rows 3 and 4) are not shown because reconstruction failed for these points and gave negative numbers.

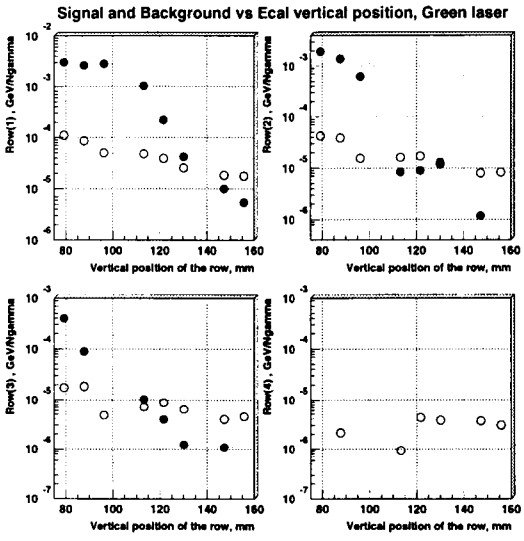

Figure 40: Reconstructed signal (closed circles) and background (open circles) for all GREEN laser data runs. Signal and background are normalized to the number of photons - GeV/Nγ. 4 plots corresponds to 4 rows of ECAL. Some points for the signal (in row 4) are not shown because reconstruction failed for these points and gave negative numbers.

7.4 Data collection strategy

To study the dependence of the nonlinear scattering process on laser intensity, data were taken at several different laser energies between 10 mJ and 800 mJ. Both IR ($\lambda = 1053$ nm) and green ($\lambda = 527$ nm) laser pulses were used, always with circular polarization. At the highest intensity there were over 10^7 photons with average energy 15 GeV emitted in the forward direction. To avoid saturation, ECAL was moved well past the kinematic edge for $n = 1$ scattered electrons. However the recoil electron spectrum drops very quickly (see Fig. 41) so that it was not possible to measure more than one or two orders of multiphoton scattering at any particular position of the ECAL. Figure 42 shows the region accessible to the ECAL for different recoil electron momenta and laser energies for IR pulses. The momentum acceptance of the ECAL pads is also indicated.

To align the electron and laser beams in the transverse plane, a fluorescent flag was lowered into the path of the beam and viewed remotely. By moving the IP box, which holds the focusing mirrors, it was possible to bring the electron beam and laser images into overlap. Final adjustment is made by monitoring the forward-photon rate

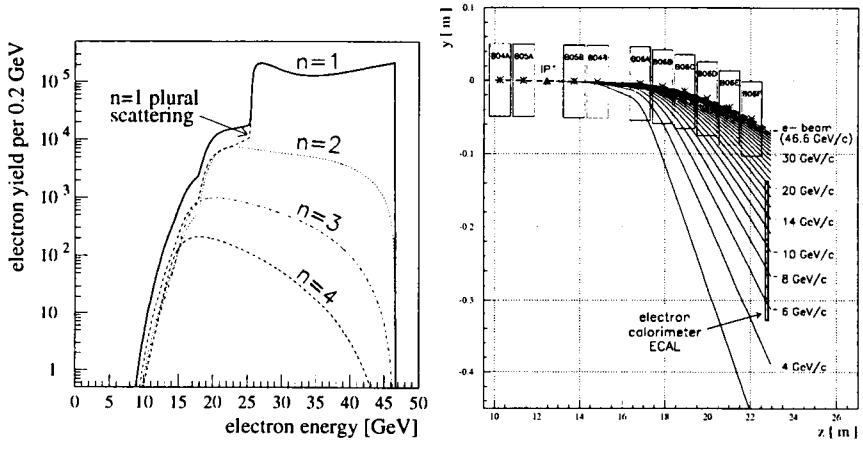

Figure 41: Left plot: recoil electron rates for linear, nonlinear and plural Compton scattering for standard laser and electron beam parameters. The solid line is the sum of all possible processes. The $n = 2$, $n = 3$ and $n = 4$ processes are shown separately as well. Right plot: calculated trajectories of electrons of different momenta through the magnetic spectrometer. W-Si electromagnetic calorimeter ECAL is shown.

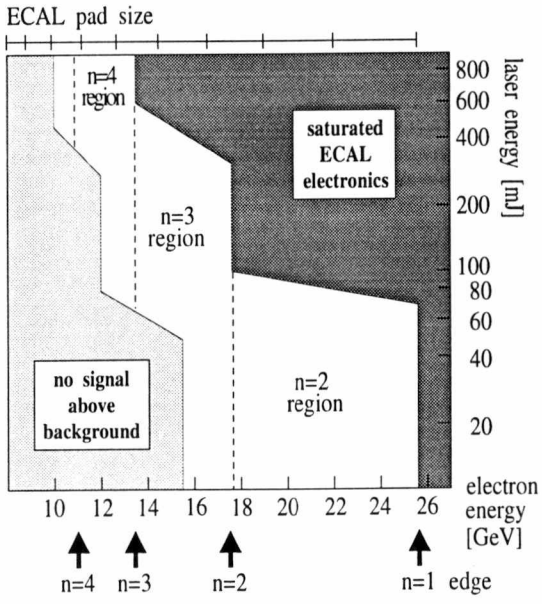

Figure 42: Data collection strategy.

as a function of transverse (x-y) position of the IP box. While the vertical overlap (y) was unambiguous, the overlap in the horizontal plane (x) depended on the relative timing of the two beams as indicated in Fig. 43(a). Thus it was necessary to carry out a scan in both the x-position of the IP box and in timing delay. This is shown in Fig. 43(b) where the linear Compton rate is plotted as a function of Δx and Δt. The correlation between the two offsets

$$\Delta x \left(\frac{1}{\sin \alpha} + \frac{1}{\tan \alpha} \right) = c \Delta t \tag{149}$$

is clearly evident. In Fig. 43(c) the nonlinear rate (specifically, $n = 2$) is plotted for the same scan. Here a large signal was obtained only when the electrons crossed through the laser beam in the focal region. By scanning both the position where the electrons intersect the laser path and the time at which the laser pulse crossed the focal waist, the XT scan identified the location where η was highest, which was an essential consideration for the experiment. The XT scan data were also used to separate unwanted backgrounds from linear ($n = 1$) processes from the desired $n > 1$ signal, based on their different shapes in the XT plane. Such XT scans were

performed frequently during the run to assure correct spatial and temporal overlap. Each XT scan was preceded by a Y scan to ensure that the electrons and photons were in the same plane, and a simple T scan to verify the scan range and $n = 1$ collision stability.

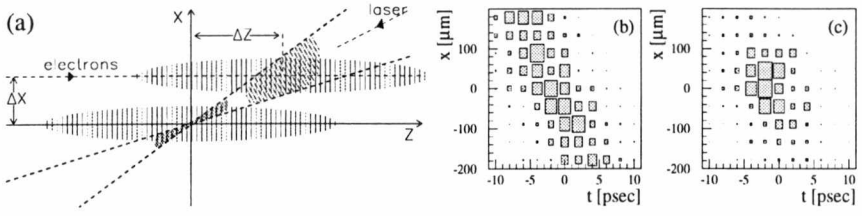

Figure 43: (a) The crossing of the laser pulse and electron beam in the X-T plane; two possible collisions are shown, each giving approximately the same linear Compton scattering rate but drastically different non-linear Compton rates. (b) Linear Compton event rate as a function of transverse beam displacement and relative timing. (c) As above but for nonlinear events.

7.5 Data analysis

The total energy in a calorimeter row is a measure of the number of electrons scattered into that particular momentum during the pulse. This yield was not constant over a run which consisted of ~1600 laser pulses and ~3200 laser off triggers. The total energy distribution is shown for a particular (IR) run in Fig. 44 for the top six rows of the calorimeter before any corrections are applied. The rapid variation of the signal with momentum is obvious, and in fact the total energy in the last two rows is compatible with zero signal. Only the first four rows for every calorimeter position have been included in the analysis. However for rows 2, 3, 4 one has to take care to correct for the feed-down contribution from the preceding row.

The spread in the energy recorded in a calorimeter row is due to several factors, the dominant one being variations in the overlap of the electron beam and laser pulse due to timing fluctuations from shot to shot. To first order these fluctuations are reflected in the number of forward photons N_γ; thus by normalizing every shot to N_γ a more stable distribution is obtained. Part of the spread is due to the distribution in

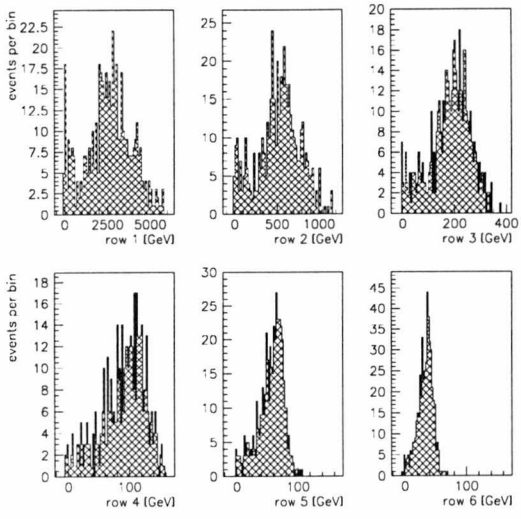

Figure 44: ECAL signal for IR laser of 400 mJ and with ECAL positioned to accept electrons with energies less than 15.5 GeV. The energy distribution obtained in the center pads for rows 1-6 is shown, with pedestals and electron-beam-only backgrounds subtracted, but without any other corrections.

laser intensity for different pulses. Only a small contribution comes from statistical fluctuations since there are usually 10-100 electrons incident per pulse on each tower.

The variation of the laser parameters over the entire data set is shown in Fig. 45 for the IR runs and in Fig. 46 for the green. While the laser energy was changed in discrete steps fluctuation about the mean amounted typically to $\pm 10\%$ so that the energy coverage was reasonably dense, and the data could be binned according to laser intensity.

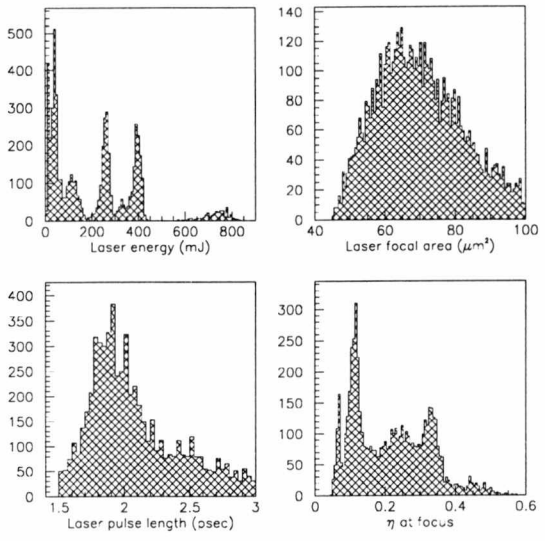

Figure 45: Laser parameters for all data taken with IR pulses.

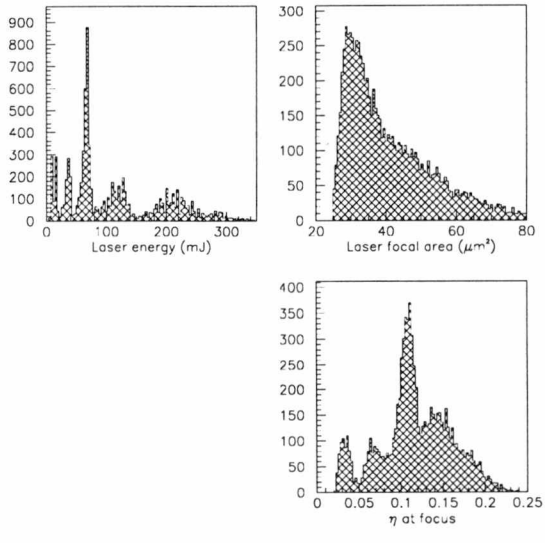

Figure 46: Laser parameters for all data taken with green pulses. Shot-by-shot measurement of pulse length was not available for the green data; a fixed estimate of 1.9 psec was used.

7.5.1 Electron calorimeter reconstruction

Two different methods were used to account for shower spreading in the ECAL and the "splash" background described previously, and both techniques gave equivalent results.

The first approach to reconstructing the ECAL signals was developed by the author and is describe in the previous section of this dissertation.

In the second approach, for each ECAL vertical position Y, a matrix $R_{ij}(Y)$ is calculated which is used to reconstruct signals of an ideal calorimeter with no shower spreading and no "splash" contamination

$$R_i = R_{ij} X_j \,, \tag{150}$$

where i labels the readout channels of the "ideal" (reconstructed) calorimeter, and j labels the readout channels of the physical calorimeter (ECAL).

The response of ECAL to an electron beam incident at a vertical position y is written as a vector $X_j(y)$. This response is known from calibration test beam data; the vector is normalized to have a sum of 1. The response of ECAL to background is written as a set of coefficients $V_j(Y)$, found from fitting the xt scans away from the nonlinear signal, and has units of "raw ECAL signal due to splash divided by the number of splash-causing Compton events". The readout of ECAL given an incident electron spectrum $f(y)$ and a splash due to N_S splash-causing Compton events is therefore given by

$$X_j(Y, N_S)[f] = N_S V_j(Y) + \int dy f(y) X_j(y) \,, \tag{151}$$

and the reconstructed signal is

$$R_i[f] = N_S R_{ij} V_j(Y) + \int dy f(y) R_{ij} X_j(y) \,, \tag{152}$$

where the sum over j is implied. Evidently, the response of reconstructed signal

i to the splash is given by $R_{ij}V_j$, while $R_{ij}X_j(y) \equiv g_i(y)$ gives the aperture function for the reconstructed signal. Ideally we optimize the coefficients R_{ij} such that, as nearly as possible, $g_i(y)$ is zero for y outside the desired aperture of channel i and is unity inside, and $R_{ij}V_j$ is zero regardless. In this way we do not need to assume a particular form for the incident electron spectrum $f(y)$.

Either reconstruction method improved the dynamic range of ECAL and made it possible to observe the kinematic edges of $n = 2$, $n = 3$ and $n = 4$ nonlinear Compton processes.

7.5.2 Cuts

Cuts were applied to eliminate events where the electron beam fluctuated in position, angle or intensity, or when there was poor overlap as determined by the ratio of the forward-photon monitor signal to the expected rate (at the particular value of laser parameters for that shot).

The total number of events before and after cuts for the IR and green are given below

	IR	Green
Events before cuts	18,344	16,322
Events after cuts	7,207	5,342

7.5.3 Binning and error analysis

From the reconstruction of the energy incident on a calorimeter tower we obtain dN/dp, the number of incident electrons per momentum interval. We then form the normalized yield

$$\frac{1}{N_\gamma}\frac{dN}{dp} \sim \frac{1}{\sigma_C}\left\langle \frac{d\sigma}{dp} \right\rangle \tag{153}$$

where N_γ is the number of high-energy photons emitted from IP1 and σ_C is the total single photon-scattering Compton cross section for the laser-electron interaction.

The quantity $\langle d\sigma/dp \rangle$ in the above equation is an ensemble average since the nonlinear differential cross section $d\sigma/dp$ depends on the laser intensity, whereas different electrons in the beam sample regions of different intensity. As shown in Fig. 43, single-photon scattering can occur over a larger fraction of the laser focus than the nonlinear scattering, so the normalized yield is also affected by the ratio of the focal volumes sampled by the different processes. These effects can be accounted for only by a detailed simulation of the experiment.

The scattered electron data points were binned according to laser intensity and electron momentum independently of the particular run, calorimeter position, or calorimeter row from which they were acquired.

The measurement error for each bin was obtained from the dispersion of the entries in the bin; reconstruction errors. Simulation errors were determined by propagating error estimates for laser and electron beam parameters through the event simulation code. When errors were combined, they were added in quadrature.

7.6 Simulation of the experiment

For a detailed simulation of strong field QED effects in electron-laser collisions two independent programs were used and good agreement was found. The processes considered in these simulations are linear and nonlinear Compton scattering and multi-photon Breit-Wheeler pair production in a circularly polarized laser field.

The first simulation tracks individual beam electrons sampled from the electron density in the beam bunch through the laser field. Based on calculated interaction probabilities and random numbers, the program decides at each step along the path whether an interaction occurred, in which case the resulting particles are then tracked from the interaction point on.

In a second approach, reaction rates and energy spectra of final particles are obtained by numerical integration of the differential cross sections over a space-time grid around the laser focus. This method has the advantage of being free from statistical

fluctuations and is used for comparison with experimental data.

The numerical integration accounts for the proper interaction geometry defined by the 17° crossing angle and possible spatial and temporal offsets between the electron bunch and the laser pulse.

Both beams are modeled as Gaussian density distributions in three dimensions. While for the electron bunch the sigmas of these distributions are assumed to be constant (cylindrical Gaussian beam), the simulation takes into account the laser focusing angle causing the distributions to narrow in the plane transverse to the direction of propagation as the pulse approaches the focus.

The small variation in the effective crossing angle between electrons and photons caused by the laser focusing angle is also accounted for by the simulation.

Furthermore, the attenuation of the electron density as the electrons enter the laser field is corrected for. The attenuation factor is calculated for each element of the grid by integration of the total scattering probability along the electron path in the laser field.

For each element of the grid, the program first calculates the interactions between the beam electrons and the laser photons, i.e., linear and nonlinear Compton scattering up to a given order n. As mentioned before, the particles emitted by these processes have a chance to interact again with the laser field, i.e., the electrons can undergo further Compton scatters. These secondary processes are calculated by stepping the volume element in the forward direction (neglecting small scattering angles of order $1/\gamma$) out of the laser field as times evolves. On each step along this path, the number spectra of electrons, positrons and emitted photons contained in the grid element are updated according to the interaction rates calculated for Compton scattering of electrons and positrons and pair production by photons. Once the element has left the laser field, these spectra are then added to the final collision spectra.

7.7 Results and comparison with theory

As already discussed, because of the continuous variation of the photon density across the laser focus and the nonlinear nature of the scattering, it is not possible, nor meaningful, to extract cross sections from the data. Instead the theoretical probability for nonlinear scattering of all orders is calculated for the experimental conditions to give the expected yield of recoil electrons

$$\frac{1}{N_\gamma}\frac{dN}{dp}$$

for a particular bin of laser intensity. This theoretical prediction is then compared directly to the experimental observations.

Figures 47 and 48 show the normalized differential yield for electrons scattered from the IR and green lasers, respectively, at six different laser intensities. The observed yield is shown as a function of momentum by the solid circles; the horizontal error bars give the width of the corresponding momentum bin and the vertical bars include systematic errors in reconstruction. The simulation is shown by the open boxes, where the laser and electron beam parameters for each shot have been used; the error bars reflect the variance of the mean expected due to fluctuations in these parameters. An overall systematic uncertainty of $\pm 30\%$ for the IR laser intensity and $+50/-30\%$ for the green laser intensity is not shown in this figure. In general each plot covers three orders of magnitude in yield. The $n = 2$ plateau and the kinematic edge (17.6 GeV for IR, 10.8 GeV for green) are clearly evident at lower laser intensities; in the green laser data, one can also recognize the $n = 3$ plateau which extends from 10.8 to 7.8 GeV.

The simulation results shown in Figs. 47 and 48 include the effects of shot-by-shot and day-by-day variations in experimental conditions such as electron and laser spot sizes, pulse lengths, and targeting error (beam overlap), as well as laser energy and recoil electron momentum.

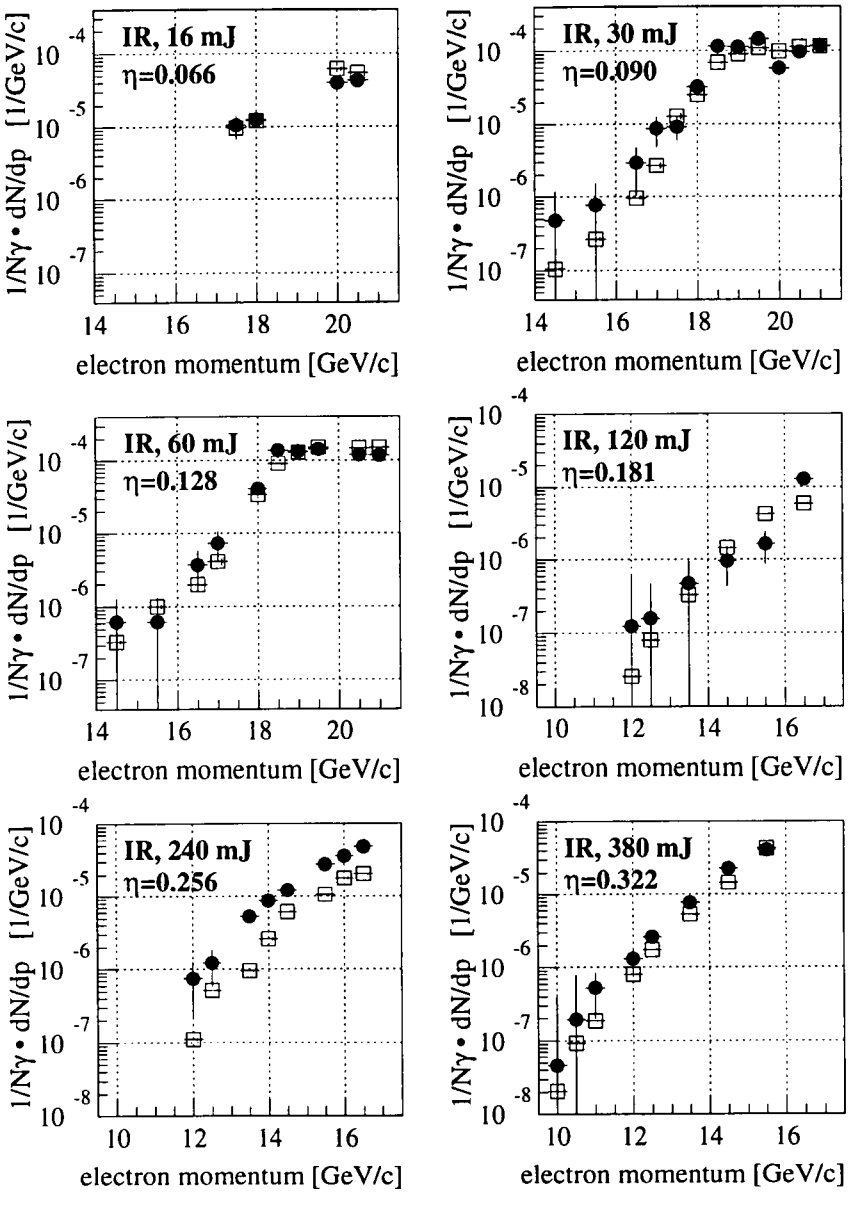

Figure 47: The normalized differential yield of nonlinearly scattered recoil electrons for six different IR laser energies. The data are the solid circles with vertical error bars corresponding to the statistical and reconstruction errors added in quadrature. The open boxes are the simulation where the vertical and horizontal heights are the magnitude of the error bars. An overall systematic uncertainty in the laser intensity of ±30% is not shown.

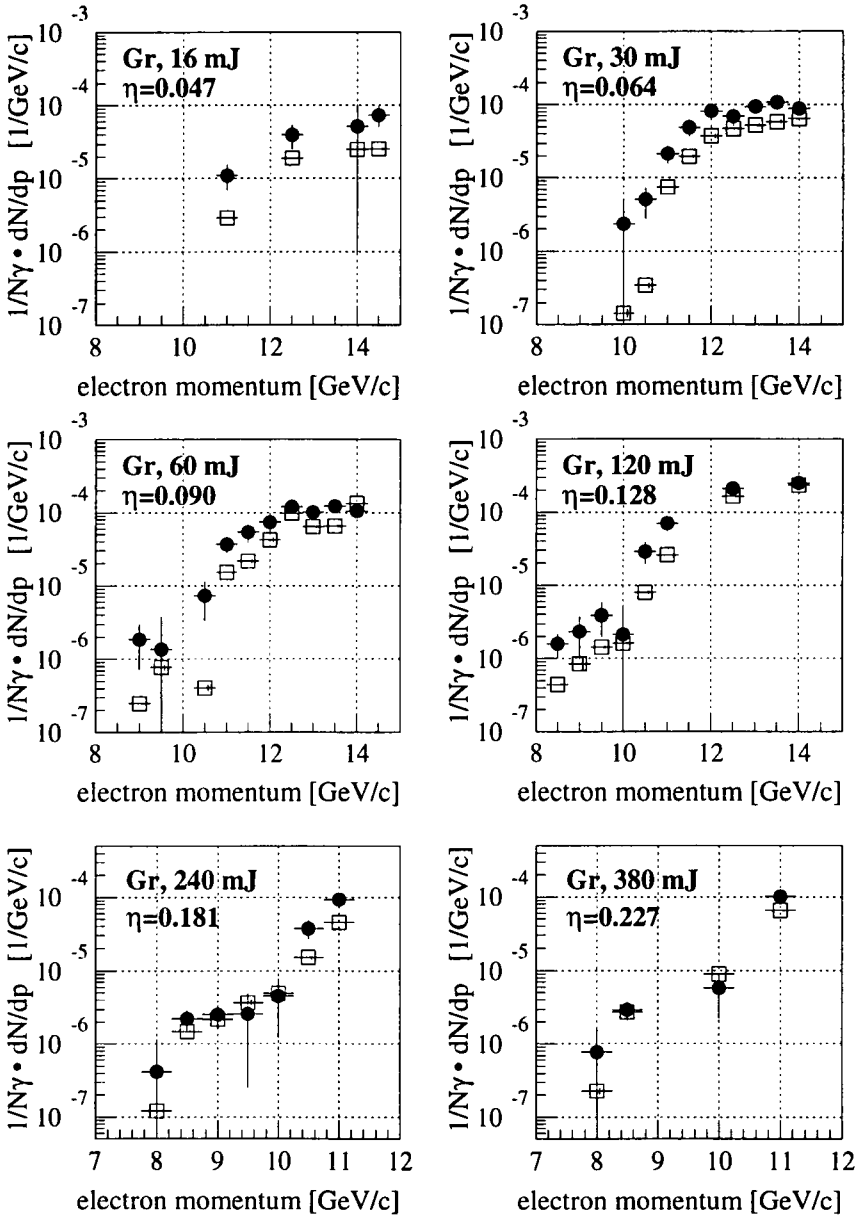

Figure 48: The normalized differential yield of nonlinearly scattered recoil electrons for six different green laser energies. The data are the solid circles with vertical error bars corresponding to the statistical and reconstruction errors added in quadrature. The open boxes are the simulation where the vertical and horizontal heights are the magnitude of the error bars. An overall systematic uncertainty in the laser intensity of $+50/-30\%$ is not shown.

To adopt a more uniform presentation, the data points can be scaled to be directly comparable with predictions using fixed parameters of laser focal volume and electron beam parameters. The numerical integration was used to produce lookup tables for scaling the data for each event to fixed parameters of 2 ps pulse-width, a focal area of 70 or 35 μm^2 (for IR or green laser, respectively), and 60 $\mu m \times 60\ \mu m \times 800\ \mu m$ electron beam size (standard deviation). The scaling factor applied was "simulated rate at standard conditions divided by simulated rate at observed conditions"; data scaled in this manner will agree with the simulation at the standard conditions if and only if the original data agreed with the simulation at the observed conditions.

The scaled data are presented in Figures 49 and 50 for IR and green respectively, for six different laser intensities. In these plots it is possible to show the expected rate as a continuous curve averaged over the discrete ECAL pads. The data are shown by the solid circles while the solid line is the simulation and includes both nonlinear Compton scattering and plural linear Compton scattering; the shaded band around the line represents the overall systematic uncertainty in the laser intensity. The dashed line is the result of the simulation when only linear Compton scattering, both single and plural, is included.

The good agreement between the simulation and the data confirms the contribution of the nonlinear Compton scattering process. In particular, the contribution of plural linear scattering is smaller than the observed scattering rates by as much as two orders of magnitude in certain cases, well outside the experimental errors, and therefore plural linear scattering alone cannot account for the observed effects. Although the estimated error bars on the data do not overlap the prediction, even after adjusting all laser intensity estimates by a constant factor, each individual data point does lie within 30% of the prediction after adjusting the laser intensity upwards by a factor of 1.15 for IR and 1.25 for green. Such an overall scale factor in intensity is well within our estimates for the overall systematic laser intensity measurement error.

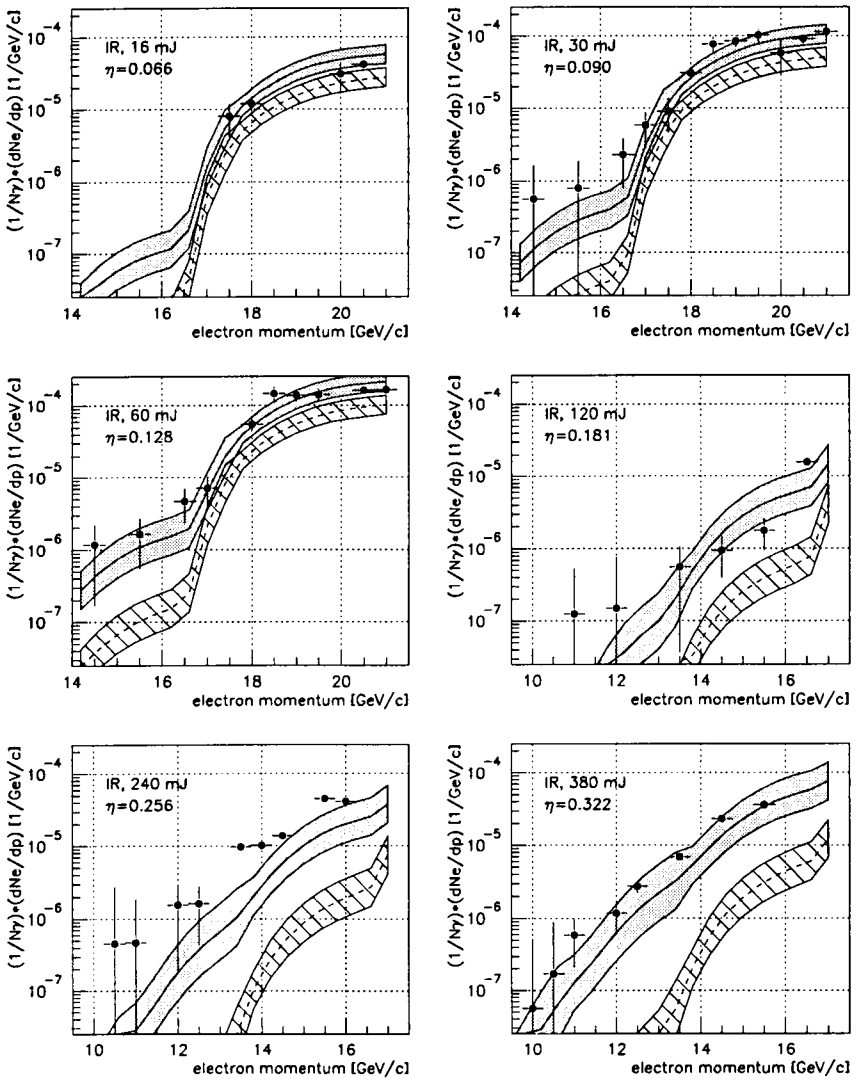

Figure 49: The scaled normalized differential yield of nonlinearly scattered recoil electrons for six different IR laser energies. The solid circles are the data. The solid line is the simulation that includes both nonlinear Compton scattering and plural Compton scattering, with a shaded band showing the ±30% uncertainty in the laser intensity. The dashed line is the simulation for plural linear Compton scattering only.

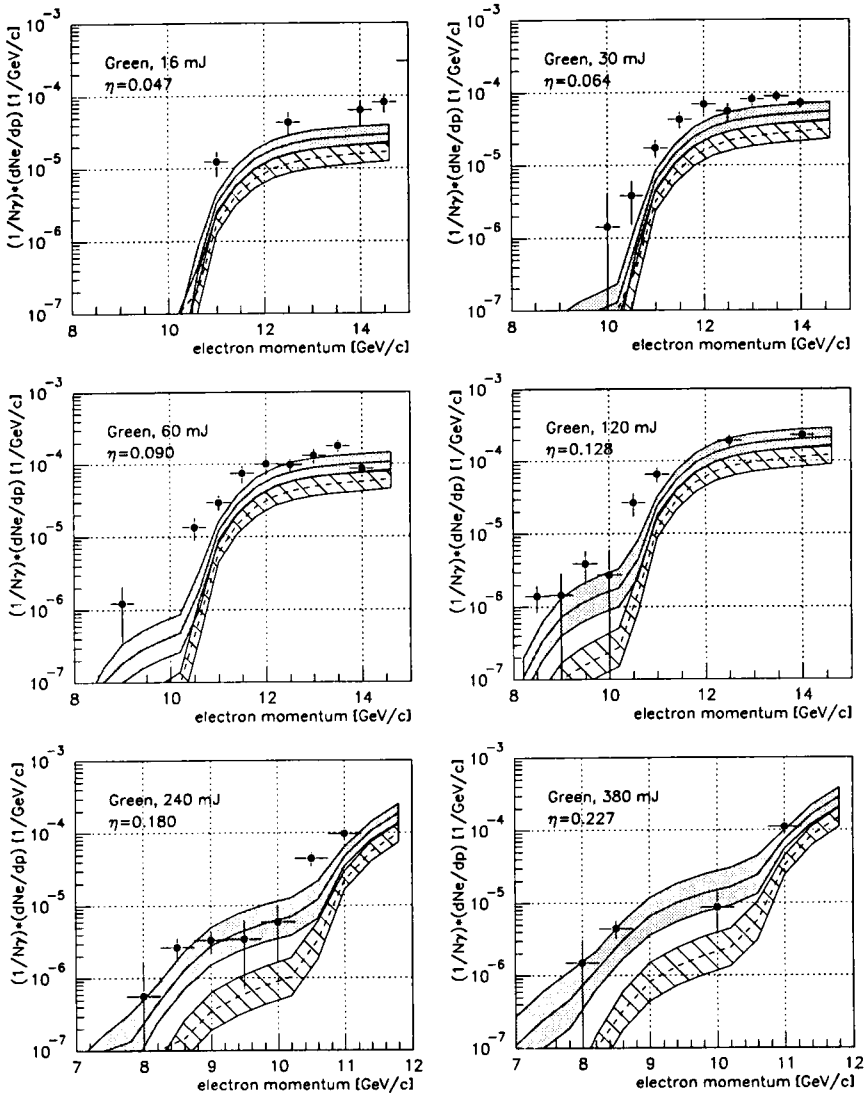

Figure 50: The scaled normalized differential yield of nonlinearly scattered recoil electrons for six different green laser energies. The solid circles are the data. The solid line is the simulation that includes both nonlinear Compton scattering and plural Compton scattering, with a shaded band showing the $+50/-30\%$ uncertainty in the laser intensity. The dashed line is the simulation for plural linear Compton scattering only.

To show the highly nonlinear behavior of the data as a function of laser intensity, it is instructive to present the data at fixed momentum as a function of laser intensity. We then expect the normalized rate to scale as

$$\frac{1}{N_\gamma}\frac{dN}{dp} \sim \eta^{2(n-1)} \sim I^{n-1}. \tag{154}$$

Data at fixed momentum within a small fixed momentum range ($\Delta p \simeq 0.5$ GeV) are plotted in Figs. 51 and 52 as a function of laser intensity for the IR and green; momenta corresponding to different numbers of absorbed photons have been selected.

In general the predicted behavior is obeyed by the data in spite of the extreme difference in the experimental conditions for different laser intensities. The shaded area indicates the range of scattering rates predicted by the simulation and represents the uncertainty in the laser parameters. The dependence on the power of the laser intensity is clearly evident, and the absolute rate is in agreement with the predictions as described above.

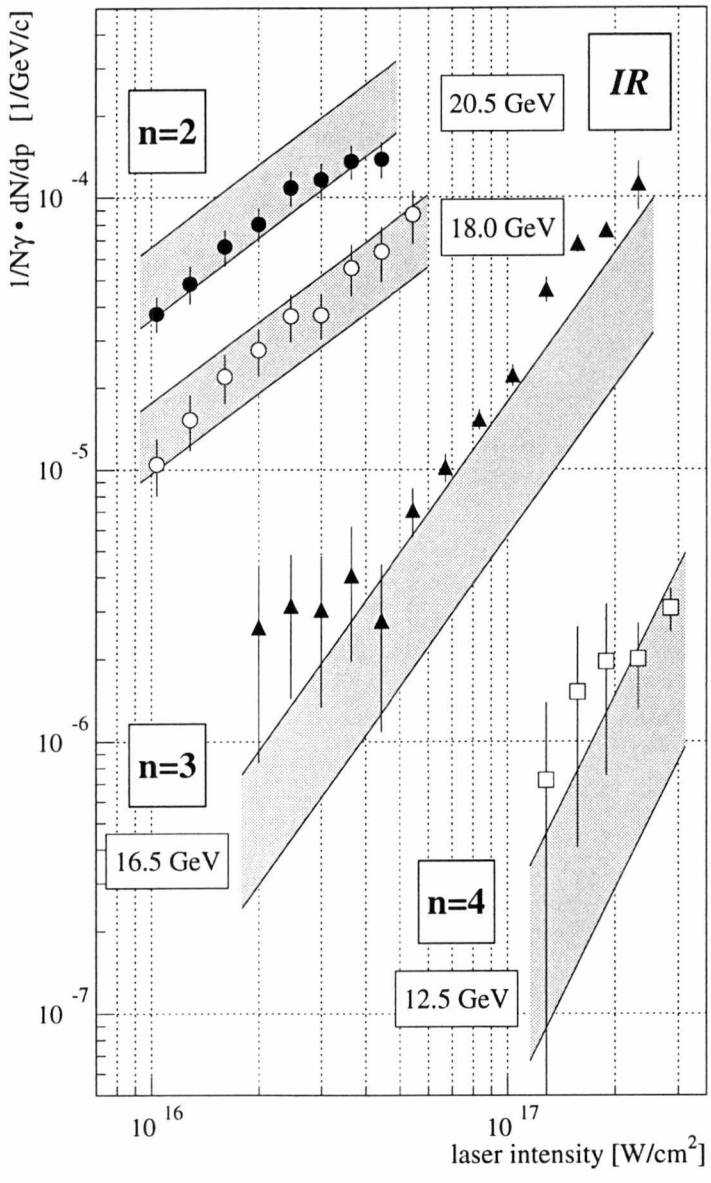

Figure 51: The scaled recoil electron yield versus IR laser intensity for 4 representative momenta. The solid and open circles are the data for the two photon absorption nonlinear Compton process. The triangles are the data for the $n = 3$ process and the open squares for the $n = 4$. The simulation for each process is shown as bands representing the 30% uncertainty in the laser intensity. The slopes of the bands are characteristic of the order of the nonlinear process.

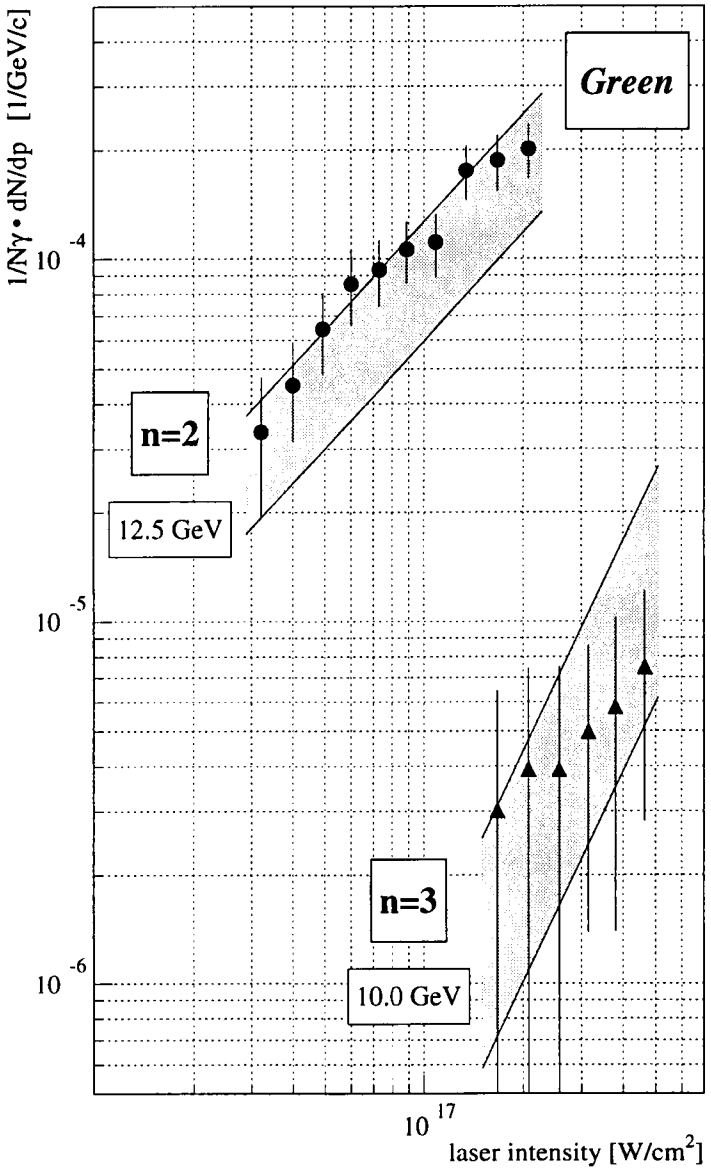

Figure 52: The scaled recoil electron yield versus green laser intensity for 2 representative momenta. The solid circles are the data for the two photon absorption nonlinear Compton process. The triangles are the data for the $n = 3$ process. The simulation for each process is shown as bands representing the $+50/-30$uncertainty in the laser intensity. The slopes of the bands are characteristic of the order of the nonlinear process.

8 Nonlinear Compton scattering of 46.6 GeV electrons by linearly polarized laser light

Nonlinear Compton data were taken In August 1996 with green linear polarized laser photons incident on the 46.6 GeV SLC electron beam.

The beam pipe on top of ECAL and vacuum chamber in front of ECAL were modified before the run in order to reduce backgrounds in ECAL. These modifications were modeled with GEANT v3.21 Monte Carlo and the following changes recommended by such optimization were made:

- Increase the vertical size of the beam pipe on top of ECAL from 4.5" to 8.0" in order to contain not only the original 46.6 GeV electron beam but also N=1 spectrum of scattered electrons. Electrons from interaction of 46.6 GeV electron beam with green laser involving only one laser photon (N=1 electrons) have much higher rate than electrons from the N=3/N=4 spectrum at laser intensities $\eta = 0.2 - 0.3$ explored by this measurement. N=1 electrons produce significant background to N=3/N=4 measurements when crossing the beam pipe at small angles. This effect was observed in previous runs with the IR laser where it significantly complicated measurements. After the increase of the diameter of the beam pipe from 4.5" to 8.0" part of the N=2 electron spectrum was also contained within the vacuum pipe making it impossible to do measurements in N=2 spectrum.

- The thickness of the beam pipe on top of ECAL was made as small as possible. Beam pipe thickness has been reduced to 1/16" along the line where N=2 electrons cross the beam pipe.

- Thickness of the vacuum chamber in front of ECAL was reduced to 1/8".

- The vacuum flanges behind ECAL were moved as far from ECAL as possible. The flanges are part of the vacuum transition region necessary to separate

electron and γ beams into separate lines after the electron beam is bent by the permanent magnets. They contain significant amount of materials (Fe) and albedo from N=1 electrons hitting these flanges (backsplash) creates backgrounds in ECAL. This effect was also observed in previous runs with the IR laser. Because the flanges were moved farther from ECAL, the albedo flux was reduced. In order to reduce it even more Pb absorbers (Pb-bricks) were placed between the vacuum flanges an ECAL below the path of N=1 electrons.

As a result of the above modifications backgrounds in ECAL were reduced by more than order of magnitude compared to the previous runs. Backgrounds represented only small fraction of the N=3,4 signal in ECAL and they were easily dealt with by reconstruction procedure described previously.

For the data analysis only those runs were used in which ECAL was positioned at different vertical positions with 8mm steps - called ECAL scans. Because each ECAL scan has 10-12 steps these scans permit measurements of part of the spectrum reachable only by N=3,4 electrons within a single run. Position of the edges of the electron momentum spectrum reachable by N=1,2,3,4,5,6 electrons are defined by the following equation:

$$p_{e^-}^{(min)} = E_e \frac{1+\eta^2}{1+N\,x+\eta^2}$$

where parameter $x = 1.641$ for Green laser with $\omega = 2.35$ eV crossing 46.6 GeV electron beam at 17°. Position of the edges for $\eta = 0.14$ and $\eta = 0.30$ are calculated in Table 6.

Measurements by the top row of ECAL (row 1) for step $i+2$ overlapped with the second row (row 2) for step i. This allows a cross-check of the measurements and verification of the reconstruction procedure for different rows.

Each row of ECAL is a separate detector that samples part of the electron spectrum; the signal is maximum in the top-most row of ECAL and minimum in the lowest row. Because of the dynamic range of the calorimeter $\approx 10^3$ only the four top

Table 6: Position of the kinematic edges for N=1,2,3,4,5,6 electrons calculated for two field intensities $\eta = 0.14$ and $\eta = 0.30$. This edges were calculated for 46.6 GeV electron beam and green laser 2.35 eV crossing the electron beam at 17°; corresponding parameter $x = 1.641$.

	$\eta = 0.14$	$\eta = 0.30$
N=1	17.86 GeV	18.60 GeV
N=2	11.05 GeV	11.62 GeV
N=3	8.00 GeV	8.45 GeV
N=4	6.27 GeV	6.64 GeV
N=5	5.15 GeV	5.46 GeV
N=6	4.37 GeV	4.64 GeV

rows measured significant signals; the typical ratio of the signals in rows 4 and 1 was 1:1000.

Reconstruction error was minimum for row 1. Signals in rows 2,3 and 4 have contribution from the leakage between rows and errors in signal reconstruction for these rows are significantly higher. In the final stage of the analysis only data from the row 1 of ECAL were analyzed and compared with simulations in the region of N=3,4 electrons because rows 2,3 and 4 repeated the same measurements with larger errors. Reconstruction of the low part of the spectrum for N=5,6 electrons that can be reached only by rows 3 and 4 was unreliable because of the low rate (less than 1 electron per electron-laser crossing) and comparably large backgrounds.

Laser energy was measured by the joule-meter in the laser diagnostic setup; laser focal area and pulse width measurements were unreliable. In order to reconstruct the laser intensity the nonlinear Compton rates from N=2 and N=3 electrons were measured by Cerenkov detectors installed in the path of the scattered electrons. These detectors measure the total particle flux (not the energy flux) of electrons at momentum gaps that correspond to N=2 and N=3 nonlinear processes. N=2 and N=3

Cerenkov counters intercept the same electron spectrum that is incident to the ECAL but counters are located in more energetic part of the spectrum. However contrary to ECAL, N=2 and N=3 counters do not provide reliable absolute measurements of the rate of electrons at fixed electron momenta. This is due to the uncertainty in the counter positions and their momentum calibration. Then their ratios were used to extract laser focus parameters (together with N=1 counter) as will be explained in the section on positron analysis. As a result of the constraining procedure described in the positron section, actual absolute signals in N=2,3 counters were different from ones predicted by simulations by large factors - up to 10. Hence these counters can not be considered as independent measurement of the electron spectrum in N=2,3 region. ECAL does provide such measurements in N=3,4 region. Even if these counters measured the rate of electrons correctly they would represent measurements of the electron spectrum only at two additional points while ECAL measures the entire nonlinear Compton spectrum reachable by N=3,N=4 electrons.

8.1 Event selection

Events were selected according to the following criteria:

- Electron beam cut. Electron beam parameters were required to be within $\pm 3\sigma$ of their normal values for each run. Parameters include electron beam positions x and y, angles x' and y', beam current, beam energy, accelerator beam phase, and the difference in accelerator current measured by two independent toroids. The last cut was necessary to check if the beam was partially lost or scattered in the FFTB between two measurements - an important precondition to eliminate background from electrons of the beam scattered in the beam pipe ahead of the detectors.

- Laser cut. Laser diagnostics show normal conditions with a measurement of the laser intensity available.

- Overlap cut (overlap between electron and laser beams due to timing). The ratio of the measured γ-flux to the simulated one without accounting for jitter was required to be more than 0.7, $\frac{N_\gamma^{(Meas)}}{N_\gamma^{(Sim)}} > 0.7$. The distribution of the above ratio for one run is shown in Fig. 53. The ratio represents effective overlap between electron and laser beams. It should be 1 if $N_\gamma^{(simulated)}$ were calculated correctly and there was perfect overlap between electron and laser beam (peak densities of both beam occur at the same time at the same point). The fact that peak value ($\approx$ 1.3 for the run presented in the example) is different from 1 is due to unknown error in electron beam parameters for each individual run. Only the average parameters of the electron beam were known and were used for calculation of $N_\gamma^{(simulated)}$. Overlap factor below 1 is due to the time jitter in electron-laser overlap that reduces the measured γ-flux $N_\gamma^{(measured)}$.

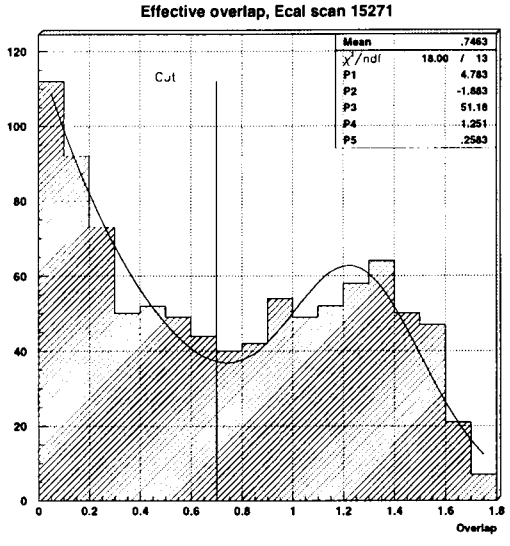

Figure 53: Ratio $\frac{N_\gamma^{(measured)}}{N_\gamma^{(simulated)}}$ for the ECAL scan 15271. Cut in overlap parameter 0.7 is also shown. Curve represents the fit of the data by exponent plus Gaussian distribution - two first parameters are for the exponent, the next three for the Gaussian fit.

- DAQ cut. No unusually long trigger delay between two readouts was observed. This condition helps avoid long pauses in DAQ readout due to the beam loss

that sometime confused the DAQ system. In addition, after beam loss, the accelerator starts a new cycle with an unstable electron beam that can produce unusually large backgrounds. The above condition ensures that data were taken in a normal way, as a continuous stream without interruptions.

- ECAL cut. Events were discarded if ECAL was saturated. Saturation in ECAL occurs if more than 10 TeV of energy is deposited in one row due to dynamic range of the electronics. Individual channels of ECAL (each row is sum of 6 channels) saturate at ≈ 6 TeV . The signal is considered to be dangerously high if more than 2 channels measure energy deposition above 3 TeV and such events were discarded.

8.2 Correction for the leakage in ECAL

Correction for the leakages due to the electromagnetic shower profile in ECAL was done according to procedure described in the preceding sections. Background subtraction was also done to take into account possible backgrounds from $N = 1$ electrons scattered in the same laser focus and rescattered into ECAL by different absorbers. We should note that due to improved beam pipe geometry, backgrounds in ECAL were negligible in $N = 3, 4$ regions. Example of the signal in the outer pads of ECAL compared to one in central pads is shown in Fig. 54 for two different laser intensities.

There is a unique correspondence between momentum of an electron originating in the laser focus and the vertical position of the ECAL row this electron is incident on. Electrons with higher momentum have higher vertical incident position, with lower momentum - lower vertical incident position. The data (ECAL rate) are normalized to the measured γ-flux N_γ according to the formula

$$\textbf{ECAL rate} = \frac{1}{N_\gamma}\frac{dN_e}{dp}.$$

Two sets of runs with different laser intensities are shown in Fig. 54: $\eta = 0.27$ and $\eta = 0.18$. Because both signal and background are normalized to the γ-flux the

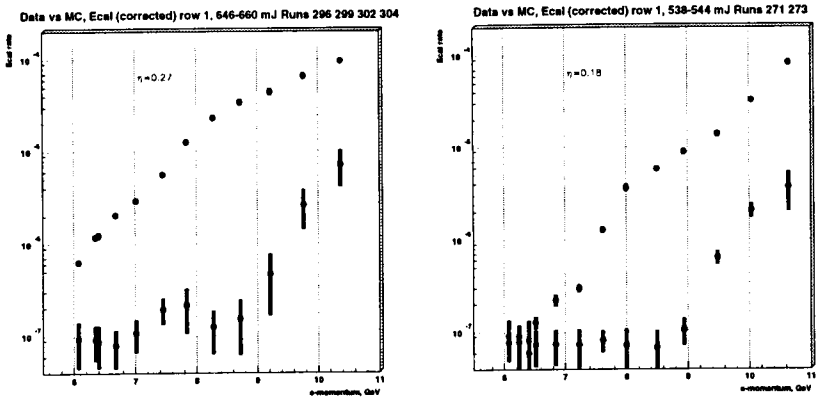

Figure 54: Reconstructed ECAL spectrum in central pads of ECAL (solid circles) and background in outer pads of ECAL (open circles with error bars) versus momentum of electrons originated in the laser focus and bended by the magnet. Plotted ECAL rate $\frac{1}{N_\gamma}\frac{dN_e}{dp}$ is the rate of electrons per unit momentum bin normalized by the measured γ flux N_γ. Two sets of runs with different laser intensities are shown: $\eta = 0.27$ (left plot) and $\eta = 0.18$ (right plot).

normalized background is almost the same for two laser conditions (backgrounds are proportional to $N = 1$ electron rate) though the signal changes by order of magnitude.

These plots show that normalized background decreases rapidly to the level of 10^{-7} electrons/1 GeV/1γ at $p_{e^-} \approx 9$ GeV and then does not change. Because the nonlinear Compton signal is rapidly decreasing with momentum to the same level, 10^{-7} for $p_{e^-} < 6$ GeV, it becomes smaller than the background. Measurements in the region $N = 5, 6$ ($p_{e^-} < 6$ GeV) were not included in the analysis because of the comparably large background in this region, and also because the electron rate drops below 1. For electron rates much smaller than 1 the average values of the energy deposition could not be calculated because the electronics noise and backgrounds errors are larger than the signal. Instead, electron cluster reconstruction procedures must be employed if possible for $N = 5, 6$ region of ECAL. Unfortunately cluster reconstruction in this region gives unreliable results because of the much higher electron flux incident at ECAL only a few centimeters away.

8.3 Weighting of different events in data samples

Data were grouped according to the laser intensity η and momentum of the electrons incident at the center of the ECAL rows.

Data were grouped in 9 intervals of laser intensity η with $\Delta\eta$ steps 0.02 from $\eta = 0.14$ to $\eta = 0.32$. These intervals allow η to vary ± 0.01 within each interval, while the error in η reconstruction was $0.012 \leq \sigma_\eta \leq 0.025$, with most probable $\sigma_\eta = 0.018$. Error in η reconstruction is the estimated difference between actual η_{act} and $\eta_{reconst}$ from the measurements in $N = 2, 3$ monitors. Hence the uncertainty in η within each bin is dominated by the reconstruction error and not by the bin size. Reconstructed error σ_η versus η is plotted in Fig. 55.

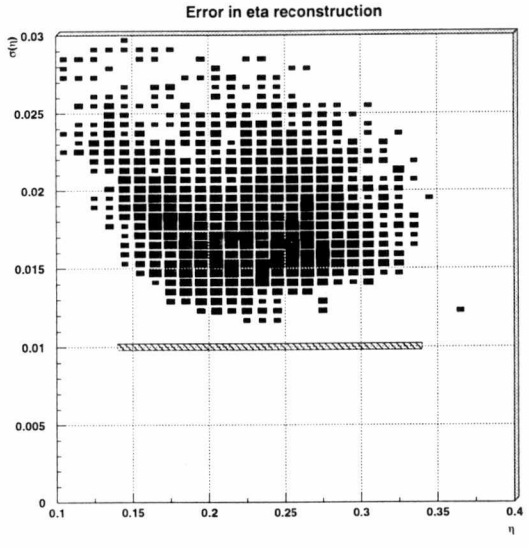

Figure 55: Error in η reconstruction for different η values is shown by boxes for different reconstructed events. Variation in η due to the final bin size 0.01 is smaller, it is shown for comparison as a line below the distribution.

Electron momentum bins were chosen in the range $p_{e^-} = 6 - 11$ GeV (N=4,3 range) with ± 0.2 GeV bin size around the central value. Data were taken at fixed ECAL positions that overlap for different ECAL scans, and most of the events within one bin have much smaller than ± 0.2 GeV variation around the central value of the bin momentum.

After selecting bins in η and electron momentum p_{e^-} events were plotted for each bin (η, p_{e^-}) (there were total ≈ 100 bins) and compared with simulated distributions. Signal distributions for $\eta = 0.19$ and different p_{e^-} bins are shown in Fig.56. Hatched histograms show measurements, not hatched - simulated events. The horizontal axis is the ECAL rate $\frac{1}{N_\gamma}\frac{dN_e}{dp}$. Measured and simulated events have similar distributions with essentially non-Gaussian shape. The average values and RMS of distributions are calculated to compare the measurements and the simulated distributions.

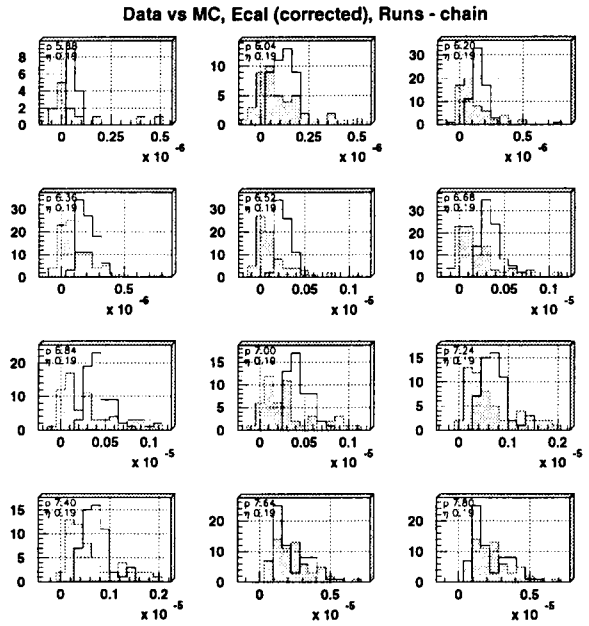

Figure 56: Measured (hatched histograms) and simulated (non-hatched histograms) distributions for $\eta = 0.19 \pm 0.01$ and p_{e^-}=5.88, 6.04, 6.20, 6.36, 6.52, 6.68, 6.84, 7.00, 7.24, 7.40, 7.64, 7.80 GeV. Horizontal axis is ECAL rate $\frac{1}{N_\gamma}\frac{dN_e}{dp}$. All ECAL scans data.

Average values are calculated according to

$$< S >= \frac{\sum_i w_i s_i}{\sum_i w_i},$$

where w_i - weights attributed for each event, s_i - measured signals.

For simulated distributions there are no statistical errors for the predicted ECAL rates if laser and electron beam parameters are known. Simulation results depend only on the laser and electron beam parameters. For finding the distribution average

and RMS, all simulated events within each bin (η, p_{e^-}) were weighted with equal weights, $w_i = 1$.

For measured distributions reconstruction procedures provide errors δs_i for the reconstructed signal in ECAL - those errors are dominated by the resolution of the calorimeter, leakages between rows and backgrounds. On the average the data have almost constant *relative* errors $(\frac{\delta s_i}{s_i} \approx Const)$ within a wide range of ECAL signals. But constant relative errors means that *absolute* errors are larger for larger ECAL signals. If measured distributions that have wide non-Gaussian shape were weighted with such errors $w_i = \frac{1}{\delta s_i{}^2}$ then the average would be much lower than one found for similar simulated spectra.

We illustrate that with the following example. Suppose ECAL measures two events: 1000 ± 100 GeV and 100 ± 10 GeV. Then the weighted with errors average will be $< S >= 110$ GeV while uniformly weighted average will be $< S >= 550$ GeV.

To compare measured and simulated distributions they should be weighted with the same weights. Below we provide arguments showing that for nonlinear Compton measurements events should be weighted with equal weights $(w_i = 1)$ to find a better estimate of the central value for each distribution.

Equal weights should be used for the data sample selected after cuts; these cuts should also include a cut on the error of the reconstructed signal to verify that the reconstruction procedure didn't fail.

If we assume that laser parameters such as η, focal area, focal width, and laser energy fluctuate around some central values, with Gaussian distributions, then nonlinear Compton processes which have strongly nonlinear dependence on the above parameters (η^6, η^8 for $N = 3, 4$) will have non-Gaussian distributions with most probable values shifted to the lower values. Examples of such distributions for $\sigma_{\eta^2} = 22\%$ variation of η^2 around its central value $\eta^2 = 0.1$ are shown in Fig. 55. $\eta^2 = 0.1 \pm 0.022$ corresponds to $\eta = 0.32 \pm 0.011$ which is even lower than error $\delta\eta = 0.18$ shown in Fig. 57. N=1,2,3,4,5,6 signals that correspond to $\eta^2 = 0.1$ were normalized to their

central values. The resulting distributions for N=3,4 signals in this example have distributions similar to the experimental data Fig. 56 with some events much higher than the central value 1.

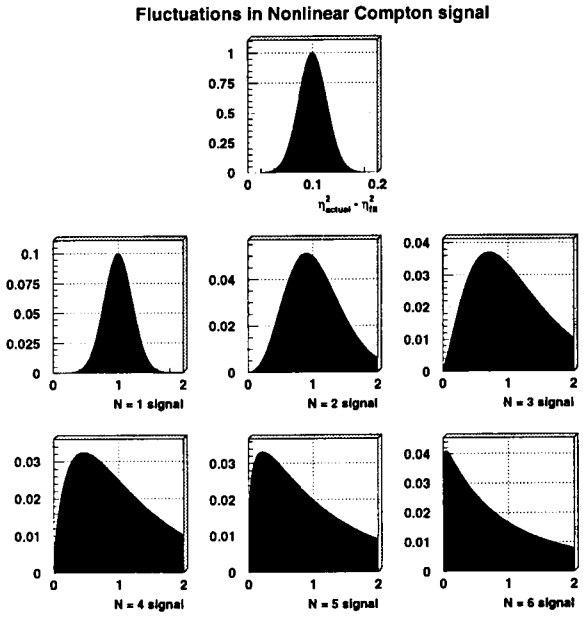

Figure 57: Plot on the top: assumed Gaussian fluctuation of the η^2_{actual} with $\sigma\eta^2_{actual} = 0.022$ around central value $\eta^2_{fit} = 0.1$. Six bottom plots: Simulated N=1,2,3,4,5,6 distributions that correspond to such fluctuations in η^2_{actual}. Signals are equal to 1 for $\eta^2_{actual} = 0.1$

As an example we weighted these distributions with equal weights $w_i = 1$ and with weights $w_i = \frac{1}{\delta s_i^2}$. The average values using two different weights are summarized in Table 7 (note that 1 corresponds to the $\eta^2 = 0.1$ in this example).

From this table one can see that average values for N=2,3,.. using equal weights are slightly biased to the higher values. For arbitrary $\delta\eta^2$ the average value will be biased to:

$$
\begin{aligned}
N &= 1 \qquad && < S >= 1\,, \\
N &= 2 \qquad && < S >= 1 + \left(\frac{\delta\eta^2}{\eta^2}\right)^2\,, \\
N &= 3 \qquad && < S >= 1 + 3\left(\frac{\delta\eta^2}{\eta^2}\right)^2\,,
\end{aligned}
$$

Table 7: Deviation of the average from the central value for N=1,2,3,4,5,6 distributions using equal weights (first column) and error-weighting (second column). Calculations are based on the assumption that η^2_{actual} fluctuates around central value $\eta^2_{reconstructed} = 0.1$ with $\delta(\eta^2) = 0.022$.

	equal weights $w_i = 1$	weights with errors $w_i = \frac{1}{\delta^2_{s,i}}$
N=1	1.00	0.89
N=2	1.04	0.62
N=3	1.14	0.32
N=4	1.29	0.12
N=5	1.50	0.035
N=6	1.80	0.010

$$N = 4 \qquad < S >= 1 + 6 \left(\frac{\delta\eta^2}{\eta^2} \right)^2 ..$$

Average values found with error-weighting are scaled by much more significant factors ≤ 0.1 from the expected value 1 and these factors strongly depend on the $\delta\eta^2$ values. One can expect that the average value found with error-weighting will give a very bad estimate. For equal-weighting the average value will be slightly higher than the central value by factor less than 2 and hence will give a good estimate of the central value (within this factor).

8.4 Nonlinear Compton rate versus electron momentum p_e- and laser intensity η

More than 5000 events from 16 ECAL runs were analyzed. The distribution of the laser intensity η and the distribution of the overlap parameter $\frac{N_\gamma^{(measured)}}{N_\gamma^{(simulated)}}$ for these runs are shown in Fig. 58.

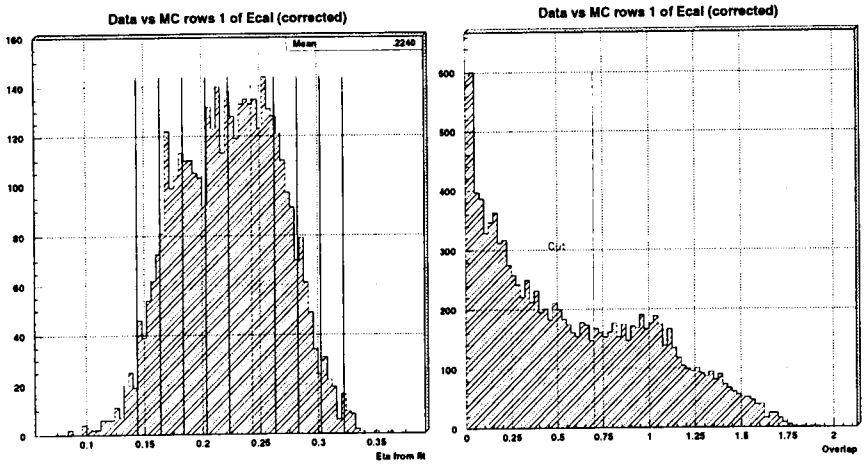

Figure 58: First plot: distribution of the laser intensity η with 9 bins selected. Second plot: distribution of the overlap parameter $\frac{N_\gamma^{(measured)}}{N_\gamma^{(simulated)}}$. Cut 0.7 is also shown as vertical line (only events above the cut were accepted for the analysis).

Data were selected using cuts as described earlier.

Data were combined in bins ($\eta \pm 0.01$, $p_{e^-} \pm 0.2$ GeV); only those bins that contain more that 5 events were analyzed and compared with simulations in order to avoid large error due to fluctuations in small data samples.

Equal weighting $w_i = 1$ was used for all events to find the distributions average and RMS. Errors were calculated as $\frac{\text{RMS}}{\sqrt{N}}$, where N is the number of events.

The number of electrons measured by the ECAL row, N_e, is normalized to the number of $N = 1$ photons, N_γ, and to the momentum acceptance of the row, Δp, which is shown in Fig. 59.

Measurements were compared with simulations for different η values versus electron momentum p_{e^-}. These are shown in Figs. 60 and Fig. 61. All plots have the same vertical range 10^{-8} to 10^{-3} /GeV, and the same horizontal range $p_{e^-} = 4 - 12$ GeV. Solid circles show measurements, open circles - simulation results.

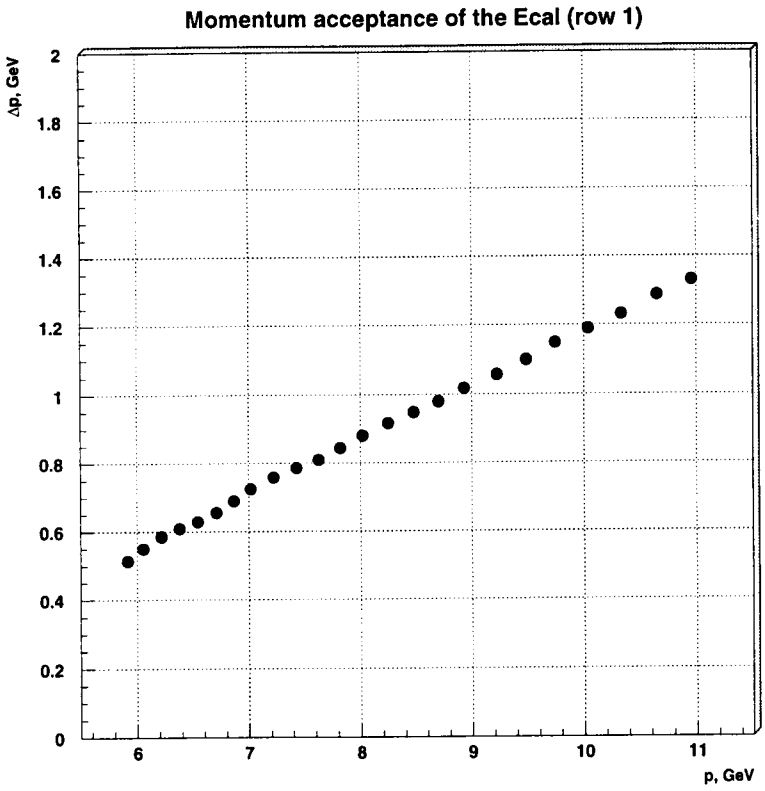

Figure 59: Momentum acceptance of the ECAL (GeV, row 1) versus the incident momentum (GeV). Smearing of the signal within each row acceptance is taking place - important effect in N=3,4 regions.

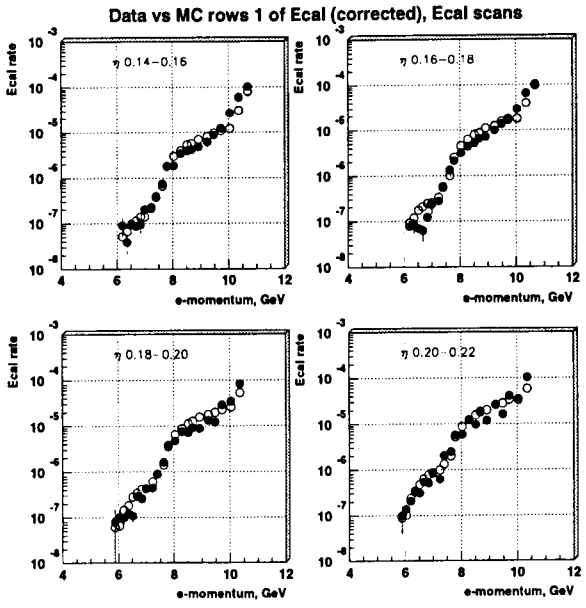

Figure 60: ECAL spectrums $\frac{1}{N_\gamma}\frac{dN_e}{dp}$ versus electron momentum p_{e^-} are plotted for 4 different η values in the range $\eta = 0.14 - 0.22$. Solid circles shows measurements, open circles - simulated results for the same laser parameters.

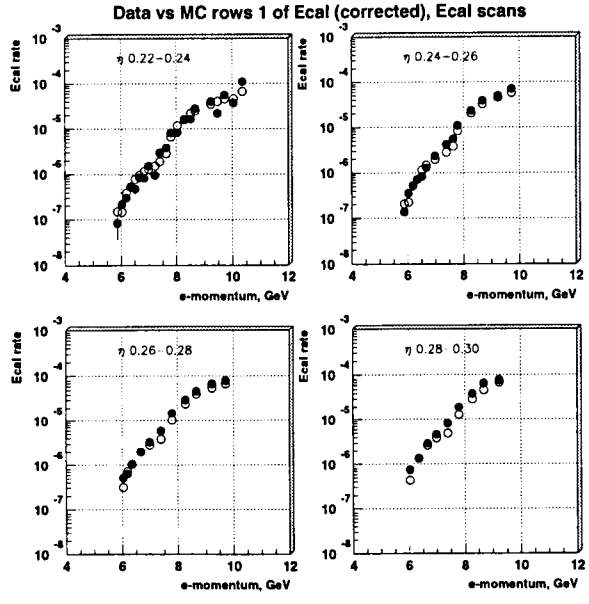

Figure 61: ECAL spectrums $\frac{1}{N_\gamma}\frac{dN_e}{dp}$ versus electron momentum p_{e^-} are plotted for 4 different η values in the range $\eta = 0.22 - 0.30$. Solid circles shows measurements, open circles - simulated results for the same laser parameters.

Measurements were also compared with simulations for different momentum bins p_{e^-} versus laser field intensity η. This is shown in Figs. Fig.62, Fig.63 and Fig.64. All plots have the same relative vertical range. Horizontal range $\eta = 0.14 - 0.40$. Solid circles show measurements, open circles - simulation results.

8.5 Discussion of results, comparison with simulation

Data presented above were compared with simulations for each bin η, p_{e^-}. Because within each bin laser parameters such as laser intensity η, laser area, and laser pulse width were distributed differently, simulation results do not correspond to a single continuous curve. No attempt has been made to scale laser parameters to the standard one in order to plot continuous distributions.

For the estimated error in the laser intensity, $\frac{\delta\eta^2}{\eta^2} \approx 22\%$, expected uncertainty in the simulated $N = 3, 4$ rates is of the order of 2. Measurements agree with simulations within this error for all data points.

Electron spectra for small laser intensities $\eta = 0.15 - 0.20$, shown in Fig. 60, have a distinct plateau in the region $p_{e^-} = 8 - 10$ GeV that corresponds to the N=3 electron region. They show transition to the N=4 electron region below 8 GeV and the N=4 region itself. Due to the acceptance of the ECAL row, $\Delta p_{e^-} = 0.5 - 1.4$ GeV, measurements always represent smearing of the actual electron spectrum over the momentum acceptance of the row (Fig. 59). Due to the smearing the N=4 plateau is not visible (compare Fig. 61) .

Dependence of the electron rates versus laser intensity η shows the expected power laws. Note that the η dependence in the Compton signal, normalized to the $N = 1$ rate, manifests nonlinearity of the process.

In the $N = 4$ region ($p_{e^-} = 6.0 - 6.7$ GeV) the ECAL rate follows the power law $\eta^{4.8-5.0}$ in agreement with simulations.

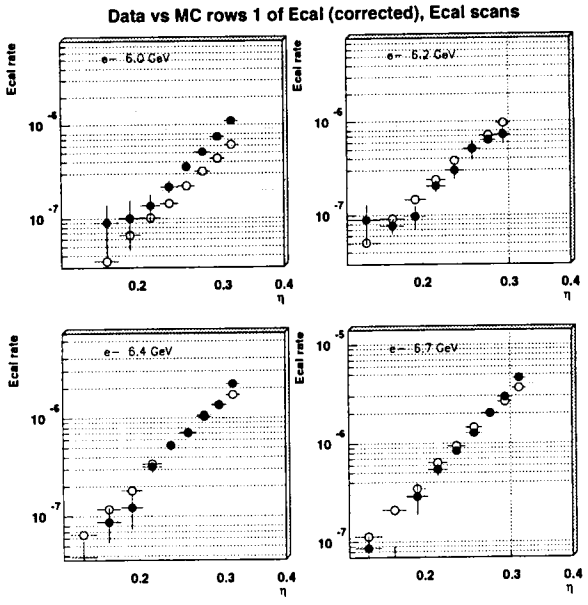

Figure 62: ECAL spectrums $\frac{1}{N_\gamma}\frac{dN_e}{dp}$ versus laser field intensity η are plotted for 4 different electron momentums p_{e^-} in the range $p_{e^-} = 6.0-6.7$ GeV. Solid circles shows measurements, open circles - simulated results for the same laser parameters.

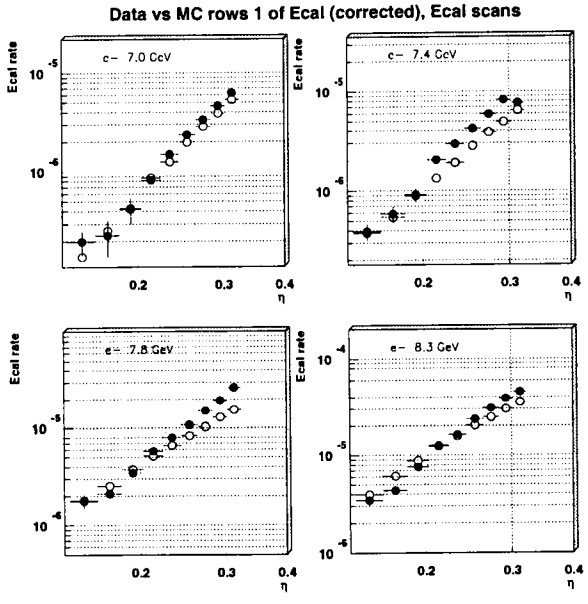

Figure 63: ECAL spectrums $\frac{1}{N_\gamma}\frac{dN_e}{dp}$ versus laser field intensity η are plotted for 4 different electron momentums p_{e^-} in the range $p_{e^-} = 7.0-8.3$ GeV. Solid circles shows measurements, open circles - simulated results for the same laser parameters.

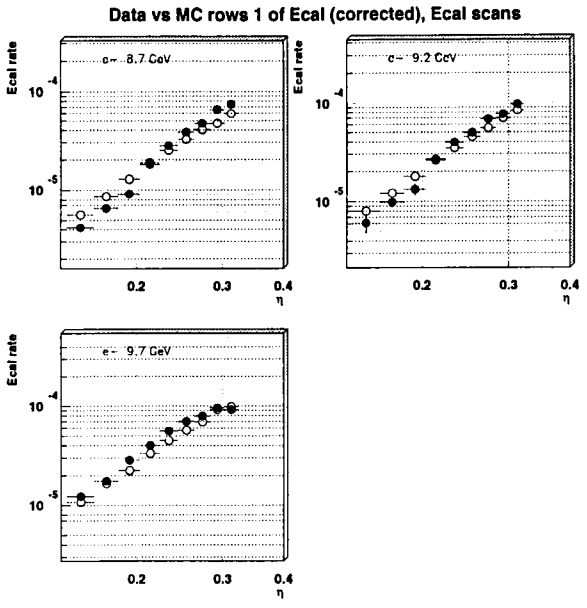

Figure 64: ECAL spectrums $\frac{1}{N_\gamma}\frac{dN_e}{dp}$ versus laser field intensity η are plotted for 3 different electron momentums p_{e^-} in the range $p_{e^-} = 8.7-9.7$ GeV. Solid circles shows measurements, open circles - simulated results for the same laser parameters.

The dependence of the ECAL rate versus η is not exactly η^6 in N=4 region (η^8 for N=4 "minus" η^2 for N=1, γ flux used for normalization) because the electron spectrum that corresponds to a fixed momentum range of the ECAL changes with field intensity η. ECAL measures different parts of the N=4 spectrum for different field intensities. This is a direct consequence of the "mass shift" effect discussed in previous sections.

In the $N = 3$ region (Figs. 63 and 64 $p_{e^-} = 8.3 - 9.7$ GeV) the ECAL rate follows the power law $\eta^{3.0-4.0}$ in agreement with simulations. It is again not exactly η^4 (η^6 for N=3 "minus" η^2 for N=1, γ flux used for normalization) because the electron spectrum that corresponds to a fixed momentum range of the ECAL changes with field intensity η.

9 Results on positron production

9.1 Experimental setup and calibration

We used the PCAL calorimeter to search for positrons produced at IP1. Figure 65 shows schematic layout of the experiment. Figure 66 shows trajectories of positrons and electrons of different momenta through the magnetic spectrometer. Because of the high flux of electrons in the ECAL calorimeter from Compton scattering it was not possible to identify the electron partners of the positrons.

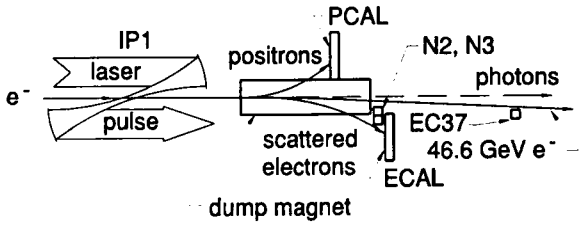

Figure 65: Schematic layout of the experiment.

We placed two Cerenkov counters refered to as N2 and N3 counters at the exit of the vacuum window of the spectrometer such that they intercept only trajectories of N=2 and N=3 electrons from Compton scattering (see Fig. 65 first plot). N2 counter intercepts N=3 trajectories as well but due to the lower rate of N=3 electrons this contribution can be corrected.

The response of PCAL to positrons originating at IP1 was studied by inserting a wire into the electron beam at IP1 to produce e^+e^- pairs by Bethe-Heitler conversion of bremsstrahlung photons. These data were used to develop an algorithm to group contiguous PCAL cells containing energy deposits into 'clusters' representing positron candidates. The clusters were characterized by their positions in the horizontal ($X_{\rm pos}$) and vertical ($Y_{\rm pos}$) direction and by their total energy deposit $E_{\rm clu}$. Using the field maps of the magnets downstream of IP1, the vertical impact position was translated into the corresponding momentum $P_{\rm clu}$. Figure 67 shows the density of clusters produced by the wire in the two planes $E_{\rm clu}/P_{\rm clu}$ *vs.* $Y_{\rm pos}$ and $Y_{\rm pos}$ *vs.* $X_{\rm pos}$. Only

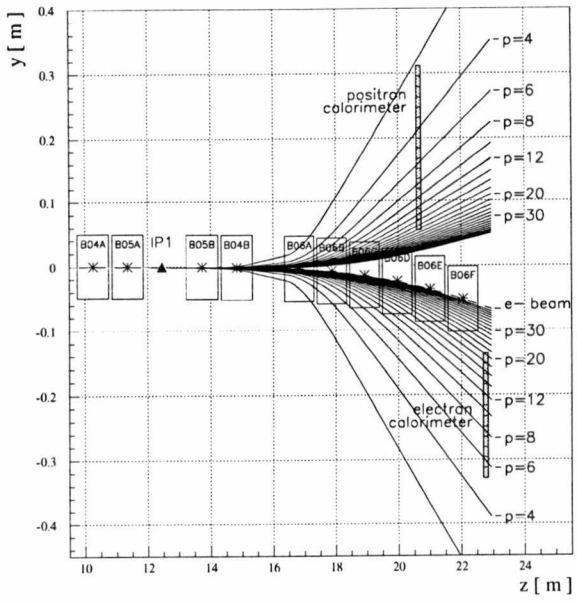

Figure 66: Calculated trajectories of positrons and electrons of different momenta through the magnetic spectrometer.

clusters within the signal regions bounded by solid lines in Fig. 67 were counted as positron candidates. The efficiency of the cluster-finding algorithm is estimated to be $93 \pm 1\%$.

9.2 Data analysis

We collected data at various laser intensities. The data from collisions with poor e-laser beam overlap were discarded when the signal in the EC37 monitor was less than 1/3 of the expected value. The number of positron candidates observed in the remaining 21,962 laser shots is 175 ± 13 and is shown as the upper distribution in Fig. 68(a) as a function of cluster momentum.

Positrons were also produced in showers of lost electrons upstream of the e-laser interaction point. The rate of these background positrons was studied in 121,216 electron-beam pulses when the laser was off, yielding a total of 379 ± 19 positron candidates. Figure 68(a) shows the momentum spectrum of these candidates as the hatched distribution, which has been scaled by 0.181, this being the ratio of the

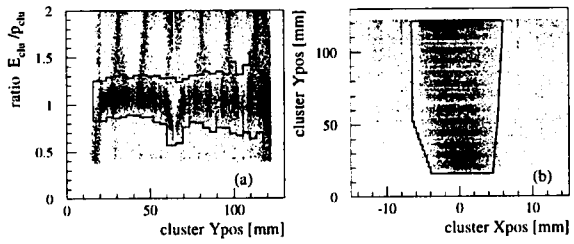

Figure 67: Cluster densities from positrons produced by a wire inserted at IP1. The solid line shows the signal region for positron candidates. (a) Ratio of cluster energy to momentum *vs.* vertical impact position above the lower edge of PCAL. The low ratios at the center of PCAL are caused by a 1.5-mm-wide inactive gap. (b) Cluster position in PCAL.

number of laser-on to laser-off pulses. After subtracting the laser-off distribution from the laser-on distribution we obtain the signal spectrum shown in Fig. 68(b) whose integral is 106 ± 14 positrons.

We have modeled the pair production as the two-step process of reaction

$$e^- + n\omega \rightarrow e^{-\prime} + \gamma\,,$$

followed by an electron positron pair production by a collision between high energy real photon and several laser photons

$$\gamma + n\omega \rightarrow e^+ + e^-\,,$$

where ω represents a photon from the strong electromagnetic wave, n indicates number of such photons absorbed, and γ represents an emitted photon which is not coherent with the incident strong electromagnetic wave.

By numerical integration over space and time in the e-laser interaction region we account for both the production of the high-energy photon (through a single or multiphoton interaction) and its subsequent multiphoton interaction within the same laser focus to produce the pair. Further Compton scattering of the positron (or electron) are also taken into account. The positron spectrum predicted by this calculation is shown as the curve in Fig. 68(b) and is in reasonable agreement with the data.

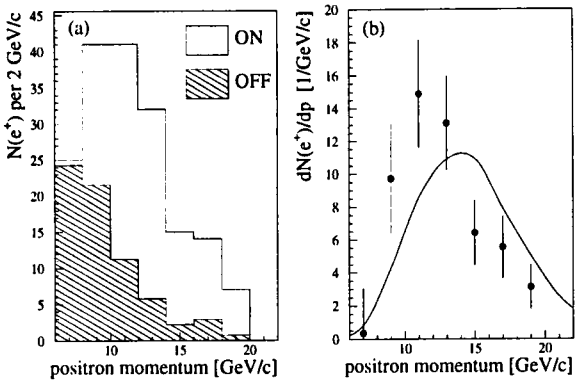

Figure 68: (a) Number of positron candidates *vs.* momentum for laser-on pulses and for laser-off pulses scaled to the number of laser-on pulses. (b) Spectrum of signal positrons obtained by subtracting the laser-off from the laser-on distribution. The curve shows the expected momentum spectrum from the model calculation.

Description of the numerical integration program is presented in [23].

To determine the effective intensity of each laser shot, *i.e.*, the peak intensity of the part of the laser beam that overlapped with the electron beam, we made use of N_1, N_2 and N_3, the numbers of electrons intercepted by the gas Čerenkov counters EC37, N2 and N3, of first-, second- and third-order Compton scattering, respectively. Ideally, the field intensity could be extracted from each of these monitors. However, because of e-laser timing jitter the effective intensity has been extracted from ratios of the monitor rates. For $\eta^2 \ll 1$, the field intensity is approximately given by $\eta^2 = k_1 N_2/N_1$ as well as $\eta^2 = k_2 N_3/N_2$.

The parameters k_1 and k_2 depend on the acceptance and efficiency of the counters as well as the spectrum of scattered electrons and were calculated over the relevant range of η^2 in the numerical simulation. We fit the observed N_i for each event to ideal values subject to the constraint $N_2^2 = (k_2/k_1)N_1 N_3$. Then the fitted N_i determined η with an average precision of 11%. Uncertainties in the acceptance, background levels, calibration and efficiency of the monitors caused a systematic error of $^{+8}_{-13}$% to the absolute value of η.

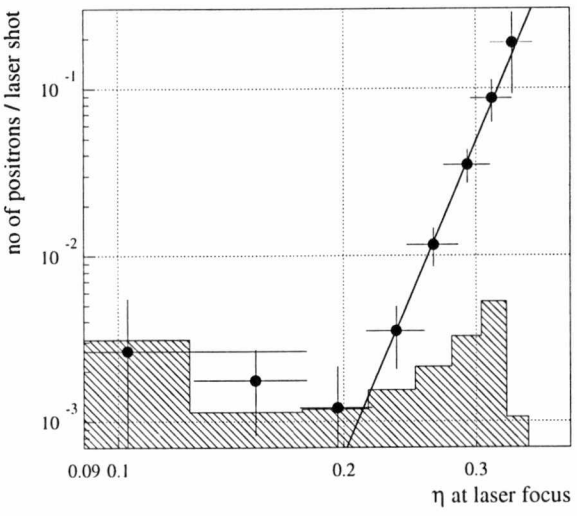

Figure 69: Dependence of the positron rate per laser shot on the laser field-strength parameter η. The line shows a power law fit to the data. The shaded distribution is the 95% confidence limit on the residual background from showers of lost beam particles after subtracting the laser-off positron rate.

9.3 Results

Fig. 69 shows the yield (R_{e^+}) of positrons/laser shot as a function of η. The line is a power law fit to the data and gives $R_{e^+} \propto \eta^{2n}$ with $n = 5.1 \pm 0.2\,(\text{stat.})\,^{+0.5}_{-0.8}\,(\text{syst.})$, where the statistical error is from the fit and the systematic error includes the effects discussed previously as well as the effect of the choice of bin size in η. Thus, the observed positron production rate is highly nonlinear, varying as the 5th power of the laser intensity. This is in good agreement with the fact that the rate of multiphoton reactions involving n laser photons is proportional to η^{2n} (for $\eta^2 \ll 1$), and with the kinematic requirement that 5 photons are needed to produce a pair near threshold. The detailed simulation indicates that on average 1.5 photons are absorbed from the laser field in reaction (1) and 4.7 in (2), but that the exponent n for the two-step process varies slightly with η and has an average value of 5.3.

Several points at low values of η seen in Fig. (69) indicate a possible residual background of about 2×10^{-3} positrons/laser shot due to showers of lost beam electrons.

The observed positron rate is shown in Fig. 70 after being normalized to the

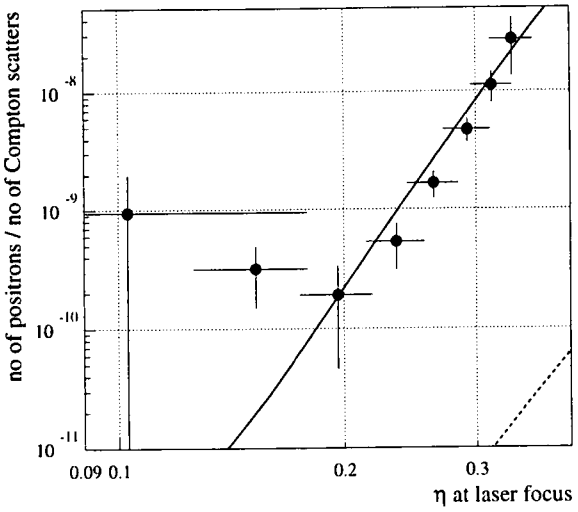

Figure 70: Dependence of the positron rate on the laser field-strength parameter η when the rate is normalized to the number of Compton scatters inferred from the EC37 monitor. The solid line is the prediction based on the numerical integration of the two-step Breit-Wheeler process. The dashed line represents the simulation for the one-step trident process with an intermediate virtual photon.

number of Compton scatters, where the latter is inferred from the measured rate in the EC37 monitor. This procedure minimizes the effect of the uncertainty in the laser focal volume and in the e-laser overlap. The simulation indicates that the variation of the positron rate over a spatial offset of ± 25 μm or a temporal offset of ± 5 ps between the electron and laser beams is 0.88 ± 0.07 of the variation in the Compton scattering rate. The solid curve in Fig. 70 shows the prediction based on the numerical integration of the two-step Breit-Wheeler process, (1) followed by (2), multiplied by the cluster-finding efficiency (0.93) and the overlap correction factor (0.88). The data are in good agreement with the simulation, both in magnitude of the observed rate and in its dependence on η.

Although we have demonstrated a signal of positron production associated with scattering of laser light we cannot immediately distinguish positrons from reaction (2) from those originating in the trident process. The trident process is a second-order process

$$e^- + n\omega \rightarrow e^- + e^- + e^+ . \qquad (155)$$

A complete theory of multiphoton trident production does not exist at present so we performed a simulation based on a two-step model in which the beam electron emits a virtual photon according to the Weizsäcker-Williams approximation and the virtual photon combines with laser photons to yield electron-positron pairs according to the theory of the multiphoton Breit-Wheeler process. The results of this simulation indicate that for the present experiment the trident process is negligible, as shown in Fig. 70 by the dashed line.

These results confirm the validity of the formalism of strong-field QED and show that the observed rates for the multiphoton reactions (1) and (2) are in agreement with the predicted values. Furthermore, in a semiclassical view these results are the first demonstration of breakdown of the vacuum by the combination of an intense and a weak electromagnetic wave, and in the quantum view they are the first observation of inelastic photon-photon scattering with real photons.

10 Conclusion

While the Quantum Electrodynamics (QED) has been tested extensively in a weak-field regime over the past few decades it has not up to present been tested in strong fields $\mathcal{E}_{\rm lab} \approx 10^{11}$ V/cm. Though experiments to study strong field QED have been discussed since the 1960-s the required field intensities became available only with the development of new laser techniques in recent years such as high intensity short pulse laser systems with high repetition rates base on the chirped-pulse amplification concept. The laser pulse duration in such systems is of the order of 1 ps, total power ≈ 1 J, and repetition rate ≈ 1 Hz. These parameters allow one to reach field intensities $\mathcal{E}_{\rm lab} \approx 10^{11}$ V/cm at the laser focus. At such field intensities multiphoton effects are dominant in the interaction of electrons with the field, and processes are strongly nonlinear with field intensity.

In order to reach the Quantum Electrodynamics Critical Field $\mathcal{E}_{\rm crit} \approx 1.3 \times 10^{16}$ V/cm a high energy electron beam is required. In the electron rest frame the $\mathcal{E}_{\rm lab} \approx 10^{11}$ V/cm field is boosted by the relativistic 2γ factor to a field strength $\mathcal{E}^* = 2\gamma\,\mathcal{E}_{\rm lab} \approx \mathcal{E}_{\rm crit}$. Relativistic electrons with energy $10 - 50$ GeV produced at the modern high energy colliders are required. At the Critical Field the quantum effects of the spontaneous vacuum break-down play an important role resulting in multiple e^+e^- pair production.

Strong field QED effects are important for understanding of fundamental principles of physics such as vacuum polarization and break down of the vacuum in strong fields. Strong field QED effects have many practical applications, and are important for the design of future linear electron-positron colliders. Below we summarize both fundamental research topics and practical applications based on the understanding of strong field QED:

- Study of QED at super-critical fields $\eta \gg 1$, $\Upsilon \gg 1$. Effects of the strong vacuum polarization and break-down of the vacuum by an electromagnetic field.

- Study of possible bound e^+e^- states (positronium) created in a strong field. Some authors have speculated that at high field QED undergoes a phase transition to a confining state, which would have bound e^+e^- states [58]. If such states exist then the measurement of the mass spectrum of e^+e^- pairs will reveal resonance peaks similar to those in atomic systems. e^+e^- bound states in a strong QED field have not been observed in experiments.

- Application for a low emittance positron source. Positrons which are produced in the interaction of laser light with high energy photons have a small transverse momentum $p_\perp/p \sim m_e/E_\gamma \approx 10^{-5}$ for $E_\gamma \sim 10$ GeV. This is contrary to the conventional positron source where positrons are produced in the interaction of electrons with bulk of matter, and transverse positron momentum is large due in part to multiple Coulomb scattering in the target. If a laser is used to generate the positrons then their emittance will be little greater than that of the initial electrons and there is no effect of multiple Coulomb scattering here. That eliminates the need for expensive positron damping rings. High energy photons could be produced either by electrons in a thin foil or by backscattering of laser photons from electrons as it is in the E144 experiment. Optimization of the configuration can be made based on E144 experience.

- The electron beam disruption effects in critical electromagnetic field. These effects could have a major impact on the performance of future linear e^+e^- colliders.

- Possibility of laser acceleration of electrons and positrons based on nonlinear QED effects. The principles of such acceleration are not clear at this time though experimental results on electron acceleration from rest to the energy 0.9 MeV by a high-intensity laser have been reported recently [59]. In a weak field regime electron acceleration in vacuum contradicts the Lawson-Woodward theorem [60].

- Effects of strong QED effects in laser-driven wakefield acceleration of electrons in plasma.

In this experiment we have demonstrated for the first time that inelastic light-by-light scattering is possible involving only real photons. A signal of 104 ± 14 positrons above background has been observed. Result are in agreement with theoretical calculations. We also observed multiphoton Compton scattering in which up to 4 laser photons interact with an electron. These results are also in agreement with theoretical calculations.

New methods for modeling the processes of electron-laser beam interactions have been developed. These methods will allow one to design and optimize the electron laser interaction region for future nonlinear QED experiments and will have applications for future linear colliders.

The theoretical understanding of nonlinear QED processes involving polarized particles has been greatly improved as well.

REFERENCES

References

[1] V. Balakin et al., Phys. Rev. Lett. **74**, 2479 (1995).

[2] C.D. Anderson, Science **76**, 238 (1932); Phys. Rev. **43**, 491 (1933).

[3] H.A. Bethe and W. Heitler, Proc. Roy. Soc. **A146**, 83 (1934).

[4] G. Breit and J.A. Wheeler, Collision of Two Light Quanta, Phys. Rev. **46**, 1087 (1934).

[5] O.C. De Jager *et al.* , *Estimate of the Intergalactic Infrared Radiation Field from γ-Ray Observations of the Galaxy Mrk421*, Nature **369**, 294 (1994).

[6] H.R. Reiss, *Absorption of Light by Light*, J. Math. Phys. **3**, 59 (1962). Production of Electron Pairs from a Zero-Mass State, Phys. Rev. Lett. **26**, 1072-1075 (1971).

[7] A.I. Nikishov and V.I. Ritus, Quantum Processes in the Field of a Plane electromagnetic Wave and in a Constant Field, Soviet Physics JETP **19**, 529 (1964).

[8] A.I. Nikishov and V.I. Ritus, Nonlinear Effects in Compton Scattering and Pair Production Owing to Absorption of Several Photons, Soviet Physics JETP **20**, 757 (1965).

[9] N.B. Narozhnyi, A.I. Nikishov and V.I. Ritus, Quantum Processes in the Field of a Circularly Polarized Electromagnetic Wave, Soviet Physics JETP **20**, 622 (1965).

[10] C.I. Moore, J.P. Knauer, and D.D. Meyerhofer, Phys. Rev. Lett. **74**, 2439 (1995).

[11] R.H. Milburn, Electron Scattering by an Intense Polarized Photon Field, Phys. Rev. Lett. **10**, 75 (1963).

[12] D. Strickland and G. Mourou, Compression of Amplified-Chirped Optical Pulses, Opt. Comm. **55**, 447 (1985); G. Mourou *et al.*, How Pulse Compression Techniques Can Be Applied to High-Energy Laser Amplifiers, Laser Focus, p. 104 (June, 1986); M. Pessot, P. Maine and G. Mourou, Opt. Comm. **62**, 419 (1987).

[13] F. Sauter, Z. Phys. **69**, 742 (1931).

[14] W. Heisenberg and H. Euler, Z. Phys. **98**, 718 (1936).

[15] W. Greiner and J. Reinhardt, Quantum Electrodynamics, Berlin, Springer, 1992, p. 285.

[16] I.F. Ginzburg *et al.* , Nucl. Instr. and Meth. **355**, (1995).

[17] A.I. Ahiezer, V.B. Berestetsky, Quantum Electrodinamics, Nauka, 66 (1981); F. Sauter, Zeits. f. Phys. **69**, 742 (1931).

[18] O. Klein, Zeits. f. Phys. **53**, 157 (1929); O. Klein and Y. Nishina, Zeits. f. Phys. **52**, 853 (1929); F. Sauter, Zeits. f. Phys. **69**, 742 (1931).

[19] D.M. Volkov, Zeits. f. Phys. **94**, 250 (1935).

[20] Review of Particle Physics, Phys. Rev. D **54**, 175 (1996).

[21] J.D. Jackson, Classical Electrodynamics, J. Wiley, 2nd ed. (J. Wiley, New York, 1975), p. 272 and p. 695.

[22] L.B. Okun, Leptons and Quarks, Nauka, p.285-287 (1981).

[23] Christian Bula, A numeric Integration Program..., E144 note, June 1997.

[24] V.B. Berestetskii, E.M. Lifshitz and L.P. Pitaevskii, Quantum Electrodynamics, 2nd ed. Pergamon Press, New York, 1982, secs. 40 and 101.

[25] C. Bula et al., Observation of Nonlinear Effects in Compton Scattering, Phys. Rev. Lett. **76**, 3116 (1996).

[26] Theofilos Kotseroglou, Observation of Nonlinear Compton Scattering, Ph.D. Thesis, University of Rochester UR-1459 (1996).

[27] Th. Kotseroglou et al., Picosecond timing of Terawatt laser pulses with the SLAC 46 GeV electron beam, SLAC-PUB-7130; Nucl. Instrum. Methods A **383** pp. 309-317 (1996).

[28] N.D. Sengupta, Bull. Math. Soc. (Calcutta) **44**, 175 (1952).

[29] L.S. Brown and T.W.B. Kibble, Phys. Rev. **133A**, 705 (1964); T.W.B. Kibble, Phys. Rev. Lett. **16**, 1060 (1966).

[30] M. Bell and J.S. Bell, Part. Acc. **24**, 1 (1988).

[31] R. Blankenbecler and S.D. Drell, Phys. Rev. Lett. **61**, 2324 (1988).

[32] M. Jacob and T.T. Wu, Nucl. Phys. **B303**, 373, 389 (1989).

[33] P. Chen and K. Yokoya, Phys. Rev. Lett. **61**, 1101 (1988); V.N. Baier, V.M. Katkov and V.M. Strakhovenko, Nucl. Phys. **B328**, 387 (1989).

[34] R. Bonvincini et al., Phys. Rev. Lett. **62**, 2381 (1989).

[35] J. Schwinger, Proc. Nat. Acad. Sci. **40**, 132 (1954).

[36] A. Belkacem et al., Phys. Lett. **B177**, 211 (1986); Phys. Lett. **B206**, 561 (1988); R. Medenwalt et al., Phys. Lett. **B227**, 483 (1989).

[37] J. Schweppe et al., Phys. Rev. Lett. **51**, 2261 (1983); T. Cowan et al., Phys. Rev. Lett. **56**, 444 (1986); P. Salabura et al., Phys. Lett. **B245**, 153 (1990); W. Koenig et al., Phys. Lett. **B218**, 12 (1989).

[38] The NLC Design Group, Zeroth-Order Design Report for the Next Linear Collider, Volume I, SLAC-474/LBNL-5424/UCRL-ID-124161/UC-414 (1996).

[39] D.D. Meyerhofer, J.P. Knauer, S.J. McKnaught, and C.I. Moore, J. Opt Soc. Am. **B13**, 113 (1996).

[40] C. Bamber et al., 0.5 Hz Phase-Stabilized Terawatt Laser System with Nd:Glass Slab Amplifier for Nonlinear QED Experiments, University of Rochester Report UR-1428, submitted to Laser Physics.

[41] W.S. Martin and J.P. Chernoch, Multiple Internal Reflection Face Pumped Laser, U.S. Patent 3633126 (1972); M.J. Shoup III and J.H. Kelly, A High-Energy Short-Pulse Multiwavelength Slab-Geometry Nd:Phosphate Glass Laser Source, presented at CLEO 89, Baltimore, MD, (April 1989).

[42] O.E. Martinez, IEEE J. Quan. Elec. **QE-23**, 59 (1987).

[43] R.S. Craxton et al., IEEE J. Quan. Elec. **QE-17**, 1782 (1981).

[44] Model OAP 12-017-036Q, Space Optics Research Labs, Chelmsford, MA.

[45] G. Bowden, et al., SLAC-PUB-95-6132; Nucl. Instrum. Methods A **368**, 579 (1996).

[46] A.E. Siegman, Lasers, University Science Books, pp. 386, 664 (1986).

[47] U. Haug, Focusing of a Pulsed Terawatt Laser, Diplomarbeit, University of Stuttgart.

[48] RF/Microwave fiber-optic transmitter, Model 3540A and receiver, Model 4510A, Ortel Co.; Optical fiber cable, 6HJ-9336A, Sumitomo Electric Industries Ltd., Yokohama, Japan.

[49] Model 1000 Timing Stabilizer Lightwave Electronics Co., Mountain View, CA; see also M.J.W. Rodwell, D.M. Bloom and K.J. Weingarten, IEEE J. of Quantum Electrons **25**, 817 (1989).

[50] M.C. Ross, et al., in *Conference Record of the 1991 IEEE Particle Accelerator Conference* (IEEE, 1991), Vol. 2, p. 1201.

[51] Robert Holtzapple, Longitudinal dynamics at the Stanford Linear Collider, Ph.D. Thesis, Stanford University; SLAC-0487 (1996).

[52] S.H. Rokni, et al., SLAC publication SLAC-PUB-6784-REV, 1996; submitted to Health Phys.

[53] S.C. Berridge et al., IEEE Trans. Nuc. Sci. **37**, 1191 (1990).

[54] E. Prebys, Possible Readout for the E-144 Calorimeters. Internal Note (1992).

[55] C. Field, Nucl. Instrum. Methods A **360**, 467 (1995).

[56] L.M. Delves and J. Walsh, Numerical Solution of Integral Equations, Clarendon Press, Oxford, (1974).

[57] The Electron - Gamma Shower (EGS4) Code System, SLAC-Report-265, Dec. 1985.

[58] S.L. Adler, A New Embedding of Quantum Electrodynamics in a Non-Abelian Gauge Structure, Phys. Lett. **B221**, 39 (1981); D.G.Caldi, Comments Nuc. Part. Phys. **19**, 137 (1989).

[59] G. Malka *et al.* , Experimental Observation of Electrons Accelerated in Vacuum to Relativistic Energies by a High-Intensity Laser, Phys. Rev. Lett. **28**, 3314 (1997).

[60] J.D. Lawson, Lasers and Accelerators, IEEE Trans. on Nucl. Sc., **NS-26 No. 3**, 4217, 1979.

APPENDICES

A Polarization of high energy photons produced in interaction of intense linear polarized laser with unpolarized electron beam

Consider an unpolarized electron beam propagating in the COM frame along $-z$ direction. Electron scatters from linear polarized laser propagating along $+z$ direction (see Fig. 71). We choose x axis of the COM coordinate system in the electron scattering plane. Electron scatters by an angle Θ in $x-z$ plane.

Note that 17° crossing angle between electron and laser beams in the LAB frame for E144 configuration is taken into account automatically by invariant definition of kinematic variables u,u_n and s (see definitions in Section 2.7). In the COM frame collisions occur head-on.

Polarization of the photon $\vec{e_a}$ is in $x-y$ plane with an angle ϕ to the x-axis; polarization is characterized by 4-dimensional vector $\epsilon_a = (0, \vec{\epsilon}_a) = (0\,, \cos\phi\,, \sin\phi\,, 0)$.

Consider two states of the linear polarization of backscattered photon: ϵ_1 with polarization vector in the scattering plane, and ϵ_2 with polarization vector perpendicular to the scattering plane

$$\begin{aligned} \epsilon_1 &= (0, \cos\Theta, 0, -\sin\Theta)\,, \\ \epsilon_2 &= (0, 0, 1, 0)\,. \end{aligned}$$

A schematic view of the reaction and polarization vectors in the COM frame is shown in Fig. 71.

We will call σ_1 the cross-section of the process with photon backscattered into polarization state ϵ_1, and σ_2 with photon backscattered into polarization state ϵ_2.

In all formulae we suppress the index n that corresponds to the number of laser photons taking part in the reaction. If index n is not mentioned then the results are applicable for all orders n if otherwise stated. The total cross section is the sum of

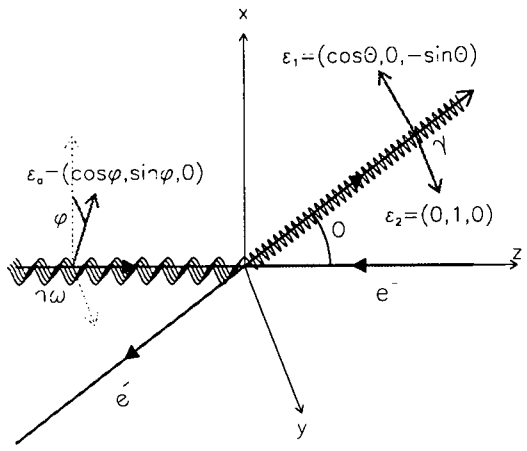

Linear photon polarizations ε_0, ε_1, ε_2.

Figure 71: Linear polarization: schematic diagram for multi-photon Compton scattering. Laser photons have linear polarization $\vec{\epsilon}_a$, backscattered photon is in one of linear polarization states $\vec{\epsilon}_1$ in the photon scattering plane or $\vec{\epsilon}_2$ perpendicular to the photon scattering plane.

cross sections for all orders n.

Using FORM and MAPLE (programs for symbolic computation) we derived cross sections for two polarizations for order n where n is the number of interacting photons

$$
\begin{aligned}
d\sigma_1 &= 2r_0^2 \frac{m^2}{(s-m^2)} \frac{1}{\eta^2} \frac{du\, d\phi}{(1+u)^2} \\
&\left[-2A_0^2 + 2\eta^2 (A_1^2 \cos(2\phi) - A_0 A_2) + \eta^2 \left(2 + \frac{u^2}{(1+u)} \right) (A_1^2 - A_0 A_2) \right], \\
d\sigma_2 &= 2r_0^2 \frac{m^2}{(s-m^2)} \frac{1}{\eta^2} \frac{du\, d\phi}{(1+u)^2} \\
&\left[-2\eta^2 (A_1^2 \cos(2\phi) - A_0 A_2) + \eta^2 \left(2 + \frac{u^2}{(1+u)} \right) (A_1^2 - A_0 A_2) \right],
\end{aligned}
$$

and for total unpolarized cross-section ($\sigma_{Unp} = \sigma_1 + \sigma_2$)

$$
d\sigma_{Unp} = 2r_0^2 \frac{m^2}{(s-m^2)} \frac{1}{\eta^2} \frac{du\, d\phi}{(1+u)^2} \left[-2A_0^2 + 2\eta^2 \left(2 + \frac{u^2}{(1+u)} \right) (A_1^2 - A_0 A_2) \right]. \quad (156)
$$

Unpolarized cross-section $d\sigma_{Unp}$ still depends on ϕ (through functions A_0, A_1 and A_2) and hence we should keep $d\phi$ in the above expression.

Formula Eq. (156) is equivalent to one derived in [7] by different method.

One can see that the dimension of the cross-section is defined by r_0^2. Due to the factor $\frac{m^2}{(\mathrm{s}-m^2)}$ cross-section of the Compton scattering asymptotically goes as $\frac{1}{\mathrm{s}}$ at high energies. For the E144 experiment

$$\begin{aligned} \mathrm{s} &= 2.64\,m^2\,, \quad \frac{m^2}{\mathrm{s}-m^2} = \frac{1}{1.64} \qquad \text{for green laser}\,, \\ \mathrm{s} &= 1.82\,m^2\,, \quad \frac{m^2}{\mathrm{s}-m^2} = \frac{1}{0.82} \qquad \text{for IR laser}\,. \end{aligned}$$

We can rewrite the above formulae in more symmetric way

$$\begin{aligned} d\sigma_1 &= \frac{1}{2} d\sigma_{Unp} + d\sigma_{pol}\,, \\ d\sigma_2 &= \frac{1}{2} d\sigma_{Unp} - d\sigma_{pol}\,, \\ d\sigma_{Pol} &= 2r_0^2 \frac{m^2}{(\mathrm{s}-m^2)} \frac{1}{\eta^2} \frac{du\,d\phi}{(1+u)^2} \\ &\quad \left[-A_0^2 + 2\eta^2 (A_1^2(1+2\cos(2\phi)) - A_0 A_2)\right]\,. \end{aligned} \tag{157}$$

Cross-sections $d\sigma_1$ and $d\sigma_2$ are not useful for experimental measurements. From the experimental point of view it is important to calculate differential cross-sections for backscattered photons which have linear polarization parallel $\sigma_{||}$ or perpendicular $\sigma_{\perp}$ to the polarization of the laser.

For a photon backscattered at an angle Θ with the direction of the original laser photons, parallel or perpendicular polarization condition is not well-defined in general case. What does it mean that linear polarizations of two photons are parallel if photons have some angle between them? If translation to a frame where two photons have parallel momenta $\vec{k_1} \parallel \vec{k_2}$ is made, then we can define parallel or perpendicular

orientation of photon polarizations in this frame. A process for which the polarization of backscattered photons will be important is sequential pair creation in the same laser focus. In the general case transformation from the COM frame of Compton scattering to the COM frame of a new process (pair creation) should be made. This transformation depends on the number of photons involved in each process and field intensity and in general case is not trivial.

We use the following approximation which is valid for the most of the energy spectrum of backscattered photons except the lowest energies. Consider backscattered photons with angles Θ close to 180° in the COM frame. We know from kinematics that these photons have maximum energy in the LAB frame and will have a major contribution to the pair creation. For these photons we will neglect the correction due to the angle of $(\Theta - 180°)$ and calculate cross-sections $\sigma_{||}$ and $\sigma_{\perp}$ for "almost" parallel and perpendicular orientation of polarizations. For this purpose we note that both polarizations can be presented as combinations of polarizations ϵ_1 and ϵ_2 for backscattered photons

$$\begin{aligned} \epsilon_{||} &= \epsilon_1 \cos\phi - \epsilon_2 \sin\phi\,, \\ \epsilon_{\perp} &= \epsilon_1 \sin\phi + \epsilon_2 \cos\phi\,, \end{aligned}$$

where ϕ is the angle between laser polarization and scattering plane $X - Z$. Then we derive

$$\begin{aligned} d\sigma_{||} &= \frac{1}{2} d\sigma_{Unp} + d\sigma_{Pol}\,, \\ d\sigma_{\perp} &= \frac{1}{2} d\sigma_{Unp} - d\sigma_{Pol}\,, \\ d\sigma_{Pol} &= 2r_0^2 \frac{m^2}{(s - m^2)} \frac{1}{\eta^2} \frac{du\, d\phi}{(1+u)^2} \\ &\quad \left[-A_0^2 \left(1 + \frac{(u_n - u)}{u} (1+\eta^2)(1 - \cos(2\phi)) \right) + 2\eta^2 (A_1^2 - A_0 A_2) \right] \end{aligned} \quad (158)$$

Note that for $\phi = 0$ these cross-sections are equivalent to Eq. (157).

We will use the kinematic parameter σ (don't confuse with the total cross section σ) defined as in [7]

$$\sigma = 2\,\eta^2 \left[\frac{n}{4\beta} - \frac{1}{2} - \left(\frac{\alpha}{8\beta} \right)^2 \right] . \tag{159}$$

We use the same symbol σ for this parameter because it was first defined in [7]; we use the same symbol σ for the total cross section and will point out the difference where it can cause confusion.

Using expression Eq. (70) for parameters α and β we can express parameter σ in terms of kinematic variables u, u_n and $\cos(2\phi)$

$$\sigma = 1 + \frac{(u_n - u)(\eta^2 + 1)(1 - \cos(2\phi))}{2u} .$$

The polarization term in Eq. (158) can be presented using parameter σ in order to compare with the results obtained in [7]

$$d\sigma_{Pol} = 2r_0^2 \frac{m^2}{(s - m^2)} \frac{1}{\eta^2} \frac{du\, d\phi}{(1+u)^2} \left[-A_0^2(2\sigma - 1) + 2\eta^2 (A_1^2 - A_0 A_2) \right] . \tag{160}$$

We can also rewrite $\sigma_{||}$ and $\sigma_{\perp}$ in Eq. (158) using the parameter σ

$$\begin{aligned} d\sigma_{||} &= 2r_0^2 \frac{m^2}{(s - m^2)} \frac{1}{\eta^2} \frac{du\, d\phi}{(1+u)^2} \\ &\quad \left[-2A_0^2 \sigma + 4\eta^2 \left(1 + \frac{u^2}{4(1+u)} \right) (A_1^2 - A_0 A_2) \right] , \\ d\sigma_{\perp} &= 2r_0^2 \frac{m^2}{(s - m^2)} \frac{1}{\eta^2} \frac{du\, d\phi}{(1+u)^2} \\ &\quad \left[-2A_0^2 (1 - \sigma) + \eta^2 \frac{u^2}{1+u} (A_1^2 - A_0 A_2) \right] . \end{aligned} \tag{161}$$

The above result is the original result obtained by the author for the nonlinear Compton scattering of an electron by linear polarized laser light. It should be

noted that it has "similar" form if compared with cross section for pair production by linear polarized photons interacting with linear polarized laser obtained in [7]. Cross-sections for Compton scattering are similar to those for pair production due to crossing symmetry between two processes (different definitions of kinematic variables and phase space should be taken into account).

Note that Eqs. (158) and (161) are valid for photons with close to 180° backscattering angle and hence their limits at 0° or equivalently $u \to 0$ are not valid.

Polarization P(u) of the backscattered γ-beam is defined as

$$P(u) = \frac{d\sigma_{||} - d\sigma_{\perp}}{d\sigma_{||} + d\sigma_{\perp}}.$$

Fraction of photons with polarization $\sigma_{||}$ will be

$$P_{||}(u) = \frac{d\sigma_{||}}{d\sigma_{||} + d\sigma_{\perp}} = \frac{1+P}{2}.$$

One can also define the average polarization of the backscattered photons $< P >$ (for each order n)

$$< P >= \frac{1}{\sigma_{Unp}} \int P(u) \frac{d\sigma_{Unp}}{du} du = \frac{\sigma_{||} - \sigma_{\perp}}{\sigma_{||} + \sigma_{\perp}}.$$

The difference $(d\sigma_{||} - d\sigma_{\perp})$ is the difference between polarization conserving process and polarization flipping processes. Hence positive polarization of backscattered photons in our case means that more photons backscatter with the same polarization as the original laser photons.

Some useful expressions can be derived for polarized and unpolarized cross-sections at the limit $u \to u_n$ for arbitrary field intensity η. This limit is especially interesting because at $u = u_n$ backscattered photons have maximum energy and hence have the dominant contribution to e^+e^- pair creation.

Below we use the powerful MAPLE capabilities to evaluate the limits and simplify expressions. Most of the expressions were obtained by representing formulae as series in field intensity η and then finding the limits for different number of terms in series.

If those limits were independent of the field intensity η or had the same η dependence for arbitrary large number of terms in series (as for cross sections) then the results were interpret as valid for all field intensities.

By evaluating expressions for $d\sigma_{||}$ and $d\sigma_{\perp}$ at the limit $u \to u_n$ we get

$$\begin{aligned}
\lim_{u\to u_n} P(u) &= \frac{2(u_n+1)}{(u_n+1)^2+1} && \text{for odd } n = 1,3,5,\ldots;\\
\lim_{u\to u_n} P(u) &= 0 && \text{for even } n = 2,4,6,\ldots;\\
\lim_{u\to u_n} \frac{d\sigma_{Unp}}{du\,d\phi} &= 2r_0^2 \frac{m^2}{(s-m^2)} \eta^{2n-2} \frac{K_n}{2} \left(\frac{1}{1+u_n} + \frac{1}{(1+u_n)^3} \right) && \text{for odd } n = 1,3,5,\ldots;\\
\lim_{u\to u_n} \frac{d\sigma_{Unp}}{du\,d\phi} &= 2r_0^2 \frac{m^2}{(s-m^2)} \eta^{2n-2} \frac{1}{4} \frac{{u_n}^2}{(1+u_n)^3} && \text{for even } n = 2,4,6,\ldots;\\
K_n &= 1, \left(\frac{3}{4}\right)^2, \left(\frac{25}{32}\right)^2, \ldots \text{ for } n = 1,3,5,\ldots.
\end{aligned}$$

We failed to find an exact analytical evaluation for constants K_n for arbitrary n; one can see though that K_n is decreasing from 1 to 1/2 such that cross-sections for the odd and even n asymptotically approach each other for $n \to \infty$.

The above results are valid for arbitrary field intensity η as it is explained above. Note that for large η the maximum energy of backscattered photons

$$\omega_{max} = \omega(u_n) = E_{tot} \frac{n\,x}{1+n\,x+\eta^2},$$

decreases with the field intensity. In the above expression n is the number of laser photons involved, η is the field intensity and $x = \dfrac{2\,(k_1\,p_1)}{m^2}$. Still the above limits for polarization and cross section are independent of η for $u \to u_n$.

Dependence of polarization $P(u)$ for different orders n versus the kinematic variable u and photon energy ω/E_{tot} is shown in Fig. 72. Two plots are equivalent if correspondence between u and ω is taken into account

$$\omega = E_{tot} \frac{u}{1+u}.$$

Total cross section for each order n of multi-photon Compton scattering has the leading term proportional to $1/\eta^{2n-2}$. In addition the total cross section depends on

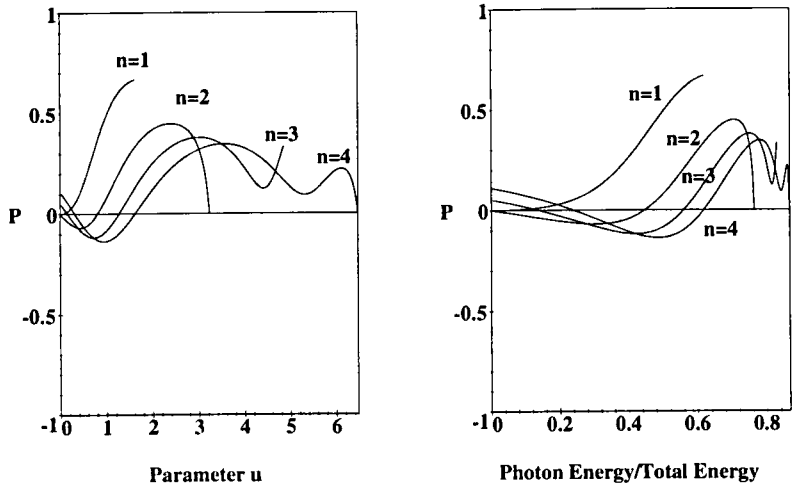

Figure 72: $n = 1, 2, 3, 4$ polarization versus u and fractional photon energy for E144 Green linear polarized laser and 46.6 GeV electron beam. Higher orders n have higher u_n.

the field intensity because the range of u decreases with the field intensity for each order n.

For instance for $n = 1$ the total cross-section and average polarization up to the terms proportional to η^2

$$\lim_{x\to 0} \sigma^{(1)}_{Unp} = 4\pi r_0^2 \frac{m^2}{(\mathrm{s} - m^2)} \frac{2}{3} x \left(1 - 1.35\eta^2\right),$$
$$\lim_{x\to 0} < P >^{(1)} = \frac{1}{2}\left(1 - 0.33\eta^2\right),$$
$$\lim_{x\to \infty} \sigma^{(1)}_{Unp} = 4\pi r_0^2 \frac{m^2}{(\mathrm{s} - m^2)} \left(\frac{1}{4}\left(1 - 5\eta^2\right) + \frac{1}{2}\ln(x)\right),$$
$$\lim_{x\to \infty} < P >^{(1)} = 0\,.$$

The above result is valid for small field intensities only; it is obtained by expansion of the total cross section Eq. (156) in series of η and keeping terms proportional up to η^2 only.

For $n = 2$ the total cross section and the average polarization up to the terms proportional to η^4

$$\lim_{x\to 0}\sigma^{(2)}_{Unp} = 4\pi r_0^2 \frac{m^2}{(s-m^2)}\,\eta^2\,\frac{7}{10}x\,(1-2.82\eta^2)\,,$$
$$\lim_{x\to 0} < P >^{(2)} = \frac{2}{3}\,(1-0.34\eta^2)\,,$$
$$\lim_{x\to\infty}\sigma^{(2)}_{Unp} = 4\pi r_0^2 \frac{m^2}{(s-m^2)}\,\eta^2\,\left(\frac{3}{4}\,(1-1.83\eta^2)\right)\,,$$
$$\lim_{x\to\infty} < P >^{(2)} = 0\,.$$

Average polarization $< P >$ for linear polarized laser as a function of kinematic variable x is shown in Fig. 73 for intensity $\eta \approx 0$. Average polarization goes to 0 at $x \to \infty$ (see above). In E144 not the average polarization $< P >$ but the differential polarization at the limit $u \to u_n$, $P(u_n)$ is important because only the highest energy photons contribute to e^+e^- pair production in subsequent photon photon scattering. If positrons were produced above threshold for $n = 1$ laser photon then the average polarization $< P >$ is important for the total positron production rate and $P(u_n)$ defines the rate of positrons produced with the maximum energy.

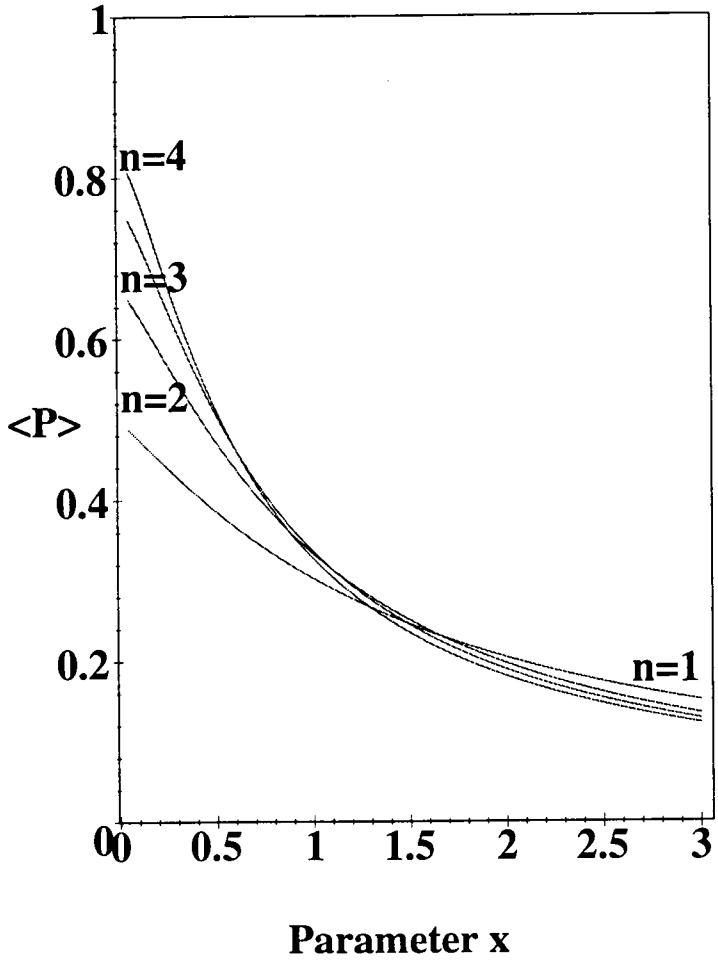

Figure 73: $n = 1, 2, 3, 4$ average polarization $< P >$ versus the parameter x for linear polarized laser and field intensity $\eta \approx 0$. E144 parameters are $x = 1.64$ for green laser and $x = 0.82$ for IR laser.

Examples of unpolarized and polarized differential cross-sections as a function of the fractional photon energy for $n = 1, 2, 3, 4$ and $\eta = 0.1$ are shown in Fig. 7 (Section 2.12).

Finally we find the leading terms of the total cross sections Eqs. (156), (158), (161) presented as series in field intensity η. For $n = 1$ the unpolarized cross section Eq. (156) should be equivalent to the Klein-Nishina formula for Compton scattering (see for example [17]) which provides cross-check for calculations.

To find the leading term we expand differential cross sections in series of η using MAPLE series expansions, find the leading term and integrate over ϕ and over $u = [0...x]$. For $n = 1$ we get

$$\begin{aligned}
\frac{d\sigma^{(1)}_{Unp}}{du} &= 2\pi r_0^2 \frac{m^2}{\mathrm{s}-m^2}\left(\frac{1}{(u+1)^3}+\frac{1}{u+1}-4\frac{u}{(u+1)^2\,x}+4\frac{u^2}{(u+1)^2\,x^2}\right), \\
\sigma^{(1)}_{Unp} &= 2\pi r_0^2 \frac{m^2}{\mathrm{s}-m^2} \\
&\quad \left(\frac{x^3+18x^2+32x+16}{2\,x\,(x+1)^2}+\frac{x^2-4x-8}{x^2}\ln(x+1)\right),
\end{aligned} \tag{162}$$

which is well known Klein-Nishina formula for Compton scattering.

The same calculations for $\sigma_{||}$ cross section give

$$\begin{aligned}
\frac{d\sigma^{(1)}_{||}}{du} &= 2\pi r_0^2 \frac{m^2}{\mathrm{s}-m^2}\left(\frac{1}{2(u+1)^3}+\frac{1}{2(u+1)}-2\frac{u}{(u+1)^2\,x}+3\frac{u^2}{(u+1)^2\,x^2}\right), \\
\sigma^{(1)}_{||} &= 2\pi r_0^2 \frac{m^2}{\mathrm{s}-m^2}\left(\frac{x^3+22x^2+44x+24}{4\,x\,(x+1)^2}+\frac{x^2-4x-12}{2\,x^2}\ln(x+1)\right),
\end{aligned}$$

and $\sigma_{\perp}$

$$\begin{aligned}
\frac{d\sigma^{(1)}_{\perp}}{du} &= 2\pi r_0^2 \frac{m^2}{\mathrm{s}-m^2}\left(\frac{1}{2(u+1)^3}+\frac{1}{2(u+1)}-2\frac{u}{(u+1)^2\,x}+\frac{u^2}{(u+1)^2\,x^2}\right), \\
\sigma^{(1)}_{\perp} &= 2\pi r_0^2 \frac{m^2}{\mathrm{s}-m^2}\left(\frac{x^3+14x^2+20x+8}{4\,x\,(x+1)^2}+\frac{x^2-4x-4}{2\,x^2}\ln(x+1)\right).
\end{aligned}$$

The above cross sections for $\sigma_{||}$ and $\sigma_{\perp}$ are original results derived by the author. One can easily cross-check that at $u = u_n$

$$\begin{aligned}
\lim_{u\to u_n} \frac{d\sigma_{||}^{(1)}}{du} &= 4\pi r_0^2 \frac{m^2}{(\mathrm{s}-m^2)} \frac{1}{2}\left[\frac{1}{2}\left(\frac{1}{1+u_n}+\frac{1}{(1+u_n)^3}\right)+\frac{1}{(1+u_n)^2}\right], \\
\lim_{u\to u_n} \frac{d\sigma_{\perp}^{(1)}}{du} &= 4\pi r_0^2 \frac{m^2}{(\mathrm{s}-m^2)} \frac{1}{2}\left[\frac{1}{2}\left(\frac{1}{1+u_n}+\frac{1}{(1+u_n)^3}\right)-\frac{1}{(1+u_n)^2}\right], \\
\lim_{u\to u_n} P(u) &= \frac{2(u_n+1)}{(u_n+1)^2+1},
\end{aligned}$$

are in agreement with the result derived previously.

For $n = 2$ the leading term of the the total unpolarized cross section expanded in series of field intensity η

$$\begin{aligned}
\sigma_{Unp}^{(2)} &= 2\pi r_0^2 \frac{m^2}{\mathrm{s}-m^2}\eta^2 \times \qquad (163) \\
&\left(\frac{(4x^4-x^3-49x^2-48x-12)(3x+2)}{2\,x^3\,(2x+1)^2}+\frac{5x^3-30x^2-60x-24}{4\,x^4}\ln(2x+1)\right).
\end{aligned}$$

The above result is different from one obtained in [8]. (This is not important for this experiment because neither formulae was used for calculation of the nonlinear rates)

Comparison of total cross sections $\sigma_{Unp}^{(1)}$ and $\sigma_{Unp}^{(2)}/\eta^2$ for linear laser polarization is shown in Fig. 6. Note that $n = 2$ cross-section is larger for circular polarization than that for linear. $n = 1$ cross section is the same for two polarizations.

Some examples of polarization $P(u)$ and polarized cross sections for linear polarized laser for $n = 1$ and $n = 2$ laser photons are presented in Figs. 74 and 75 for E144 green laser and 46.6 GeV electron beam.

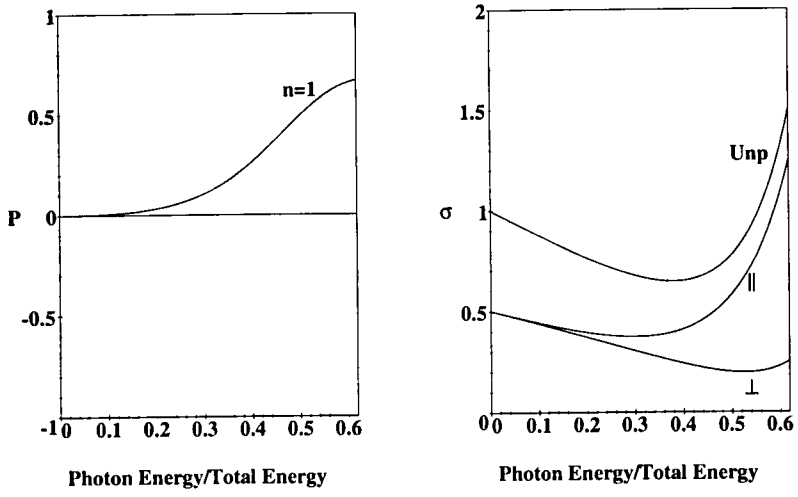

Figure 74: $n = 1$ Compton scattering, linear polarized laser. Polarization of backscattered photons (left plot) and differential cross-sections $\frac{d\sigma_{Unp}}{d\omega\, d\phi}$, $\frac{d\sigma_{\|}}{d\omega\, d\phi}$ and $\frac{d\sigma_{\perp}}{d\omega\, d\phi}$ (right plot) versus the photon energy for E144 configuration with green laser and field intensity $\eta = 0.1$. Cross-sections are in $2r_0^2 m^2/(\mathrm{s} - m^2)$ units.

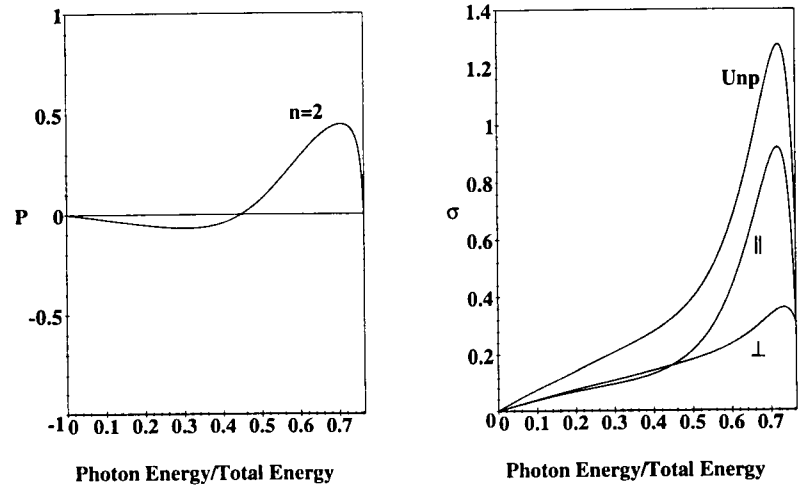

Figure 75: $n = 2$ Compton scattering, linear polarized laser. Polarization of backscattered photons (left plot) and differential cross-sections $\frac{d\sigma_{Unp}}{d\omega\, d\phi}$, $\frac{d\sigma_{\|}}{d\omega\, d\phi}$ and $\frac{d\sigma_{\perp}}{d\omega\, d\phi}$ (right plot) versus the photon energy for E144 configuration with green laser and field intensity $\eta = 0.1$. Cross-sections are in $2r_0^2 m^2/(\mathrm{s} - m^2)$ units. Cross-sections for $n = 2$ are additionally multiplied by factor $1/\eta^2$.

B Polarization of high energy photons produced in interaction of intense circular polarized laser with unpolarized electron beam

Consider laser light that is circularly polarized.

Circular polarized photons are characterized by their helicity. Helicity is defined as the projection of spin to the direction of momentum $\vec{k}$ (normalized to 1). Because photons are massless particles they can only be in 2 helicity states: +1 (positive helicity) and -1 (negative helicity). We assume that laser photons have positive helicity, negative helicity can be considered similarly. Polarization of the circular polarized photon with positive helicity is characterized by polarization 4-vector $\epsilon_a = (0, \vec{\epsilon}_a) = 1/\sqrt{2}(0\,,1\,,+i\,,0)$, where $i = \sqrt{-1}$.

We ignore the polarization of scattered electron.

Consider two states of circular polarization of backscattered photons: ϵ_p for photons with positive helicity, and ϵ_n for photons with negative helicity

$$\begin{aligned} \epsilon_p &= \frac{1}{\sqrt{2}}(0\,,\cos\Theta\,,+i\,,-\sin\Theta)\,, \\ \epsilon_n &= \frac{1}{\sqrt{2}}(0\,,\cos\Theta\,,-i\,,-\sin\Theta)\,, \end{aligned}$$

where Θ is the scattering angle in the COM frame.

A schematic view of the reaction and polarization vectors in the COM frame are shown in Fig. 76.

Then using FORM and MAPLE we derive

$$\begin{aligned} d\sigma_p &= \frac{1}{2}d\sigma_{Unp} + d\sigma_{Pol}\,, \\ d\sigma_n &= \frac{1}{2}d\sigma_{Unp} - d\sigma_{Pol}\,, \end{aligned}$$

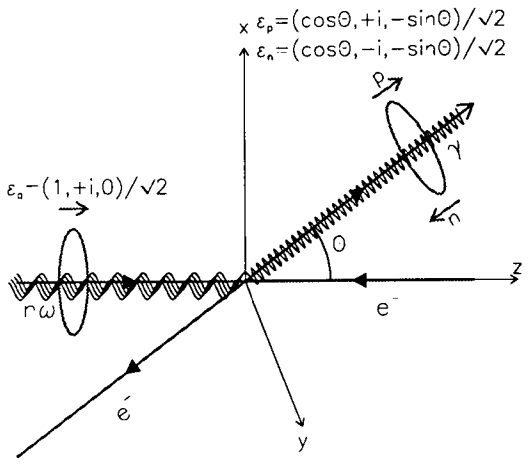

Circular photon polarizations ε_a, ε_p, ε_n.

Figure 76: Circular polarization: schematic diagram for multi-photon Compton scattering. Laser photons have circular polarization $\vec{\epsilon}_a$, backscattered photon is in one of circular polarization states $\vec{\epsilon}_p$ (positive helicity) or $\vec{\epsilon}_n$ (nagative helicity).

$$d\sigma_{Pol} = 4\pi r_0^2 \frac{m^2}{(s-m^2)} \frac{1}{\eta^2} \frac{du}{(1+u)^2} \left[\frac{\eta\sqrt{1+\eta^2}}{2} \left(1 + \frac{u^2}{2(1+u)} \right) (J_{n-1} - J_{n+1}) J_n \frac{2u - u_n}{\sqrt{u(u_n - u)}} \right], \quad (164)$$

where $d\sigma_p$ is the differential cross-section for photons with positive helicity (helicity-conserved process) and $d\sigma_n$ is the differential cross-section for photon with negative helicity (helicity-flip process). $d\sigma_{Unp}$ is the cross section for unpolarized process

$$d\sigma_{Unp} = 4\pi r_0^2 \frac{m^2}{(s-m^2)} \frac{1}{\eta^2} \frac{du}{(1+u)^2} \left[-2\,J_n{}^2 + \eta^2 \left(1 + \frac{u^2}{2\,(u+1)} \right) \left(J_{n-1}{}^2 + J_{n+1}{}^2 - 2\,J_n{}^2 \right) \right]. \quad (165)$$

Formula Eq. (165) is equivalent to one derived in [9] by different method. Formulas Eqs. (164) for polarized cross sections is the original result derived for the first time in this dissertation.

Bessel functions J_n are functions of argument α. Using the following relation

between Bessel functions J_{n-1}, J_{n+1},J_n and equation (71)

$$\alpha\, J_{n-1} + \alpha\, J_{n+1} = 2\, n\, J_n\,, \quad \alpha = -2\, n \frac{\sqrt{u(u_n - u)}}{u_n} \frac{\eta}{\sqrt{1+\eta^2}}\,,$$

we can rewrite polarized cross-sections Eq. (164) in the form

$$\begin{aligned} d\sigma_p &= 4\pi r_0^2 \frac{m^2}{(s - m^2)} \frac{1}{\eta^2} \frac{du}{(1+u)^2} \\ &\left[-{J_n}^2 + \frac{\eta^2}{2} \left(1 + \frac{u^2}{2\,(u+1)} \right) \left(2(1 - \frac{u}{u_n})\, {J_{n-1}}^2 + 2\frac{u}{u_n}\, {J_{n+1}}^2 - 2\, {J_n}^2 \right) \right], \\ d\sigma_n &= 4\pi r_0^2 \frac{m^2}{(s - m^2)} \frac{1}{\eta^2} \frac{du}{(1+u)^2} \\ &\left[-{J_n}^2 + \frac{\eta^2}{2} \left(1 + \frac{u^2}{2\,(u+1)} \right) \left(2\frac{u}{u_n}\, {J_{n-1}}^2 + 2(1 - \frac{u}{u_n})\, {J_{n+1}}^2 - 2\, {J_n}^2 \right) \right] \end{aligned} \quad (166)$$

Formula Eq. (166) for polarized cross sections is the original result derived for the first time in this dissertation.

Polarization $P(u)$ of the backscattered γ-beam is defined as

$$P(u) = \frac{d\sigma_n - d\sigma_p}{d\sigma_n + d\sigma_p}\,.$$

The fraction of photons with polarization σ_n

$$P_n(u) = \frac{d\sigma_n}{d\sigma_n + d\sigma_p} \quad = \frac{1+P}{2}\,.$$

The average polarization of the backscattered photons $< P >$ (for each order n)

$$< P >= \frac{1}{\sigma_{Unp}} \int P(u) \frac{d\sigma_{Unp}}{du} du = \frac{\sigma_n - \sigma_p}{\sigma_p + \sigma_n}\,.$$

Note that the difference $(d\sigma_n - d\sigma_p)$ is the difference between helicity-flip and helicity-conserved processes. Hence positive polarization in our definition means that more photons backscatter by flipping their helicity (as it will be shown later). This has a simple classical analogy: if polarization of the original laser photon is characterized by the electric field vector $\vec{E}$ rotating clockwise along the Z-axis of propagation of

the photon then the photon backscattered by 180° will have the same polarization vector $\vec{\mathbf{E}}$ rotating in the same direction but the photon will propagate in the opposite direction and hence its helicity will flip. In some sense helicity-flip process for circular polarized laser is similar to the polarization-conserved process (parallel polarization between two photons) for linear polarized laser.

Again by analogy with linear polarized laser some useful expressions can be derived for polarized and unpolarized cross-sections at the limit $u \to u_n$. Evaluating expressions for $d\sigma_p$ and $d\sigma_n$ at the limit $u \to u_n$ we get

$$\begin{aligned}
\lim_{u\to u_n} P(u) &= 1 \quad \text{for any } n\,; \\
\lim_{u\to u_n} \frac{d\sigma_{Unp}}{du} &= 4\pi r_0^2 \frac{m^2}{(\mathrm{s}-m^2)} \frac{1}{2}\left[\frac{1}{1+u_n} + \frac{1}{(1+u_n)^3}\right] \quad \text{for } n=1\,; \\
\lim_{u\to u_n} \frac{d\sigma_{Unp}}{du} &= 0 \quad \text{for } n>1\,.
\end{aligned}$$

Note again that the above results are valid for arbitrary field intensity η. By comparing them with similar results for linear polarized laser one can conclude that

1. The polarization is higher for circular laser than for linear laser for photons with maximum energy $(u \to u_n)$;

2. Unpolarized differential cross-sections are the same for circular and linear laser polarization at $u \to u_n$ for $n = 1$ Compton scattering for arbitrary field intensity η;

3. Unpolarized differential cross-section goes to 0 at $u \to u_n$ for higher orders $n > 1$.

This last result can be explained by angular momentum conservation. The initial state has the total spin of the electron + n-laser photons $(n \pm 1/2)$; final state for exactly backscattered photons has the total spin $(1 \pm 1/2)$ and no relative angular momentum; the only n when they can be equal in the spin-flip process is $n = 1$

$$1 \pm \frac{1}{2} = 1 \pm \frac{1}{2},$$
$$n \pm \frac{1}{2} \neq 1 \pm \frac{1}{2} \text{ for any } n > 1 .$$

The maximum energy of backscattered photons

$$\omega_{max} = \omega(u_n) = E_{tot} \frac{n\,x}{1 + n\,x + \eta^2},$$

decreases with the field intensity.

Dependence of polarization $P(u)$ for different orders n versus the kinematic variable u and photon energy ω/E_{tot} is shown on Fig. 77.

The total cross section for each order n of the multi-photon Compton scattering has a leading term proportional to $1/\eta^{2n-2}$. In addition the total cross-section depends on the field intensity because the range of u decreases with the field intensity for each order n.

For $n = 1$ the total cross-section and average polarization up to the terms proportional to η^2

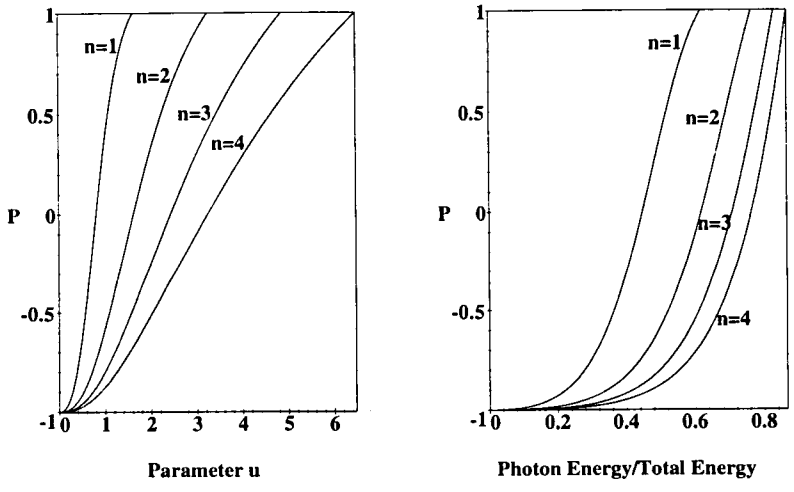

Figure 77: $n = 1, 2, 3, 4$ polarization versus u and fractional photon energy for E144 Green circular polarized laser and 46.6 GeV electron beam. Higher orders n have higher $u_{max} = u_n$ and higher photon energy.

$$\lim_{x\to 0}\sigma^{(1)}_{Unp} = 4\pi r_0^2 \frac{m^2}{(s-m^2)}\,\frac{2}{3}x\,(1-1.4\eta^2)\,,$$
$$\lim_{x\to 0} < P >^{(1)} = 0\,,$$
$$\lim_{x\to\infty}\sigma^{(1)}_{Unp} = 4\pi r_0^2 \frac{m^2}{(s-m^2)}\,\left(\frac{1}{4}\,(1-6\eta^2)+\frac{1}{2}\ln(x)\right)\,,$$
$$\lim_{x\to\infty} < P >^{(1)} = -1\,.$$

The cross sections for circular polarized laser are similar to one for linear polarized laser except that η-dependence is a little different: $(1-1.4\eta^2)$ instead of $(1-1.35\eta^2)$ and $(1-6\eta^2)$ instead of $(1-5\eta^2)$. The average photon polarization for $n=1$ circular laser changes from 0 to -1 for x from 0 to ∞.

For $n=2$ the total cross-section and average polarization up to the terms proportional to η^4

$$\lim_{x\to 0}\sigma^{(2)}_{Unp} = 4\pi r_0^2 \frac{m^2}{(s-m^2)}\,\eta^2\,\frac{4}{5}x\,(1-\eta^2)\,,$$
$$\lim_{x\to 0} < P >^{(2)} = 0\,,$$
$$\lim_{x\to\infty}\sigma^{(2)}_{Unp} = 4\pi r_0^2 \frac{m^2}{(s-m^2)}\,\eta^2\,,$$
$$\lim_{x\to\infty} < P >^{(2)} = -\frac{1}{3}\,.$$

The average polarization $< P >$ for circular polarized laser as a function of kinematic variable x is shown on Fig. 78 for field intensity $\eta \approx 0$. Average polarization is higher for larger x. It goes from 0 to $-\dfrac{1}{2n-1}$ for x from 0 to ∞ (see above). In E144 not the average polarization $< P >$ but differential polarization at the limit u_n, $P(u_n)$ is important because only the highest energy photons contribute to e^+e^- pair production in subsequent photon photon scattering. If positrons were produced above threshold for $n=1$ photon then the average polarization $< P >$ is important for the total positron production rate and $P(u_n)$ defines the rate of positrons produced with the maximum energy.

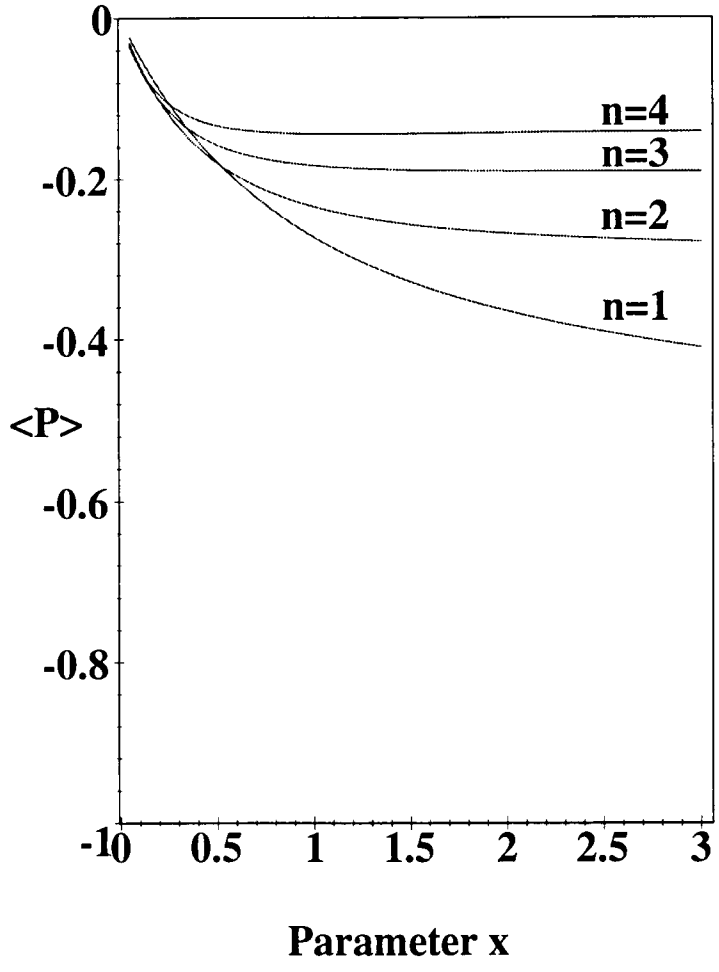

Figure 78: $n = 1, 2, 3, 4$ average polarization $< P >$ versus parameter x for circular polarized laser and field intensity $\eta \approx 0$. E144 parameters are $x = 1.64$ for green laser and $x = 0.82$ for IR laser. Higher orders n have less (negative) polarization.

Examples of unpolarized and polarized differential cross-sections as a function of the fractional photon energy for $n = 1, 2, 3, 4$ and $\eta = 0.1$ are shown in Fig. 8 for 46.6 GeV electron beam and Green laser (E144) (Section 2.12).

Finally we will derive the leading terms of the total cross-sections Eqs. (164) expanded in series of field intensity η. For $n = 1$ unpolarized the cross section was found to be again in the form of Klein-Nishina formula Eq. (162) that provided the cross-check for calculations

$$\begin{aligned}
\frac{d\sigma^{(1)}_{Unp}}{du} &= 2\pi r_0^2 \frac{m^2}{\mathrm{s}-m^2}\left(\frac{1}{(u+1)^3}+\frac{1}{u+1}-4\frac{u}{(u+1)^2\,x}+4\frac{u^2}{(u+1)^2\,x^2}\right), \\
\sigma^{(1)}_{Unp} &= 2\pi r_0^2 \frac{m^2}{\mathrm{s}-m^2}\left(\frac{x^3+18x^2+32x+16}{2\,x\,(x+1)^2}+\frac{x^2-4x-8}{x^2}\ln(x+1)\right). \quad (167)
\end{aligned}$$

Leading term for the *unpolarized* cross section for $n = 1$ (Klein Nishina formula) is independent of the polarization of the laser and should be the same for circular and linear polarizations.

For σ_n we get

$$\begin{aligned}
\frac{d\sigma^{(1)}_{n}}{du} &= 2\pi r_0^2 \frac{m^2}{\mathrm{s}-m^2}\left(\frac{u^3}{(u+1)^3\,x}+2\frac{u^2}{(u+1)^2\,x^2}\right), \\
\sigma^{(1)}_{n} &= 2\pi r_0^2 \frac{m^2}{\mathrm{s}-m^2}\left(\frac{2x^3+13x^2+18x+8}{2\,x\,(x+1)^2}-\frac{3x+4}{x^2}\ln(x+1)\right),
\end{aligned}$$

and for σ_p:

$$\begin{aligned}
\frac{d\sigma^{(1)}_{p}}{du} &= 2\pi r_0^2 \frac{m^2}{\mathrm{s}-m^2}\left(\frac{1}{(u+1)^3}+\frac{1}{(u+1)}-\frac{u(u+2)^2}{(u+1)^3\,x}+2\frac{u^2}{(u+1)^2\,x^2}\right), \\
\sigma^{(1)}_{p} &= 2\pi r_0^2 \frac{m^2}{\mathrm{s}-m^2}\left(-\frac{x^2-6x-8}{2\,x\,(x+1)}+\frac{x^2-x-4}{x^2}\ln(x+1)\right).
\end{aligned}$$

The above results for polarized cross sections for $n = 1$ Compton scattering are the original result derived for the first time in this dissertation.

One can easily cross-check that at $u = u_n$

$$\lim_{u\to u_n}\frac{d\sigma_n^{(1)}}{du} = 4\pi r_0^2\frac{m^2}{(s-m^2)}\frac{1}{2}\left(\frac{1}{1+u_n}+\frac{1}{(1+u_n)^3}\right),$$
$$\lim_{u\to u_n}\frac{d\sigma_p^{(1)}}{du} = 0,$$
$$\lim_{u\to u_n}P(u) = 1.$$

in agreement with the result that was derived previously.

For $n=2$ the leading term of the series expansions will give the total cross-section

$$\sigma_{Unp}^{(2)} = 2\pi r_0^2\frac{m^2}{s-m^2}\eta^2\times \left(\frac{4\,(3x^4+2x^3-23x^2-24x-6)}{3\,x^3\,(2x+1)}+\frac{2\,(x^2-4x-2)(x+1)}{x^4}\ln(2x+1)\right). \quad (168)$$

Comparison of total cross-sections $\sigma_{Unp}^{(1)}$ and $\sigma_{Unp}^{(2)}/\eta^2$ for circular laser polarization is shown in Fig. 6. Note that $n=2$ cross-section is different for circular and linear polarizations (circular is higher) though $n=1$ cross-section is the same for two polarizations. $\sigma_{Unp}^{(2)}$ cross-section is divided by η^2 because the leading term is proportional to η^2).

Some examples of polarization $P(u)$ and cross-sections for circular polarized laser for $n=1$ and $n=2$ laser photons can be found in Figs. 79 and 80 for E144 Green laser and 46.6 GeV electron beam.

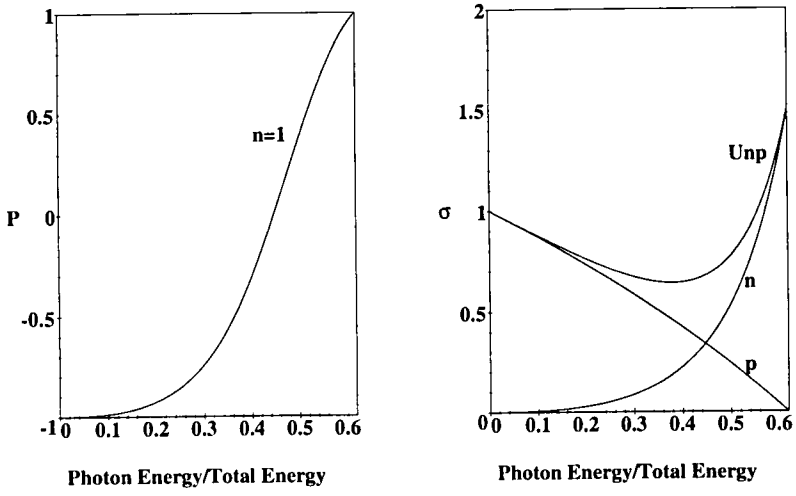

Figure 79: $n = 1$ Compton scattering, circular polarized laser. Polarization of backscattered photons (left plot) and differential cross-sections $\frac{d\sigma_{Unp}}{d\omega\, d\phi}$, $\frac{d\sigma_n}{d\omega\, d\phi}$ and $\frac{d\sigma_p}{d\omega\, d\phi}$ (right plot) versus the photon energy for E144 configuration with green laser and field intensity $\eta = 0.1$. Cross-sections are in $2r_0^2m^2/(\mathrm{s} - m^2)$ units.

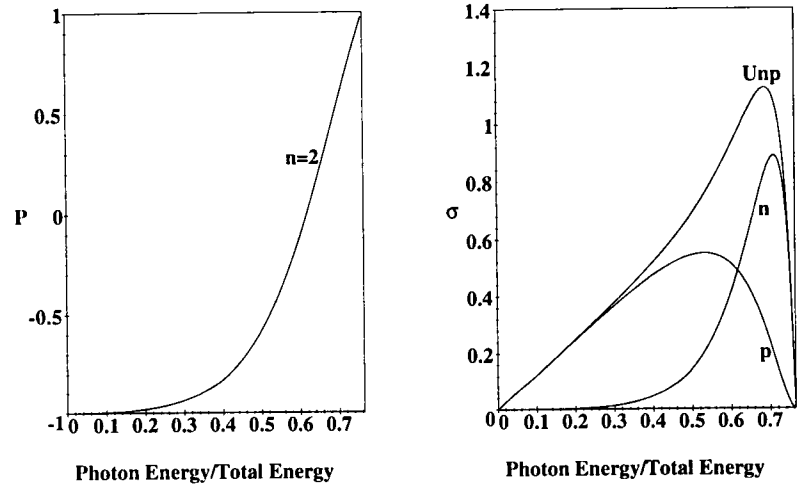

Figure 80: $n = 2$ Compton scattering, circular polarized laser. Polarization of backscattered photons (left plot) and differential cross-sections $\frac{d\sigma_{Unp}}{du\, d\phi}$, $\frac{d\sigma_n}{du\, d\phi}$ and $\frac{d\sigma_p}{du\, d\phi}$ (right plot) versus the photon energy for E144 configuration with green laser and field intensity $\eta = 0.1$. Cross-sections are in $2r_0^2m^2/(\mathrm{s} - m^2)$ units. Cross-sections for $n = 2$ are additionally multiplied by factor $1/\eta^2$.

C e^+e^- pair production in interaction of intense linear polarized laser with linear polarized photons

We consider the process $n\,k_1 + k_2 \to q_1 + q_2$ where $n\,k_1$ stands for n laser photons, k_2 the high energy photon, q_1 and q_2 - electron and positron. Differential cross-sections can be immediately derived from those for the Compton scattering of the electron Eqs. (158),(160) and (161) for $n\,k_1 + q_1 \to k_2 + q_2$ by substitution $k_2 \to -k_2$, $q_1 \to -q_1$ as the two processes are related by crossing symmetry.

To obtain cross-sections for pair production from those for Compton scattering one needs to take into account the difference in definition of u and different final state phase space as well as different spin-statistics and normalization of wave functions in the initial state. We summarized these rules below

$$
\begin{aligned}
\frac{u^2}{(u+1)} &\to -4u \qquad \text{(definition of u)}\,,\\
\frac{m^2}{(\mathrm{s}-m^2)} &\to \frac{m^2}{\mathrm{s}} \qquad \text{(massless photon in the initial state)}\,,\\
\frac{du}{(1+u)^2} &\to -\frac{du}{4\,u\sqrt{u(u-1)}} \qquad \text{(final state phase space)}\,,\\
1 &\to 2 \qquad \text{(factor 2 more due to spin-statistics for polarized photons)}\,,\\
1 &\to 1 \qquad \text{(the same spin-statistics factor for unpolarized photons)}\,,\\
1 &\to 2 \qquad \text{(factor 2 more due to normalization in the initial state)}\,. \qquad (169)
\end{aligned}
$$

Spin-statistics factors arise from the necessity to average over polarizations of initial states and sum over polarizations of final states of particle involved in the reaction.

We derived e^+e^- cross-section by unpolarized photons interacting with linear polarized laser

$$d\sigma_{Unp} = 2\,r_0^2 \frac{m^2}{\mathrm{s}} \frac{1}{\eta^2} \frac{du\,d\phi}{u\sqrt{u(u-1)}} \left[A_0^2 + 2\eta^2(2u-1)(A_1^2 - A_0 A_2)\right] . \qquad (170)$$

Formula Eq. (170) is equivalent to one derived in [7] by different method.

Cross sections for e^+e^- pairs produced by photons with parallel and perpendicular to the laser polarization is

$$\begin{aligned}
d\sigma_{||} &= d\sigma_{Unp} + d\sigma_{Pol}\,, \\
d\sigma_{\perp} &= d\sigma_{Unp} - d\sigma_{Pol}\,, \\
d\sigma_{Pol} &= 2r_0^2 \frac{m^2}{\mathrm{s}} \frac{1}{\eta^2} \frac{du\,d\phi}{u\sqrt{u(u-1)}} \\
&\quad \left[+A_0^2 \left(1 + \frac{(u_n - u)}{u}(1+\eta^2)(1-\cos(2\phi))\right) - 2\eta^2(A_1^2 - A_0 A_2)\right] \qquad (171)
\end{aligned}$$

Note that different spin-statistics of the initial state results in new relation between total and polarized cross-sections:

$$d\sigma_{Unp} = \frac{d\sigma_{||} + d\sigma_{\perp}}{2} .$$

Using parameter σ defined by Eq. (159) we (compare to Eq. (161 for Compton scattering)

$$\begin{aligned}
d\sigma_{||} &= 2r_0^2 \frac{m^2}{\mathrm{s}} \frac{1}{\eta^2} \frac{du\,d\phi}{u\sqrt{u(u-1)}} \\
&\quad \left[+2A_0^2\sigma + 4\eta^2(u-1)(A_1^2 - A_0 A_2)\right] , \\
d\sigma_{\perp} &= 2r_0^2 \frac{m^2}{\mathrm{s}} \frac{1}{\eta^2} \frac{du\,d\phi}{u\sqrt{u(u-1)}} \\
&\quad \left[+2A_0^2(1-\sigma) + 4\eta^2 u(A_1^2 - A_0 A_2)\right] , \\
\sigma &= 2\,\eta^2 \left[\frac{n}{4\beta} - \frac{1}{2} - \left(\frac{\alpha}{8\beta}\right)^2\right] . \qquad (172)
\end{aligned}$$

Cross-sections Eqs. (171) and (172) are equivalent. Formulae Eqs. (172) is equivalent to one derived in [7] by different method.

Note that because the initial state photons collide at 180° in their COM frame polarized cross-sections are free from possible ambiguity in definition of parallel and perpendicular orientation of polarizations. This ambiguity does exist in Compton scattering and is discussed in Appendix A.

We define differential asymmetry A in e^+e^- pair production due to different photon polarization

$$A(u) = \frac{d\sigma_{||} - d\sigma_{\perp}}{d\sigma_{||} + d\sigma_{\perp}}.$$

The total asymmetry A_{tot} for the pair production is

$$A_{tot} = \frac{1}{\sigma_{Unp}} \int A(u) \frac{d\sigma_{Unp}}{du} du = \frac{\sigma_{||} - \sigma_{\perp}}{\sigma_{||} + \sigma_{\perp}}.$$

First we study analytical behavior of differential asymmetry $A(u)$.

We use again the power of MAPLE series expansions to presenting formulae as series in field intensity η and then to find the limits for different number of terms in series. Results that were independent of field intensity η are interpret as valid for all field intensities.

We derive expressions at the limit $u \to u_n$.

In the LAB frame $u = u_n$ corresponds to the minimum and maximum energy of the positron E_{e^+}. It will be shown below that for $u_n \gg 1$ most of the positrons are created close to $u = u_n$ and for $u_n \sim 1$ most of the positrons are created close to $u = 1$.

By evaluating expressions for $d\sigma_{||}$ and $d\sigma_{\perp}$ at the limit $u \to u_n$ we get

$$\begin{aligned} \lim_{u \to u_n} A(u) &= -\frac{1}{2u_n - 1} \quad \text{for odd } n = 1, 3, 5, \ldots, \\ \lim_{u \to u_n} A(u) &= 0 \qquad\quad \text{for even } n = 2, 4, 6, \ldots, \end{aligned}$$

$$\lim_{u\to u_n}\frac{d\sigma_{Unp}}{du\,d\phi} = 2r_0^2\frac{m^2}{s}\eta^{2n-2}\,\frac{K_n}{2}\,\frac{(2u_n-1)}{u_n\sqrt{u_n(u_n-1)}} \quad \text{for odd } n=1,3,5,\ldots,$$

$$\lim_{u\to u_n}\frac{d\sigma_{Unp}}{du\,d\phi} = 2r_0^2\frac{m^2}{s}\eta^{2n-2}\,\frac{1}{2}\,\frac{u_n}{u_n\sqrt{u_n(u_n-1)}} \quad \text{for even } n=2,4,6,\ldots,$$

$$K_n = 1,\ \left(\frac{3}{4}\right)^2,\ \left(\frac{25}{32}\right)^2,\ \ldots \quad \text{for } n=1,3,5,\ldots,$$

where K_n are the same as for Compton scattering (see Appendix A).

We should notice that the asymmetry $A(u)$ at $u \to u_n$ is negative i.e. pair production by photons with the same polarization as the laser is unfavorable. Differential unpolarized cross sections for different orders n have very similar form as those for the electron Compton scattering. Due to the fact that $K_n \to 1/2$ for large n differential unpolarized cross sections for odd and even orders n asymptotically approach each other at $n \to \infty$. This is another similarity with the electron Compton scattering.

The above results are valid for arbitrary field intensity η.

For large η the "gap" of kinematically allowed energies of positrons (electrons) is reduced by the field. The energy of the positron (electron) in the LAB frame that corresponds to invariant u is

$$E_{e^+} = \frac{E_{Tot}}{2}\left(1 \pm \sqrt{1-\frac{1}{u}}\right). \tag{173}$$

A single value of u corresponds to two energies of the positron symmetrical with respect to the energy $E_{Tot}/2$ in the LAB frame. (These two energies correspond to the positron angles Θ and $(\pi - \Theta)$ in the COM frame). Because the differential cross section should be the same when positron and electron are interchanged it should be symmetric with respect to $E_{Tot}/2$ in the LAB frame. The range of positron energies that corresponds to $u = [1...u_n]$ is

$$E_{e^+} = \left[E_{Tot}/2 \quad \ldots \quad E_{Tot}/2\left(1 \pm \sqrt{1-\frac{1}{u_n}}\right)\right],$$

$$[E_{min}...E_{max}] = \left[E_{Tot}/2\left(1-\sqrt{1-\frac{1}{u_n}}\right) \quad \ldots \quad E_{Tot}/2\left(1+\sqrt{1-\frac{1}{u_n}}\right)\right] =$$

$$= \quad E_{Tot}/2\left(1 \pm \sqrt{1 - \frac{1+\eta^2}{n\,x}}\right) .$$

From the last equation one can see that the energy range available for the pair creation is less for higher field intensities η.

If positrons are created well above the threshold ($u_n \gg 1$) then the positron (electron) energy range is extended to all available energies $[0...E_{Tot}]$. On the other hand for positrons created near the threshold ($u_n \simeq 1$) the energy range is small compared to E_{tot} and is centered around $E_{Tot}/2$. This is the case for the E144 experiment.

In the limit $u \to 1$, evaluation of A(u) does not have a simple analytical approximation in general case. Below the result for $n = 1$ (valid for arbitrary field intensity η) is shown

$$\lim_{u\to 1} A(u) \quad = \quad -\frac{1}{u_1^2 + 2u_1 - 2} .$$

In the LAB frame $u = 1$ corresponds to the positron energy equal to half of the total energy $E_{e+} = \frac{1}{2}E_{tot}$. Note that the asymmetry $A(u)$ is negative.

The dependence of differential asymmetry $A(u)$ in positron production for different orders n versus the kinematic variable u and positron fractional energy E_{e+}/E_{tot} is shown in Fig. 81. Two plots are equivalent if relation Eq. (173) between u and E_{e+} is taken into account.

The total asymmetry A_{tot} in pair production for linear polarized laser as a function of kinematic variable $u_n > 1$ is shown in Fig. 82 for $\eta = 0.1$. A_{tot} as a function of u_n is an oscillating function. Higher the order n, more oscillations it has. The second derivative $\partial^2 A_{tot}/\partial u_n^2$ has n regions with constant (positive or negative) sign.

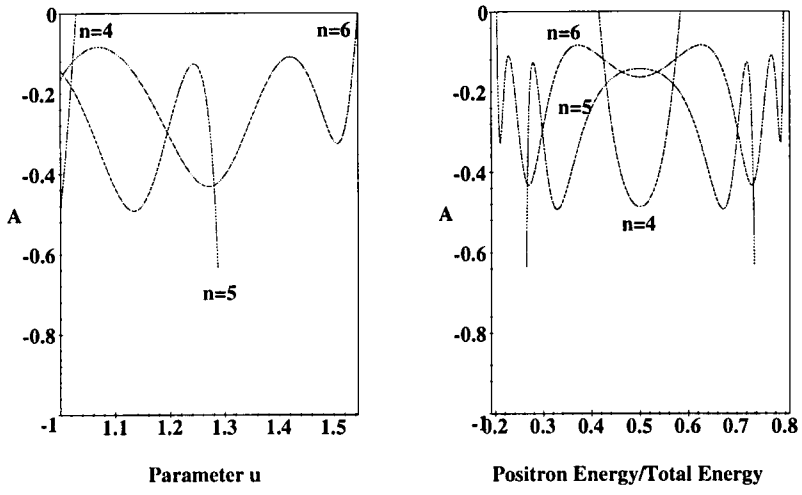

Figure 81: $n = 4, 5, 6$ asymmetry versus u and fractional positron energy for E144 Green linear polarized laser and $E_{tot} = 29$ GeV photon. Higher orders n have higher $u_{max} = u_n$ and higher maximum positron energy.

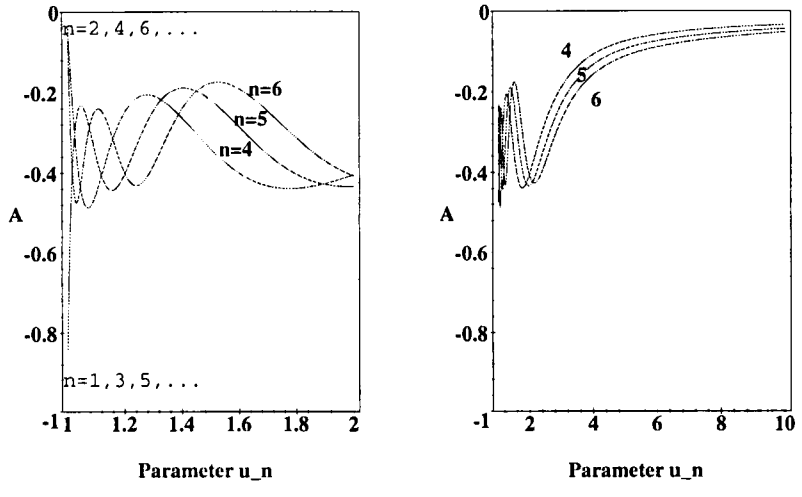

Figure 82: $n = 4, 5, 6$ total asymmetry A_{tot} in pair production versus u_n for linear polarized laser. Two plots differs by horizontal scale only. (These plots are for arbitrary laser frequency, photon energy and field intensity; $n = 4, 5, 6$ are shown because of the relevance to the E144 experiment.)

The asymptotic behavior of A_{tot} is the following

$$\begin{aligned}
\lim_{u_n \to 1} A_{tot} &= -1 \qquad \text{for odd } n = 1, 3, 5, \ldots , \\
\lim_{u_n \to 1} A_{tot} &= 0 \qquad \text{for even } n = 2, 4, 6, \ldots , \\
\lim_{u_n \to \infty} A_{tot} &= 0 \qquad \text{for any } n .
\end{aligned}$$

From the above relations it follows that positron production is suppressed at the threshold ($A_{tot} = -1$) for odd powers n including the important case $n = 1$ for positron production above the threshold.

The average polarization is higher for small x and goes to 0 at $x \to \infty$ (see above) by analogy with Compton scattering for linear polarized laser.

Examples of unpolarized and polarized differential cross-sections as a function of the fractional positron energy $n = 4, 5, 6$ and $\eta = 0.1$ are shown in Fig. 9 (Section 2.12).

We present leading terms in field intensity η for the total cross sections Eqs. (172) for $n = 1$.

Expanding expression $\frac{1}{\eta^2}\left[A_0^2 + 2\eta^2(2u-1)(A_1^2 - A_0 A_2)\right]$ in series of η and integrating over ϕ and then over $u = [0...x]$ we get

$$\begin{aligned}
\frac{d\sigma_{Unp}}{du} &= 4\pi r_0^2 \frac{m^2}{\mathrm{s}} \left(\frac{(2u-1)x^2 + 2u(x-u)}{2x^2 u\sqrt{u(u-1)}} \right) , \\
\sigma_{Unp} &= 4\pi r_0^2 \frac{m^2}{\mathrm{s}} \left(\frac{3 - w^4}{2} \ln \frac{1+w}{1-w} - w(2 - w^2) \right) ,
\end{aligned} \tag{174}$$

where we use variable w

$$w = \sqrt{1 - \frac{1}{x}} = \sqrt{1 - \frac{(2m)^2}{\mathrm{s}}} . \tag{175}$$

The variable w is another convenient representation of the energy available for creation of e^+e^- pair. The minimum and the maximum energy of the positron (electron) is related to w by

$$E_{e^+,max,min} = E_{Tot}\frac{1 \pm w}{2}\,.$$

Equation (174) is the well-known Breit-Wheeler equation (see for example [17]).

Cross sections with polarized photon for $n = 1$ in the weak field approximation are

$$\begin{aligned}
\frac{d\sigma_{\|}}{du} &= 4\pi r_0^2 \frac{m^2}{\mathrm{s}}\left(\frac{(2u-1)x^2 + 2u(x-\frac{3}{2}u)}{2x^2u\sqrt{u(u-1)}}\right), \\
\sigma_{\|} &= 4\pi r_0^2 \frac{m^2}{\mathrm{s}}\left(\frac{(5-3w^2)(1+w^2)}{4}\ln\frac{1+w}{1-w} - \frac{w(5-3w^2)}{2}\right), \qquad (176)
\end{aligned}$$

$$\begin{aligned}
\frac{d\sigma_{\perp}}{du} &= 4\pi r_0^2 \frac{m^2}{\mathrm{s}}\left(\frac{(2u-1)x^2 + 2u(x-\frac{1}{2}u)}{2x^2u\sqrt{u(u-1)}}\right), \\
\sigma_{\perp} &= 4\pi r_0^2 \frac{m^2}{\mathrm{s}}\left(\frac{7-2w^2-w^4}{4}\ln\frac{1+w}{1-w} - \frac{w(3-w^2)}{2}\right). \qquad (177)
\end{aligned}$$

Eqs. (176) and (177) are the original results that were obtained by the author.

Note that the difference between parallel and perpendicular orientations of polarization is in terms $(x - \frac{3}{2}u) \leftrightarrow (x - \frac{1}{2}u)$ in differential cross-section. The cross section for polarization of high energy photon parallel to one for laser photons is always less than perpendicular orientation. The asymmetry is maximum for $u = u_n$ ($u_n = x$ in the weak field approximation $n = 1$) and minimum for $u = 1$. Dependence of the total asymmetry in pair production versus x is shown in Fig. 83 for $n = 1$.

The asymptotic behavior of the Breit-Wheeler cross-sections for $w \to 0$ (positron production near the threshold) is

$$\begin{aligned}
\sigma_{Unp}(w \to 0) &= 4\pi r_0^2 \frac{m^2}{\mathrm{s}}\left(w + 2w^3 + O(w^4)\right), \\
\sigma_{\|}(w \to 0) &= 4\pi r_0^2 \frac{m^2}{\mathrm{s}}\left(\frac{10}{3}w^3 + O(w^4)\right), \\
\sigma_{\perp}(w \to 0) &= 4\pi r_0^2 \frac{m^2}{\mathrm{s}}\left(2w + \frac{2}{3}w^3 + O(w^4)\right).
\end{aligned}$$

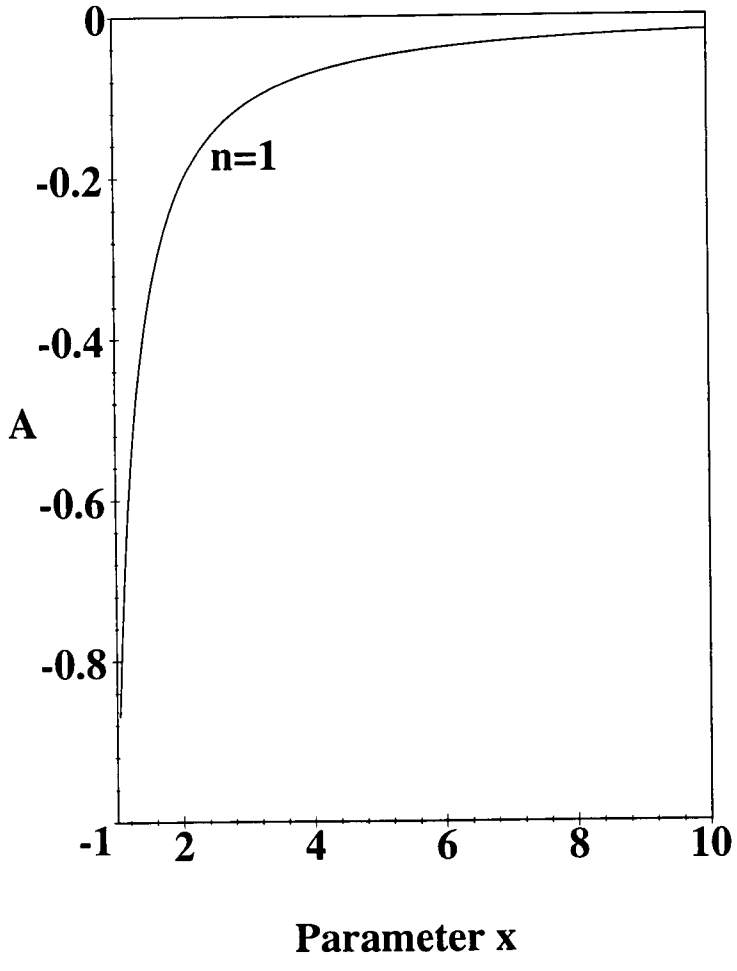

Figure 83: Total asymmetry for $n = 1$ positron production in the focus of linear polarized laser versus the parameter x for arbitrary laser frequency.

The asymmetry in positron production near the threshold has the following asymptotic form

$$\begin{aligned} A_{tot}(w \to 0) &= -1 + \frac{10}{3}w^2 + O(w^3)\,, \qquad \lim_{w\to 0} A = -1\,, \\ A_{tot}(x \to \infty) &= -\frac{1}{2x(\ln(4x) - 1)} + O\left(\frac{1}{x^2}\right)\,, \qquad \lim_{x\to\infty} A = 0\,. \end{aligned}$$

D e^+e^- pair production in interaction of intense circular polarized laser with circular polarized photons

We repeat calculations of the previous section for electron-positron pairs produced by circular polarized photons interacting with circular polarized laser.

Unpolarized cross-section for e^+e^- pair in photon-photon interaction is

$$d\sigma_{Unp} = 4\pi r_0^2 \frac{m^2}{\mathrm{s}} \frac{1}{\eta^2} \frac{du}{u\sqrt{u(u-1)}} \left[{J_n}^2 + \frac{\eta^2}{2}(2u-1)({J_{n-1}}^2 + {J_{n+1}}^2 - 2\,{J_n}^2) \right] . \quad (178)$$

Formula Eq. (178) is equivalent to one derived in [9] by different method.

Cross-sections for e^+e^- produced by photon with the positive and negative helicities (laser assumed to have positive helicity) are

$$\begin{aligned} d\sigma_p &= d\sigma_{Unp} + d\sigma_{Pol}\,, \\ d\sigma_n &= d\sigma_{Unp} - d\sigma_{Pol}\,, \\ d\sigma_{Pol} &= 4\pi r_0^2 \frac{m^2}{\mathrm{s}} \frac{1}{\eta^2} \frac{du}{u\sqrt{u(u-1)}} \\ &\quad \left[\frac{\eta\sqrt{1+\eta^2}}{2}(2u-1)(J_{n-1} - J_{n+1}) J_n \frac{2u-u_n}{\sqrt{u(u_n-u)}} \right] . \end{aligned} \quad (179)$$

Using relation between Bessel functions $\alpha\, J_{n-1} + \alpha\, J_{n+1} = 2\,n\,J_n$ and equation (71) we get

$$\begin{aligned} d\sigma_p &= 4\pi r_0^2 \frac{m^2}{\mathrm{s}} \frac{1}{\eta^2} \frac{du}{u\sqrt{u(u-1)}} \\ &\quad \left[-{J_n}^2 + \frac{\eta^2}{2}(2u-1) \left(2(1-\frac{u}{u_n})\, {J_{n-1}}^2 + 2\frac{u}{u_n}\, {J_{n+1}}^2 - 2\,{J_n}^2 \right) \right] , \end{aligned}$$

$$
\begin{aligned}
d\sigma_n &= 4\pi r_0^2 \frac{m^2}{s}\frac{1}{\eta^2}\frac{du}{u\sqrt{u(u-1)}} \\
&\quad \left[-{J_n}^2 + \frac{\eta^2}{2}(2u-1)\left(2\frac{u}{u_n}\,{J_{n-1}}^2 + 2(1-\frac{u}{u_n})\,{J_{n+1}}^2 - 2\,{J_n}^2\right)\right], \\
d\sigma_{Unp} &= \frac{d\sigma_p + d\sigma_n}{2}. \qquad (180)
\end{aligned}
$$

Formulae Eqs. (180) for polarized cross sections is the original result derived for the first time in this dissertation.

Differential asymmetry A in e^+e^- pairs production is defined as

$$A(u) = \frac{d\sigma_n - d\sigma_p}{d\sigma_n + d\sigma_p}.$$

The total asymmetry A_{tot} for pair production is

$$A_{tot} = \frac{1}{\sigma_{Unp}}\int A(u)\frac{d\sigma_{Unp}}{du}\,du = \frac{\sigma_n - \sigma_p}{\sigma_n + \sigma_p}.$$

First we examine analytical behavior of the differential asymmetry $A(u)$ in pair production.

By evaluating expressions for $d\sigma_p$ and $d\sigma_n$ at the limit $u \to u_n$ (maximum/minimum positron energy) we get

$$
\begin{aligned}
\lim_{u\to u_n} A(u) &= -1 \qquad \text{for any } n, \\
\lim_{u\to u_n} \frac{d\sigma_{Unp}}{du} &= 4\pi r_0^2 \frac{m^2}{s}\,\frac{1}{2}\,\frac{(2u_n-1)}{u_n\sqrt{u_n(u_n-1)}} \qquad \text{for } n = 1, \\
\lim_{u\to u_n} \frac{d\sigma_{Unp}}{du} &= 0 \qquad\qquad\qquad \text{for } n > 1.
\end{aligned}
$$

The above results are valid for arbitrary field intensity η.

Asymmetry $A(u)$ is negative at $u = u_n$. Production of positrons with maximum (minimum) energy is strongly suppressed for photons with the opposite helicities (e.g. n-state for high energy photon and p-spate for laser photons). This result can be explained by the angular momentum conservation. Indeed suppose that a high energy

photon with negative helicity interacts with n laser photons with positive helicity and produce a e^+e^- pair with electron and positron going in forward-backward direction with no relative angular momentum. The total final state angular momentum for e^+e^- pair is 0 because of the parity conservation. The total initial state angular momentum for photons is $n-1$. Hence the only configuration when positron or electron can be produced with maximum energy is $n=1$ and opposite helicities of photons.

The above observation is an important argument against positron production by electron beam in the laser focus. *Because backscattered photons with the maximum energy have helicity opposite to one of the laser they cannot produce positrons near $u \approx u_n$ (maximum positron energy) through interaction with the same laser. This effect can be reversed if one can use a second laser interaction point with opposite polarization (opposite photon helicity) for positron production.*

At the limit $u \to 1$

$$\lim_{u\to 1} A(u) \;=\; -\frac{u_n(2-u_n)}{u_n^2+2u_n-2} \qquad \text{for any } n\,.$$

In the LAB frame $u=1$ corresponds to the positron energy equal half of the total energy $E_{e^+} = \frac{1}{2}E_{tot}$. The asymmetry $A(1)$ is negative below $u_n = 2$ and positive above $u_n = 2$ (see the above formula). If pair creation occurs near the threshold $u_n \approx 1$ then $A(1) = -1$.

The differential asymmetry $A(u)$ in positron production for different orders n versus the kinematic variable u and positron fractional energy E_{e^+}/E_{tot} is shown in Fig. 84. Two plots are equivalent if relation Eq. (173) between u and E_{e^+} is taken into account.

The total asymmetry A_{tot} in pair production for circular polarized laser as a function of kinematic variable u_n ($u_n \geq 1$) is shown in Fig. 85 for $\eta = 0.1$. The total asymmetry A_{tot} as a function of u_n is a slow decreasing function. The higher the order n, the faster the decrease.

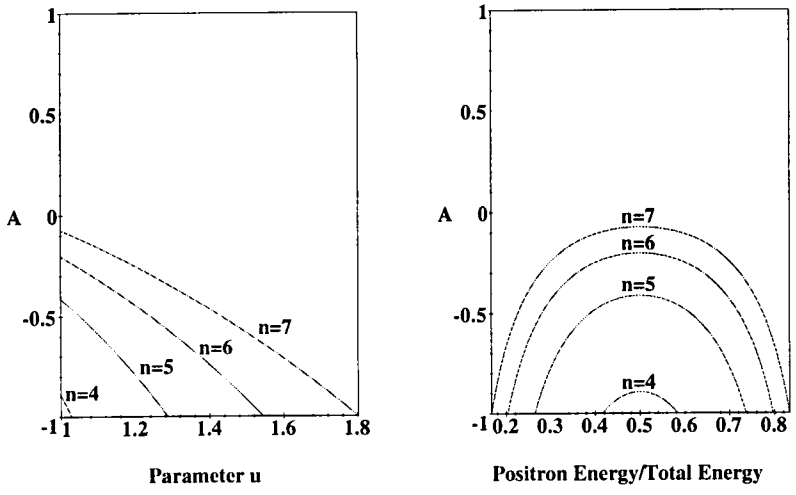

Figure 84: $n = 4, 5, 6, 7$ asymmetry versus u and fractional positron energy for E144 Green circular polarized laser and $E_{tot} = 29$ GeV photon. Higher orders n have higher $u_{max} = u_n$ and higher maximum positron energy.

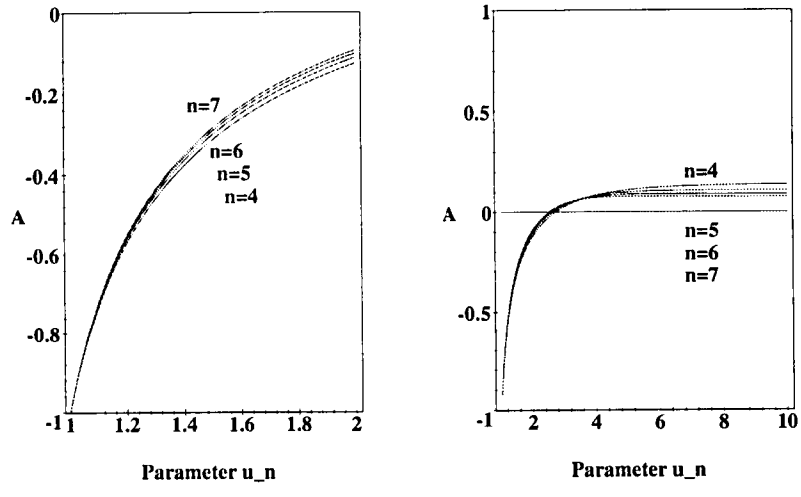

Figure 85: $n = 4, 5, 6, 7$ total asymmetry A_{tot} in pair production versus u_n for circular polarized laser. (These plots are for arbitrary laser frequency, photon energy and field intensity; $n = 4, 5, 6, 7$ are shown because of the relevance to E144.)

Asymptotic behavior of A_{tot} is

$$\lim_{u_n \to 1} A_{tot} = -1 \qquad \text{for any } n,$$
$$\lim_{u_n \to \infty} A_{tot} = +\frac{1}{2n-1}.$$

From the above relations it follows that positron production is suppressed at threshold ($A_{tot} = -1$) for all powers n including an important case $n = 1$ for positron production above the threshold.

Examples of unpolarized and polarized differential cross-sections as a function of the fractional positron energy for $n = 4, 5, 6, 7$ and $\eta = 0.1$ are shown on Fig. 10 (Section 2.12).

We derive leading terms of the cross sections Eqs. (179) expanded in series of field intensity η for $n = 1$.

Expanding expression $\frac{1}{\eta^2}\left[{J_n}^2 + \frac{\eta^2}{2}(2u-1)({J_{n-1}}^2 + {J_{n+1}}^2 - 2\,{J_n}^2)\right]$ in series of η and integrating over $u = [0...x]$ we get

$$\frac{d\sigma_{Unp}}{du} = 4\pi r_0^2 \frac{m^2}{s}\left(\frac{(2u-1)x^2 + 2u(x-u)}{2x^2 u\sqrt{u(u-1)}}\right),$$
$$\sigma_{Unp} = 4\pi r_0^2 \frac{m^2}{s}\left(\frac{3-w^4}{2}\ln\frac{1+w}{1-w} - w(2-w^2)\right). \qquad (181)$$

It is the same Breit Wheeler formula as one obtained for linear polarized laser Eq. (174). Variable w is defined by Eq. (175)

$$w = \sqrt{1 - \frac{1}{x}} = \sqrt{1 - \frac{(2m)^2}{s}}.$$

Cross sections for polarized high energy photon interacting with $n = 1$ laser photon in the approximation of a weak field are

$$\frac{d\sigma_p}{du} = 4\pi r_0^2 \frac{m^2}{s}\left(\frac{u^2(2x-1)}{x^2 u\sqrt{u(u-1)}}\right),$$

$$\sigma_p = 4\pi r_0^2 \frac{m^2}{s}\left(\frac{(1-w^2)(1+w^2)}{2}\ln\frac{1+w}{1-w} + w(1+w^2)\right), \qquad (182)$$

$$\frac{d\sigma_n}{du} = 4\pi r_0^2 \frac{m^2}{s}\left(\frac{(x-u)(2ux-x-u)}{x^2 u\sqrt{u(u-1)}}\right),$$

$$\sigma_n = 4\pi r_0^2 \frac{m^2}{s}\left(\frac{5-w^4}{2}\ln\frac{1+w}{1-w} - w(5-w^2)\right). \qquad (183)$$

The difference between "p" (positive helicity) and "n" (negative helicity) polarizations has the form

$$\frac{d\sigma_p}{du} - \frac{d\sigma_n}{du} = 4\pi r_0^2 \frac{m^2}{s}\left(\frac{x(2u-x)(2u-1)}{x^2 u\sqrt{u(u-1)}}\right).$$

The sign of the above expression is defined by $(2u-x)$. Because u varies in the range $u=1$ to $u=x$ "p" cross section is always less than "n" cross section in the region $u=[1...x/2]$, always higher in the region $u=[x/2...x]$ and equal to "n" cross section for $u=x/2$.

The total asymmetry in pair production will depend on the relative contributions from the regions $u=[1..x/2]$ and $u=[x/2..x]$. It is negative for the parameter $x\approx 1$ near the threshold where the pair creation is dominated by the region $u=1$ and it is positive for $x\gg 1$ far from threshold where the pair creation is dominated by $u=x$. Dependence of the total asymmetry versus the parameter x for $n=1$ is plotted in Fig. 86. It has the above features: negative total asymmetry for $x\approx 1$ and positive total asymmetry for $x\gg 1$. Zero total asymmetry $A_{tot}=0$ corresponds to the parameter $x\approx 3.804$. The asymptotic behavior of the total asymmetry is

$$A_{tot}(w\to 0) = -1+\frac{8}{3}w^2+O(w^3), \qquad \lim_{w\to 0} A = -1,$$

$$A_{tot}(x\to\infty) = +\frac{\ln(4x)-3}{\ln(4x)-1}+O\left(\frac{1}{x}\right), \qquad \lim_{x\to\infty} A = +1.$$

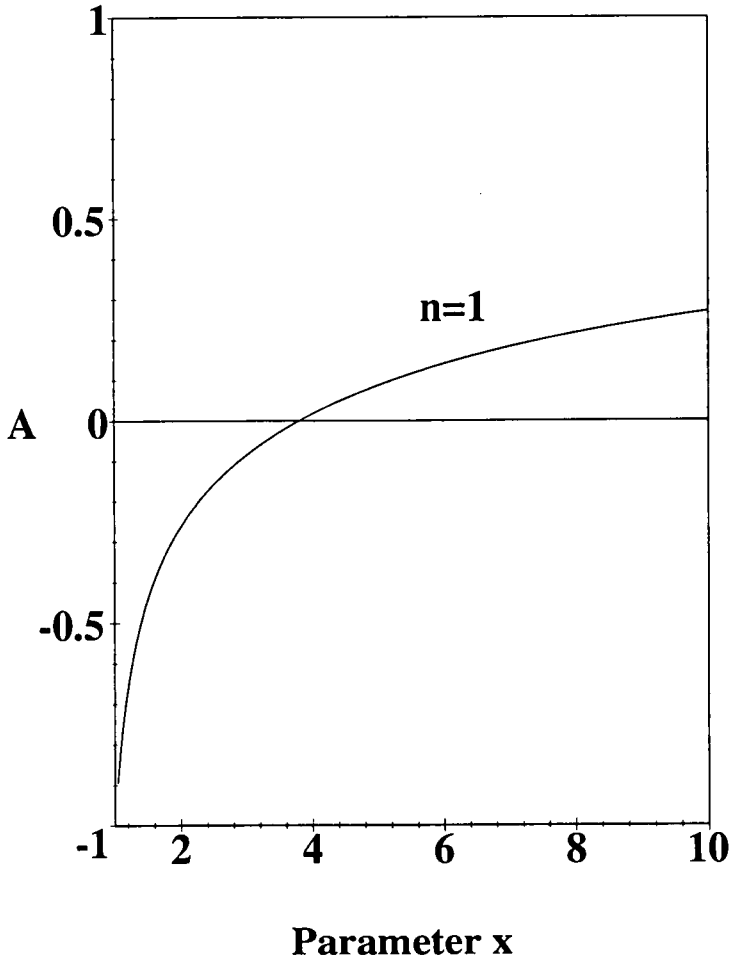

Figure 86: Total asymmetry for $n = 1$ positron production in the focus of circular polarized laser versus the parameter x for arbitrary laser frequency.

The asymptotic behavior of the Breit-Wheeler cross sections for $w \to 0$ (positron production at the threshold) is

$$\begin{aligned}
\sigma_{Unp}(w \to 0) &= 4\pi r_0^2 \frac{m^2}{\mathrm{s}} \left(w + 2w^3 + O(w^4) \right) , \\
\sigma_{p}(w \to 0) &= 4\pi r_0^2 \frac{m^2}{\mathrm{s}} \left(2w + \frac{4}{3} w^3 + O(w^4) \right) , \\
\sigma_{n}(w \to 0) &= 4\pi r_0^2 \frac{m^2}{\mathrm{s}} \left(\frac{8}{3} w^3 + O(w^4) \right) .
\end{aligned}$$

E η^2 series expansions of the multi-photon cross-section for circular and linear polarized laser and unpolarized electron beam

We present series expansion of cross sections in terms of the field intensity η for nonlinear Compton scattering of an electron incident on green laser with linear and circular polarizations.

We start with cross section formulae for linear and circular polarizations Eqs. (156) and (165)

$$\sigma_{Unp,Lin} = 4\pi r_0^2 \frac{m^2}{(\mathrm{s}-m^2)} \frac{1}{\eta^2} \frac{1}{2\pi} \int_{u=0}^{u_n} \int_{\phi=0}^{2\pi} \frac{du\, d\phi}{(1+u)^2} \left[-2A_0^2 + 2\eta^2 \left(2 + \frac{u^2}{(1+u)} \right) (A_1^2 - A_0 A_2) \right] ,$$

$$\sigma_{Unp,Circ} = 4\pi r_0^2 \frac{m^2}{(\mathrm{s}-m^2)} \frac{1}{\eta^2} \int_{u=0}^{u_n} \frac{du}{(1+u)^2} \left[-2\, {J_n}^2 + \eta^2 \left(1 + \frac{u^2}{2\,(u+1)} \right) ({J_{n-1}}^2 + {J_{n+1}}^2 - 2\, {J_n}^2) \right] .$$

For 46.6 GeV electron beam incident on 2.35 eV (Green) laser at 17° $\mathrm{s} = 2.64\, m^2$ and

$$4\pi r_0^2 \frac{m^2}{\mathrm{s}-m^2} = 0.61 \text{ barn} .$$

Series expansion of the integrals in the right side of the above expressions in terms of the field intensity η for $n = 1, 2, 3, 4, 5, 6, 7$ laser photons are

$$\sigma_1^{(c)} = \left[.510 - .513\, \eta^2 + .595\, \eta^4 - .710\, \eta^6 + O(\eta^8) \right] \times 0.61 \text{ barn} ,$$
$$\sigma_1^{(l)} = \left[.510 - .448\, \eta^2 + .463\, \eta^4 - .505\, \eta^6 + O(\eta^8) \right] \times 0.61 \text{ barn} ,$$

$$\sigma_2^{(c)} = \left[.406\,\eta^2 - .990\,\eta^4 + 1.86\,\eta^6 - 3.12\,\eta^8 + O(\eta^{10})\right] \times 0.61 \text{ barn},$$
$$\sigma_2^{(l)} = \left[.309\,\eta^2 - .684\,\eta^4 + 1.19\,\eta^6 - 1.85\,\eta^8 + O(\eta^{10})\right] \times 0.61 \text{ barn},$$

$$\sigma_3^{(c)} = \left[.447\,\eta^4 - 1.76\,\eta^6 + 4.63\,\eta^8 - 10.0\,\eta^{10} + O(\eta^{12})\right] \times 0.61 \text{ barn},$$
$$\sigma_3^{(l)} = \left[.298\,\eta^4 - 1.09\,\eta^6 + 2.68\,\eta^8 - 5.42\,\eta^{10} + O(\eta^{12})\right] \times 0.61 \text{ barn},$$

$$\sigma_4^{(c)} = \left[.571\,\eta^6 - 3.12\,\eta^8 + 10.5\,\eta^{10} - 27.9\,\eta^{12} + O(\eta^{14})\right] \times 0.61 \text{ barn},$$
$$\sigma_4^{(l)} = \left[.350\,\eta^6 - 1.78\,\eta^8 + 5.62\,\eta^{10} + O(\eta^{12})\right] \times 0.61 \text{ barn},$$

$$\sigma_5^{(c)} = \left[.794\,\eta^8 - 5.52\,\eta^{10} + 22.7\,\eta^{12} - 71.5\,\eta^{14} + O(\eta^{16})\right] \times 0.61 \text{ barn},$$
$$\sigma_5^{(l)} = \left[.450\,\eta^8 - 2.93\,\eta^{10} + 11.3\,\eta^{12} + O(\eta^{14})\right] \times 0.61 \text{ barn},$$

$$\sigma_6^{(c)} = \left[1.16\,\eta^{10} - 9.79\,\eta^{12} + 47.5\,\eta^{14} - 173.\,\eta^{16} + O(\eta^{18})\right] \times 0.61 \text{ barn},$$
$$\sigma_6^{(l)} = \left[.611\,\eta^{10} - 4.83\,\eta^{12} + 22.0\,\eta^{14} + O(\eta^{16})\right] \times 0.61 \text{ barn},$$

$$\sigma_7^{(c)} = \left[1.75\,\eta^{12} - 17.4\,\eta^{14} + 97.5\,\eta^{16} - 404.\,\eta^{18} + O(\eta^{20})\right] \times 0.61 \text{ barn},$$
$$\sigma_7^{(l)} = \left[.860\,\eta^{12} - 8.00\,\eta^{14} + 42.1\,\eta^{16} + O(\eta^{18})\right] \times 0.61 \text{ barn},$$

where $\sigma_n^{(c)}$ is the cross-section for n circular polarized laser photons; $\sigma_n^{(l)}$ is the cross-section for n linear polarized laser photons.

Note that higher order Compton cross sections for linear polarized laser are lower than that for circular polarized laser.

F η^2 series expansions of the cross-sections for e^+ e^- pair production for circular and linear polarized laser and unpolarized electron beam

We present series expansion of cross-sections in terms of the field intensity η for e^+e^- pair production in interaction of a high energy photon incident on green laser with linear and circular polarizations.

We start with cross section formulae for linear and circular polarizations Eqs. (170) and (178)

$$\sigma_{Unp,Lin} = 4\pi\, r_0^2 \frac{m^2}{\mathrm{s}} \frac{1}{\eta^2} \frac{1}{2\pi} \int_{u=1}^{u_n} \int_{\phi=0}^{2\pi} \frac{du\, d\phi}{u\sqrt{u(u-1)}} \left[A_0^2 + 2\eta^2(2u-1)(A_1^2 - A_0 A_2)\right] ,$$

$$\sigma_{Unp,Circ} = 4\pi r_0^2 \frac{m^2}{\mathrm{s}} \frac{1}{\eta^2} \int_{u=1}^{u_n} \frac{du}{u\sqrt{u(u-1)}} \left[{J_n}^2 + \frac{\eta^2}{2}(2u-1)({J_{n-1}}^2 + {J_{n+1}}^2 - 2\, {J_n}^2) \right] .$$

We use examples of 200 GeV, 30 GeV and 29 GeV high energy photons incident on 2.35 eV (Green) laser. 200 GeV is an example of positron production above the threshold for $n = 1$ laser photon, 29 GeV and 30 GeV are energies close to the maximum energy of $n = 1$ backscattered laser photon ($\omega_{\mathrm{max}} = 28.9$ GeV at $\eta = 0$) in E144 experiment.

For 200 GeV photon $\mathrm{s} = 7.20\, m^2$ and $4\pi r_0^2 \frac{m^2}{\mathrm{s}} = 0.14$ barn.

For 29 GeV and 30 GeV photons $\mathrm{s} = 1.04\, m^2$ and $1.08\, m^2$ correspondently and $4\pi r_0^2 \frac{m^2}{\mathrm{s}} = 0.96$ barn and 0.93 barn correspondently.

Series expansion of the integrals in the right side of the above expressions in terms

of the field intensity η for 200 GeV high energy photon and $n = 1, 2, 3, 4, 5, 6, 7$ Green laser photons are

$$\begin{aligned}
\sigma_1^{(c)} &= \left[2.36 - 2.74\,\eta^2 + 4.62\,\eta^4 + O(\eta^6)\right] \times 0.14 \text{ barn}, \\
\sigma_1^{(l)} &= \left[2.36 - 1.87\,\eta^2 + 1.91\,\eta^4 + O(\eta^6)\right] \times 0.14 \text{ barn}, \\
\\
\sigma_2^{(c)} &= \left[3.35\,\eta^2 - 9.09\,\eta^4 + 12.1\,\eta^6 + O(\eta^8)\right] \times 0.14 \text{ barn}, \\
\sigma_2^{(l)} &= \left[2.74\,\eta^2 - 5.77\,\eta^4 + 9.62\,\eta^6 + O(\eta^8)\right] \times 0.14 \text{ barn}, \\
\\
\sigma_3^{(c)} &= \left[3.81\,\eta^4 - 14.1\,\eta^6 + 33.9\,\eta^8 + O(\eta^{10})\right] \times 0.14 \text{ barn}, \\
\sigma_3^{(l)} &= \left[2.64\,\eta^4 - 9.03\,\eta^6 + 21.0\,\eta^8 + O(\eta^{10})\right] \times 0.14 \text{ barn}, \\
\\
\sigma_4^{(c)} &= \left[4.30\,\eta^6 - 21.7\,\eta^8 + 68.6\,\eta^{10} + O(\eta^{12})\right] \times 0.14 \text{ barn}, \\
\sigma_4^{(l)} &= \left[2.69\,\eta^6 - 12.8\,\eta^8 + 38.5\,\eta^{10} + O(\eta^{12})\right] \times 0.14 \text{ barn}, \\
\\
\sigma_5^{(c)} &= \left[5.35\,\eta^8 - 34.9\,\eta^{10} + 137.\,\eta^{12} + O(\eta^{14})\right] \times 0.14 \text{ barn}, \\
\sigma_5^{(l)} &= \left[3.02\,\eta^8 - 18.6\,\eta^{10} + 69.1\,\eta^{12} + O(\eta^{14})\right] \times 0.14 \text{ barn}, \\
\\
\sigma_6^{(c)} &= \left[7.16\,\eta^{10} - 57.9\,\eta^{12} + 272.\,\eta^{14} + O(\eta^{16})\right] \times 0.14 \text{ barn}, \\
\sigma_6^{(l)} &= \left[3.71\,\eta^{10} - 28.6\,\eta^{12} + 125.\,\eta^{14} + O(\eta^{16})\right] \times 0.14 \text{ barn}, \\
\\
\sigma_7^{(c)} &= \left[10.2\,\eta^{12} - 98.0\,\eta^{14} + 535.\,\eta^{16} + O(\eta^{18})\right] \times 0.14 \text{ barn}, \\
\sigma_7^{(l)} &= \left[5.15\,\eta^{12} - 43.9\,\eta^{14} + 213.\,\eta^{16} + O(\eta^{18})\right] \times 0.14 \text{ barn}.
\end{aligned}$$

Series expansion of the integrals in terms of the field intensity η for 29 GeV high energy photon and $n = 4, 5, 6, 7$ Green laser photons are

$$\sigma_4^{(c)} = \left[.0000599\,\eta^6 - .0126\,\eta^8 + .963\,\eta^{10} + O(\eta^{12})\right] \times 0.96 \text{ barn},$$
$$\sigma_4^{(l)} = \left[.225\,\eta^6 - .882\,\eta^8 + 2.25\,\eta^{10} + O(\eta^{12})\right] \times 0.96 \text{ barn},$$

$$\sigma_5^{(c)} = \left[.330\,\eta^8 - 6.65\,\eta^{10} + 59.1\,\eta^{12} + O(\eta^{14})\right] \times 0.96 \text{ barn},$$
$$\sigma_5^{(l)} = \left[.939\,\eta^8 - 5.60\,\eta^{10} + 18.0\,\eta^{12} + O(\eta^{14})\right] \times 0.96 \text{ barn},$$

$$\sigma_6^{(c)} = \left[2.34\,\eta^{10} - 35.0\,\eta^{12} + 252.\,\eta^{14} + O(\eta^{16})\right] \times 0.96 \text{ barn},$$
$$\sigma_6^{(l)} = \left[1.82\,\eta^{10} - 18.4\,\eta^{12} + 79.2\,\eta^{14} + O(\eta^{16})\right] \times 0.96 \text{ barn},$$

$$\sigma_7^{(c)} = \left[7.56\,\eta^{12} - 104.\,\eta^{14} + 711.\,\eta^{16} + O(\eta^{18})\right] \times 0.96 \text{ barn},$$
$$\sigma_7^{(l)} = \left[4.44\,\eta^{12} - 48.2\,\eta^{14} + +O(\eta^{16})\right] \times 0.96 \text{ barn}.$$

Series expansion of the integrals in terms of the field intensity η for 30 GeV high energy photon and $n = 4, 5, 6, 7$ Green laser photons are

$$\sigma_4^{(c)} = \left[.00270\,\eta^6 - .190\,\eta^8 + 4.92\,\eta^{10} + O(\eta^{12})\right] \times 0.93 \text{ barn},$$
$$\sigma_4^{(l)} = \left[.319\,\eta^6 - 1.38\,\eta^8 + 3.39\,\eta^{10} + O(\eta^{12})\right] \times 0.93 \text{ barn},$$

$$\sigma_5^{(c)} = \left[.512\,\eta^8 - 9.19\,\eta^{10} + 73.9\,\eta^{12} + O(\eta^{14})\right] \times 0.93 \text{ barn},$$
$$\sigma_5^{(l)} = \left[.990\,\eta^8 - 6.49\,\eta^{10} + 22.2\,\eta^{12} + O(\eta^{14})\right] \times 0.93 \text{ barn},$$

$$\sigma_6^{(c)} = \left[2.91\,\eta^{10} - 40.9\,\eta^{12} + 280.\,\eta^{14} + O(\eta^{16})\right] \times 0.93 \text{ barn},$$
$$\sigma_6^{(l)} = \left[2.75\,\eta^{10} - 11.9\,\eta^{12} + 76.8\,\eta^{14} + O(\eta^{16})\right] \times 0.93 \text{ barn},$$

$$\sigma_7^{(c)} = \left[8.54\,\eta^{12} - 112.\,\eta^{14} + 747.\,\eta^{16} + O(\eta^{18})\right] \times 0.93 \text{ barn},$$

$$\sigma_7^{(l)} = \left[11.3\,\eta^{12} - 44.9\,\eta^{14} + O(\eta^{16})\right] \times 0.93 \text{ barn}\,.$$

Evaluation of the ratio Linear over Circular cross section for pair production for each order n is summarized in Table 8.

Table 8: Ratio of e^+e^- pair production rates for Linear/Circular laser polarizations versus the number of laser photons for lase intensity $\eta = 0.158$. 29 GeV, 30 GeV, 200 GeV monochromatic photon beams incident at 2.35 eV laser beam at 17°. Calculations from series expansions.

Number of laser photons	1	2	3	4	5	6	7
Circular/Linear ratio, 29 GeV	-	-	-	.0017	0.25	1.14	1.54
Circular/Linear ratio, 30 GeV	-	-	-	.0036	0.39	0.82	0.89
Circular/Linear ratio, 200 GeV	0.99	1.20	1.43	1.59	1.76	1.91	1.92

Above the threshold (200 GeV example) e^+e^- pair production cross-section for circular laser polarization is larger than that for linear laser polarization. At the threshold (29 GeV, 30 GeV and $n = 4, 5$) cross-section for linear laser polarization is larger. The latter has an explanation in the relative angular momentum of the e^+e^- pair created near the threshold by circular polarized laser. Indeed spin of $n = 4$ coherent laser photons with circular polarization interacting with 1 high energy photon is 4 ± 1, hence e^+e^- pair should be created with large relative angular momentum and the phase space for the final state is reduced compared to that for the linear polarized laser.

To calculate the combined effect of all orders n involved in e^+e^- pair production for a strong field one should evaluate cross-sections for different orders n for a given field intensity η. The evaluation of the ratio Linear over Circular cross section is

summarized in Table 9.

One can see that linear laser polarization is favorable for the e^+e^- pair production in E144 experiment. Total positron rate is expected to be higher for linear laser polarization (depending on the laser intensity) than that for circular laser polarization.

The difference between circular and linear laser polarizations becomes smaller at higher laser intensities and vanishes for $\eta \gg 1$.

Table 9: Ratio of e^+e^- pair production rates for Circular/Linear laser polarizations versus laser intensity. 29 GeV, 30 GeV, 200 GeV monochromatic photon beams incident at 2.35 eV laser beam at 17°.

Laser intensity η	0.05	0.087	0.158	0.274
Linear/Circular rate ratio, 29 GeV	270	99	35	9.0
Linear/Circular rate ratio, 30 GeV	91	62	29	6.8
Linear/Circular rate ratio, 200 GeV	1.00	1.00	1.00	1.00

G Discussion of polarization effects in positron production below the kinematic threshold for one laser photon: E144 experiment

In E144 experiment a 46.6 GeV electron beam collides with Green ($\omega = 2.35$ eV) or IR ($\omega = 1.17$ eV) laser at 17°, which corresponds to the parameter x for Compton scattering of 1.64 for Green laser and 0.82 for IR laser.

As an example we calculate the maximum energy of backscattered photons

$$\omega_n^{max} = E_e \frac{n\,x}{1+\eta^2+n\,x}\,,$$
$$\omega_n^{max} = 28.9\,(n=1) \quad 35.7\,(n=2) \text{ GeV for green laser, } \eta = 0\,,$$
$$\omega_n^{max} = 21.0\,(n=1) \quad 28.9\,(n=2) \text{ GeV for IR laser, } \eta = 0\,.$$

The maximum energy of backscattered photons is lower for higher field intensities η.

In general case if the high energy photon is produced through multiphoton Compton scattering of an electron involving n_0 laser photons in a region with intensity η_0, and an e^+e^- pair is produced through interaction of this photon with n laser photons in a region with intensity η then the kinematic parameter x is

$$x \geq \frac{2}{n}\left(1+\sqrt{1+\frac{n}{n_0}\frac{1+\eta_0^2}{1+\eta^2}}\right)(1+\eta^2)\,.$$

The equal sign in the above equation corresponds to the e^+e^- pair production at the threshold for corresponding field intensities. We will call this value $x(n,n_0)$. The condition for pair production can be written then as

$$x(n,n_0) = \frac{2}{n}\left(1+\sqrt{1+\frac{n}{n_0}\frac{1+\eta_0^2}{1+\eta^2}}\right)(1+\eta^2)\,,$$
$$x(n,n_0) \leq x\,.$$

Value of the parameter $x(n, n_0)$ at $\eta = \eta_0 = 0$ for different n, n_0 are presented below

$$
\begin{aligned}
x(1,1) &= 4.83 \quad x(1,2) = 4.45 \quad x(1,3) = 4.31 \quad x(1,4) = 4.24 \\
x(2,1) &= 2.73 \quad x(2,2) = 2.41 \quad x(2,3) = 2.29 \quad x(2,4) = 2.22 \\
x(3,1) &= 2.00 \quad x(3,2) = 1.72 \quad x(3,3) = 1.61 \quad x(3,4) = 1.55 \\
x(4,1) &= 1.62 \quad x(4,2) = 1.37 \quad x(4,3) = 1.26 \quad x(4,4) = 1.21 \\
x(5,1) &= 1.38 \quad x(5,2) = 1.15 \quad x(5,3) = 1.05 \quad x(5,4) = 1.00 \\
x(6,1) &= 1.22 \quad x(6,2) = 1.00 \quad x(6,3) = 0.91 \quad x(6,4) = 0.86 \\
x(7,1) &= 1.09 \quad x(7,2) = 0.89 \quad x(7,3) = 0.81 \quad x(7,4) = 0.76 \\
x(8,1) &= 1.00 \quad x(8,2) = 0.81 \quad x(8,3) = 0.73 \\
x(9,1) &= 0.93 \quad x(9,2) = 0.74 \\
x(10,1) &= 0.86
\end{aligned}
$$

Because $x(n, n_0)$ is less than $x = 1.64$ for Green laser and $x = 0.82$ for IR laser the total number of photons $N = n + n_0$ involved in positron production should be at least 5 ($n = 4, n_0 = 1$) for Green laser and 10 ($n = 8, n_0 = 2$ or $n = 7, n_0 = 3$) for IR laser.

By minimization of the expression for $x(n, n_0)$ it is easy to show that for a given x the minimum number of laser photons required to produce a pair is $N = \dfrac{8}{x}$ where $N = n + n_0$, $n_0 = \frac{1}{4} N$ and $n = \frac{3}{4} N$.

For instance $x = 0.82$ (IR laser) corresponds to $N = 9.7$, $n_0 = 2.4$ and $n = 7.3$. The closest integer numbers are $N = 10$, $n_0 = 3$, $n = 7$ and $N = 10$, $n_0 = 2$, $n = 8$ in agreement with the above result.

The above arguments suggest that the minimum configuration to produce a pair with green laser is $N = 5$, $n_0 = 1$ and $n = 4$. But $N = 5, n = 4$ process is only possible at very small field intensities $\eta \to 0$ ($x(4,1) = 1.62$ versus $x = 1.64$) when

positron rate is also negligible. At higher field intensities value of $x(4,1)$ increases - for instance $x(4,1) = 1.66$ for $\eta = 0.2$, $\eta_0 = 0$ and positron production is forbidden kinematically. For positron production cross-sections to be large enough field intensity should be high $\eta > 0.2$ and hence $N = 5$ channel is forbidden kinematically. Positrons are produced in E144 through $N = 6$ process with n=4 $(x(4,2)_{min} = 1.37)$ or n=5 $(x(5,1)_{min} = 1.38)$. Processes with $n = 3, 2, 1$ are negligible because they have larger $x(n, n_0)$ (for example $x(3,3)_{min} = 1.61$). For $n = 5$ $A_{tot} = -1$ at $u_n = 1$ but rapidly increases to the level $A_{tot} = -0.3$ at $u_n > 1.05$; for $n = 4$ $A_{tot} = 0$ at $u_n = 1$ and also rapidly decreases to the level $A_{tot} = -0.3$ (Figure 82). Involvement of higher orders N reduces the cross-section proportional to η^{-2N} but increases the "gap" of allowed positron energies.

We will assume that the main contribution to the pair production is from the $N = 6$ processes: $(n = 5, n_0 = 1)$ or $(n = 4, n_0 = 2)$. Then

$$N_{tot}^{(n=5,n_0=1)} \approx N_{tot,Unp}^{(n=5,n_0=1)} \left(1 + P(u_1)\, A_{tot}^{(n=5)}\right),$$
$$N_{tot}^{(n=4,n_0=2)} \approx N_{tot,Unp}^{(n=4,n_0=2)} \left(1 + P(u_2)\, A_{tot}^{(n=4)}\right).$$

For linear polarized laser: Taking $P(u_1) \approx 0.67$ $P(u_2) \approx 0$ (Figure 72) and $A_{tot}^{(n=4,5)} \approx -0.3 \div -0.4$ (Figure 82) (average of fast oscillating total asymmetry functions versus u_n for $n = 4, 5$) we get

$$\sigma_{tot}^{(n=5,n_0=1)} \approx 0.75 \div 0.80\, \sigma_{Unp}^{(n=5,n_0=1)}, \quad \sigma_{tot}^{(n=4,n_0=2)} \approx 1.00\, \sigma_{Unp}^{(n=4,n_0=2)}.$$

In average correction less than $-20 \div -25\%$ should be applied to calculations with unpolarized cross sections to get the correct positron rate.

A more accurate estimate should involve different weights for different processes and different orders N.

Exact calculations with numerical integration method gave the overall effect of polarization for E144 equal to factor 0.75 at $\eta = 0.2$, 0.77 at $\eta = 0.32$ and 0.82 at $\eta = 1$ in good agreement with the above estimate.

For circular polarized laser: Taking $P(u_1) = P(u_2) \approx 1$ (Figure 77) and

$$\begin{aligned} A_{tot}^{(n=4)} &\approx -1 \quad (u_n \approx 1)\,, \\ A_{tot}^{(n=5)} &\approx -0.5 \quad (u_n \approx 5/4)\,, \\ A_{tot}^{(n=6)} &\approx -0.3 \quad (u_n \approx 6/4)\,, \\ A_{tot}^{(n=7)} &\approx -0.2 \quad (u_n \approx 7/4)\,, \end{aligned}$$

we get (see Figure 85)

$$\begin{aligned} \sigma_{tot}^{(n=4)} &\approx 0.0\,\sigma_{Unp}\,, \\ \sigma_{tot}^{(n=5)} &\approx 0.5\,\sigma_{Unp}\,, \\ \sigma_{tot}^{(n=6)} &\approx 0.7\,\sigma_{Unp}\,, \\ \sigma_{tot}^{(n=7)} &\approx 0.8\,\sigma_{Unp}\,. \end{aligned}$$

Assuming again that the main contribution to the positron production for circular polarized laser is from the processes $N = 6$ $(n = 5, n_0 = 1)$ or $(n = 4, n_0 = 2)$ we conclude

$$\sigma_{tot}^{(n=5,n_0=1)} \approx 0.50\,\sigma_{Unp}^{(n=5,n_0=1)}\,, \quad \sigma_{tot}^{(n=4,n_0=2)} \approx 0.00\,\sigma_{Unp}^{(n=4,n_0=2)} = 0\,,$$

$$\sigma_{tot} < 0.5\,\sigma_{Unp}\,.$$

On average there should be more than -50% correction to calculations with unpolarized cross sections.

More accurate estimate should involve different weights for different processes and different orders N. No calculations using numerical integration method have been done so far for circular polarized laser.

From the above estimates we can conclude that for positron production in E144 linear polarization has factor > 2 advantage compared to circular polarization due to effects of polarization of intermediate photon. This is in addition to higher unpolarized cross section for linear polarization compared to circular one (see Figs. 9, 10).

VITA

Konstantin Dmitrievich Shmakov was born in Khimki, Moscow district of Russia on November 2, 1963. He graduated from the Moscow Institute of Physics and Technology (MPTI) faculty of the General and Applied Physics in 1987 with the Master of Science degree in experimental high energy and nuclear physics. From 1987 to 1991 he work as a researcher at the Institute of Theoretical and Experimental Physics (ITEP) in Moscow and was a member of L3 Collaboration at CERN. In 1991 he joint L* project at SSC and later GEM Collaboration working within a group of physicists at Oak Ridge National Laboratory and the University of Tennessee. In 1994 he joint the University of Tennessee to pursue the Doctor of Philosophy degree in Physics and joint experiment E144 at SLAC. The doctoral degree was received in 1997.